UNIVERSITA' DEGLI STUDI DI CATANIA
DIEEI: DIPARTIMENTO DI INGEGNERIA ELETTRICA
ELETTRONICA ED INFORMATICA

PhD in ENERGETIC
XXVIII CYCLE

FAULT TOLERANT SOLUTIONS FOR AC MULTIDRIVE SYSTEMS

Mario Pulvirenti

PhD Coordinator	**Prof. L. Marletta**
Tutor	**Prof. G. Scarcella**
Co-Supervisor	**Prof. G. Scelba**

A. A. 2013-2015

Acknowledgments

First of all, I would like to express deep appreciation to my supervisors: Prof. G. Scarcella and Prof. G. Scelba, this research report has been developed thanks to their guidance and valuable advices.

Secondly, I would like to thank the Department of Electrical and Electronic Engineering and Computer Science of the University of Catania and the “CePTIT” center. This center has been my second home, during the last three years, where I have studied, talked and realized many things together with other colleagues and students.

Therefore I would like to acknowledge: Angelo Sciacca, we have shared many experiences since January 2013; and all the other members of CePTIT team: Dario Bazzano, Salvo Foti, Daniele Caruso, Gianni Nobile and Luca Finocchiaro.

I would like to thank and remember our Prof. A. Consoli.

I will always appreciate the great opportunity to study for 6 months in USA, at the “WEMPEC”, Wisconsin Electrical Machine Power Electronic Consortium, of the University of Wisconsin, Madison. I need to thank Prof. R.D. Lorenz for his availability, passion and great energy; all the WEMPEC staff, in particular Mrs. H. Demont and all the WEMPEC students, especially: Huthaifa, Yukai, Caleb, Yinghan, Ramin, Yuying, Guangqi, Cong, Kang, Jiejian; and also Junjian, Apoorva, Brent, Teng and Tim^2., with them I had a great time. Special thanks also to Ryoko Imamura, the first colleague that I met in ME building, on August 19, 2014.

I would like to thank my colleagues: Eugenio, Giuseppe, Marco and Alessandro, with them I had unforgettable moments during the master degree courses.

I would like to thank my friends: Alessandro, Filippo and Rosario, we will always find, everywhere we are, few minutes to talk on Skype !

Last but not least, I need to thank my parents, my little cousins: Giorgia and Marco and all people that I am forgetting now ! :)

Mario Pulvirenti
December 10, 2015

Table of Contents

Acknowledgements ... i

Table of Contents ... ii

List of Figures ... v

List of Tables ... xii

Nomenclature ... xiii

Introduction ... 1

Research Contributions ... 1

Summary of Chapters ... 2

Chapter 1 State - of - the – Art: Review ... 3

- **1.1 Multi-drive systems** ... 3
  - **1.1.1 MDS with multiphase machines** ... 6
  - **1.1.2 MDS with reduced components** ... 9
  - **1.1.3 Fault tolerant drive systems and converter topologies** ... 15
- **1.2 Control techniques and machine modeling for post-fault operations** ... 22
  - **1.2.1 Modeling and control of an IM** ... 25
    - **A. Analytical model in healthy conditions** ... 25
    - **B. Analytical model under faulty conditions** ... 28
    - **C. Equations in qd0 variables for healthy conditions** ... 30
    - **D. Field oriented control of the healthy IM** ... 34
    - **E. Equations in qd0 variables for the faulty conditions** ... 39
    - **F. Field oriented control of the faulty IM** ... 44
  - **1.2.2 PMSM modeling and control** ... 48
    - **A. Analytical model in healthy conditions** ... 48
    - **B. Analytical model under faulty conditions** ... 50
    - **C. Equations in qd0 synchronous reference frame for healthy conditions and field orientation** ... 51
    - **D. Equations in qd0 variable for faulty conditions and field orientation** ... 54
- **1.3 Conclusions** ... 58
- **1.4 References** ... 59

Chapter 2 Fault tolerant Multi-Drive System ... 64

- **2.1 Fault Tolerant Multi-Drive Systems** ... 64

2.2 Common Mode Voltage analysis 69
2.3 Numerical simulations and experimental results 75
2.4 MDS with motors mechanically coupled 79
  2.4.1 Experimental results for mechanically coupled MDS 84
2.5 Conclusions 89
2.6 References 90

Chapter 3 Fault tolerant Wind Power Systems 92
3.1 Introduction 92
  3.1.1 Fault Tolerant Wind Power Systems 94
3.2 Functionality and operating limits 102
  3.2.1 Wind Turbine Model 102
  3.2.2 Generator Side Converter Control 109
  3.2.3 Grid Side Converter Control 110
    A. Modeling of the grid side circuit in phase variables 112
    B. Modeling of the grid side circuit in the qd0 reference frame 113
    C. LCL Filter Design 116
    D. Modeling of the grid side circuit with an open phase fault in phase and qd0 variables 117
3.3 Simulation and experimental results 123
3.4 Conclusions 133
3.5 References 134

Chapter 4 Current sharing strategies for Fault Tolerant AC Multi-Drive System 138
4.1 Current sharing control strategies 138
4.2 Losses and performance evaluation reduction 144
4.3 Simulation results 146
4.4 Experimental results 149
4.5 Conclusions 155

Chapter 5 Fault-Tolerant Mechanical Control Variables Estimation in AC Multi-Drive Systems Using Binary Hall-Effect Sensors 156
5.1 Introduction 156
  5.1.1 Model and control of a BLDC 164

5.2 Hall effect position sensors fault types and compensation 169
5.2.1 Fault Compensation 173
A. Fault compensation for the Vector Tracking Observer 173
B. Fault compensation for the Zero Order Algorithm 175
C Fault compensation for the Hybrid Observer 177
5.3 Simulation and experimental results 180
5.4 Fault tolerant Multi-Drive Systems with Binary Hall-Effect Sensors 192
5.5 Conclusions 192
5.6 References 193

Chapter 6 Conclusions and recommended future work 196

Appendix 198

Index of Figures

Figure 1.1 Series-parallel HEV by using a planetary gear unit.

Figure 1.2 Two machines HEV by using AMT and parallel axis gear trains.

Figure 1.3 Wheel drive systems for HEV and EV.

Figure 1.4 Multi Drive System configuration for heavy EV.

Figure 1.5 Standard three phase MDS topology.

Figure 1.6 Common mode current path in the proposed MDS configuration.

Figure 1.7:Connection diagram for 6-phases 2-motor system.

Figure 1.8: Two-motor five-phase drive system, supplied from a single VSI, with stator windings connected in parallel.

Figure 1.9 Reduced-switch-count ac dual drive.

Figure 1.10 Multi-motor drive configuration.

Figure 1.11 Equivalent circuits: a) inverter phase legs as voltage sources and b) ZSC of the main motor as the current return path of the two-phase motor.

Figure 1.12 Integrated dual ac drive for controlling two three-phase PM motors.

Figure 1.13 Amplitude of the maximum output voltage vectors and the maximum voltage circle obtainable with configuration of proposed in [18] (left), the maximum output voltage circle generated by a three-leg inverter (right).

Figure 1.14 Nine switch- three-phase inverter block diagram.

Figure 1.15 Configuration of the multi-machine drive system comprising n three-phase machines supplied from a (2n+1)-leg inverter.

Figure 1.16 Coupled motors configuration for submarine application.

Figure 1.17 block diagram of the dual fault- tolerant motor drive.

Figure 1.18 Topology for isolating a short circuited inverter switch.

Figure 1.19 Double switch redundant topology.

Figure 1.20 Phase redundant topology.

Figure 1.21 Cascaded inverter topology with additional triacs for fault isolation.

Figure 1.22 Fault- tolerant VSI topology.

Figure 1.23 Fault tolerant converter configuration.

Figure 1.24 Reconfiguration of the electrical connections of the two-motor system through appropriate on/off switches after a fault in one inverter leg.

Figure 1.25 Induction motor drive with machine neutral point connected to the dc bus midpoint.

Figure 1.26 Five- phase current regulated PWM inverter drive.

Figure 1.27 Phasor relationships before and after open-circuit of a) phase a, b) phase b, c) phase c.

Figure 1.28 Two pole, three phase symmetrical induction machine.
Figure 1.29 Stator and rotor windings representation in phase coordinates.
Figure 1.30 Projection of the phase coordinate quantities on the qd0 reference frame.
Figure 1.31 qd current components with the reference axes oriented to the rotor flux.
Figure 1.32 Non Linear state block diagram of the IM.
Figure 1.33 Block diagram of the Rotor Flux Field Oriented Control for IM.
Figure 1.34 Fault tolerant control block diagram for Rotor Flux Indirect Field Orientation.
Figure 1. 35 Fault tolerant IFOC for IM in normal operative conditions and after a fault on phase b.
Figure 1.36 Block diagram for the Field Orientated control of PM synchronous machine.
Figure 1.37 Fault tolerant control block diagram for FOC of PMSM.

Figure 2.1 Fault tolerant Multi-drive topology.
Figure 2.2 Sharing current strategy in case of a single faulted drive.
Figure 2.3 Sharing current strategy in case of a single faulted drive.
Figure 2.4 MDS with all drives working in healthy conditions.
Figure 2.5 MDS with one drive working in fault conditions with all the neutral point connected together.
Figure 2.6 MDS with one drive operating with an open phase fault and three drives healthy used as feedback current path for the neutral current.
Figure 2.7 Zero sequence currents flowing in each motor.
Figure 2.8 MDS Experimental Setup.
Figure 2.9 Steady state test at no load, $\omega_{rm\_IM_1}$=30rad/s, $\omega_{rm\_IM_2}$=80rad/s , and $\omega_{rm\_IM_3}$=50rad/s.
Figure 2.10 First method: Speed transients occurring at IM_2: $\omega_{rm\_IM_2}$=-30/30 rad/s and IM3: $\omega_{rm\_IM_3}$=40/-40 rad/s, while IM1operates at $\omega_{rm\_IM_1}$=50 rad/s.
Figure 2.11 MDS with two motors mechanically coupled to the same shaft.
Figure 2.12 Single open phase fault on IM_2.
Figure 2.13 Single open phase fault.
Figure 2.14 Two single open phase faults.
Figure 2.15 Torque reduction caused by the deviation from the correct field orientation.
Figure 2.16 Single open phase fault in IM_1 and two open phase faults in IM_2.
Figure 2.17 Single open phase fault in IM_2 and two open phase faults in IM_1.

Figure 2.18 Speed Transient 80 rad/s — 30 rad/s: IM_1 operates with an open phase, while IM_2 initially operates in healthy conditions and after the instant time t^* works with an open phase.

Figure 2.19 Speed Transient 0 rad/s — 50 rad/s — 0 rad/s: IM_1 operates with an open phase while IM_2 works with two open phases.

Figure 2.20 Load transient T_{total_load}=100% T_{en}, ω_r=70 rad/s. The two motors are operating under single open phase fault in each motor and controlled by imposing $\theta_{\lambda r1} = \theta_{\lambda r2}$.

Figure 2.21 Load transient in the faulty motor IM_1, T_{load} =50% T_{en}. IM_2 spins at ω_{r2}=40 rad/s at no load, while IM_1 spins at ω_{r1}=60 rad/s.

Figure 2.22 Steady state test, ω_r=80 rad/s. DC bus ripple measurement with MDS under a single open phase fault in both drives; the neutral points of both electrical machines are directly connected to the middle point of the DC bus and the motors are independently controlled $\theta_{\lambda r1} \neq \theta_{\lambda r2}$.

Figure 2.23 Steady state test, ω_r=80 rad/s. DC bus ripple measurement with MDS under a single open phase fault in both drives; the neutral points of both electrical machines are connected to each other and isolated from the DC bus; in addition, the two motors are controlled imposing that $\theta_{\lambda r1} = \theta_{\lambda r2}$.

Figure 2.24 Ratio between ΔV_o and V_1 at different ω_{r1}.

Figure 2.25 Frequency spectrum of voltage phases of the two motors running under a single fault.

Figure 3.1 Standard configuration of WPS based on DFIG.

Figure 3.2 Standard configuration of WPS based on PMSG.

Figure 3.3 Configuration of WPS based on the Electrically excited synchronous generator.

Figure 3.4 Control system of wind turbine with fault-tolerant control strategy.

Figure 3.5 Fault- tolerant back-to-back converter topology with redundant 3L-FC-based leg for NP voltage balancing in normal operation mode and for substitution of a faulty leg on generator or grid side in fault operation mode.

Figure 3.6 Schematic diagram of FTC in VSWES with power regulation loop.

Figure 3.7 Fault-tolerant converter topologies: a) under normal operating conditions; b) After fault occurrences in power switches R_1 and I_1.

Figure 3.8 Fault-tolerant converter topologies: a) under normal operating conditions (two SSTC); b) after a fault in I_1 or I_2 (five- leg converter); c) after a fault in R_1, R_3or R_5 (TSTPR and SSTC).

Figure 3.9 Fault-tolerant converter topologies: a) under normal operating conditions and b) after fault on R_1 and I_1.

Figure 3.10 Fault tolerant WECS topology with DFIG.
Figure 3.11 Fault tolerant topology without redundancy.
Figure 3.12 Block diagram of the proposed FTWPS.
Figure 3.13 Schematic representation of the FTWPS operating with an open phase fault in the generator.
Figure 3.14 Block diagram of the wind turbine model.
Figure 3.15 Representation of the power coefficient, Cp, [17].
Figure 3.16 Power- Speed characteristics of a wind turbine.
Figure 3.17 Control regions of the WPS.
Figure 3.18 Block diagram for the fault tolerant control of the PMSG Converter.
Figure 3.19 Block diagram for the control of the Grid- side converter.
Figure 3.20 Single phase equivalent circuit relative to the phase "a" of the system: inverter, filter and transformer.
Figure 3.21 Block diagram for the representation of equation(3.2.3.15) and (3.2.3.16) in complex notation.
Figure 3.22 Equivalent representation of Figure 3.21 considering a perfect decoupling of cross-coupled terms.
Figure 3.23 Performance evaluation of the PMSG control in healthy condition.
Figure 3.24 Performance evaluation of the Grid Side system control.
Figure 3.25 Performance evaluation of the PMSG control under phase c fault.
Figure 3.26 Performance evaluation of the Grid side system under phase c fault on the PMSM.
Figure 3.27 Block diagram of the experimental setup.
Figure 3.28 Steady state tests with ω_{rm}=30 rad/s: phase currents, i_{og} and rotational speed ripple in the PMSG without a) and with b) third harmonic compensation.
Figure 3.29 Steady state tests: a)amplitude ratio V_3/V_1 and b) phase shift of the third harmonic compensation voltages.
Figure 3.30 Steady state test with the generator operating under an open phase: comparison of the zero sequence crurrent flowing through the transformer i_{otr} and filter i_{of}.
Figure 3.31 Speed transient ω_{rm} = [- 30 rad/s to 30 rad/s] in the PMSG, performed at 50% of rated load, with the generator operating under an open phase fault wihile the transformer is healthy operating.

Figure 3.32 Steady state test with transformer operating in faulty conditions, at 50% of the rated load: Line to line voltages v_{abstr}, v_{bcstr} at the secondary windings and phase currents i_{aptr}, i_{bptr} at the primary windings.

Figure 3.33 Steady state test with transformer operating under an open phase and with the healthy generator working at 50% of rated load.

Figure 3.34 Load transient with transformer operating under open phase fault: rotational speed, torque current component i_{qg}, phase currents of PMSG i_{ag} and i_{bg} a); DC bus voltage, i_{otr}, phase currents i_{astr} and i_{bstr} b).

Figure 3.35 Harmonic spectrum of the phase voltage in the transformer and harmonic spectrum of V_{nN}: PMSG is controlled at different rotational speeds $\omega_{rm} = 20\div80$ rad/s, while the transformer is operating at $f_e = 30$Hz and $V_{ab\_rms} = 135$ V.

Figure 4.1 Fault tolerant Multi-drive topology.

Figure 4.2 Post fault configuration of the MDS.

Figure 4.3 Per-phase impedance versus motor rated power.

Figure 4.4 Additional zero-sequence control loops.

Figure 4.5 Flowchart used in the second and third current-sharing methods.

Figure 4.6 Sharing coefficient k_2 and k_3 computed at different α_2 and α_3.

Figure 4.7 Block diagram for the implementation of the Third current sharing method.

Figure 4.8 Additional losses P_{js} obtained by implementing the first (black rhombus) and second/third current-sharing methods (red dots).

Figure 4.9 Current sharing strategy based on the first method.

Figure 4.10 Current sharing strategy based on the second method.

Figure 4.11 Zero-sequence currents flowing in each motor when applying the first method.

Figure 4.12 Zero-sequence currents flowing in each motor when applying the second method.

Figure 4.13 Current sharing strategy based on the third method.

Figure 4.14 Zero-sequence currents flowing in each motor when applying the third method.

Figure 4.15 Zero-sequence currents flowing in each motor when applying the third method $\hat{r}_{s3} = 1.5 r_{s3}$.

Figure 4.16 Experimental setup.

Figure 4.17 Amplitude ratio and phase of the voltages used to compensate the third-harmonic currents flowing in IM_3.

Figure 4.18 Steady-state test at no load, by using the first, method: $\omega_{rm_IM1} = 30$rad/s, $\omega_{rm_IM2} = 80$rad/s and $\omega_{rm_IM3} = 50$rad/s.

Figure 4.19 First method: speed transients occurring at: IM_2: $\omega_{rm_IM2} = -30/30$rad/s and IM_3 $\omega_{rm_IM3} = -40/40$rad/s, whereas IM_1 operates at $\omega_{rm_IM1} = 50$rad/s.

Figure 4.20 Steady-state test at no load by using the first and third methods: $\omega_{rm_IM1} = 30$rad/s, $\omega_{rm_IM2} = 20$rad/s and $\omega_{rm_IM3} = 60$rad/s.

Figure 4.21 Steady-state test at no load by using the second method: $\omega_{rm_IM1} = 30$rad/s, $\omega_{rm_IM2} = 20$rad/s and $\omega_{rm_IM3} = 60$rad/s.

Figure 4.22 Steady-state test with the faulty motor operating at rated load, by using the second method: $\omega_{rm_IM1} = 30$rad/s, $\omega_{rm_IM2} = 20$rad/s and $\omega_{rm_IM3} = 60$rad/s.

Figure 4.23 Load step occurring at IM_2 with the second method: $\omega_{rm_IM1} = 30$rad/s, $\omega_{rm_IM2} = 50$rad/s and f_{e_M3}=20Hz.

Figure 5. 1 Hybrid Observer block diagram.

Figure 5.2 Cross section of a BLDC machine with misplaced Hall sensors [26].

Figure 5.3 Actual and ideal Hall sensor output signals and resultant position estimate [29].

Figure 5.4 Vector tracking observer adopted in [29].

Figure 5.5 Vector feedback position observer [32].

Figure 5.6 Permanent magnet synchronous machine [18].

Figure 5.7 Typical back-emf and current waveform of a BLDC [19].

Figure 5.8 Control scheme of a standard speed controlled BLDC drive.

Figure 5.9 Hall effect sensors signals and vector representation on the αβ plane.

Figure 5.10 Single fault affects the Hall sensors signals with H_1=1 and representation on the αβ plane.

Figure 5.11 Single fault affects the Hall sensors signals with H_1=0 and representation on the αβ plane.

Figure 5.12 Double fault affects the Hall sensors signals with H_1=1 H_3=1and representation on the αβ plane.

Figure 5.13 Double fault affects the Hall sensors signals with H_2=1 H_3=0 and representation on the αβ plane.

Figure 5.14 B lock diagram of the fault tolerant vector tracking observer with harmonic decoupling.

Figure 5.15 Alternative method for harmonics decoupling.

Figure 5.16 Block diagram of the fault tolerant ZOA.

Figure 5.17 ZOA setup in normal operation: a) $\theta_{re\_min\_sect}$ b) $\theta_{re\_max\_sect}$ c) $\Delta\theta_{re\_prev\_sect}$.

Figure 5.18 ZOA setup for H1=1 fault,operation: a) $\theta_{re\_min\_sect}$ b) $\theta_{re\_max\_sect}$ c) $\Delta\theta_{re\_prev\_sect}$.

Figure 5.19 Block diagram of the fault tolerant Hybrid observer.

Figure 5.20 HOS for: a) normal operation, b) H_1=1 fault.

Figure 5.21 Fault H_1=1 on the BLDC drive under current control.

Figure 5.22 Hall effect position sensor fault H_1=1 on a BLDC using VTO to provide the speed feedback.

Figure 5.23 Hall effect position sensor fault H_1=1 on a BLDC using the ZOA.

Figure 5.24 Hall effect position sensor fault H_1=1 on a BLDC using the HO.

Figure 5.25 Estimation position and velocity error with a)VTO, b)ZOA and c) HO.

Figure 5.26 Block diagram of the experimental setup.

Figure 5.27 No load, trapezoidal speed command tracking response: a) VTO b) ZOA c) HO.

Figure 5.28 Disturbance torque response: a) VTO b) ZOA c) HO.

Figure 5.29 Position sensors misalignment 120°+5° H_2 and -5° H_3: a) VTO b) ZOA c) HO.

Figure 5.30 Operation following a non compensated fault : a) VTO b) ZOA c) HO.

Figure 5.31 Single fault compensation: a) VTO b) ZOA c) HO at 20 rad/s.

Figure 5.32 Single fault compensation: a) VTO b) ZOA c) HO at 120 rad/s.

Figure 5.33 Double fault compensation during speed transient: a) VTO b) ZOA c) HO.

Figure 5.34 Quantized loci in the stationary reference frame in normal BLDC operation: a) position vector $H_{\alpha\beta}$ b) current vector $i_{\alpha\beta}$.

Figure 5.35 Quantized loci in the stationary reference frame for a H_1 = 1 single fault: a) position vector $H_{\alpha\beta}$ b) current vector $i_{\alpha\beta}$.

Figure 5.36 Quantized loci in the stationary reference frame for a H_1=1 and H_3=1 double fault: a) position vector $H_{\alpha\beta}$ b) current vector $i_{\alpha\beta}$.

Figure 5.37 Quantized loci in the stationary reference frame for a H_2=1 and H_3=0double fault: a) position vector $H_{\alpha\beta}$ b) current vector $i_{\alpha\beta}$.

Figure 5.38 Evolution of the $i_{\alpha\beta}$locus during a H_1=1 fault when using the fault-tolerant VTO.

Index of Tables

Table 1.1: Number of connectable machines and their phase order for an even system phase number.

Table 1.2 Decoupling transformation matrix.

Table 1.3: Connectivity matrix for 6-phase drive system.

Table 1.4 Voltage error related to the lost power switches q_{sk}.

Table 1.5 3kW IM motor parameters.

Table 2.1 Toque Capability reduction (%) of healthy PMSM drives under a Fault Condition.

Table 2.2 Common mode voltage.

Table 2.3 Technical specifications of the considered induction motors.

Table 3.1 Generator Parameters.

Table 3.2 Transformer Parameters.

Table 4.1 Technical specification of the considered induction motors.

Table 5.1 Power converter switches commutation table for counter clockwise rotation.

Table 5.2 ZOA Setup for Single Faults.

Table 5.3 ZOA Setup for Double Faults.

Table 5.4 HO Setup for Single Faults.

Table 5.5 HO setup for double faults.

Table 5.6 BLDC machine’s parameters.

Nomenclature

Abbreviations

AC	Alternating current
DC	Direct (continous) current
Common mode voltage	CMV
Multi-Drive System	MDS
magneto motive force	mmf
Voltage Source Inverter	VSI
Fault Tolerant	FT
FOC	Field Oriented Control
DFOC	Direct Field Oriented Control
IFOC	Indirect Field Oriented Control
MPC	Model Predictive control
PI	Proportional and integral controller
IM	Induction machine
PLL	Phase locked loop
PMSM	Permanent Magnet Synchrnous Machine
PWM	Pulse Width Modulation
SVM	Space vector modulation
T_s	Sample time
WPS	Wind power system

Symbols

$f_{qd} = f_q - j\, f_d$	Complex vector notation, the d-axis is 90° behind the q-axis
$f_{qd} = f_q + j\, f_d$	Complex vector notation, the q-axis is 90° behind the d-axis
$p=d/dt$	Differential operator
$1/p$	Integral operator
s	Laplace operator
ω_e, θ_e	excitation angular speed, position
ω_r, θ_r	rotor angular speed, position
$\omega_{re} = P/2\omega_r$, $\theta_{re}=P/2\ \theta_r$	

P	Total number of poles
J_p	Physical inertia
b_p	Physical viscous dumping
V, v	voltage
I, i	current
λ	flux

Subscripts

$(\ )_p, (\ )_s$	Quantity at the primary, secondary side of a transformer
$(\ )_s$	Stator
$(\ )_r$	Rotor
$(\ )_o$	zero sequence
$(\ )_g$	generator
$(\ )_{qd}$	Vector notation

Superscripts

$(\ )^s$	Stationary reference frame
$(\ )^r$	Rotor reference frame
$(\ )^e$	Excitation reference frame
$(\ )^*$	Commanded value
$(\hat{\ })$	Estimated value
$(\dot{\ })$	Differential quantity
$(\ )'$	Referred quantity from a circuit to another

Introduction

The application of adjustable speed drives has been continuously increasing during the last 30 years, thanks to a greatly development of power electronic and controller unit. Recently, reliability has become another aspect that concerns electric drive. A reliable drive need to be robust and insensible to external disturbs and, last but not least, works at different operative conditions that could be also in presence of faulty components. A common practice adopted in the past, and in general for complex and expensive systems, allowed to improve the capability to work, under the presence of faulty components by adding redundant parts, which were turned on only when the main drive didn't work. The presence of a redundant drive increases considerably the total cost and also the required installation space, therefore a possible solution can be constituted by modification of the main drive structure, adding a reduced number of additional components and exploiting itself to work after one or more faults. Although this alternative solution, during post fault operations, offers in some cases functionality with reduced performance, often it is cheaper than the previous one and can be applied also for low cost and consumer applications.

Research Contributions

The principal contribution of this work has been the development of a fault tolerant (FT) topology for multi-drive systems (MDSs), reducing the cost and minimizing the number of additional components, that will operate only after a fault. This topology, which can be realized where at least two or more drives are used in the same application to execute independent operations, has intrinsically additional degrees of freedom, that can be exploited for post fault operations, after a simple reconfiguration of the system. Pros and cons have been highlighted during post fault operations considering that a unique solution capable to operate in the same range as in normal conditions or tolerate every kind of fault does not exist.

Performance and losses have been evaluated with simulations and experimental tests with MDSs composed by three phase rotating and stationary machines.

A fault tolerant multi drive topology realized with a PMSM and a transformer has been investigated emulating a wind power system.

Although fault tolerant multi drive systems (FT-MDSs) have been realized with different electrical machines they work exploiting a common aspect based on the realization of a closed path for the current outgoing from the faulty drives, that flow on the healthy drives. A contribution has been given by studying a FT-MDS with more than two drives where this current can be split in different ways using suitable control structures.

Last contribution of this activity has been focused on a single drive which can compose a FT-MDS, but, in this case the fault tolerance has not been related on fault of the power converter or of the electrical machine but of low cost sensors used to provide the rotor position information. In case of fault of these sensors the correct rotor positions has been estimated with suitable algorithms.

Summary of Chapters

Chapter 1: a general discussion and a review of the state of the art is presented regarding different types of MDS structures. In addition, some fault tolerant power converter topologies are reviewed and different control structures are also commented for drives able to work during a fault.

Chapter 2: the proposed FT-MDS topology is presented, its functionality has been studied and proved with simulations and experimental tests. At the beginning a MDS with three IM drives independently controlled, has been analyzed and after also a MDS with two IM drives mechanically coupled has been tested.

Chapter 3: the FT-MDS topology presented in Chapter 2 has been exploited for a Wind Power System equipped with a three phase PMSM and a three phase transformer. In this case, the system performance and its capability to deliver energy to the grid have been evaluated in case of fault on the PMSM and on the transformer drive.

Chapter 4: this chapter investigates principally the zero sequence current that flows from the faulty drives to the healthy ones of a FT-MDS during post fault operations consequently to the system reconfiguration proposed in Chapter 2. In particular three different sharing strategies have been presented, evaluating their effectiveness with simulation and experimental tests.

Chapter 5: fault tolerant improvement has been presented for drive with rotor position information provided by low resolution sensors. Typically, three hall effect sensors can be employed for this type of application and in case of fault the rotor position is completely incorrect. Thanks to a suitable software compensation the rotor position can be correctly estimated also when one or two hall effect position sensors are faulty.

Chapter 6: Conclusions and recommended future works are summarized.

Chapter 1 State - of - the – Art: Review

In this chapter a review of multi-drive systems is presented. A comparison of different topologies has been made highlighting their pros and cons. Moreover, a review of some fault tolerant drive topologies is also presented, most of them are proposed for three-phase machines and converters but their structures can be easily adopted for multi-drive and multiphase systems.

Finally, different fault tolerant control techniques able to ensure high dynamic performance also under a fault condition are described as well.

1.1 Multi-drive systems

In many applications there are loads that have to be controlled independently but also in a coordinated way like industrial robots, production lines or in automotive applications. In general, the higher the number of degrees of freedom the higher is the number of required drives. A common object during the plant of a system is to reduce the cost keeping the maximum performance. Depending on the type of the systems or of the process there is not a unique solution but it is possible to assemble more drives defining a Multi-Drive System (MDS). The literature offers different type of configurations that will be reported in the following notes, that have many common aspects such as:

- Reduced number of components, (cost reduction)
- Independent controls
- Fault tolerance

Recently an area where the presence of electric drives has grown greatly is represented by Electric Vehicles (EV) or Hybrid Electric Vehicles (HEV) where high torque and power density, wide operative range with heavy torque at low speed and high power at high speed, high efficiency and reliability are required; different drives configuration have been developed including also multi machines drive systems [1].

In most cases two electric machines (EMs) systems are realized for HEV and different integration with the internal combustion engine (ICE) as proposed in Figure 1.1 and Figure 1.2; in the first one a planetary gear is employed, allowing multiple operative modes such as: series HEVs, parallel HEVs, series-parallel HEVs, battery-powered EVs, ICE vehicles, battery charging; in the second one the planetary gear is substituted by an automatic mechanical transmission (AMT) and two standard parallel axis gear trains, in this configuration the EM1 is smaller than EM2 and it can be attached to the input shaft of the AMT realizing an integrated starter-generator (ISG).

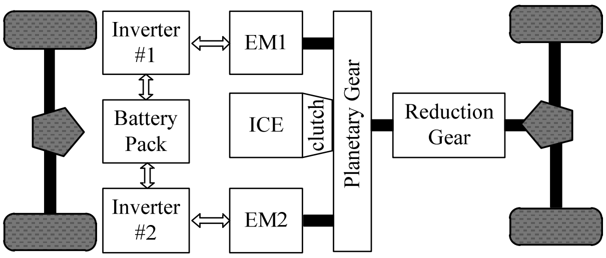

Figure 1.1 Series-parallel HEV by using a planetary gear unit.

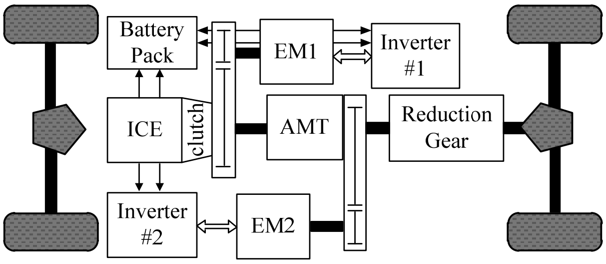

Figure 1.2 Two machines HEV by using AMT and parallel axis gear trains.

Figure 1.3 shows three different types of "Wheel drive systems"; in these cases the power electronic configurations is almost the same, while the connection between the electric machines and the wheel can be direct, as shown in picture a) for an HEV and b) for EV, or with a speed reducer as shown in c). For direct drive systems, where the EM is inside the wheel, high efficiency can be achieved, moreover compact vehicle design and space optimization can be realized. In any case, the EM should be able to operate in a wide range of torque and speed, providing high torque especially for starting time and high power for high speed but a physical constraint is imposed by the wheel size. To overcome this issue a speed reducer is adopted as shown in Figure 1.3 c) in this case the EM has a high rated speed (4000rpm÷20000rpm) and the reducer, positioned between the wheel and EM, reducing the speed can provide high torque at low speed.

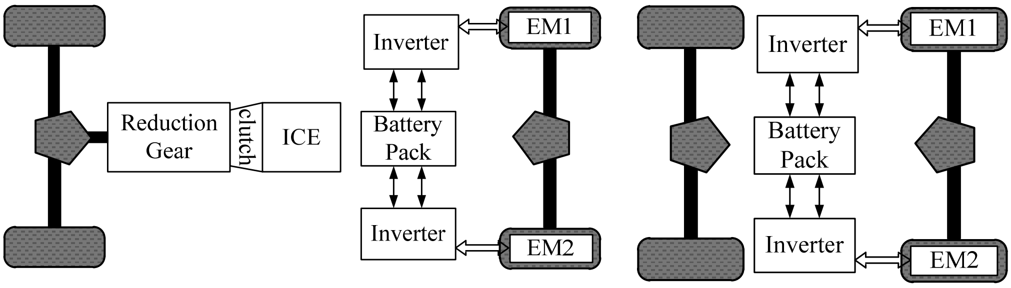

a) Split-parallel HEV with in-wheel motors

b) Direct wheel drive EV

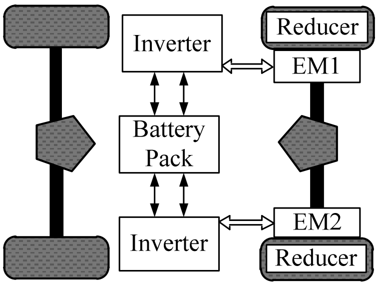

c) Wheel drive EV with reducer

Figure 1.3 Wheel drive systems for HEV and EV.

For heavy vehicles, such as buses or SUVs, the topology adopted is shown in Figure 1.4; due to the high power density required, PMSM are employed, hence two or multiple motors are mounted together to assure high power. The motors sizing can be differentiate hence one motor can be designed for working in high speed region while the other one in high torque region. The flexibility of these systems has some drawbacks such as high cost, large volume and weight.

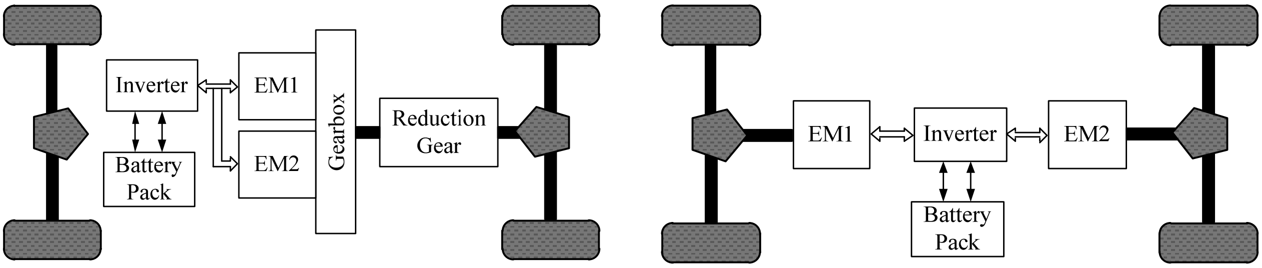

a) Centralized multi-motor drive systems b) Distributed multi-motor drive systems

Figure 1.4 Multi Drive System configuration for heavy EV.

A common aspect shown in the pictures above is given by the presence of more electric drives supplied with a single battery, a simple and useful definition of a system where two or more drives are supplied by a common DC bus, defining a MDS is suggested in [3]-[7] and it is not limited for EV applications as illustrated in Figure 1.5 where “n” three leg converters feed three phase ac-machines and a common DC bus is obtained rectifying the alternate voltage of the secondary side of a transformer.

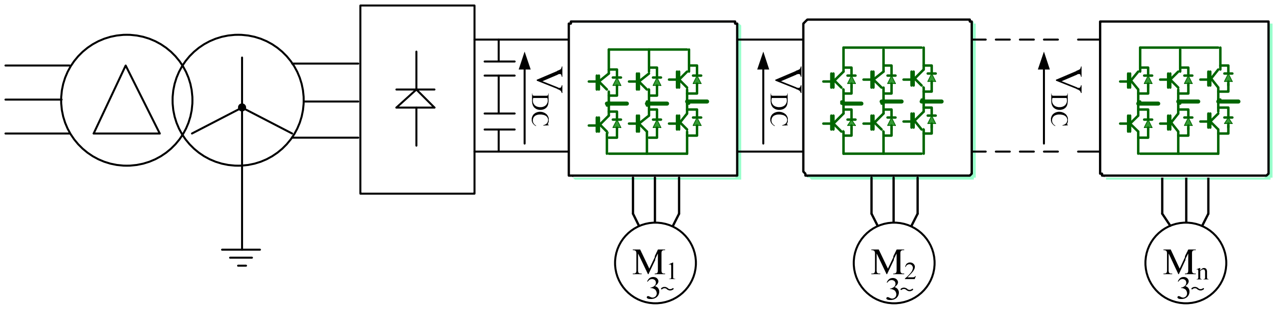

Figure 1.5 Standard three phase MDS topology.

The paper [3] presents a generic MDS structure focusing the attention on the common mode current [2] elimination suggesting a modified configuration with a RLC filters and controlling the drives with a properly space vector modulation.

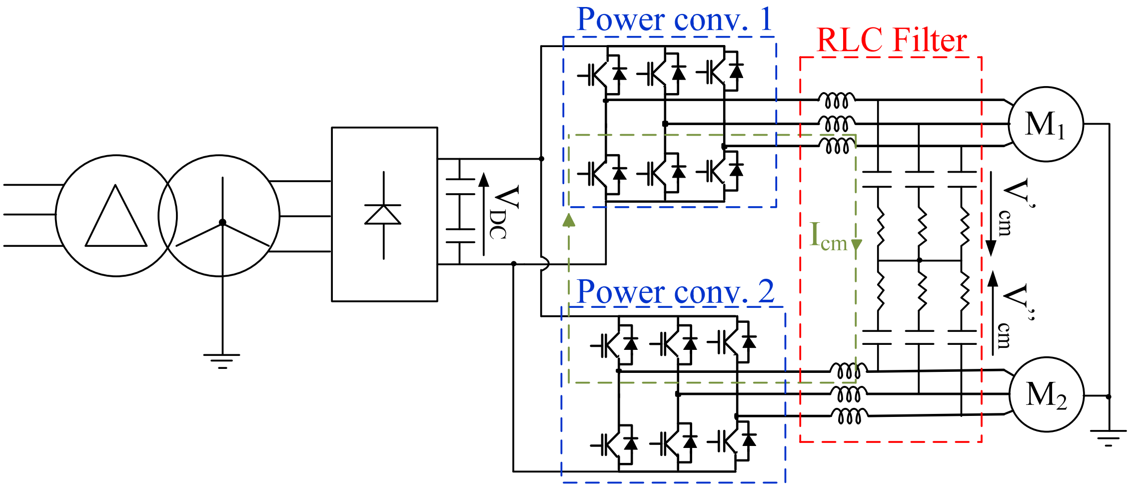

Figure 1.6 Common mode current path in the proposed MDS configuration.

1.1.1 MDS with multiphase machines

Multiphase drives, in which the number of power converter legs and machine phases is higher than 3 [8-[12], are an effective alternative to standard three phase drives and many applications such as: aircraft, naval propulsion and electric vehicles, can potentially adopt this solution. This kind of system can offer different benefits, some of the most important are: reduction of the power density per leg/phase, joule losses reduction, improving of the electromagnetic torque production via high frequency harmonics injection, independent control of torque and flux through only two current components independently of the number of phases, a more sinusoidal distribution of the mmf, additional degrees of freedom can be exploited in case of fault of one or more legs/phases to ensure a partial drive functionality [39], [41], [42], [43], [44].

The additional degrees of freedom provided by a higher number of motor phases are exploited in [4] to perform a series connection of more machines supplied by a single VSI, essentially exploiting these properties it is possible to apply a voltage set able to contemporarily impose torques and fluxes to all the motors supplied by the same power converter, exploiting a phase transposition connection that is based on the decoupling transformation matrix "C" indicated in Table 1.3 Defining with $\alpha = 2\pi/n$ the spatial displacement between two consecutive windings, the phase transposition is a function of α, while the number of the machines that can be series connected depends on the phase number "n". If the number of phases is even or odd different configurations can be defined, for even case, according to the phase transposition and to the number "n" not all the machines series connected will have the same number of phases, e.g. if a machine has n=6, only another machine can be connected in series and it will have only three phases. A summary table,

Table 1.1, is reported to define the number of connectable machines while for each case a connectivity matrix is defined for the correct phase transposition; an example of connectivity matrix for 6-phase drive is reported in Table 1.3 and Figure 1.7 shows the electrical connections.

Table 1.1: Number of connectable machines and their phase order for an even system phase number.

n= an even number, ≥6			
		Number of connectable machines	**Number of phases of machines**
n/2= prime number		k=(n-2)/2	k/2 are n-phase and k/2 are n/2-phase
n/2≠ prime number	$n=2^m$; m= 3,4,5	k=(n-2)/2	n, n/2, $n/2^2$, $n/2^{m-2}$
	All the other even numbers	k<(n-2)/2	n, n/2, n/3, n/4…as appropriate

Table 1.2 Decoupling transformation matrix.

$$C=\sqrt{\frac{2}{n}}\;\begin{array}{c|cccccccc}
\alpha & 1 & \cos\alpha & \cos2\alpha & \cos3\alpha & \dots & \cos3\alpha & \cos2\alpha & \cos\alpha \\
\beta & 0 & \sin\alpha & \sin2\alpha & \sin3\alpha & \dots & -\sin3\alpha & -\sin2\alpha & -\sin\alpha \\
x_1 & 1 & \cos2\alpha & \cos4\alpha & \cos6\alpha & \dots & \cos6\alpha & \cos4\alpha & \cos2\alpha \\
y_1 & 0 & \sin2\alpha & \sin4\alpha & \sin6\alpha & \dots & -\sin6\alpha & -\sin4\alpha & -\sin2\alpha \\
x_2 & 1 & \cos3\alpha & \cos6\alpha & \cos9\alpha & \dots & \cos9\alpha & \cos6\alpha & \cos3\alpha \\
y_2 & 0 & \sin3\alpha & \sin6\alpha & \sin9\alpha & \dots & -\sin9\alpha & -\sin6\alpha & -\sin3\alpha \\
\dots & \dots & \dots & \dots & \dots & \dots & \dots & \dots & \dots \\
x_{\frac{n-4}{2}} & 1 & \cos(\frac{n-2}{2})\alpha & \cos2(\frac{n-2}{2})\alpha & \cos3(\frac{n-2}{2})\alpha & \dots & \cos3(\frac{n-2}{2})\alpha & \cos2(\frac{n-2}{2})\alpha & \cos(\frac{n-2}{2})\alpha \\
y_{\frac{n-4}{2}} & 0 & \sin(\frac{n-2}{2})\alpha & \sin2(\frac{n-2}{2})\alpha & \sin3(\frac{n-2}{2})\alpha & \dots & -\sin3(\frac{n-2}{2})\alpha & -\sin2(\frac{n-2}{2})\alpha & -\sin(\frac{n-2}{2})\alpha \\
0_+ & 1/\sqrt{2} & 1/\sqrt{2} & 1/\sqrt{2} & 1/\sqrt{2} & \dots & 1/\sqrt{2} & 1/\sqrt{2} & 1/\sqrt{2} \\
0_- & 1/\sqrt{2} & -1/\sqrt{2} & 1/\sqrt{2} & -1/\sqrt{2} & \dots & -1/\sqrt{2} & 1/\sqrt{2} & -1/\sqrt{2}
\end{array}$$

Table 1.3: Connectivity matrix for 6-phase drive system.

	A	B	C	D	E	F
M_1	1	2	3	4	5	6
M_2	1	3	5	1	3	5

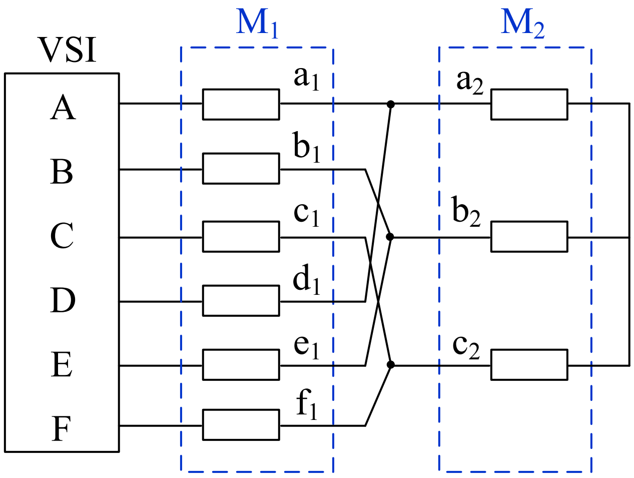

Figure 1.7:Connection diagram for 6-phases 2-motor system.

To sum up for this configuration the principles advantages are defined by:

- reduction of the required number of inverter legs, when compared to an equivalent 3-phase drive (the best reduction is obtained with odd phase number [13]);
- adopting the decoupled model obtained with the application of the matrix C on the machine equations it is possible to connect any type of AC machine in the same MDS;
- an even phases number allows to connect in the same MDS, machine with at least two different phase numbers as presented in Figure 1.7, with respect to an odd phase number.

The main drawbacks of the series connection are:

- open-end stator winding machine is required;
- increase of stator winding and stator iron losses;
- reduction of the total efficiency of the drive system when compared to an equivalent 3-phase system, the efficiency reduction is smaller in an even phase system with respect to an odd one;
- torque density cannot be increased injecting higher stator current harmonics;
- fault tolerance properties is completely lost;

The same authors present in [14] a MDS with multi-phase machines parallel connected, re-adapting the theory presented for the series connection based on the equivalence of series and parallel circuits.

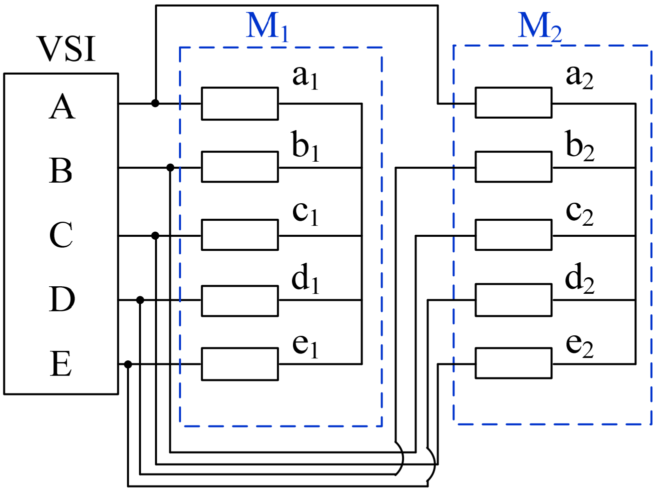

Figure 1.8: Two-motor five-phase drive system, supplied from a single VSI, with stator windings connected in parallel.

Also in this case, with the appropriate phase transposition the independent control of the two machines is achieved as already demonstrated for the series connected MDS, but this solution is not feasible due to a large and uncontrollable x-y current components that flow in each machine.

1.1.2 MDS with reduced components

Other types of MDS are developed with the principle aim to reduce the number of components employed on the drive. The authors of [15] have proposed a dual AC-drive system with reduced switch count; as shown in Figure 1.9, two four-switch inverters connected back to back sharing a single split dc-link capacitor are used to feed a two induction motors that operate at the same fundamental frequency (best work condition) with a similar current level. As described by the authors, for this configuration two line currents are regulated and are 90° shifted, while the neutral connection carries a current that is $\sqrt{2}$ larger than the line current. In this way a single-phase ac current flow through the capacitors producing a voltage ripple that has to be minimized, hence by connecting a second two-phase drive at the same dc bus, it is possible to compensate this single-phase current in the capacitors adjusting the relative phase angle of the currents in the two inverters. A total elimination of this current is achieved with a phase shift of 180° of the line currents in each inverter. This condition allows a reduction in the size of the dc-link capacitors. Experimental results for a traction vehicle application are carried out considering also that the speed of each machine can be different and with the appropriate field orientated control the single-phase current in the capacitors is eliminated, to do so the slip frequency of each machine is different.

A comparison of this system with a standard six-switch converter is also performed defining a “Switch Utilization Ratio” (SUR), that provides the same value 0.16. Considering that a three-phase machine has a higher torque density than a two-phase, some constraints should be considered during a prototype construction.

$$SUR=\frac{2V_{04}I_{04}}{qV_TI_T}$$

V_{04} and I_{04} are the rms inverter rated fundamental output voltage and current at fundamental frequency for a four-switch inverter while V_T and I_T are the peak voltage and current ratings of a switch and q is the total number of switches.

At the end the authors make a suggestion for a MDS for industrial application composed of four two-phase drives shown in Figure 1.10, where multi-machines are required to work at the same electric frequency and different speeds to control a process. With this configuration only 16 switches are required instead of 24 of a standard converter.

A significant component reduction will affect the cost of the system but also in this case a fault on a drive will cause its total work interruption, as before mentioned the torque density is lower than a three phase machine and also in the case of a dual drive, unavoidable unbalance will produce the single-phase current on the capacitor that cannot be eliminated.

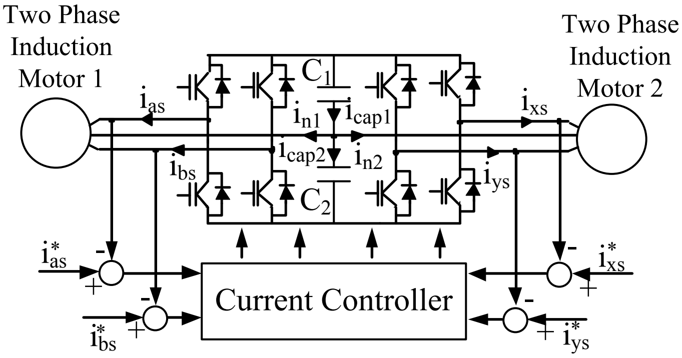

Figure 1.9 Reduced-switch-count ac dual drive.

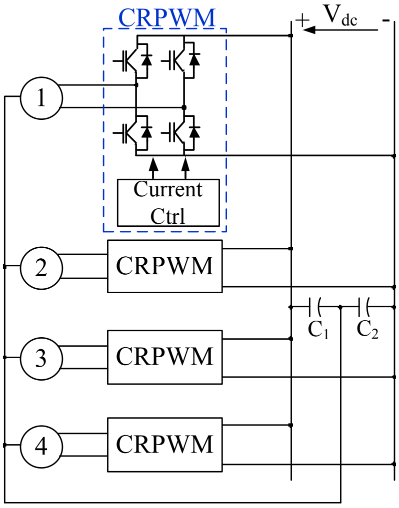

Figure 1.10 Multi-motor drive configuration.

A different MDS topology including three phase and two-phase motors is reported in [16] and [17]. In this case a five leg inverter is applied to feed a three-phase traction PM machine and a two-phase compressor PM machine, Figure 1.11 a). In this configuration both motors are connected through their neutral points, hence the sum of i_a and i_b of the two-phase machine flows through the three-phase machine and the relative three inverter legs. In this way, it is possible to avoid the utilization of the split capacitors of the dc-link, and also no constraints are imposed on the electrical speed of the two drives.

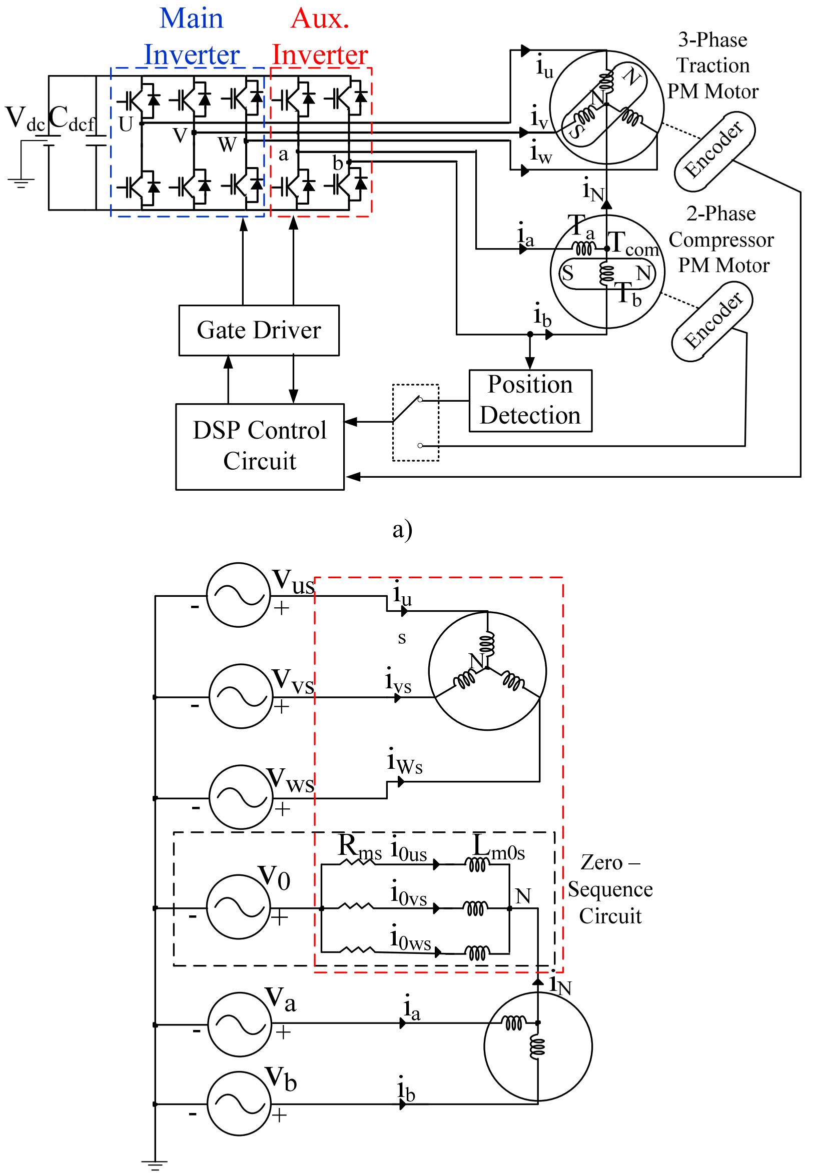

a)

b)

Figure 1.11 Equivalent circuits: a) inverter phase legs as voltage sources and b) ZSC of the main motor as the current return path of the two-phase motor.

Moreover, the single-phase current produced by the two-phase machine will not affect the fundamental flux and torque of the three-phase machine, because it involves only its zero sequence circuit (ZSC) defined by its stator resistance and leakage inductance, Figure 1.11 b). Since the stator windings of the three-phase machine are utilized as a feedback path for the current of the two-phase machine, the stator current rating should be increased to avoid current overload of the three-phase drive, but because the application field of the two drives is different, the rating of the PM machine for traction is considerably greater with respect to the PM machine for the compressor hence the overload is negligible.

In [18] the authors exploit the system configuration presented in Figure 1.11 a) for automotive application, to feed two three-phase machines due to the market diffusion of three-phase machines instead of two-phase ones. The system configuration reported on Figure 1.12, shows the main machine for traction that is fed by the main three-phase inverter and two phases B and C of the auxiliary machine for the compressor are fed by a two-leg auxiliary inverter while the phase A is connected to the neutral point of the main machine. By means of suitable Rotor-Flux-Oriented-Control (RFOC), the voltages of phases B and C are controlled in order to ensure a balanced three-phase current set to the auxiliary machine. Also in this case the main machine is used as a feedback current path for the auxiliary machine and the current on the neutral wire is seen as a zero sequence current from the main machine and it does not affect its main flux and torque because it involves only its ZSC. With respect to the configuration of Figure 1.13, similar control performances are achieved. In addition to the extra copper and iron losses in the main machine caused by the neutral current, another two drawbacks are mentioned, regarding the maximum output voltage of the auxiliary inverter that is at least half of that generated by a three-leg inverter, as shown on Figure 1.13, due to almost fixed voltage of phase A and the common mode voltage that is now generated by the switching of the main inverter (1.1.1) summed to a component caused by the zero sequence current coming from the auxiliary machine, related to 1/3 of the stator resistance and the leakage inductance of the ZSC (1.1.2).

$$v_{comM} = \frac{v_u + v_v + v_w}{3} \tag{1.1.1}$$

$$v_{comM2} = \frac{r_s}{3} i_A + \frac{L_l}{3} \frac{di_A}{dt} \tag{1.1.2}$$

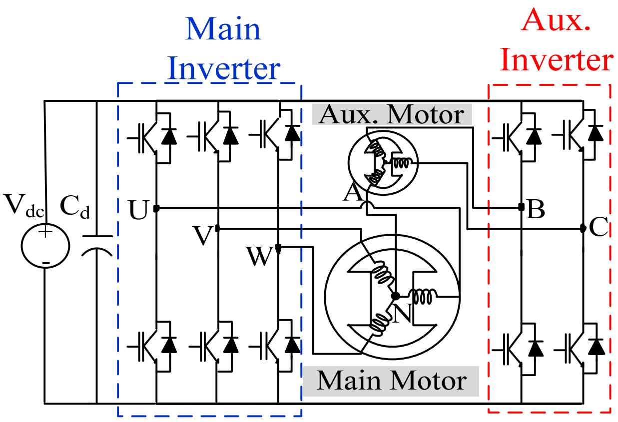

Figure 1.12 Integrated dual ac drive for controlling two three-phase PM motors.

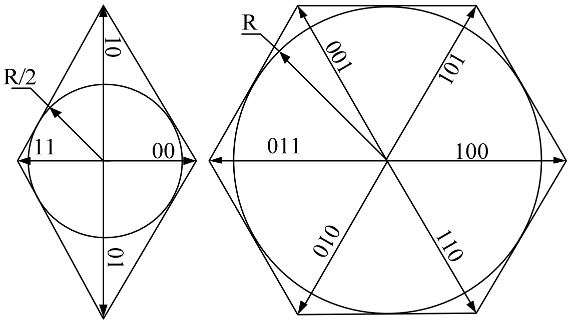

Figure 1.13 Amplitude of the maximum output voltage vectors and the maximum voltage circle obtainable with configuration of proposed in [18] (left), the maximum output voltage circle generated by a three-leg inverter (right).

A comparison between the five leg inverter topology and a nine switch inverter for independent control of two three phase machines is presented in [19].

Figure 1.14 shows the nine switch three-phase inverter for independent control of two ac machines [20]; with respect to a standard solution where two, two levels three-leg inverters can be employed, three switches are saved, and compared to a five – leg inverter, one switch is saved. Basically, with the proposed topology the switches in the middle, namely with M_A, M_B and M_C are shared with the upper devices U_A, U_B and U_C composing the Inverter 1 and with the lower devices L_A, L_B and L_C, composing the Inverter 2. PWM and SVM techniques are adopted for minimizing the losses in a sample period. The main drawback of this topology is the DC link utilization that is equal to 50% compared to a standard three-phase inverter, thus it is necessary to have a DC-bus voltage double.

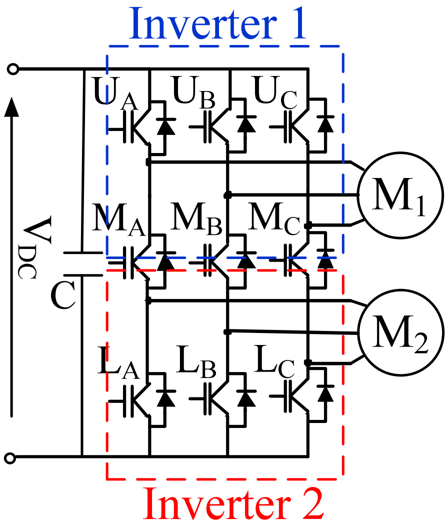

Figure 1.14 Nine switch- three-phase inverter block diagram.

Figure 1.15 shows a MDS topology presented in [5], where "n" three-phase machines are supplied by a N=(2n+1)-leg inverter. Phases a and b of each machine are independently supplied from two inverter legs while phase c of each machine is connected to a common inverter leg, in this way 2(n-1) switches are saved. A suitable PWM strategy is developed and independent control of each drive is performed. Although also in this configuration there is not any kind of problem with the dc-link capacitor bank, the structure suffers a very limited dc-bus voltage utilization depending on the modulation index of each drive; moreover, the rated power of the n-leg has to be selected considering that it is affected by the sum of all phase c currents of the n machines.

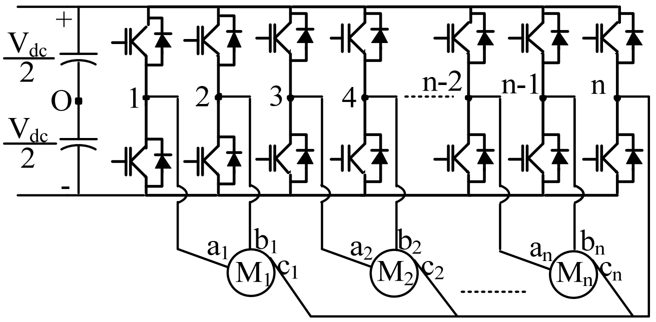

Figure 1.15 Configuration of the multi-machine drive system comprising n three-phase machines supplied from a (2n+1)-leg inverter.

Other MDS topologies are composed of two-machines mechanically coupled, as presented in [6], [21] and [22], this configuration is adopted when the torque load is too high for a single electric machine that cannot have the appropriate rated torque. Hence, a second machine is coupled. The rated power of the two machines can be equal or different, depending on the speed range and the torque demand of the drive. This topology allows improvement in the efficiency with respect to a system with a single machine that does not operate always at the rated power. The reliability is increased: in case of a fault, if one machine is out of service the other can continue the operation.

Figure 1.16, shows a MDS with brushless DC machine coupled to the same shaft through a mechanical clutch for submarine applications [22]. The rated power of the two machines is respectively two thirds and one third, therefore the operation region of the MDS is divided into three sub-regions. Depending on the torque demand of the propeller, the smaller machine for low loads will operate to improve the total efficiency; if the power demanded is higher than the rated power of the smaller machine and lower than the bigger machine, only the last one will operate and the smaller machine will be disconnected by the clutch; both motors will operate together for larger loads. The torque contribution provided by each drive, in the last operative region, is defined by two coefficient K_1 and K_2,calculated taking into account the rated torque of each machine.

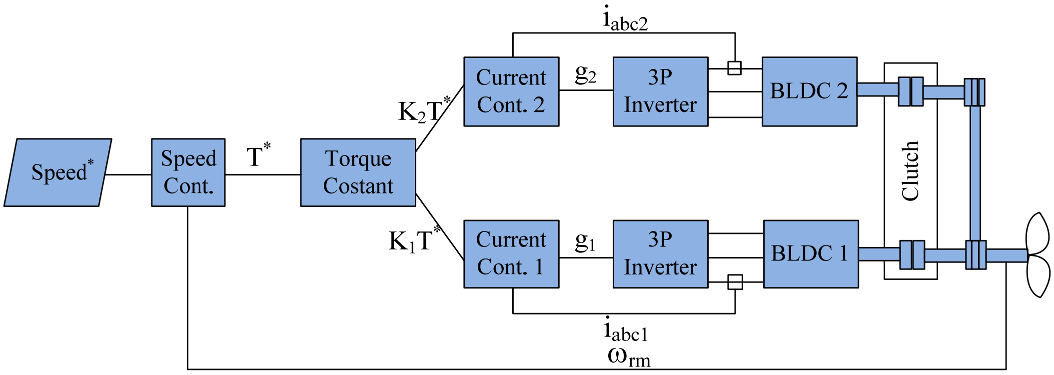

Figure 1.16 Coupled motors configuration for submarine application.

1.1.3 Fault tolerant drive systems and converter topologies

A Fault Tolerant (FT) drive is a system able to work after one or more component failures. Many types of faults can appear on a drive as it is composed of many components. Typical faults have been indicated in [23], [28]:

- dc-link capacitor bank;
- Power converter: the most common are open circuit or short circuit of a power device [24];
- Motor: the most common are open circuit or short circuit in stator windings [25] [26], but it is possible to have a fault also on mechanical parts such as in ball bearings [27];
- Sensors: there are many type of sensors in a drive, the most common are: current sensors, voltage sensors and position sensor; whenever a sensor is faulted, it provides a wrong feedback signal causing system instability and thus loss of control [23].

The principal actions that can be taken when a fault occurs is the identification and isolation of the faulted component. Hence, depending on the gravity and on the fault condition, the drive has to re-configure itself in order to work also in this new condition without any service interruption.

Many research activities are focused on fault identification methods [29], [30], [31], , fault tolerant power converter [33[34[35] and motors [32]; all these solutions are devoted to improve the reliability of the drive. Some of them require suitable control techniques to achieve a true fault tolerant drive.

In this section different fault tolerant drive topologies are reviewed; single solution does not exist but depends on the application, and one solution can be better than another one.

In general the smaller the number of components the lower is the fault probability, but a fault event could have "catastrophic" effects.

The topology structures presented in Figure 1.7, Figure 1.9, Figure 1.11, Figure 1.12, Figure 1.14, Figure 1.15 are not fault tolerant; thus, in case of fault of a drive, the last has to be stopped. One form of fault tolerant MDS, known as "**Redundant topology**" can be seen in Figure 1.16, in this case the reliability of the system is increased because two drives supply a common load hence if one drive is forced to stop its operation, the other one is able to partially feed the load demand.

The block diagram shown in Figure 1.17, [21], represents another drive, belonging to the category of Redundant topology. Fault tolerant level is higher than the structures of Figure 1.16 because each drive has its own DC-link.

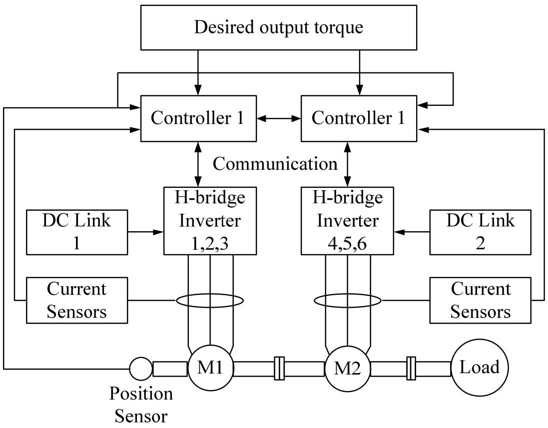

Figure 1.17 block diagram of the dual fault- tolerant motor drive.

In the following different power converter topologies are reviewed to isolate a faulted drive element. The topology presented in [33] contains few fuses and triacs as shown on Figure 1.18, that are able to isolate an inverter leg when one inverter's switch fails in a short-circuit. In this case one of the motor phases is always connected to the positive or to the negative side of the dc-link, causing a control instability. To isolate the faulted leg a coordinate control of the system is necessary, hence after the short-circuited device identification the other switch in the same leg is opened and the appropriate triac indicated with TR_a, TR_b or TR_c is turned on; in this way a short circuit with the dc-link capacitors is realized and the energy stored in them is used to burn the fuse and isolate the faulted leg. At the end of this process the drive will continue to work using the two-phase control [38], discussed in the next paragraph, and the neutral point of the stator windings is connected to the middle point of dc-link capacitors with the activation of TR. An important issue is related to the fuse selection that is made considering the time integral of current squared $\int i^2 dt$, that can be approximated to I^2t; to be sure that the fuse is burned from the energy stored in the capacitors, its I^2t has to be lower than the I^2t of the triac.

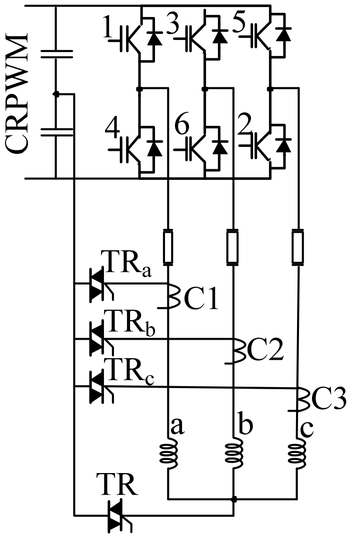

Figure 1.18 Topology for isolating a short circuited inverter switch.

The topology presented in [35] and shown in Figure 1.19 was first presented in [34] for a PMSM drive; it is able to isolate all types of faults. The power converter is made by four-leg and other components are added to realize the isolation of the faulty part, such as: two fuses and two SCRs for each leg and two capacitors. When a fault is detected a control signal is sent to the appropriate SCRs and they are turned on, this generates a short circuit through the dc-link and capacitor C_i, the SCR and fuse. The additional capacitors C_i have to have a suitable size to ensure a high enough current, capable of burning the fuse. In addition a dc-link short circuit, caused by a fault on the dc-link capacitors does not involve the SCRs and the IGBTs in the phase. The post-fault control strategy, in terms of currents is that one proposed in [38], but, as the neutral point of the stator windings is connected to a fourth leg, the problem of voltage perturbation at the dc-link capacitors does not occur; moreover, to increase the dc-link utilization, the neutral voltage can be controlled.

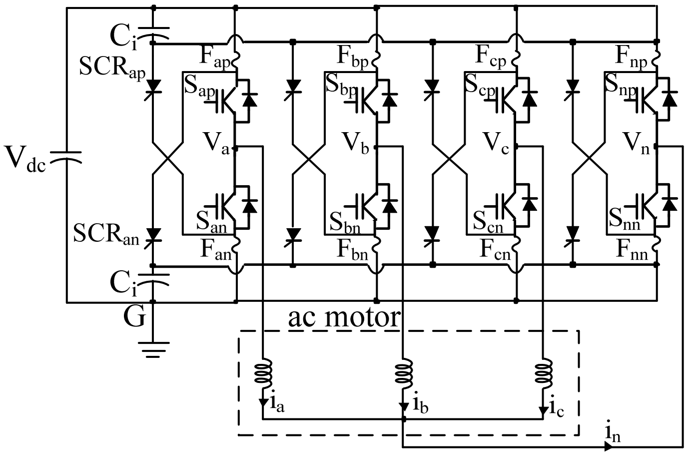

Figure 1.19 Double switch redundant topology.

The topology presented in Figure 1.20, [35], is derived from the previous structure shown in, Figure 1.19. In this case, the fourth leg is activated to the relative phase through the triac TR_a, TR_b and TR_c, after having isolated the faulty leg. This configuration can maintain the rated power in the post-fault operating mode, but the control signals for this spare leg have to be selected properly in accordance with the faulty leg.

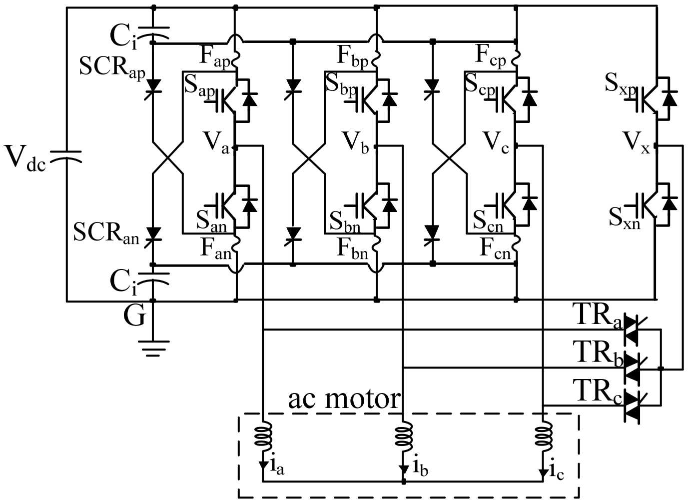

Figure 1.20 Phase redundant topology.

The fault tolerant cascaded inverter topology [35] is shown in Figure 1.21. In this case, each phase is supplied by a single-phase inverter (H-bridge), thus the number of components is double with respect to a standard three-phase configuration. Therefore, higher power losses during normal operation are observed in this topology. The configuration proposed with the additional TRIACs allows it to be fault tolerant to single switch short-circuits, single switch open-circuit and phase-leg open circuits. Also in this case for the post-fault operation a suitable two-phase current control can be applied [38].

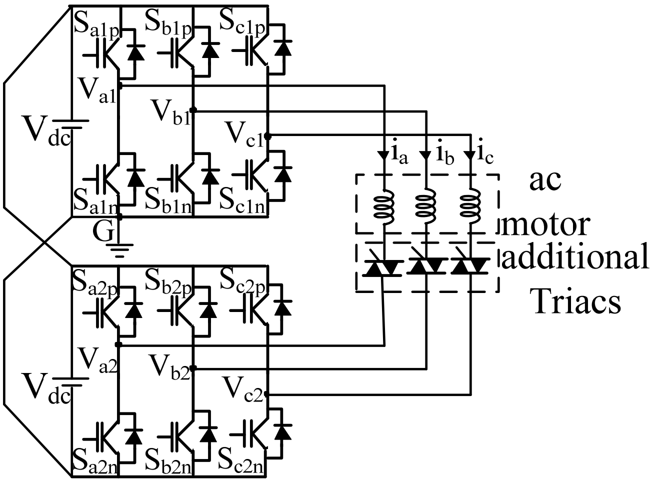

Figure 1.21 Cascaded inverter topology with additional triacs for fault isolation.

The authors of [36] have presented a fault tolerant three-phase drive, shown in Figure 1.22, with a four leg inverter with the same functionality discussed for the topology shown with Figure 1.20. With respect to the topology discussed in Figure 1.20, this structure does not use additional fuses but only thyristors to isolate the faulted leg. The type of faults that can be managed are: single-switch open circuit; phase-leg open circuit; single switch short-circuit while simultaneous faults in two switches cannot be handled.

In the case of an open- circuit fault, after its detection and identification the gate signals of the faulty leg and the isolating thyristor: IS_a, IS_b or IS_c are blocked (turned-off), hence the gate signals of the faulty leg are transferred to the fourth leg and the corresponding thyristor: TH_a, TH_b or TH_c; is turned on.

For a short circuit fault, the transient procedure is different; after having operated the detection and identification of the faulted device, the gate signals of all the other switches are turned-off. Before turning on the thyristors TH_a, TH_b or TH_c, the zero crossing of the short-circuit current is detected, hence to accelerate this process the thyristors: IS_a, IS_b or IS_c are turned-off and the machine phases are completely disconnected. The last step, after the short-circuit current has reached zero, is to transfer the gate signals of the faulted leg to the redundant leg and at the same time the other thyristor: TH_a, TH_b or TH_c, are turned-on. To be sure that the isolating thyristor IS_a, IS_b and IS_c are completely turned-off, a delay time can be inserted before performing the last step.

This topology reduces the number of additional components required to fault isolation, although it cannot tolerate the short circuit of an inverter leg. In addition, the thyristor IS_a, IS_b and IS_c are always in conduction but their power losses are small compared to other switches e.g. IGBTs.

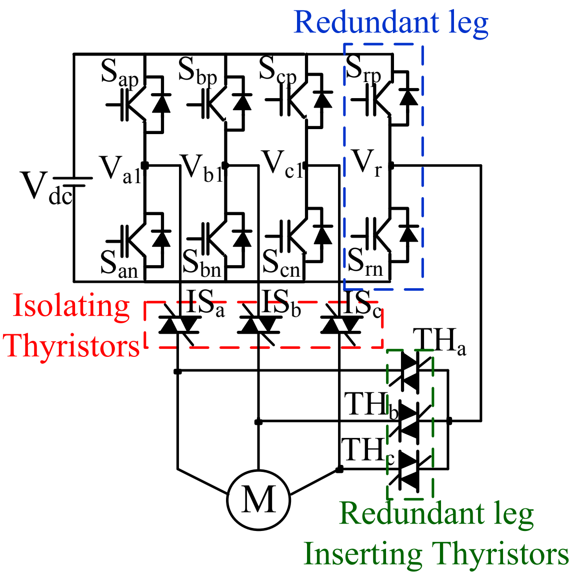

Figure 1.22 Fault- tolerant VSI topology.

Figure 1.23 a) shows a fault tolerant AC/AC drive system [37], composed of a controlled three-phase rectifier connected to the grid and a three-phase inverter connected to an AC machine. The fault tolerant operation is guaranteed by the triacs: TR_a, TR_b, TR_c; in case of fault of one or both the devices of the inverter leg the corresponding triac will be turned on after the isolation of the faulty elements, joining the phase of the machine with the rectifier leg and vice versa. Although the isolation method is not specified, Figure 1.23 b) shows the post fault configuration in case of a fault on the third leg of the inverter.

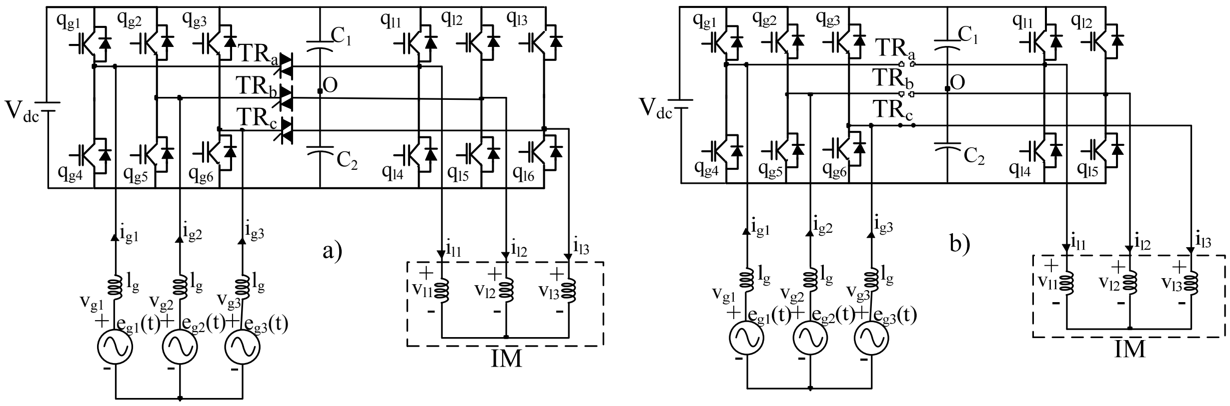

a) before the fault

b) post fault configuration

Figure 1.23 Fault tolerant converter configuration.

The aforementioned paper proposes also a method for the fault detection and identification based on the analysis of the voltage error, obtained from the comparison of the pole voltage and the relative commanded voltage summarized in Table 1.4, a modified PWM and a vector modulation for the post-fault operation, taking into account that two voltages are equal because one leg is shared.

Table 1.4 Voltage error related to the lost power switches q_{sk}.

Fault	ε_{10}	e_{20}	E_{30}
q_{s1}	Δv_{10}	0	0
q_{s2}	0	Δv_{20}	0
q_{s3}	0	0	Δv_{30}
q_{s4}	$- \Delta v_{10}$	0	0
q_{s5}	0	$- \Delta v_{20}$	0
q_{s6}	0	0	Δv_{30}

$\varepsilon_{k0} = v^{*}_{ko} - v'_{ko}$, represent the error due to the modulation technique adopted in post fault operation.

$v'_{ko} = v_{ko} \pm \Delta v_{ko}$

Δv_{ko} is the deviation in the pole voltage due to a fault in the generic switch q_{sk}, where the subscript "s" stands for "g" or "l".

The fault tolerant MDS, shown in Figure 1.24 and proposed in [7] represents a six leg inverter that feeds two three phase ac-machines. In each phase of the machines there is, connected in series, a switch that in reality could be a triac as already seen in previous figures, hence in case of fault it will be turned-on to isolate the faulty leg and by means of another diagonal switch the open phase of a machine is connected to the corresponding leg of the other inverter. This topology, during post fault operation, has already been proposed as a Reduced switch count topology, Figure 1.15, where the main aim is to require a minimum number of components. During post-fault operation, as one inverter leg is shared by two phases, there is a reduced dc bus utilization; an improvement of the dc-bus utilization is achieved by exploiting a finite control set (FCS) – model predictive control (MPC) and the results are compared with a standard FOC for induction machine.

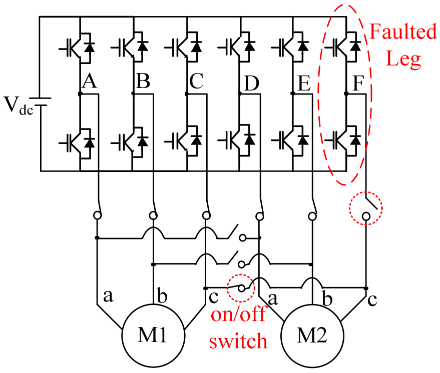

Figure 1.24 Reconfiguration of the electrical connections of the two-motor system through appropriate on/off switches after a fault in one inverter leg.

1.2 Control techniques and machine modeling for post-fault operations

After the previous discussion about some fault tolerant power converter topologies a deeper discussion will be made in this paragraph about the control structures to guarantee the independent control of torque and flux also during these unusual work conditions.

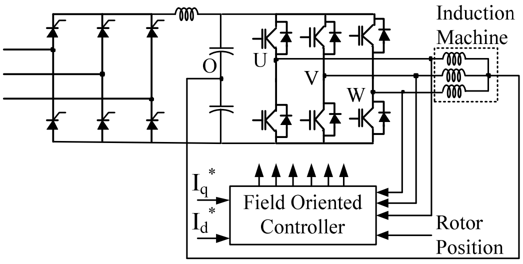

Figure 1.25 Induction motor drive with machine neutral point connected to the dc bus midpoint.

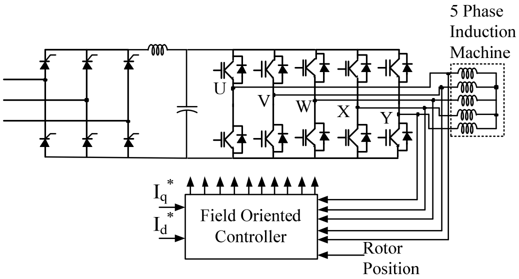

Figure 1.26 Five- phase current regulated PWM inverter drive.

The block diagram reported on Figure 1.25, [38], depicts an improved topology and control strategies that allows continuous operation of a three phase drive also with the loss of one leg of the power converter or a motor phase. The authors suggest to connect the neutral point of the stator windings, at the beginning, directly to the middle point of the dc-link capacitors. During normal operation the standard PWM with FOC is implemented for a three-phase induction machine and the current flowing to the neutral wire is almost zero. When a fault occurs and one converter's leg or one phase results open, a new control strategy has to be applied to achieve the correct field orientation, avoiding pulsating torque. To achieve this control it is necessary to feed the two healthy phases with two independent current shifted by 60° electrical and with the amplitude increased by $\sqrt{3}$. In this way the mmf is equal to that generated during normal operation, while in the neutral wire a current provided by the sum of the current of the two healthy phases will flow.

$$I_{as} = I\cos(\omega t+\phi) \qquad (1)$$

$$I_{bs} = I\cos(\omega t+\phi - 2\pi/3) \qquad (2)$$

$$I_{cs} = I\cos(\omega t+\phi + 2\pi/3) \qquad (3)$$

$$mmf = mmf_a + mmf_b + mmf_c = NI_{as} + aNI_{bs} + a^2NI_{cs} \qquad (4)$$

where $a=1\angle 120°$ and N is the number of effective stator turns per phase.

Substituting (1)-(3) into (4) and assuming $F = NI$ and $\theta = (\omega t + \phi)$

$$mmf = \frac{3}{2} F\, e^{j\theta} = \frac{3}{2} F\,(\cos\theta + j\sin\theta) \qquad (5)$$

During a fault the controller has to apply the same magneto motive force $mmf' = mmf$.

$$mmf' = aNI'_{bs} + a^2NI'_{cs} = -\frac{1}{2}N(I'_{bs} + I'_{cs}) + j\frac{\sqrt{3}}{2}N(I'_{bs} - I'_{cs}) \quad \text{phase “a” fault} \tag{6}$$

$$mmf' = NI'_{as} + a^2NI'_{cs} = NI'_{as} + \left(-\frac{1}{2} - j\frac{\sqrt{3}}{2}\right)NI'_{cs} \quad \text{phase “b” fault} \tag{7}$$

$$mmf' = NI'_{as} + aNI'_{bs} = NI'_{as} + \left(-\frac{1}{2} + j\frac{\sqrt{3}}{2}\right)NI'_{bs} \quad \text{phase “c” fault} \tag{8}$$

Solving each case for the real and imaginary part separately:

$$\frac{3}{2}F\cos\theta = \mathrm{Re}\{mmf'\} \tag{9}$$

$$\frac{3}{2}F\sin\theta = \mathrm{Imm}\{mmf'\} \tag{10}$$

It is possible to obtain the following results that are also graphically showed in Figure 1.27:

$$\begin{cases} I'_{bs} = \sqrt{3}\,I\cos(\omega t+\phi-5\pi/6) \\ I'_{cs} = \sqrt{3}\,I\cos(\omega t+\phi+5\pi/6) \end{cases} \quad \text{phase “a” fault} \tag{11}$$

$$\begin{cases} I'_{as} = \sqrt{3}\,I\cos(\omega t+\phi+\pi/6) \\ I'_{cs} = \sqrt{3}\,I\cos(\omega t+\phi+\pi/2) \end{cases} \quad \text{phase “b” fault} \tag{12}$$

$$\begin{cases} I'_{as} = \sqrt{3}\,I\cos(\omega t+\phi-\pi/6) \\ I'_{bs} = \sqrt{3}\,I\cos(\omega t+\phi-\pi/2) \end{cases} \quad \text{phase “c” fault} \tag{13}$$

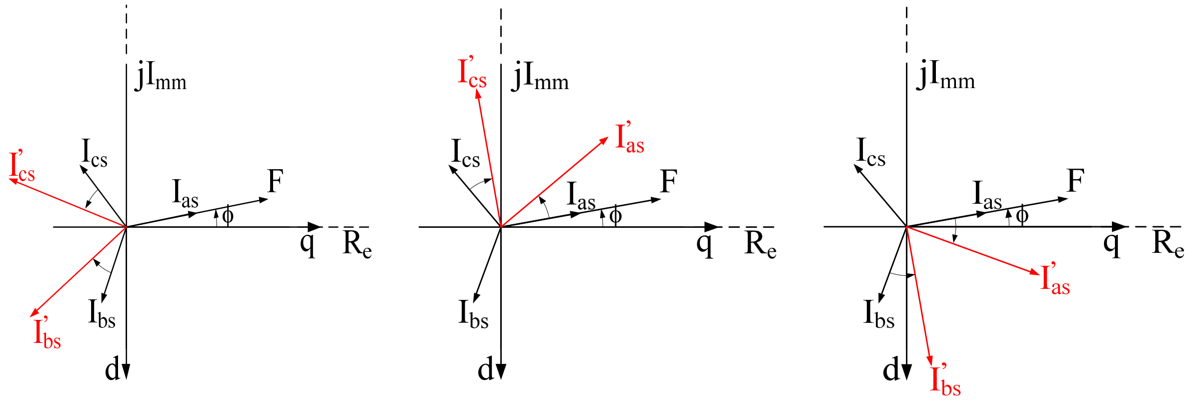

a) b) c)

Figure 1.27 Phasor relationships before and after open-circuit of a) phase a, b) phase b, c) phase c.

Naturally, this current will produce a voltage pulsation on the dc-link capacitors; to reduce this effect two damping resistors can be added in parallel to the capacitors and also their value can be chosen to reduce the voltage pulsation. In addition this topology does not allow a full dc-link utilization because the neutral point has a potential fixed to $V_{dc}/2$, hence the authors suggest to connect the neutral point of the stator windings to the dc-link capacitors with a triac; it is turned off for normal operation and a standard balanced three phase current set is used to generate the mmf instead it will be turned on only in case of fault adopting the modified current set.

The authors of [39] have generalized the approach proposed in [38] for multiphase (n-phase > 3) machine, Figure 1.26; in this case exploiting the additional degrees of freedom of n-phase machine, with "n" even or odd, there is not a unique solution to define the mmf' during one or more faults equal to the mmf of normal operations. Different constraints can be applied to achieve the better solution such as: loss minimization, equal current magnitude for each healthy phase or the elimination of the neutral connection.

A different approach based on the qd0 transformation theory can be exploited and the model reported in the following section is used to implement the FOC also in case of fault; in particular, the model for three-phase induction machine (IM) [40] and permanent magnet synchronous machine (PMSM) [45], will be analyzed since these electrical machines have been used for the study presented in the following chapters; similar modeling in case of fault for both n-phase IM and PMSM with n higher than 3, are also presented in literature [41], [42], [43], [44].

1.2.1 Modeling and control of an IM

A. Analytical model in healthy conditions

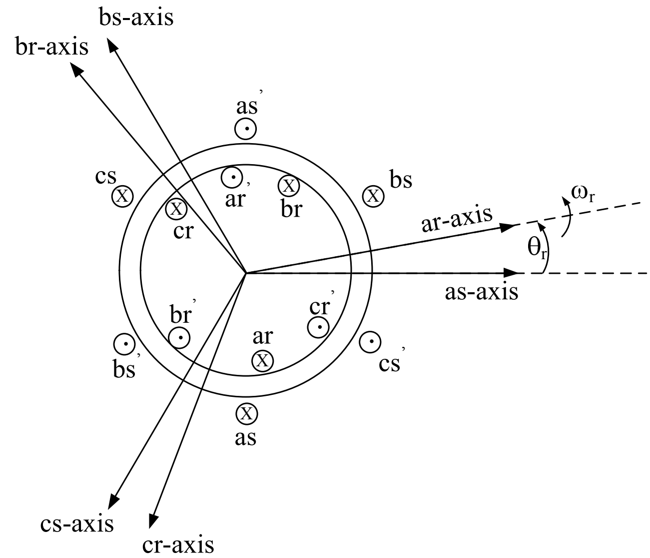

Figure 1.28 Two pole, three phase symmetrical induction machine.

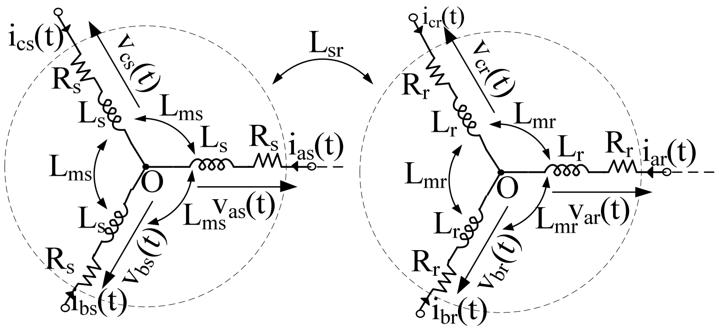

Figure 1.29 Stator and rotor windings representation in phase coordinates.

Figure 1.28 displays a 2-pole, 3-phase, symmetrical induction machine, with wye-connected and sinusoidally distributed stator windings, composed of Ns equivalent turns, displaced by 120°. The voltage and flux equations are reported below [46]. For the purpose also the rotor windings are considered sinusoidally distributed, displaced by 120° with Nr equivalent turns, Figure 1.29.

$$\begin{cases} \mathbf{v}_{abcs} = \mathbf{r}_s \, \mathbf{i}_{abcs} + p \, \boldsymbol{\lambda}_{abcs} \\ \mathbf{v}_{abcr} = \mathbf{r}_r \, \mathbf{i}_{abcr} + p \, \boldsymbol{\lambda}_{abcr} \end{cases} \tag{1.2.1}$$

All the bold letters represent a vector or a matrix, hence: $\mathbf{v}_{abcs}$ and $\mathbf{v}_{abcr}$ are the stator and rotor voltage vectors, while $\mathbf{i}_{abcs}$ and $\mathbf{i}_{abcr}$ are the stator and rotor currents, $\boldsymbol{\lambda}_{abcs}$ and $\boldsymbol{\lambda}_{abcr}$ are the stator and rotor fluxes. “f” stands for voltage v, current, i, or flux , λ.

$$(\mathbf{f}_{abcs})^T = [\ f_{as}\ \ f_{bs}\ \ f_{cs}\ ] \tag{1.2.2}$$

$$(\mathbf{f}_{abcr})^T = [\ f_{ar}\ \ f_{br}\ \ f_{cr}\ ] \tag{1.2.3}$$

The flux linkage can be expressed in a matrix form as indicated in (1.2.4):

$$\begin{bmatrix} \lambda_{abcs} \\ \lambda_{abcr} \end{bmatrix} = \begin{bmatrix} \mathbf{L}_s & \mathbf{L}_{sr} \\ (\mathbf{L}_{sr})^T & \mathbf{L}_r \end{bmatrix} \begin{bmatrix} \mathbf{i}_{abcs} \\ \mathbf{i}_{abcr} \end{bmatrix} \tag{1.2.4}$$

$$\mathbf{r}_s = R_s \begin{bmatrix} 1 & 0 & 0 \\ 0 & 1 & 0 \\ 0 & 0 & 1 \end{bmatrix} \qquad \mathbf{r}_r = R_r \begin{bmatrix} 1 & 0 & 0 \\ 0 & 1 & 0 \\ 0 & 0 & 1 \end{bmatrix}$$

$$\mathbf{L}_s = \begin{bmatrix} L_{ls} + L_{ms} & -\frac{1}{2} L_{ms} & -\frac{1}{2} L_{ms} \\ -\frac{1}{2} L_{ms} & L_{ls} + L_{ms} & -\frac{1}{2} L_{ms} \\ -\frac{1}{2} L_{ms} & -\frac{1}{2} L_{ms} & L_{ls} + L_{ms} \end{bmatrix}$$

$$\mathbf{L}_r = \begin{bmatrix} L_{lr} + L_{mr} & -\frac{1}{2} L_{mr} & -\frac{1}{2} L_{mr} \\ -\frac{1}{2} L_{mr} & L_{lr} + L_{mr} & -\frac{1}{2} L_{mr} \\ -\frac{1}{2} L_{mr} & -\frac{1}{2} L_{mr} & L_{lr} + L_{mr} \end{bmatrix}$$

$$\mathbf{L}_{sr} = L_{sr} \begin{bmatrix} \cos(\theta_r) & \cos(\theta_r + \frac{2\pi}{3}) & \cos(\theta_r - \frac{2\pi}{3}) \\ \cos(\theta_r - \frac{2\pi}{3}) & \cos(\theta_r) & \cos(\theta_r + \frac{2\pi}{3}) \\ \cos(\theta_r + \frac{2\pi}{3}) & \cos(\theta_r - \frac{2\pi}{3}) & \cos(\theta_r) \end{bmatrix}$$

where R_s, R_r are the stator and rotor winding resistance, L_{ls}, L_{lr} are the leakage inductances, L_{ms}, L_{mr} are the magnetizing inductances, L_{sr} is the mutual inductance between stator and rotor, θ_r is the electrical rotor position.

For the sake of simplicity, as common practice, all the rotor variable are referred to the stator, introducing the following fictitious quantities:

$$\mathbf{i}'_{abcr} = \frac{N_r}{N_s} \mathbf{i}_{abcr}$$

$$\mathbf{v}'_{abcr} = \frac{N_s}{N_r}\mathbf{v}_{abcr}$$

$$\lambda'_{abcr} = \frac{N_s}{N_r}\lambda_{abcr}$$

Introducing the previous quantities in voltage and flux equations, it is possible to define:

$$L_{ms} = \frac{N_s}{N_r}L_{sr}$$

$$L_{mr} = \left(\frac{N_s}{N_r}\right)^2 L_{ms}$$

$$\mathbf{r}'_r = \left(\frac{N_s}{N_r}\right)^2 \mathbf{r}_r$$

$$\mathbf{L}'_{sr} = \frac{N_s}{N_r}\mathbf{L}_{sr}$$

$$\mathbf{L}'_r = \left(\frac{N_s}{N_r}\right)^2 \mathbf{L}_r$$

$$L'_{lr} = \left(\frac{N_s}{N_r}\right)^2 L_{lr}$$

These relations are reasonable as the magnetizing inductance and the mutual inductance are associated to the same magnetic flux path. This allows to define the so called "T" equivalent circuit and the previous equations can be rewritten as follow:

$$\begin{cases} \mathbf{v}_{abcs} = \mathbf{r}_s\,\mathbf{i}_{abcs} + p\,\lambda_{abcs} \\ \mathbf{v}'_{abcr} = \mathbf{r}'_r\,\mathbf{i}'_{abcr} + p\,\lambda'_{abcr} \end{cases} \qquad (1.2.5)$$

$$\begin{bmatrix} \lambda_{abcs} \\ \lambda'_{abcr} \end{bmatrix} = \begin{bmatrix} \mathbf{L}_s & \mathbf{L}'_{sr} \\ (\mathbf{L}'_{sr})^T & \mathbf{L}'_r \end{bmatrix} \begin{bmatrix} \mathbf{i}_{abcs} \\ \mathbf{i}'_{abcr} \end{bmatrix} \qquad (1.2.6)$$

$$\mathbf{r}'_r = R'_r \begin{bmatrix} 1 & 0 & 0 \\ 0 & 1 & 0 \\ 0 & 0 & 1 \end{bmatrix}$$

$$\mathbf{L}'_{sr} = \frac{N_s}{N_r}\mathbf{L}_{sr} = L_{ms} \begin{bmatrix} \cos(\theta_r) & \cos(\theta_r + \frac{2\pi}{3}) & \cos(\theta_r - \frac{2\pi}{3}) \\ \cos(\theta_r - \frac{2\pi}{3}) & \cos(\theta_r) & \cos(\theta_r + \frac{2\pi}{3}) \\ \cos(\theta_r + \frac{2\pi}{3}) & \cos(\theta_r - \frac{2\pi}{3}) & \cos(\theta_r) \end{bmatrix}$$

$$\mathbf{L}'_r = \begin{bmatrix} L'_{lr} + L_{ms} & -\frac{1}{2}L_{ms} & -\frac{1}{2}L_{ms} \\ -\frac{1}{2}L_{ms} & L'_{lr} + L_{ms} & -\frac{1}{2}L_{ms} \\ -\frac{1}{2}L_{ms} & -\frac{1}{2}L_{ms} & L'_{lr} + L_{ms} \end{bmatrix}$$

The electrical model, in machine variables, is completed adding the electromagnetic torque expression. The electromagnetic torque is related to the energy stored in the coupling field and assuming a linear behavior of the magnetic circuit the field energy W_f is equal to the coenergy W_c.

$$T_e(i_j,\theta_r) = \left(\frac{P}{2}\right)\frac{\partial W_c(i_j,\theta_r)}{\partial \theta_r} = \left(\frac{P}{2}\right)(\mathbf{i}_{abcs})^T \frac{\partial}{\partial \theta_r}[\mathbf{L}'_{sr}]\,\mathbf{i}'_{abcr} \qquad (1.2.7)$$

$$\begin{aligned} T_e = -\left(\frac{P}{2}\right)L_{ms}\Bigg\{\Bigg[\, & i_{as}\left(i'_{ar} - \frac{1}{2}i'_{br} - \frac{1}{2}i'_{cr}\right) + i_{bs}\left(i'_{br} - \frac{1}{2}i'_{ar} - \frac{1}{2}i'_{cr}\right) + \\ & + i_{cs}\left(i'_{cr} - \frac{1}{2}i'_{br} - \frac{1}{2}i'_{ar}\right)\Bigg]\sin\theta_r + \frac{\sqrt{3}}{2}\Big[\, i_{as}\big(i'_{br} - i'_{cr}\big) + i_{bs}\big(i'_{cr} - i'_{ar}\big) + \\ & i_{cs}\big(i'_{ar} - i'_{br}\big)\Big]\cos\theta_r\Bigg\} \end{aligned} \qquad (1.2.8)$$

B. Analytical model under faulty conditions

By assuming a fault condition in the drive that can be isolated and yielding the system to operate with one stator phase not supplied, in the previous model a stator current is constantly equal to zero and the model in machine variable can be defined deleting one raw and one column [40] of the matrices previously defined for the healthy model. Considering the equations with the rotor variables referred to the stator the generalized expression are defined as follow:

$$\begin{cases} \mathbf{v}_{ijs} = \mathbf{r}_{sf}\,\mathbf{i}_{ijs} + p\,\boldsymbol{\lambda}_{ijs} \\ \mathbf{v}'_{abcr} = \mathbf{r}'_r\,\mathbf{i}'_{abcr} + p\,\boldsymbol{\lambda}'_{abcr} \end{cases} \qquad (1.2.9)$$

$$\begin{bmatrix} \boldsymbol{\lambda}_{ijs} \\ \boldsymbol{\lambda}'_{abcr} \end{bmatrix} = \begin{bmatrix} \mathbf{L}_{sf} & \mathbf{L}'_{sfr} \\ (\mathbf{L}'_{sfr})^T & \mathbf{L}'_r \end{bmatrix} \begin{bmatrix} \mathbf{i}_{ijs} \\ \mathbf{i}'_{abcr} \end{bmatrix} \qquad (1.2.10)$$

The subscript index i and j:

$$(i, j) = \begin{cases} \text{b,c fault stator phase a} \\ \text{a,c fault stator phase b} \\ \text{a,b fault stator phase c} \end{cases} \qquad (1.2.11)$$

It is assumed that the rotor is healthy and the matrices $\mathbf{r}'_r$ and $\mathbf{L}'_r$ are not modified, while $\mathbf{r}_{sf}$, $\mathbf{L}_{sf}$, $\mathbf{L}'_{sr}$ become:

$$\mathbf{r}_{sf} = R_s \begin{bmatrix} 1 & 0 \\ 0 & 1 \end{bmatrix}$$

$$\mathbf{L}_{sf} = \begin{bmatrix} L_{ls} + L_{ms} & -\frac{1}{2} L_{ms} \\ -\frac{1}{2} L_{ms} & L_{ls} + L_{ms} \end{bmatrix}$$

$$\mathbf{L}'_{sfr} = L_{ms} \begin{bmatrix} \cos(\alpha) & \cos(\beta) & \cos(\gamma) \\ \cos(\delta) & \cos(\phi) & \cos(\rho) \end{bmatrix}$$

$$\begin{matrix}(\alpha,\beta,\gamma) \\ (\delta,\phi,\rho)\end{matrix} = \begin{cases} \theta_r - \frac{2\pi}{3},\ \theta_r,\ \theta_r + \frac{2\pi}{3} & \\ & \text{fault stator phase a} \\ \theta_r + \frac{2\pi}{3},\ \theta_r - \frac{2\pi}{3},\ \theta_r & \\ \theta_r,\ \theta_r + \frac{2\pi}{3},\ \theta_r - \frac{2\pi}{3} & \\ & \text{fault stator phase b} \\ \theta_r + \frac{2\pi}{3},\ \theta_r - \frac{2\pi}{3},\ \theta_r & \\ \theta_r,\ \theta_r + \frac{2\pi}{3},\ \theta_r - \frac{2\pi}{3} & \\ & \text{fault stator phase c} \\ \theta_r - \frac{2\pi}{3},\ \theta_r,\ \theta_r + \frac{2\pi}{3} & \end{cases}$$

The electromagnetic torque can be expressed using the same definition of the coenergy, assuming the linear behavior of the magnetic circuit:

$$T_e(i_j,\theta_r) = \left(\frac{P}{2}\right) \frac{\partial W_c(i_j,\theta_r)}{\partial \theta_r} = \left(\frac{P}{2}\right) (\mathbf{i}_{ijs})^T \frac{\partial}{\partial \theta_r} [\mathbf{L}'_{sfr}]\, \mathbf{i}'_{abcr} \qquad (1.2.12)$$

Obtaining:

For stator phase a fault

$$\begin{aligned} T_e = -\left(\frac{P}{2}\right) L_{ms} \Big\{ & \Big[i_{bs}\Big(i'_{br} - \frac{1}{2} i'_{ar} - \frac{1}{2} i'_{cr} \Big) + i_{cs}\Big(i'_{cr} - \frac{1}{2} i'_{br} - \frac{1}{2} i'_{ar} \Big)\Big] \sin\theta_r + \\ & + \frac{\sqrt{3}}{2}\Big[i_{bs}\big(i'_{cr} - i'_{ar} \big) + i_{cs}\big(i'_{ar} - i'_{br} \big) \Big] \cos\theta_r \Big\} \end{aligned} \qquad (1.2.13)$$

For stator phase b fault

$$\begin{aligned} T_e = -\left(\frac{P}{2}\right) L_{ms} \Big\{ & \Big[i_{as}\Big(i'_{ar} - \frac{1}{2} i'_{br} - \frac{1}{2} i'_{cr} \Big) + i_{cs}\Big(i'_{cr} - \frac{1}{2} i'_{br} - \frac{1}{2} i'_{ar} \Big)\Big] \sin\theta_r + \\ & + \frac{\sqrt{3}}{2}\Big[i_{as}\big(i'_{br} - i'_{cr} \big) + i_{cs}\big(i'_{ar} - i'_{br} \big) \Big] \cos\theta_r \Big\} \end{aligned} \qquad (1.2.14)$$

For stator phase c fault

$$T_e = -\left(\frac{P}{2}\right) L_{ms} \left\{ \left[i_{as}\left(i'_{ar} - \frac{1}{2} i'_{br} - \frac{1}{2} i'_{cr} \right) + i_{bs}\left(i'_{br} - \frac{1}{2} i'_{ar} - \frac{1}{2} i'_{cr} \right) \right] \sin\theta_r + \right.$$
$$\left. + \frac{\sqrt{3}}{2} \left[i_{as}\left(i'_{br} - i'_{cr} \right) + i_{bs}\left(i'_{cr} - i'_{ar} \right) \cos\theta_r \right] \right\} \tag{1.2.15}$$

C. Equations in qd0 variables for healthy conditions

It is quite useful adopt the "Reference-frame theory" to develop a model in qd0 variables referring all stator and rotor machine variables in an arbitrary reference frame [46], [47]. For the induction machine, because of the isotropy structure, the machines variables can be referred to a qd0 stationary frame, as well as to a rotating reference frame that can be synchronous with the rotor or with the air-gap mmf or more in general rotating at the angular speed ω.

Defining the transformation matrix $\mathbf{K}_X$ and $f_{qd} = f_q\text{-}jf_d$; "f" can represent: voltages, currents and fluxes.

$$\mathbf{f}_{qd0x} = \mathbf{K}_X\, \mathbf{f}_{abcx} \tag{1.2.16}$$

$$\mathbf{f}_{abcx} = \mathbf{K}_X^{-1}\, \mathbf{f}_{qd0x} \tag{1.2.17}$$

$(\mathbf{f}_{qd0x})^T = [\, f_{qx} \;\; f_{dx} \;\; f_{0x} \,]$

$(\mathbf{f}_{abcx})^T = [\, f_{ax} \;\; f_{bx} \;\; f_{cx} \,]$

$$\mathbf{K}_X = \frac{2}{3} \begin{bmatrix} \cos\gamma_X & \cos\left(\gamma_X - \frac{2\pi}{3}\right) & \cos\left(\gamma_X + \frac{2\pi}{3}\right) \\ \sin\gamma_X & \sin\left(\gamma_X - \frac{2\pi}{3}\right) & \sin\left(\gamma_X + \frac{2\pi}{3}\right) \\ \frac{1}{2} & \frac{1}{2} & \frac{1}{2} \end{bmatrix} \tag{1.2.18}$$

$$\mathbf{K}_X^{-1} = \begin{bmatrix} \cos\gamma_X & \sin\gamma_X & 1 \\ \cos\left(\gamma_X - \frac{2\pi}{3}\right) & \sin\left(\gamma_X - \frac{2\pi}{3}\right) & 1 \\ \cos\left(\gamma_X + \frac{2\pi}{3}\right) & \sin\left(\gamma_X + \frac{2\pi}{3}\right) & 1 \end{bmatrix} \tag{1.2.19}$$

$\gamma_X = \theta - \theta_X$

$$\theta = \theta(0) + \int_0^t \omega(t)dt \qquad \theta_X = \theta_X(0) + \int_0^t \omega_X(t)dt \tag{1.2.20}$$

θ and ω are the angle and the angular velocity of the qd0 frame

θ_x and ω_x are the angle and the angular velocity of the "abcx" variable, x will be "s" or "r" if stator or rotor variables are considered.

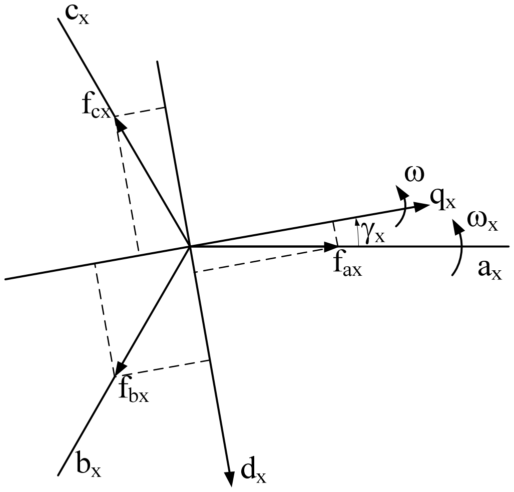

Figure 1.30 Projection of the phase coordinate quantities on the qd0 reference frame.

For a better specification of the transformation matrix also an upper script can be used to specify the qd0 reference frame; hence, in case of transformation of stator variables in a qd0 stationary frame, assuming zero all the initial positions, the transformation matrix $\mathbf{K}_x$ becomes $\mathbf{K}_s^s$ and the angle will be: $\gamma_s = \theta - \theta_s = 0 - 0 = 0$.

Instead for a transformation of rotor variables in a qd0 stationary frame, the transformation matrix $\mathbf{K}_x$ becomes $\mathbf{K}_r^s$, also in this case the initial positions are set to 0 and the transformation angle is: $\gamma_r = \theta - \theta_r = 0 - \theta_r = -\theta_r$.

Exploiting these relations, the model in machine variables introduced previously can be transformed using the qd0 variables in an arbitrary reference frame.

The equations in machine variables are here reported:

$$\begin{cases} \mathbf{v}_{abcs} = \mathbf{r}_s \, \mathbf{i}_{abcs} + p \, \boldsymbol{\lambda}_{abcs} \\ \mathbf{v}'_{abcr} = \mathbf{r}'_r \, \mathbf{i}'_{abcr} + p \, \boldsymbol{\lambda}'_{abcr} \end{cases}$$

$$\begin{bmatrix} \boldsymbol{\lambda}_{abcs} \\ \boldsymbol{\lambda}'_{abcr} \end{bmatrix} = \begin{bmatrix} \mathbf{L}_s & \mathbf{L}'_{sr} \\ (\mathbf{L}'_{sr})^T & \mathbf{L}'_r \end{bmatrix} \begin{bmatrix} \mathbf{i}_{abcs} \\ \mathbf{i}'_{abcr} \end{bmatrix}$$

$$\mathbf{K}_S = \frac{2}{3}\begin{bmatrix} \cos\theta & \cos\left(\theta - \frac{2\pi}{3}\right) & \cos\left(\theta + \frac{2\pi}{3}\right) \\ \sin\theta & \sin\left(\theta - \frac{2\pi}{3}\right) & \sin\left(\theta + \frac{2\pi}{3}\right) \\ \frac{1}{2} & \frac{1}{2} & \frac{1}{2} \end{bmatrix} \qquad (1.2.21)$$

$$(\mathbf{K}_S)^{-1} = \begin{bmatrix} \cos\theta & \sin\theta & 1 \\ \cos\left(\theta - \frac{2\pi}{3}\right) & \sin\left(\theta - \frac{2\pi}{3}\right) & 1 \\ \cos\left(\theta + \frac{2\pi}{3}\right) & \sin\left(\theta + \frac{2\pi}{3}\right) & 1 \end{bmatrix} \qquad (1.2.22)$$

$$\mathbf{K}_r = \frac{2}{3}\begin{bmatrix} \cos(\theta - \theta_r) & \cos\left(\theta - \theta_r - \frac{2\pi}{3}\right) & \cos\left(\theta - \theta_r + \frac{2\pi}{3}\right) \\ \sin(\theta - \theta_r) & \sin\left(\theta - \theta_r - \frac{2\pi}{3}\right) & \sin\left(\theta - \theta_r + \frac{2\pi}{3}\right) \\ \frac{1}{2} & \frac{1}{2} & \frac{1}{2} \end{bmatrix} \qquad (1.2.23)$$

$$(\mathbf{K}_r)^{-1} = \begin{bmatrix} \cos(\theta - \theta_r) & \sin(\theta - \theta_r) & 1 \\ \cos\left(\theta - \theta_r - \frac{2\pi}{3}\right) & \sin\left(\theta - \theta_r - \frac{2\pi}{3}\right) & 1 \\ \cos\left(\theta - \theta_r + \frac{2\pi}{3}\right) & \sin\left(\theta - \theta_r + \frac{2\pi}{3}\right) & 1 \end{bmatrix} \qquad (1.2.24)$$

Substituting (1.2.21)-(1.2.24) can be obtained (1.2.25) and (1.2.26).

$$\begin{cases} \mathbf{v}_{qd0s} = \mathbf{K}_S\,\mathbf{r}_S\,(\mathbf{K}_S)^{-1}\mathbf{i}_{qd0s} + \mathbf{K}_S\,p\left[\,(\mathbf{K}_S)^{-1}\lambda_{qd0s}\,\right] \\ \mathbf{v}'_{qd0r} = \mathbf{K}_r\,\mathbf{r}'_r\,(\mathbf{K}_r)^{-1}\mathbf{i}'_{qd0r} + \mathbf{K}_r\,p\left[\,(\mathbf{K}_r)^{-1}\lambda'_{qd0r}\,\right] \end{cases} \qquad (1.2.25)$$

$$\begin{bmatrix} \lambda_{qd0s} \\ \lambda'_{qd0r} \end{bmatrix} = \begin{bmatrix} \mathbf{K}_S\mathbf{L}_S(\mathbf{K}_S)^{-1} & \mathbf{K}_S\mathbf{L}'_{sr}\,(\mathbf{K}_r)^{-1} \\ \mathbf{K}_r\,(\mathbf{L}'_{sr})^T\,(\mathbf{K}_S)^{-1} & \mathbf{K}_r\,\mathbf{L}'_r\,(\mathbf{K}_r)^{-1} \end{bmatrix}\begin{bmatrix} \mathbf{i}_{qd0s} \\ \mathbf{i}'_{qd0r} \end{bmatrix} \qquad (1.2.26)$$

Equations (1.2.25) and (1.2.26) are below verified:

$$\mathbf{K}_S\mathbf{r}_S(\mathbf{K}_S)^{-1} = R_S\begin{bmatrix} 1 & 0 & 0 \\ 0 & 1 & 0 \\ 0 & 0 & 1 \end{bmatrix} = \mathbf{r}_S$$

$$\mathbf{K}_S\,p\left[\,(\mathbf{K}_S)^{-1}\lambda_{qd0s}\,\right] = \mathbf{K}_S(\mathbf{K}_S)^{-1}p\lambda_{qd0s} + \mathbf{K}_S\,p[(\mathbf{K}_S)^{-1}]\lambda_{qd0s} = p\lambda_{qd0s} +$$

$$+\begin{bmatrix} 0 & \omega & 0 \\ -\omega & 0 & 0 \\ 0 & 0 & 0 \end{bmatrix} \lambda_{qd0s}$$

$$\mathbf{K}_r \mathbf{r}'_r (\mathbf{K}_r)^{-1} = R'_r \begin{bmatrix} 1 & 0 & 0 \\ 0 & 1 & 0 \\ 0 & 0 & 1 \end{bmatrix} = \mathbf{r}'_r$$

$$\mathbf{K}_r\, p \left[(\mathbf{K}_r)^{-1} \lambda'_{qd0r} \right] = \mathbf{K}_r\, (\mathbf{K}_r)^{-1}\ p\lambda'_{qd0r} + \mathbf{K}_r p[(\mathbf{K}_r)^{-1}]\ \lambda'_{qd0r} = p\lambda'_{qd0r} +$$

$$+\begin{bmatrix} 0 & (\omega - \omega_r) & 0 \\ -(\omega - \omega_r) & 0 & 0 \\ 0 & 0 & 0 \end{bmatrix} \lambda'_{qd0r}$$

$$\mathbf{K}_s \mathbf{L}_s (\mathbf{K}_s)^{-1} = \begin{bmatrix} L_{ls}+L_M & 0 & 0 \\ 0 & L_{ls}+L_M & 0 \\ 0 & 0 & L_{ls} \end{bmatrix}$$

$$\mathbf{K}_s \mathbf{L}'_{sr}\, (\mathbf{K}_r)^{-1} = \mathbf{K}_r\, (\mathbf{L}'_{sr})^T\, (\mathbf{K}_s)^{-1} = \begin{bmatrix} L_M & 0 & 0 \\ 0 & L_M & 0 \\ 0 & 0 & 0 \end{bmatrix}$$

$$\mathbf{K}_r\, \mathbf{L}'_r\, (\mathbf{K}_r)^{-1} = \begin{bmatrix} L'_{lr}+L_M & 0 & 0 \\ 0 & L'_{lr}+L_M & 0 \\ 0 & 0 & L'_{lr} \end{bmatrix}$$

$$L_M = \frac{3}{2} L_{ms}$$

The final qd0 model equations, in the arbitrary frame, are reported below in scalar form; it can be noted that the rotor voltages can be set to 0 because the rotor circuit is in general short circuited:

$$\begin{cases} v_{qs} = R_s\, i_{qs} + p\, \lambda_{qs} + \omega\, \lambda_{ds} \\ v_{ds} = R_s\, i_{ds} + p\, \lambda_{ds} - \omega\, \lambda_{qs} \\ v_{0s} = R_s\, i_{0s} + p\, \lambda_{0s} \\ v'_{qr} = R'_r\, i'_{qr} + p\, \lambda'_{qr} + (\omega - \omega_r)\, \lambda'_{dr} \\ v'_{dr} = R'_r\, i'_{dr} + p\, \lambda^{'s}_{dr} - (\omega - \omega_r)\, \lambda'_{qr} \\ v'_{0r} = R'_r\, i'_{0r} + p\, \lambda'_{0r} \end{cases} \qquad (1.2.27)$$

$$\begin{cases} \lambda_{qs} = L_{ls}\, i_{qs} + L_M(i_{qs} + i'_{qr}) \\ \lambda_{ds} = L_{ls}\, i_{ds} + L_M(i_{ds} + i'_{dr}) \\ \lambda_{0s} = L_{ls}\, i_{0s} \\ \lambda'_{qr} = L'_{lr}\, i'_{qr} + L_M(i'_{qr} + i_{qs}) \\ \lambda'_{dr} = L'_{lr}\, i'_{dr} + L_M(i'_{dr} + i_{ds}) \\ \lambda'_{0r} = L'_{lr}\, i'_{qr} \end{cases} \qquad (1.2.28)$$

The electromagnetic torque can be calculated exploiting the equation written in terms of machine variable and substituting the expression: $f_{abcx} = \mathbf{K}_x^{-1}\, f_{qd0x}$ it is possible to write:

$$\begin{aligned} T_e(i_j,\theta_r) &= \left(\frac{P}{2}\right)\frac{\partial W_c(i_j,\theta_r)}{\partial\theta_r} = \left(\frac{P}{2}\right)(\mathbf{i}_{abcs})^T \frac{\partial}{\partial\theta_r}[\mathbf{L}'_{sr}]\, \mathbf{i}'_{abcr} = \\ &= \left(\frac{P}{2}\right)((\mathbf{K}_s)^{-1}\, \mathbf{i}_{qd0s})^T \frac{\partial}{\partial\theta_r}[\mathbf{L}'_{sr}](\mathbf{K}_r)^{-1}\, \mathbf{i}'_{qd0r} \end{aligned} \qquad (1.2.29)$$

After simple algebraic manipulations:

$$T_e = \frac{3}{2}\left(\frac{P}{2}\right) L_M\, (i_{qs}\, i'_{dr} - i_{ds}\, i'_{qr}) \qquad (1.2.30)$$

Equivalent expression can also be obtained substituting the current with the flux expressions:

$$T_e = \frac{3}{2}\left(\frac{P}{2}\right) (\lambda'_{qr}\, i'_{dr} - \lambda'_{dr}\, i'_{qr}) \qquad (1.2.31)$$

$$T_e = \frac{3}{2}\left(\frac{P}{2}\right) (\lambda_{ds}\, i_{qs} - \lambda_{qs}\, i_{ds}) \qquad (1.2.32)$$

It is worth noting that the torque expression does not depend on the reference frame transformation.

D. Field oriented control of the healthy IM

The type of control adopted in the simulations and experimental results shown in the next chapters is the field oriented control or vector control; this control allows an independent regulation of the torque and flux of the induction machine, ensuring high dynamic performance thanks to regulation of both the amplitude and the phase of the ac excitation [48], [49].

There are many variants of this type of control such as: stator flux-oriented, rotor flux-oriented and air-gap flux oriented; the main aim of this control category is to keep a 90° spatial orientation between the main field components similarly to DC motor drives [49]. These controls can be implemented in different ways; the direct method is based on the knowledge of the flux by means of sensors positioned inside the machine but this is not practical and in most cases the flux can be estimated through “observer” based on the machine model; the indirect method consists of the suitable definition of the angular velocity slip, that is the necessary and sufficient condition to achieve the field orientation. For this study only the indirect rotor-flux field oriented control (IFOC) is considered.

To achieve the correct decoupling considering the qd0 model for the general analysis, the only qd0 reference frame that can be chosen is the one synchronous with the rotor flux , i. e $\omega = \omega_{\lambda r}$ and the phase $\theta = \theta_{\lambda r}$ is selected in order to have the rotor flux aligned with the d-axis, this implying $\lambda_{qr}' = 0$. In this reference frame the d-axis stator current components is aligned with the rotor flux while the q-axis component is in quadrature with respect to the rotor flux as shown in Figure 1.31.

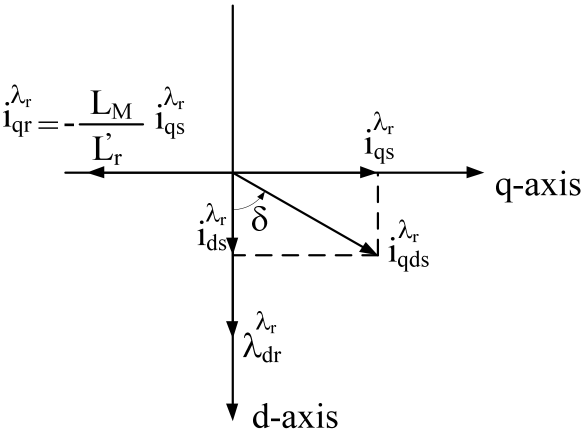

Figure 1.31 qd current components with the reference axes oriented to the rotor flux.

Considering the qd0 equations in this reference frame:

$$\begin{cases} v_{qs}^{\lambda r} = R_s\, i_{qs}^{\lambda r} + p\, \lambda_{qs}^{\lambda r} + \omega_{\lambda r}\lambda_{ds}^{\lambda r} \\ v_{ds}^{\lambda r} = R_s\, i_{ds}^{\lambda r} + p\, \lambda_{ds}^{\lambda r} - \omega_{\lambda r}\, \lambda_{qs}^{\lambda r} \\ v_{0s}^{\lambda r} = R_s\, i_{0s}^{\lambda r} + p\, \lambda_{0s}^{\lambda r} \\ 0 = R_r'\, i_{qr}^{'\lambda r} + p\, \lambda_{qr}^{'\lambda r} + (\omega_{\lambda r} - \omega_r)\, \lambda_{dr}^{'\lambda r} \\ 0 = R_r'\, i_{dr}^{'\lambda r} + p\, \lambda_{dr}^{'\lambda r} - (\omega_{\lambda r} - \omega_r)\, \lambda_{qr}^{'\lambda r} \\ 0 = R_r'\, i_{0r}^{'\lambda r} + p\, \lambda_{0r}^{'\lambda r} \end{cases} \qquad (1.2.33)$$

$$\begin{cases} \lambda_{qs}^{\lambda r} = L_{ls}\, i_{qs}^{\lambda r} + L_M (i_{qs}^{\lambda r} + i'^{\lambda r}_{qr}) \\ \lambda_{ds}^{\lambda r} = L_{ls}\, i_{ds}^{\lambda r} + L_M (i_{ds}^{\lambda r} + i'^{\lambda r}_{dr}) \\ \lambda_{0s}^{\lambda r} = L_{ls}\, i_{0s}^{\lambda r} \\ \lambda'^{\lambda r}_{qr} = L'_{lr}\, i'^{\lambda r}_{qr} + L_M (i'^{\lambda r}_{qr} + i_{qs}^{\lambda r}) = 0 \\ \lambda'^{\lambda r}_{dr} = L'_{lr}\, i'^{\lambda r}_{dr} + L_M (i'^{\lambda r}_{dr} + i_{ds}^{\lambda r}) \\ \lambda'^{\lambda r}_{0r} = L'_{lr}\, i'^{\lambda r}_{0r} \end{cases} \tag{1.2.34}$$

$$T_e = \frac{3}{2}\left(\frac{P}{2}\right)\frac{L_M}{L_r}\,(\lambda'^{\lambda r}_{dr}\, i_{qs}^{\lambda r}) \tag{1.2.35}$$

The following results can be derived as follow, considering for simplicity the upper script λ_r that indicates the reference frame will not be reported.

a) From the flux equation, because $\lambda'_{qr} = 0$ follow → $i'_{qr} = -\dfrac{L_M}{L'_r}\, i_{qs}$

From relation a) if the flux is kept constant, an instantaneous change in i_{qs} corresponds to an instantaneous change of the torque T_e.

b) $0 = R'_r\, i'_{qr} + (\omega_{\lambda r} - \omega_r)\, \lambda'_{dr}$

From b) the slip frequency, $\omega_{s\lambda r} = (\omega_{\lambda r} - \omega_r)$, that assures the field orientation, can be calculated

$$\omega_{s\lambda r} = L_M \frac{R'_r}{L'_r}\frac{i_{qs}}{\lambda'_{dr}}$$

An important relation between the stator current component i_{ds} and the rotor flux can be defined.

c) From the flux equation, the current i'_{dr} is equal to $i'_{dr} = \dfrac{\lambda'_{dr} - L_M\, i_{ds}}{L'_r}$

d) Substituting c) in the voltage equation $0 = R'_r\, i'_{dr} + p\, \lambda'_{dr} \rightarrow p\, \lambda'_{dr} = -\dfrac{R'_r}{L'_r}\, \lambda'_{dr} + \dfrac{R'_r}{L'_r} L_M\, i_{ds} \rightarrow$

$$\left(\frac{1}{\tau_r} + p\right)\lambda'_{dr} = \frac{L_M}{\tau_r}\, i_{ds} \rightarrow \lambda'_{dr} = \frac{L_M}{\left(1 + \tau_r\, p\right)}\, i_{ds}$$

From d) it is shown that a variation of the i_{ds} does not produce an instantaneous variation of the rotor flux but its changing depends on the rotor time constant τ_r, $\tau_r = \frac{L_r'}{R_r'}$; while at steady state

$\lambda_{dr}' = L_M\, i_{ds}$ and $i_{dr}' = 0$

e) From d) a relation between i_{ds} and i_{dr}', solving the voltage equation can be also defined $0 = R_r'\, i_{dr}' + p\, \lambda_{dr}'$ for the current, obtaining→ $i_{dr}' = -\frac{L_M\, p\, i_{ds}}{R_r'\left(1 + \tau_r\, p\right)}$

The relation e) clearly shows that i_{dr}' exists only when i_{ds} is changing (there is a flux variation) and its dynamic depends on the rotor time constant.

f) The final expression of the slip frequency can be obtained substituting in equation b) the result obtained in d)

$$\omega_{s\lambda r} = \frac{1}{\tau_r}\frac{i_{qs}}{i_{ds}}(1 + \tau_r\, p)$$

The field oriented control is an example of No Linear State Feedback (NLSFb) [50].
Adjusting the previous equations and considering the equation (1.2.31) of the torque and the rotor voltage equations of (1.2.33), the block diagram reported in Figure 1.32 can be defined, this simple and insightful representation allows to understand how it is possible to achieve the decoupling between torque and flux performing the No Linear Decoupling State Feedback (NLDSFb) [50]. In this block diagram the two q and d axis components of the stator current are the manipulated inputs, assuming that :

$$(\omega - \omega_r)\, \lambda_{dr}' = \frac{R_r'}{L_r'} L_M\, i_{qs} \quad \rightarrow \quad (\omega - \omega_r) = L_M \frac{R_r'}{L_r'}\frac{i_{qs}}{\lambda_{dr}'} \qquad (1.2.36)$$

the decoupling between the torque and flux is achieved and (1.2.36) confirm the already founded in (b), slip condition.

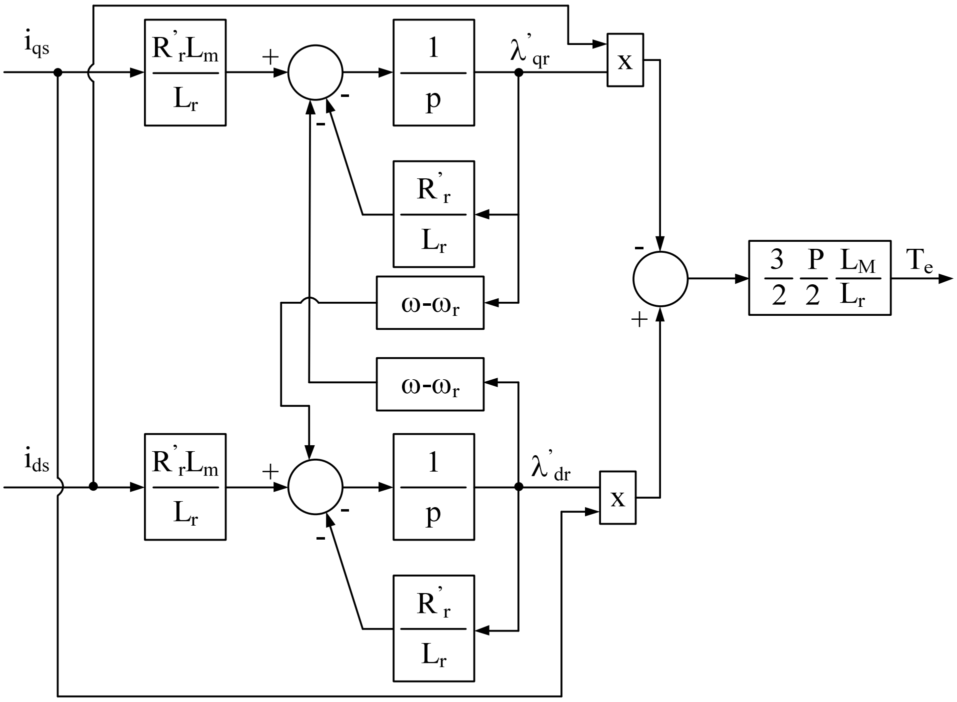

Figure 1.32 Non Linear state block diagram of the IM.

A typical block diagram for the implementation of the IFOC is shown in Figure 1.33.

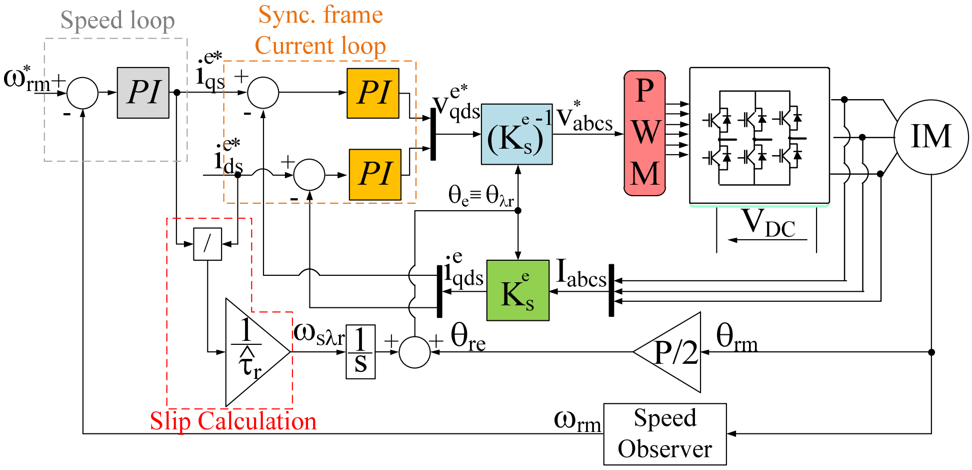

Figure 1.33 Block diagram of the Rotor Flux Field Oriented Control for IM.

In the block diagram an inner current loop is evident, where the reference values of the q and d – axis current components are compared with the feedback currents, measured through appropriate current sensors and transformed in the qd0 reference frame synchronous with the rotor flux using the transformation matrix K_S^e. The rotor flux angle is obtained summing the electrical rotor position and the slip angle obtained by the integration of the slip frequency (Slip calculation). In this way the PI controllers elaborate dc quantities [51]. In this block diagram the slip equation is simplified,

$\omega_{s\lambda r} = \frac{1}{\hat{\tau}_r} \frac{i_{qs}^{e*}}{i_{ds}^{e*}}$, because does not include the dynamic of the rotor flux, always true when the flux level is kept constant (I_{ds}^{e*} = const); instead, if it is necessary to change, continuously the value of the flux, it is useful to take into account the rotor flux dynamic, adopting a slightly different block diagram as suggested in [49]. The rotor time constant is indicated with the overstrike "^", because in general the exact value of the rotor resistance and the inductance is not known hence this will affect the slip calculation producing a not perfect field orientation. Two synchronous frame PI current controllers are adopted to provide the correct voltage that reduce the current error to 0; this voltage, v_{qs}^{e*} and v_{ds}^{e*} are transformed in "abc" frame through the inverse transformation matrix $(K_s^e)^{-1}$ and the PWM modulator will provide the gate signals for the inverter's power devices.

The q-axis reference current that produces the torque is defined by the outer speed loop, also in this case a PI controller is employed to reduce the speed error to zero providing the correct value of the torque current component, i_{qs}^{e*}.

E. Equations in qd0 variables for the faulty conditions

As aforementioned, the model of the motor is modified in case of faulty operation, with respect to the healthy model, thus to obtain the qd0 model a suitable transformation matrix is adopted. For the three-phase induction machine working with two-phase the model for the c-stator phase fault was developed in [40]; in the following paragraph the model will be reported and extended also for phase a and b faulty.

The equations in machine variables are below reported for simplicity:

$$\begin{cases} \mathbf{v}_{ijs} = \mathbf{r}_{sf}\,\mathbf{i}_{ijs} + p\,\boldsymbol{\lambda}_{ijs} \\ \mathbf{v}'_{abcr} = \mathbf{r}'_r\,\mathbf{i}'_{abcr} + p\,\boldsymbol{\lambda}'_{abcr} \end{cases}$$

$$\begin{bmatrix} \boldsymbol{\lambda}_{ijs} \\ \boldsymbol{\lambda}'_{abcr} \end{bmatrix} = \begin{bmatrix} \mathbf{L}_{sf} & \mathbf{L}'_{sfr} \\ (\mathbf{L}'_{sfr})^T & \mathbf{L}'_r \end{bmatrix} \begin{bmatrix} \mathbf{i}_{ijs} \\ \mathbf{i}'_{abcr} \end{bmatrix}$$

$$(i, j) = \begin{cases} \text{b,c fault stator phase a} \\ \text{a,c fault stator phase b} \\ \text{a,b fault stator phase c} \end{cases}$$

The rotor circuit is assumed always healthy, hence the rotor resistance and inductance matrix are equal to the healthy case. The authors adopt the convention $f_{dq} = f_d + jf_q$.

The transformation in the qd0 variables, it is performed adopting the following transformation matrices, take into account that the final model equations are referred to the a stationary reference frame.

For the stator circuit, the transformation matrix $\mathbf{T}_s^s$ is obtained from a set of eigenvectors associated to the eigenvalues of the matrix $\mathbf{L}_{sf}$, keeping out the leakage inductance.

For fault of phase a and c:

$$\mathbf{T}_s^s = \frac{\sqrt{2}}{2}\begin{bmatrix} 1 & -1 \\ 1 & 1 \end{bmatrix} \tag{1.2.37}$$

$$(\mathbf{T}_s^s)^{-1} = \frac{\sqrt{2}}{2}\begin{bmatrix} 1 & 1 \\ -1 & 1 \end{bmatrix} \tag{1.2.38}$$

For fault of phase b:

$$\mathbf{T}_s^s = (\mathbf{T}_s^s)^{-1} = \frac{\sqrt{2}}{2}\begin{bmatrix} -1 & 1 \\ 1 & 1 \end{bmatrix} \tag{1.2.39}$$

The coefficient of the eigenvector $\frac{\sqrt{2}}{2}$ is chosen to satisfy the constraint $\left|f_{dq}\right| = \sqrt{f_d^2 + f_q^2} = \left|f_s\right|$ where $\left|f_s\right|$ is the module of the “ij” stator variable: voltages, currents and fluxes.

The standard transformation matrix is used for the rotor circuit, as it is a balanced three phases system:

$$K_r^r = \sqrt{\frac{2}{3}}\begin{bmatrix} 1 & -\frac{1}{2} & -\frac{1}{2} \\ 0 & \frac{\sqrt{3}}{2} & -\frac{\sqrt{3}}{2} \\ \frac{1}{\sqrt{2}} & \frac{1}{\sqrt{2}} & \frac{1}{\sqrt{2}} \end{bmatrix} \tag{1.2.40}$$

$$(K_r^r)^{-1} = \sqrt{\frac{2}{3}}\begin{bmatrix} 1 & 0 & \frac{1}{\sqrt{2}} \\ -\frac{1}{2} & \frac{\sqrt{3}}{2} & \frac{1}{\sqrt{2}} \\ -\frac{1}{2} & -\frac{\sqrt{3}}{2} & \frac{1}{\sqrt{2}} \end{bmatrix} \tag{1.2.41}$$

The constant gain $\sqrt{\frac{2}{3}}$ allows to have a so-called “power invariant” transformation, and also the inverse matrix corresponds to direct matrix transposed; but $\left|f_{dq}\right| \neq \left|f_r\right|$, $\left|f_r\right|$ is the module of the "abc" rotor variables. Substituting the previous matrices in the equations (1.2.9) and (1.2.10) can be obtained (1.2.42) and (1.2.43).

$$\begin{cases} \mathbf{v}^{s}_{dqs} = \mathbf{T}^{s}_{s}\, \mathbf{r}_{sf}\, (\mathbf{T}^{s}_{s})^{-1}\, \mathbf{i}^{s}_{dqs} + \mathbf{T}^{s}_{s}\, p\left[(\mathbf{K}^{s}_{s})^{-1} \lambda^{s}_{dqs} \right] \\ \mathbf{v}'^{r}_{dqr} = \mathbf{K}^{r}_{r}\, \mathbf{r}'_{r}\, (\mathbf{K}^{r}_{r})^{-1}\, \mathbf{i}'^{r}_{dqr} + \mathbf{K}^{r}_{r}\, p\left[(\mathbf{K}^{r}_{r})^{-1} \lambda'^{r}_{dqr} \right] \end{cases} \tag{1.2.42}$$

$$\begin{bmatrix} \lambda^{s}_{dqs} \\ \lambda'^{r}_{dqr} \end{bmatrix} = \begin{bmatrix} \mathbf{T}^{s}_{s}\mathbf{L}_{sf}(\mathbf{T}^{s}_{s})^{-1} & \mathbf{T}^{s}_{s}\mathbf{L}'_{sfr}\, (\mathbf{K}^{r}_{r})^{-1} \\ \mathbf{K}^{r}_{r}\, (\mathbf{L}'_{sfr})^{T}\, (\mathbf{T}^{s}_{s})^{-1} & \mathbf{K}^{r}_{r}\, \mathbf{L}'_{r}\, (\mathbf{K}^{r}_{r})^{-1} \end{bmatrix} \begin{bmatrix} \mathbf{i}^{s}_{dqs} \\ \mathbf{i}'^{r}_{dqr} \end{bmatrix} \tag{1.2.43}$$

(1.2.42) and (1.2.43) are below verified.

$$\mathbf{T}^{s}_{s}\, \mathbf{r}_{sf}\, (\mathbf{T}^{s}_{s})^{-1} = R_{s} \begin{bmatrix} 1 & 0 \\ 0 & 1 \end{bmatrix} = \mathbf{r}_{sf}$$

$$\mathbf{T}^{s}_{s}\, p\left[(\mathbf{T}^{s}_{s})^{-1} \lambda^{s}_{dqs} \right] = p\, \lambda^{s}_{dqs}$$

$$\mathbf{K}^{r}_{r}\, \mathbf{r}'_{r}\, (\mathbf{K}^{r}_{r})^{-1} = R'_{r} \begin{bmatrix} 1 & 0 & 0 \\ 0 & 1 & 0 \\ 0 & 0 & 1 \end{bmatrix} = \mathbf{r}'_{r}$$

$$\mathbf{K}^{r}_{r}\, p\left[(\mathbf{K}^{r}_{r})^{-1} \lambda'^{r}_{dqr} \right] = p\, \lambda'^{r}_{dqr}$$

$$\mathbf{L}_{ss} = \mathbf{T}^{s}_{s}\mathbf{L}_{sf}(\mathbf{T}^{s}_{s})^{-1} = \begin{bmatrix} L_{ls} + \frac{3}{2}L_{ms} & 0 \\ 0 & L_{ls} + \frac{1}{2}L_{ms} \end{bmatrix}$$

For phase a-fault;

$$\mathbf{L}_{srf} = \mathbf{T}^{s}_{s}\mathbf{L}'_{sfr}\, (\mathbf{K}^{r}_{r})^{-1} = L_{ms} \begin{bmatrix} \frac{3}{2}\sin(\theta_{r}) & \frac{3}{2}\cos(\theta_{r}) \\ -\frac{\sqrt{3}}{2}\cos(\theta_{r}) & \frac{\sqrt{3}}{2}\sin(\theta_{r}) \end{bmatrix}$$

$$(\mathbf{L}_{srf})^{T} = \mathbf{K}^{r}_{r}\, (\mathbf{L}'_{sfr})^{T}\, (\mathbf{T}^{s}_{s})^{-1} = L_{ms} \begin{bmatrix} \frac{3}{2}\sin(\theta_{r}) & -\frac{\sqrt{3}}{2}\cos(\theta_{r}) \\ \frac{3}{2}\cos(\theta_{r}) & \frac{\sqrt{3}}{2}\sin(\theta_{r}) \end{bmatrix}$$

For phase b-fault

$$\mathbf{L}_{srf} = \mathbf{T}^{s}_{s}\mathbf{L}'_{sfr}\, (\mathbf{K}^{r}_{r})^{-1} = L_{ms} \begin{bmatrix} \frac{3}{2}\cos(\theta_{r} + \frac{5\pi}{6}) & \frac{3}{2}\sin(\theta_{r} - \frac{\pi}{6}) \\ -\frac{\sqrt{3}}{2}\sin(\theta_{r} - \frac{\pi}{6}) & \frac{\sqrt{3}}{2}\cos(\theta_{r} + \frac{5\pi}{6}) \end{bmatrix}$$

$$(\mathbf{L}_{srf})^{T} = \mathbf{K}_{r}^{r}\,(\mathbf{L}'_{sfr})^{T}\,(\mathbf{T}_{s}^{s})^{-1} = \mathrm{L}_{ms}\begin{bmatrix} \frac{3}{2}\cos(\theta_r + \frac{5\pi}{6}) & -\frac{\sqrt{3}}{2}\sin(\theta_r - \frac{\pi}{6}) \\ \frac{3}{2}\sin(\theta_r - \frac{\pi}{6}) & \frac{\sqrt{3}}{2}\cos(\theta_r + \frac{5\pi}{6}) \end{bmatrix}$$

For phase c-fault

$$\mathbf{L}_{srf} = \mathbf{T}_{s}^{s}\mathbf{L}'_{sfr}\,(\mathbf{K}_{r}^{r})^{-1} = \mathrm{L}_{ms}\begin{bmatrix} \frac{3}{2}\cos(\theta_r + \frac{\pi}{6}) & -\frac{3}{2}\sin(\theta_r + \frac{\pi}{6}) \\ \frac{\sqrt{3}}{2}\sin(\theta_r + \frac{\pi}{6}) & \frac{\sqrt{3}}{2}\cos(\theta_r + \frac{\pi}{6}) \end{bmatrix}$$

$$(\mathbf{L}_{srf})^{T} = \mathbf{K}_{r}^{r}\,(\mathbf{L}'_{sfr})^{T}\,(\mathbf{T}_{s}^{s})^{-1} = \mathrm{L}_{ms}\begin{bmatrix} \frac{3}{2}\cos(\theta_r + \frac{\pi}{6}) & \frac{\sqrt{3}}{2}\sin(\theta_r + \frac{\pi}{6}) \\ -\frac{3}{2}\sin(\theta_r + \frac{\pi}{6}) & \frac{\sqrt{3}}{2}\cos(\theta_r + \frac{\pi}{6}) \end{bmatrix}$$

$$\mathbf{L}_{rr} = \mathbf{K}_{r}^{r}\,\mathbf{L}'_{r}\,(\mathbf{K}_{r}^{r})^{-1} = \begin{bmatrix} \mathrm{L}'_{lr} + \frac{3}{2}\mathrm{L}_{ms} & 0 \\ 0 & \mathrm{L}'_{lr} + \frac{3}{2}\mathrm{L}_{ms} \end{bmatrix}$$

To refer the rotor variables from the qd0 rotor frame to the stationary frame, a suitable transformation matrix, $\mathbf{K}_{r}^{s}$, depending on the faulty phase, is implemented in order to delete “sin” and “cos” terms from the coupling inductance matrix $\mathbf{L}_{srf}$.

$$\mathbf{K}_{r}^{s} = \begin{bmatrix} \cos(\theta_r + \alpha) & -\sin(\theta_r + \alpha) \\ \sin(\theta_r + \alpha) & \cos(\theta_r + \alpha) \end{bmatrix} \tag{1.2.44}$$

$$(\mathbf{K}_{r}^{s})^{-1} = \begin{bmatrix} \cos(\theta_r\,\alpha) & \sin(\theta_r + \alpha) \\ -\sin(\theta_r + \alpha) & \cos(\theta_r + \alpha) \end{bmatrix} \tag{1.2.45}$$

$$\alpha = \left\{ \begin{matrix} -\frac{\pi}{2} & \text{phase a-fault} \\ \frac{5\pi}{6} & \text{phase b-fault} \\ \frac{\pi}{6} & \text{phase c-fault} \end{matrix} \right\}$$

$$\begin{cases} \mathbf{v}_{dqs}^{s} = \mathbf{r}_{sf}\,\mathbf{i}_{dqs}^{s} + p\,\lambda_{dqs}^{s} \\ \mathbf{v}_{dqr}^{\prime s} = \mathbf{K}_{r}^{s}\,\mathbf{r}'_{r}\,(\mathbf{K}_{r}^{s})^{-1}\,\mathbf{i}_{dqr}^{\prime s} + \mathbf{K}_{r}^{s}\,p\left[(\mathbf{K}_{r}^{s})^{-1}\lambda_{dqr}^{\prime s}\right] \end{cases} \tag{1.2.46}$$

$$\begin{bmatrix} \lambda_{dqs}^{s} \\ \lambda_{dqr}^{\prime r} \end{bmatrix} = \begin{bmatrix} \mathbf{L}_{ss} & \mathbf{L}_{srf}\,(\mathbf{K}_r^s)^{-1} \\ \mathbf{K}_r^s\,(\mathbf{L}_{srf})^T & \mathbf{K}_r^s\,\mathbf{L}_{rr}\,(\mathbf{K}_r^s)^{-1} \end{bmatrix} \begin{bmatrix} \mathbf{i}_{dqs}^{s} \\ \mathbf{i}_{dqr}^{\prime s} \end{bmatrix} \qquad (1.2.47)$$

$$\mathbf{K}_r^s\,\mathbf{r}_r'\,(\mathbf{K}_r^s)^{-1} = \mathbf{r}_r'$$

$$\mathbf{K}_r^s\,p\left[(\mathbf{K}_r^s)^{-1}\lambda_{dqr}^{\prime s}\right] = p\,\lambda_{dqr}^{\prime s} + \begin{bmatrix} 0 & -\omega_r \\ \omega_r & 0 \end{bmatrix}\lambda_{dqr}^{\prime s}$$

$$\mathbf{L}_{srf}\,(\mathbf{K}_r^s)^{-1} = \mathbf{K}_r^s\,(\mathbf{L}_{srf})^T = \begin{bmatrix} \frac{3}{2}L_{ms} & 0 \\ 0 & \frac{\sqrt{3}}{2}L_{ms} \end{bmatrix}$$

$$\mathbf{K}_r^s\,\mathbf{L}_{rr}\,(\mathbf{K}_r^s)^{-1} = \mathbf{L}_{rr}$$

To sum up, the final “dq” model in the stationary frame is reported below in scalar form:

$$\begin{cases} v_{ds}^{s} = R_s\,i_{ds}^{s} + p\,\lambda_{ds}^{s} \\ v_{qs}^{s} = R_s\,i_{qs}^{s} + p\,\lambda_{qs}^{s} \\ 0 = R_r'\,i_{dr}^{\prime s} + p\,\lambda_{dr}^{\prime s} - \omega_r\,\lambda_{qr}^{\prime s} \\ 0 = R_r'\,i_{qr}^{\prime s} + p\,\lambda_{qr}^{\prime s} + \omega_r\,\lambda_{dr}^{\prime s} \end{cases} \qquad (1.2.48)$$

$$\begin{cases} \lambda_{ds}^{s} = L_{ls}\,i_{ds}^{s} + M_d(i_{ds}^{s} + i_{dr}^{\prime s}) = L_{ds}\,i_{ds}^{s} + M_d\,i_{dr}^{\prime s} \\ \lambda_{qs}^{s} = L_{ls}\,i_{qs}^{s} + M_q(\frac{i_{qs}^{s}}{\sqrt{3}} + i_{qr}^{\prime s}) = L_{qs}\,i_{qs}^{s} + M_q\,i_{qr}^{\prime s} \\ \lambda_{dr}^{\prime s} = L_{lr}'\,i_{dr}^{\prime s} + M_d(i_{dr}^{\prime s} + i_{ds}^{s}) = L_r'\,i_{dr}^{\prime s} + M_d\,i_{ds}^{s} \\ \lambda_{qr}^{\prime s} = L_{lr}'\,i_{qr}^{\prime s} + L_M(i_{qr}^{\prime s} + \sqrt{3}\frac{i_{qs}^{s}}{3}) = L_r'\,i_{qr}^{\prime s} + M_q\,i_{qs}^{s} \end{cases} \qquad (1.2.49)$$

$$L_{ds} = L_{ls} + \frac{3}{2}L_{ms} \qquad L_{qs} = L_{ls} + \frac{1}{2}L_{ms} \qquad L_r' = L_{lr}' + \frac{3}{2}L_{ms}$$

$$M_d = \frac{3}{2}L_{ms} \qquad M_q = \frac{\sqrt{3}}{2}L_{ms}$$

The torque equations can be expressed with the following equation:

$$T_e(i_j,\theta_r) = \left(\frac{P}{2}\right)\frac{\partial W_c(i_j,\theta_r)}{\partial\theta_r} = \left(\frac{P}{2}\right)(\mathbf{i}_{ijs})^T \frac{\partial}{\partial\theta_r}[\mathbf{L}'_{sfr}]\,\mathbf{i}'_{abcr} =$$

$$= \left(\frac{P}{2}\right)((\mathbf{T}^s_s)^{-1}\,\mathbf{i}^s_{dqs})^T\frac{\partial}{\partial\theta_r}[\mathbf{L}'_{sfr}](\mathbf{K}^r_r)^{-1}(\mathbf{K}^s_r)^{-1}\,\mathbf{i}'^s_{dqr}$$

$$T_e = \frac{P}{2}(M_q\, i'^s_{dr}\, i^s_{qs} - M_d\, i'^s_{qr}\, i^s_{ds}) \tag{1.2.50}$$

F. Field oriented control of the faulty IM

Rotor-flux field orientation can be implemented also for the IM working under unbalanced conditions, , but to avoid pulsating torque the rotation matrix, transforming the stator current components, $\mathbf{i}^s_{dqs}$ from the stationary frame to the rotating frame synchronous with the rotor flux, is modified introducing the two mutual induction M_d and M_q to balance the unbalanced model. Applying this transformation the two phase currents will be shifted by 60° as previously defined in the paragraph 1.2, only in this way is possible to generate a balanced MMF.

$$\begin{bmatrix} i^e_{ds} \\ i^e_{qs} \end{bmatrix} = \begin{bmatrix} \sqrt{\frac{M_d}{M_q}}\cos(\theta_e) & \sqrt{\frac{M_q}{M_d}}\sin(\theta_e) \\ -\sqrt{\frac{M_d}{M_q}}\sin(\theta_e) & \sqrt{\frac{M_q}{M_d}}\cos(\theta_e) \end{bmatrix} \begin{bmatrix} i^s_{ds} \\ i^s_{qs} \end{bmatrix} \tag{1.2.51}$$

$$\begin{bmatrix} i^s_{ds} \\ i^s_{qs} \end{bmatrix} = \begin{bmatrix} \sqrt{\frac{M_q}{M_d}}\cos(\theta_e) & -\sqrt{\frac{M_q}{M_d}}\sin(\theta_e) \\ \sqrt{\frac{M_d}{M_q}}\sin(\theta_e) & \sqrt{\frac{M_d}{M_q}}\cos(\theta_e) \end{bmatrix} \begin{bmatrix} i^e_{ds} \\ i^e_{qs} \end{bmatrix} \tag{1.2.52}$$

$$T^e_s = \begin{bmatrix} \sqrt{\frac{M_d}{M_q}}\cos(\theta_e) & \sqrt{\frac{M_q}{M_d}}\sin(\theta_e) \\ -\sqrt{\frac{M_d}{M_q}}\sin(\theta_e) & \sqrt{\frac{M_q}{M_d}}\cos(\theta_e) \end{bmatrix}$$

$$(T^e_s)^{-1} = \begin{bmatrix} \sqrt{\frac{M_q}{M_d}}\cos(\theta_e) & -\sqrt{\frac{M_q}{M_d}}\sin(\theta_e) \\ \sqrt{\frac{M_d}{M_q}}\sin(\theta_e) & \sqrt{\frac{M_d}{M_q}}\cos(\theta_e) \end{bmatrix}$$

For the rotor variable variables that are reported in the stationary frame the standard rotation matrix can be used.

$$\begin{bmatrix} i_{dr}^{e} \\ i_{qr}^{e} \end{bmatrix} = \begin{bmatrix} \cos(\theta_e) & \sin(\theta_e) \\ -\sin(\theta_e) & \cos(\theta_e) \end{bmatrix} \begin{bmatrix} i_{dr}^{s} \\ i_{qr}^{s} \end{bmatrix} \qquad (1.2.53)$$

$$\begin{bmatrix} i_{dr}^{s} \\ i_{qr}^{s} \end{bmatrix} = \begin{bmatrix} \cos(\theta_e) & -\sin(\theta_e) \\ \sin(\theta_e) & \cos(\theta_e) \end{bmatrix} \begin{bmatrix} i_{dr}^{e} \\ i_{qr}^{e} \end{bmatrix} \qquad (1.2.54)$$

Taking into account this transformation both direct or indirect field orientation can be implemented, for the purpose of this activity the IFOC is tested.

Transforming the model equations in the rotor - flux reference frame, aligning the rotor flux along the d-axis, ($\lambda_{qr}^{e} = 0$), the slip frequency that allow to achieve the field orientation can be calculated, considering the rotor equations:

$$0 = r_r\, i_{dr}^{e} + p\, \lambda_{dr}^{e}$$

$$0 = r_r\, i_{qr}^{e} + (\omega_e - \omega_r)\, \lambda_{dr}^{e}$$

$$\lambda_{dr}^{e} = \sqrt{M_d\, M_q}\, i_{ds}^{e} + L_r\, i_{dr}^{e}$$

$$\lambda_{qr}^{e} = \sqrt{M_d\, M_q}\, i_{qs}^{e} + L_r\, i_{qr}^{e} = 0$$

$$T_e = \frac{P}{2} \frac{\sqrt{M_d\, M_q}}{L_r}\, i_{qs}^{e}\, \lambda_{dr}^{e}$$

From qr - flux equation can be obtained the current i_{qr}^{e}:

$$i_{qr}^{e} = -\frac{\sqrt{M_d\, M_q}}{L_r}\, i_{qs}^{e}$$

Substituting in the dr – voltage equation, solving for the slip frequency $\omega_{s\lambda r} = (\omega_e - \omega_r)$:

$$\omega_{s\lambda r} = \frac{R_r}{L_r} \sqrt{M_d\, M_q}\, \frac{i_{qs}^{e}}{\lambda_{dr}^{e}}$$

In the slip equation instead of L_M there is the coefficient $\sqrt{M_d\, M_q}$

The slip frequency expressed in terms of stator current components, writing and substituting the expression of the dr-flux:

$$\lambda_{dr}^{e} = \frac{\sqrt{M_d\, M_q}}{(1 + p\tau_r)}\, i_{ds}^{e}$$

$$\omega_{s\lambda r} = \frac{1}{\tau_r}\frac{i_{qs}^{e}}{i_{ds}^{e}}(1 + p\, \tau_r)$$

For steady state it becomes:

$$\omega_{s\lambda r} = \frac{1}{\tau_r}\frac{I_{qs}^{e}}{I_{ds}^{e}}$$

$\tau_r = \frac{L_r}{R_r}$ is the rotor time constant.

Under a generic open phase fault, the slip frequency equation, expressed in terms of the stator currents components, is equal to the healthy case already shown in the paragraph 1.2.1 D.

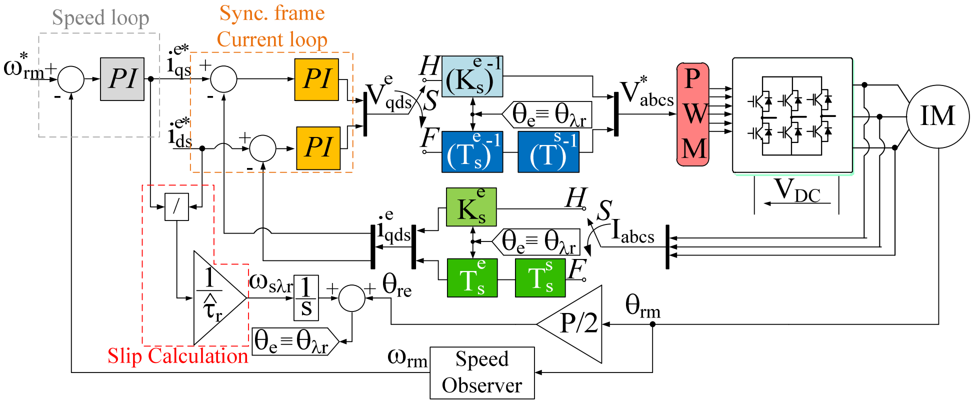

Figure 1.34 Fault tolerant control block diagram for Rotor Flux Indirect Field Orientation.

Some simulations of the fault tolerant IFOC for IM are reported in Figure 1. 35. A 3kW IM whose parameters are reported in Table 1.5, is simulated and the drive is speed controlled operating at a constant speed of 50 rad/s, at 1s a torque load of 50% of the rated value is applied, at 1.2s the phase b is opened; in this case the fault detection and identification of the fault is not implemented but the capability of the control to handle the fault is tested, therefore due to the application of the fault there is a sag on the speed and on the torque, caused by a transient on the q-axis current. The stator phase currents are also shown and after the fault the remaining two phase currents a and c are increased in amplitude and shifted by 60° while the neutral current is not zero; at the end of this transient the drive can satisfy the required speed and torque command.

Table 1.5 3kW IM motor parameters.

Rated Power [kW]	3	R_s, R_r [Ω]	2, 1.66
Rated Voltage [V]	400	L_{ls}, L_{lr} [H]	0.0105, 0.0105
Rated frequency [Hz]	50	L_{ms} [H]	0.171
Rated speed [rpm]	1430	Poles (P)	4
Rated current [A rms]	6.9	Rotor Inertia [Kgm^2]	0.014

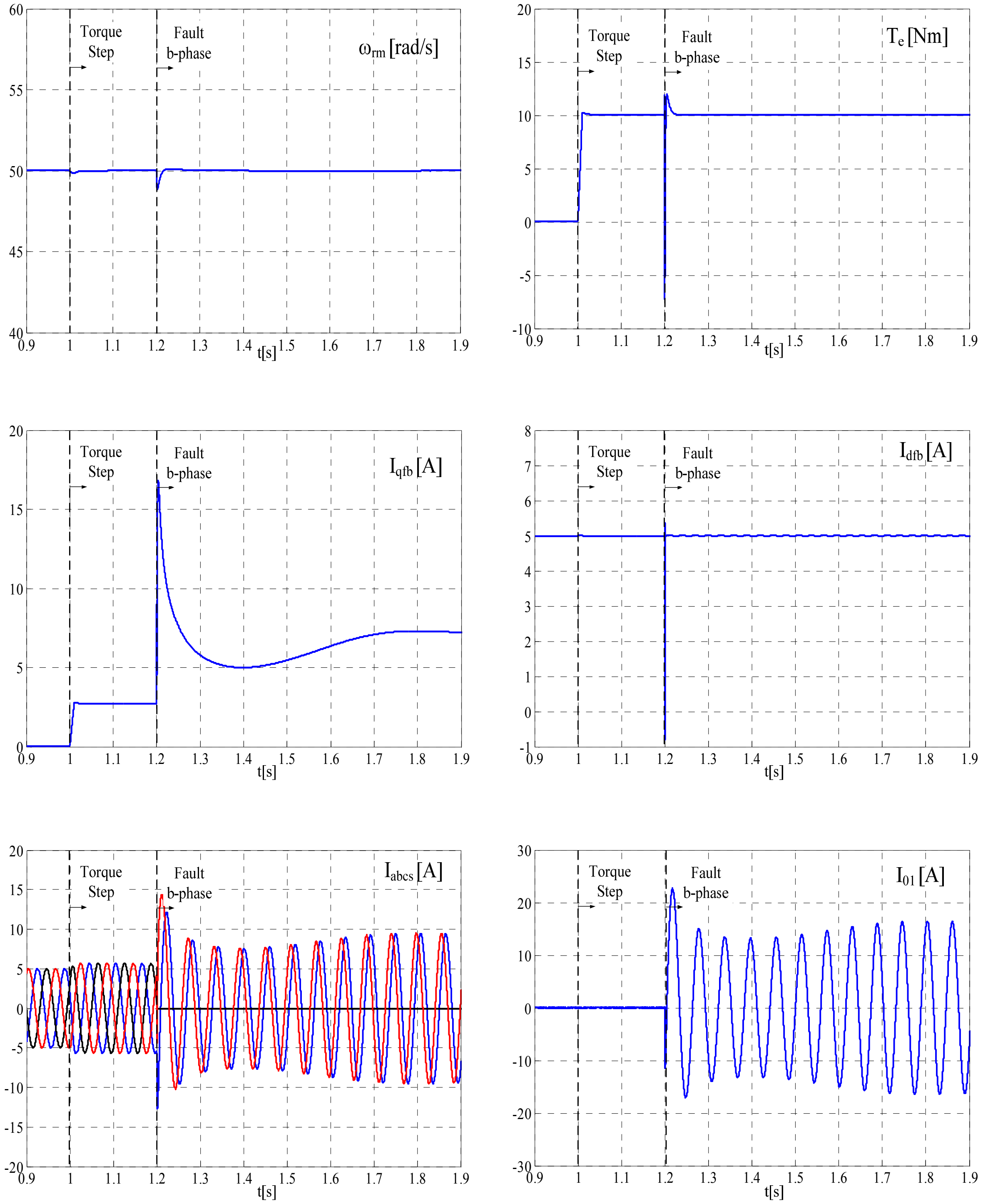

Figure 1. 35 Fault tolerant IFOC for IM in normal operative conditions and after a fault on phase b.

1.2.2 PMSM modeling and control

In a similar way, as already for the IM, the PMSM model in machine variables and in qd0 reference frame are reported in case of healthy and faulty working conditions [45], [46]. Similarly to the IM model, PMSM described in the following does not include the iron losses or saturation effect of the ferromagnetic circuits as the latter is not the objective of this activity.

A. Analytical model in healthy conditions

A 3-phase PMSM synchronous machine is composed of a stator circuit where the 3-phase stator windings shifted to each other by 120 electrical degrees are positioned, and the rotor circuit consisting of permanent magnets structure substituting the field winding to provide the excitation field. The use of PM allows to reduce the weight and increase the efficiency and the dynamic performances of the motor, [46], [47]. The excitation field is directed along a particular direction indicated as “d-axis” and shifted by 90° electrical from that defined as “q-axis”. The stator windings distribution can define a sinusoidal or a trapezoidal MMF, while the rotor structure can be wound or anisotropy; hence, in the second one there is a magnetic saliency that defines a different value of the inductance depending on the rotor position [46]. In the first type of rotor structure the permanent magnets are positioned on the surface, defining the so called “surface mounted permanent magnet synchronous machine”, indicated also as PMSM, while in the second type the permanent magnets are buried in the rotor, defining the “interior mounted permanent magnet synchronous machine”, called also IPM. In the following, the equations in machine variables are reported for sinusoidally distributed stator windings and no damper windings in the rotor are considered [46].

$$\begin{cases} \mathbf{v}_{abcs} = \mathbf{r}_s \, \mathbf{i}_{abcs} + p \, \boldsymbol{\lambda}_{abcs} \\ \boldsymbol{\lambda}_{abcs} = \mathbf{L}_s \, \mathbf{i}_{abcs} + \boldsymbol{\lambda}_m' \end{cases} \tag{1.2.55}$$

$$\mathbf{r}_s = R_s \begin{bmatrix} 1 & 0 & 0 \\ 0 & 1 & 0 \\ 0 & 0 & 1 \end{bmatrix}$$

$$\mathbf{L}_s = \begin{bmatrix} L_{ls} + L_A - L_B\cos(2\theta_r) & -\frac{1}{2}L_A - L_B\cos2(\theta_r - \frac{\pi}{3}) & -\frac{1}{2}L_A - L_B\cos2(\theta_r + \frac{\pi}{3}) \\ -\frac{1}{2}L_A - L_B\cos2(\theta_r - \frac{\pi}{3}) & L_{ls} + L_A - L_B\cos2(\theta_r - \frac{2\pi}{3}) & -\frac{1}{2}L_A - L_B\cos2(\theta_r + \pi) \\ -\frac{1}{2}L_A - L_B\cos2(\theta_r + \frac{\pi}{3}) & -\frac{1}{2}L_A - L_B\cos2(\theta_r + \pi) & L_{ls} + L_A - L_B\cos2(\theta_r + \frac{2\pi}{3}) \end{bmatrix}$$

The matrix $\mathbf{L}_S$ contains the leakage inductance L_{ls} and the self and mutual inductance of the stator windings that are defined by a constant term L_A and variable term L_B function of two times the rotor position. For a wound rotor structure $L_B = 0$.

Assuming $L_{mq} = \frac{3}{2}\left(L_A - L_B \right)$ and $L_{md} = \frac{3}{2}\left(L_A + L_B \right)$, can be possible to write $L_A = \frac{1}{3}\left(L_{mq} + L_{md} \right)$ and $- L_B = \frac{1}{3}\left(L_{mq} - L_{md} \right)$ or alternatively $L_q = L_{ls} + L_{mq}$,. $L_d = L_{ls} + L_{md}$, $L_A = \frac{1}{3}\left(L_q + L_d - 2\, L_{ls} \right)$, $- L_B = \frac{1}{3}\left(L_q - L_d \right)$.

$$\lambda_m' = \lambda_m \begin{bmatrix} \sin(\theta_r) \\ \sin(\theta_r - \frac{2\pi}{3}) \\ \sin(\theta_r + \frac{2p}{3}) \end{bmatrix} \tag{1.2.56}$$

λ_m' is a matrix that describes the permanent magnet flux, as seen from the stator, linkages with the stator windings, that is function of the rotor position; λ_m is the amplitude of the flux linkages established by the permanent magnet.

The electromagnetic torque is function of the energy stored in the coupling field and can be expressed by the differentiation of the coenergy, under the assumption of linear system, with the following relation:

$$\begin{aligned} T_e(i_j,\theta_r) &= \left(\frac{P}{2}\right)\frac{\partial W_c(i_j,\theta_r)}{\partial \theta_r} = \left(\frac{P}{4}\right)(\mathbf{i}_{abcs})^T \frac{\partial}{\partial \theta_r}[\mathbf{L}_s - L_{ls}\mathbf{I}]\, \mathbf{i}_{abcs} + \\ &+ \left(\frac{P}{2}\right)(\mathbf{i}_{abcs})^T \frac{\partial}{\partial \theta_r}[\lambda_m'] = T_e^r + T_e^e \end{aligned} \tag{1.2. 57}$$

$$\begin{aligned} T_e^r = -\left(\frac{P}{2}\right)\left(\frac{L_q - L_d}{3}\right)\Big[& \left(i_{as}^2 - \frac{1}{2} i_{bs}^2 - \frac{1}{2} i_{cs}^2 - i_{as}\, i_{bs} - i_{as}\, i_{cs} + 2\, i_{bs}\, i_{cs} \right) \sin(2\,\theta_r) + \\ & + \frac{\sqrt{3}}{2}\left(i_{bs}^2 - i_{cs}^2 - 2\, i_{as}\, i_{bs} + 2\, i_{as}\, i_{cs} \right) \cos(2\,\theta_r) \Big] \end{aligned} \tag{1.2. 58}$$

$$T_e^e = \left(\frac{P}{2}\right)\lambda_m \left[\frac{\sqrt{3}}{2}\left(i_{bs} - i_{cs} \right) \sin(\theta_r) + \left(i_{as} - \frac{1}{2} i_{bs} - \frac{1}{2} i_{cs} \right)\cos(\theta_r) \right] \tag{1.2. 59}$$

T_e^r is the electromagnetic torque associated to the saliency of the machine in fact it depends on L_q and L_d instead T_e^e is an excitation torque due to the permanent magnet flux linkage.

B. Analytical model under faulty conditions

Assuming that one of the three stator phases is not supplied, the model equation has to be modified to describe the system correctly.

$$\begin{cases} \mathbf{v}_{ijs} = \mathbf{r}_{sf}\,\mathbf{i}_{ijs} + p\,\lambda_{ijs} \\ \lambda_{ijs} = \mathbf{L}_{sf}\,\mathbf{i}_{ijs} + \lambda'_{mf} \end{cases} \tag{1.2. 60}$$

The subscript index i and j:

$$\mathbf{(i, j) =} \begin{cases} \text{b,c fault stator phase a} \\ \text{a,c fault stator phase b} \\ \text{a,b fault stator phase c} \end{cases}$$

$$\mathbf{r}_{sf} = R_s \begin{bmatrix} 1 & 0 \\ 0 & 1 \end{bmatrix}$$

$$\mathbf{L}_{sf} = \begin{bmatrix} L_{ls} + L_A - L_B\cos 2(\theta_r + \beta_1) & -\frac{1}{2}L_A - L_B\cos 2(\theta_r + \beta_2) \\ -\frac{1}{2}L_A - L_B\cos 2(\theta_r + \beta_2) & L_{ls} + L_A - L_B\cos 2(\theta_r + \beta_3) \end{bmatrix}$$

$$\lambda'_m = \lambda_m \begin{bmatrix} \sin(\theta_r + \beta_1) \\ \sin(\theta_r + \beta_3) \end{bmatrix}$$

$$(\beta_1, \beta_2, \beta_3) = \begin{cases} \left(-\frac{2\pi}{3}, 0, \frac{2\pi}{3}\right) \text{ fault stator phase a} \\ \left(0, \frac{\pi}{3}, \frac{2\pi}{3}\right) \text{ fault stator phase b} \\ \left(0, -\frac{\pi}{3}, -\frac{2\pi}{3}\right) \text{ fault stator phase c} \end{cases}$$

The torque equation can be expressed with:

$$\begin{aligned} T_e(i_j,\theta_r) &= \left(\frac{P}{2}\right)\frac{\partial W_c(i_j,\theta_r)}{\partial\theta_r} = \left(\frac{P}{4}\right)(\mathbf{i}_{ijs})^T \frac{\partial}{\partial\theta_r}[\mathbf{L}_{sf} - L_{ls}\mathbf{I}]\,\mathbf{i}_{ijs} + \\ &+ \left(\frac{P}{2}\right)(\mathbf{i}_{ijs})^T \frac{\partial}{\partial\theta_r}[\lambda'_{mf}] = T^r_{ef} + T^e_{ef} \end{aligned} \tag{1.2.61}$$

$$\begin{aligned} T^r_{ef} = -\left(\frac{P}{2}\right)\left(\frac{L_q - L_d}{3}\right)\Big[& \sin 2(\theta_r + \beta_1) i^2_{is} + 2\sin 2(\theta_r + \beta_2) i_{is} i_{js} + \\ & + \sin 2(\theta_r + \beta_1) i^2_{js} \Big] \end{aligned} \tag{1.2.62}$$

$$T_{ef}^{e} = \left(\frac{P}{2}\right) \lambda_m \Big[\big(- i_{is} \sin(\beta_1) - i_{js} \sin(\beta_3) \big) \sin(\theta_r) + \\ + \big(i_{is} \cos(\beta_1) + i_{js} \cos(\beta_3) \big) \cos(\theta_r) \Big] \tag{1.2.63}$$

These two generalized expressions can be also obtained setting to zero the current of the phase fault in the torque equations previous defined for the healthy model.

C. Equations in qd0 synchronous reference frame for healthy conditions and field orientation

The representation of the PMSM model in the qd0 reference frame can be performed by means of the transformation matrix introduced in the paragraph 1.2.1 C, with respect to the IM the electrical rotor quantities are directly expressed in qd0 variables and a wide benefit can be obtained, transforming the stator circuits using the Park's transformation [46]; in fact, by referring the stator quantities to a qd0 reference frame synchronous with rotor and considering the assumption of linear system, the dependency of the inductance with the rotor position does not exist leading to only constant parameters.

The equations in machine variables are below reported for simplicity.

$$\begin{cases} \mathbf{v}_{abcs} = \mathbf{r}_s \, \mathbf{i}_{abcs} + p \, \boldsymbol{\lambda}_{abcs} \\ \boldsymbol{\lambda}_{abcs} = \mathbf{L}_s \, \mathbf{i}_{abcs} + \boldsymbol{\lambda}_m' \end{cases}$$

The transformation matrix is applied directly to refer the stator equation in machine variables to the qd0 frame synchronous with the rotor, hence the transformation matrix adopted is reported below. Considering the transformation angle γ_x it will be in this case: $\gamma_s = \theta - \theta_s = \theta_r - 0 = \theta_r$, where θ the position of the qd0 frame is set equal to θ_r instead θ_s the position of the "abc" stator is considered equal to 0.

$$\mathbf{K}_s^r = \frac{2}{3} \begin{bmatrix} \cos\theta_r & \cos\left(\theta_r - \frac{2\pi}{3}\right) & \cos\left(\theta_r + \frac{2\pi}{3}\right) \\ \sin\theta_r & \sin\left(\theta_r - \frac{2\pi}{3}\right) & \sin\left(\theta_r + \frac{2\pi}{3}\right) \\ \frac{1}{2} & \frac{1}{2} & \frac{1}{2} \end{bmatrix}$$

$$(\mathbf{K}_s^r)^{-1} = \begin{bmatrix} \cos\theta_r & \sin\theta_r & 1 \\ \cos\left(\theta_r - \frac{2\pi}{3}\right) & \sin\left(\theta_r - \frac{2\pi}{3}\right) & 1 \\ \cos\left(\theta_r + \frac{2\pi}{3}\right) & \sin\left(\theta_r + \frac{2\pi}{3}\right) & 1 \end{bmatrix}$$

Applying the relations $f^r_{qd0s} = \mathbf{K}^r_s f_{abc}$ and $f_{abc} = (\mathbf{K}^r_s)^{-1} f^r_{qd0s}$

$$\begin{cases} \mathbf{v}^r_{qd0s} = \mathbf{K}^r_s \mathbf{r}_s (\mathbf{K}^r_s)^{-1} \mathbf{i}^r_{qd0s} + \mathbf{K}^r_s \, p\left[(\mathbf{K}^r_s)^{-1} \lambda^r_{qd0s} \right] \\ \lambda^r_{qd0s} = \mathbf{K}^r_s \mathbf{L}_s (\mathbf{K}^r_s)^{-1} \mathbf{i}^r_{qd0s} + \mathbf{K}^r_s \lambda'_m \end{cases} \tag{1.2.64}$$

$$\mathbf{K}^r_s \mathbf{r}_s (\mathbf{K}^r_s)^{-1} = R_s \begin{bmatrix} 1 & 0 & 0 \\ 0 & 1 & 0 \\ 0 & 0 & 1 \end{bmatrix} = \mathbf{r}_s$$

$$\mathbf{K}^r_s \, p\left[(\mathbf{K}^r_s)^{-1} \lambda^r_{qd0s} \right] = p\,\lambda^r_{qd0s} + \begin{bmatrix} 0 & \omega_r \\ -\omega_r & 0 \end{bmatrix} \lambda^r_{qd0s}$$

Substituting $L_A = \frac{1}{3}\left(L_q + L_d - 2 L_{ls} \right)$ and $- L_B = \frac{1}{3}\left(L_q - L_d \right)$ in the $\mathbf{L}_s$:

$$\mathbf{K}^r_s \mathbf{L}_s (\mathbf{K}^r_s)^{-1} = \begin{bmatrix} L_q & 0 & 0 \\ 0 & L_d & 0 \\ 0 & 0 & L_{ls} \end{bmatrix}$$

With: $L_q = L_{ls} + L_{mq}$; $L_d = L_{ls} + L_{md}$; $L_{mq} = \frac{3}{2}\left(L_A - L_B \right)$; $L_{md} = \frac{3}{2}\left(L_A + L_B \right)$

$$\mathbf{K}^r_s \lambda'_m = \lambda_m \begin{bmatrix} 0 \\ 1 \\ 0 \end{bmatrix}$$

The torque expression in qd0 variables:

$$\begin{gathered} T_e(i_j,\theta_r) = \left(\frac{P}{2}\right) \frac{\partial W_c(i_j,\theta_r)}{\partial\theta_r} = \left(\frac{P}{4}\right)\left((\mathbf{K}^r_s)^{-1} \mathbf{i}^r_{qd0s}\right)^T \frac{\partial}{\partial\theta_r}[\mathbf{L}_s - L_{ls}\mathbf{I}]\, (\mathbf{K}^r_s)^{-1} \mathbf{i}^r_{qd0s} + \\ + \left(\frac{P}{2}\right) \left((\mathbf{K}^r_s)^{-1} \mathbf{i}^r_{qd0s}\right)^T \frac{\partial}{\partial\theta_r}[\lambda'_m] = T^r_e + T^e_e \end{gathered} \tag{1.2.65}$$

$$T^r_e = \frac{3}{2}\frac{P}{2} (L_d - L_q)\, i^r_{ds}\, i^r_{qs} \tag{1.2.66}$$

$$T_e^e = \frac{3}{2}\frac{P}{2}\lambda_m i_{qs}^r \tag{1.2.67}$$

To sum up, the equations in scalar form are below reported.

$$\begin{cases} v_{qs}^r = R_s\, i_{qs}^r + p\, \lambda_{qs}^r + \omega_r\, \lambda_{ds}^r \\ v_{ds}^r = R_s\, i_{ds}^r + p\, \lambda_{ds}^r - \omega_r\, \lambda_{qs}^r \\ \lambda_{qs}^r = L_q\, i_{qs}^r \\ \lambda_{ds}^r = L_d\, i_{ds}^r + \lambda_m \\ \lambda_{0s} = L_{ls}\, i_{0s} \end{cases} \tag{1.2.68}$$

$$T_e = \frac{3}{2}\frac{P}{2}\left[\lambda_m\, i_{qs}^r + (L_d - L_q)\, i_{ds}^r\, i_{qs}^r\right] \tag{1.2.69}$$

A quite simple representation of a PMSM is achieved with the qd0 variables referred to a synchronous rotor frame, fundamentally two pure RL circuits are describing the electrical model of the machine if a decoupling of the rotational terms $\omega_r\, \lambda_{ds}^r$ and $-\omega_r\, \lambda_{qs}^r$ is performed.

For the PMSM the field orientation description is introduced together with the qd0 modeling because it is simpler than the IM. Practically, the same concept discussed for the IM field orientation is applied here, but in this case, since the rotor flux is always aligned with the d-axis and it is synchronous with rotor, the only way to achieve the field orientation is to transform the model in the qd0 reference frame synchronous with the rotor, Figure 1.36 reports the block diagram for this type of control.

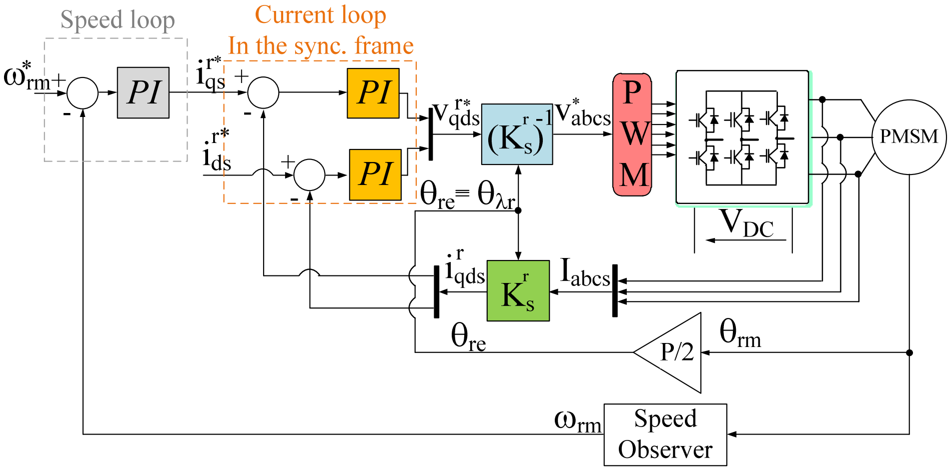

Figure 1.36 Block diagram for the Field Orientated control of PM synchronous machine.

D. Equations in qd0 variable for faulty conditions and field orientation

The qd0 model valid for open-phase fault is defined in [45], following a different approach with respect to that one proposed for the IM in [40]; also in this case at the end of the process the phase current of the healthy phases will be shifted by 60°. In this case different transformation matrices are used to transform voltages / fluxes and currents equations compared to the IM model. The transformation process is reported below.

The first transformation matrix **A** is obtained from the eigenvectors associated to the eigenvalues of the constant part of the matrix $\mathbf{L}_{sf}$; that is rewritten in terms of L_q and $.L_d$.

$$\mathbf{L}_{sf} = \begin{bmatrix} L_{ls} + L_A - L_B\cos2(\theta_r + \beta_1) & -\frac{1}{2}L_A - L_B\cos2(\theta_r + \beta_2) \\ -\frac{1}{2}L_A - L_B\cos2(\theta_r + \beta_2) & L_{ls} + L_A - L_B\cos2(\theta_r + \beta_3) \end{bmatrix} =$$

$$= \begin{bmatrix} L_{ls} + \left(\frac{L_d + L_q - 2\,L_{ls}}{3}\right) & -\frac{1}{2}\left(\frac{L_d + L_q - 2\,L_{ls}}{3}\right) \\ -\frac{1}{2}\left(\frac{L_d + L_q - 2\,L_{ls}}{3}\right) & L_{ls} + \left(\frac{L_d + L_q - 2\,L_{ls}}{3}\right) \end{bmatrix} +$$

$$-\left(\frac{L_d - L_q}{3}\right)\begin{bmatrix} \cos2(\theta_r + \beta_1) & \cos2(\theta_r + \beta_2) \\ \cos2(\theta_r + \beta_2) & \cos2(\theta_r + \beta_3) \end{bmatrix}$$

$$\mathbf{A} = \begin{bmatrix} 1 & 1 \\ 1 & -1 \end{bmatrix} \qquad (\mathbf{A})^{-1} = \frac{1}{2}\mathbf{A} \tag{1.2.70}$$

Voltage and flux equations in the qd0 stationary frame are:

$$\begin{cases} \mathbf{v}_{qds}^{su1} = \mathbf{A}\,\mathbf{r}_{sf}\,(\mathbf{A})^{-1}\mathbf{i}_{qds}^{su1} + \mathbf{A}\,p\left[(\mathbf{A})^{-1}\lambda_{qds}^{su1}\right] \\ \lambda_{qds}^{su1} = \mathbf{A}\,\mathbf{L}_{sf}\,(\mathbf{A})^{-1}\mathbf{i}_{qds}^{su1} + \mathbf{A}\,\lambda_m' \end{cases} \tag{1.2.71}$$

$$\mathbf{A}\,\mathbf{r}_{sf}\,(\mathbf{A})^{-1} = \mathbf{r}_{sf}$$

$$\mathbf{A}\,p\left[(\mathbf{A})^{-1}\lambda_{qds}^{su1}\right] = p\,\lambda_{qds}^{su1}$$

$$\mathbf{L}_{sf2} = \mathbf{A}\,\mathbf{L}_{sf}\,(\mathbf{A})^{-1} = \begin{bmatrix} \frac{1}{3}\left[2L_{ls} + \left(\frac{L_d + L_q}{2}\right)\right] & 0 \\ 0 & \left(\frac{L_d + L_q}{2}\right) \end{bmatrix} +$$

$$-\frac{1}{2}\left(\frac{L_d - L_q}{3}\right)\begin{bmatrix} \cos2(\theta_r + \beta_2) & -2\sin2\left(\frac{\beta_1 - \beta_3}{2}\right)\sin2\left(\theta_r + \frac{\beta_1 - \beta_3}{2}\right) \\ -2\sin2\left(\frac{\beta_1 - \beta_3}{2}\right)\sin2\left(\theta_r + \frac{\beta_1 - \beta_3}{2}\right) & -3\cos2(\theta_r + \beta_2) \end{bmatrix}$$

$$\lambda'_{m2} = \mathbf{A}\,\lambda'_{m} = \lambda_m \begin{bmatrix} 2\cos\left(\frac{\beta_1 - \beta_3}{2}\right)\sin\left(\theta_r + \frac{\beta_1 - \beta_3}{2}\right) \\ -2\sin\left(\frac{\beta_1 - \beta_3}{2}\right)\cos\left(\theta_r + \frac{\beta_1 - \beta_3}{2}\right) \end{bmatrix}$$

The upper-script “u” means “unbalance”.

For balancing the matrix λ'_{m2} the matrix **B** is introduced and a transformation in another qd0 stationary frame is defined as follow.

$$\mathbf{B} = \begin{bmatrix} \left[2\cos\left(\frac{\beta_1 - \beta_3}{2}\right)\right]^{-1} & 0 \\ 0 & \left[2\cos\left(\frac{\beta_1 - \beta_3}{2}\right)\right]^{-1} \end{bmatrix}$$

$$(\mathbf{B})^{-1} = \begin{bmatrix} 2\cos\left(\frac{\beta_1 - \beta_3}{2}\right) & 0 \\ 0 & 2\sin\left(\frac{\beta_1 - \beta_3}{2}\right) \end{bmatrix}$$

$$\mathbf{v}^{su}_{qds} = \mathbf{B}\,\mathbf{v}^{su1}_{qds} \tag{1.2.72}$$

$$\lambda^{su}_{qds} = \mathbf{B}\,\lambda^{su1}_{qds} \tag{1.2.73}$$

$$\begin{cases} \mathbf{v}^{su}_{qds} = \mathbf{B}\,\mathbf{r}_{sf}\,(\mathbf{B})^{-1}\mathbf{i}^{su}_{qds} + \mathbf{B}\,p\left[(\mathbf{B})^{-1}\lambda^{su}_{qds}\right] \\ \lambda^{su}_{qds} = \mathbf{B}\,\mathbf{L}_{sf2}\,(\mathbf{B})^{-1}\mathbf{i}^{su}_{qds} + \mathbf{B}\,\lambda'_{m2} \end{cases} \tag{1.2.74}$$

$$\mathbf{B}\,\mathbf{L}_{sf2}\,(\mathbf{B})^{-1} =$$

$$= -\frac{1}{2}\left(\frac{L_d - L_q}{3}\right)\begin{bmatrix} \cos 2(\theta_r + \beta_2) & -\left(2\sin\left(\frac{\beta_1 - \beta_3}{2}\right)\right)^2 \sin 2(\theta_r + \beta_2) \\ -\left(2\cos\left(\frac{\beta_1 - \beta_3}{2}\right)\right)^2 \sin 2(\theta_r + \beta_2) & -3\cos 2(\theta_r + \beta_2) \end{bmatrix}$$

$$\mathbf{B}\,\lambda'_{m2} = \lambda_m \begin{bmatrix} \sin(\theta_r + \beta_2) \\ \cos(\theta_r + \beta_2) \end{bmatrix}$$

From the value of β, before defined it is obtained for whatever fault:

$$\left(2\sin\left(\frac{\beta_1 - \beta_3}{2}\right)\right)^2 = 3 \qquad \left(2\cos\left(\frac{\beta_1 - \beta_3}{2}\right)\right)^2 = 1$$

The voltage terms does not change after the application of **B** matrix.

The model in the qd reference frame synchronous with the rotor is obtained with the application of the rotational matrix **R** for voltages and fluxes and $\mathbf{R_I}$ for currents.

$$\mathbf{R} = \begin{bmatrix} \cos(\theta_r + \beta_2) & -\sin(\theta_r + \beta_2) \\ \sin(\theta_r + \beta_2) & \cos(\theta_r + \beta_2) \end{bmatrix} \qquad (1.2.75)$$

$$(\mathbf{R})^{-1} = \mathbf{R}^T \qquad (1.2.76)$$

$$\mathbf{R}_I = \frac{1}{\det(\mathbf{R}_I)^{-1}} \begin{bmatrix} d\cos(\theta_r + \beta_2) & -b\sin(\theta_r + \beta_2) \\ c\sin(\theta_r + \beta_2) & a\cos(\theta_r + \beta_2) \end{bmatrix} \qquad (1.2.77)$$

$$(\mathbf{R}_I)^{-1} = \begin{bmatrix} a\cos(\theta_r + \beta_2) & b\sin(\theta_r + \beta_2) \\ -c\sin(\theta_r + \beta_2) & d\cos(\theta_r + \beta_2) \end{bmatrix} \qquad (1.2.78)$$

The coefficients introduced in the $\mathbf{R}_I$ matrix are exploited to balance the model and cancel the dependency from the rotor position, obtaining a model with constant coefficient that can produce constant electromagnetic torque.

$$\mathbf{v}^r_{qds} = \mathbf{R}\,\mathbf{v}^{su}_{qds} \qquad \lambda^r_{qds} = \mathbf{R}\,\lambda^{su}_{qds} \qquad \mathbf{i}^r_{qds} = \mathbf{R}_I\,\mathbf{i}^{su}_{qds} \qquad (1.2.79)$$

$$\begin{cases} \mathbf{v}^r_{qds} = \mathbf{R}\,\mathbf{r}_{sf}\,(\mathbf{R}_I)^{-1}\,\mathbf{i}^r_{qds} + \mathbf{R}\,p\left[(\mathbf{R})^{-1}\lambda^r_{qds}\right] \\ \lambda^r_{qds} = \mathbf{R}\,\mathbf{L}_{sf2}\,(\mathbf{R}_I)^{-1}\,\mathbf{i}^{su}_{qds} + \mathbf{R}\,\lambda'_{m2} \end{cases} \qquad (1.2.80)$$

Setting a=3c; b=3d and c=d=1 quite the same model of the faulty PMSM machine is obtained compared to the healthy one. The only difference is introduced in the resistance matrix and in the leakage inductance terms becoming rotor dependent and cross-coupled between q and d- axis, but because their value is relatively small they do not produce significant disturbance as demonstrated in [45].

$$\mathbf{R}\,\mathbf{r}_{sf}\,(\mathbf{R}_I)^{-1} = 2\,R_s \begin{bmatrix} 1 & 0 \\ 0 & 1 \end{bmatrix} + R_s \begin{bmatrix} \cos 2(\theta_r + \beta_2) & \sin 2(\theta_r + \beta_2) \\ \sin 2(\theta_r + \beta_2) & -\cos 2(\theta_r + \beta_2) \end{bmatrix}$$

$$\mathbf{R}\,p\left[(\mathbf{R})^{-1}\,\lambda^r_{qds}\right] = p\,\lambda^r_{qds} + \begin{bmatrix} 0 & \omega_r \\ -\omega_r & 0 \end{bmatrix} \lambda^r_{qds}$$

$$\mathbf{R}\,\mathbf{L}_{sf2}\,(\mathbf{R}_I)^{-1} = \begin{bmatrix} L_{ls} + L_q & 0 \\ 0 & L_{ls} + L_d \end{bmatrix} + L_{ls} \begin{bmatrix} \cos 2(\theta_r + \beta_2) & \sin 2(\theta_r + \beta_2) \\ \sin 2(\theta_r + \beta_2) & -\cos 2(\theta_r + \beta_2) \end{bmatrix}$$

$$\mathbf{R}\,\lambda'_{m2} = \lambda_m \begin{bmatrix} 0 \\ 1 \end{bmatrix}$$

$$T_e(i_j, \theta_r) = \left(\frac{P}{2}\right) \frac{\partial W_c(i_j, \theta_r)}{\partial \theta_r} =$$

$$= \left(\frac{P}{4}\right)\left((\mathbf{A})^{-1} (\mathbf{B})^{-1} (\mathbf{R_I})^{-1} \mathbf{i}^{r}_{qd0s} \right)^{T} \frac{\partial}{\partial\theta_r}[\mathbf{L}_{sf} - L_{ls}\mathbf{I}]\, (\mathbf{A})^{-1} (\mathbf{B})^{-1} (\mathbf{R_I})^{-1} \mathbf{i}^{r}_{qd0s} +$$

$$+ \left(\frac{P}{2}\right)\left((\mathbf{A})^{-1} (\mathbf{B})^{-1} (\mathbf{R_I})^{-1} \mathbf{i}^{r}_{qd0s} \right)^{T} \frac{\partial}{\partial\theta_r}[\lambda'_m] = T^{r}_{e} + T^{e}_{e}$$

$$T^{r}_{e} = \frac{3}{2}\frac{P}{2}(L_d - L_q)\, i^{r}_{ds}\, i^{r}_{qs}$$

$$T^{e}_{e} = \frac{3}{2}\frac{P}{2}\lambda_m\, i^{r}_{qs}$$

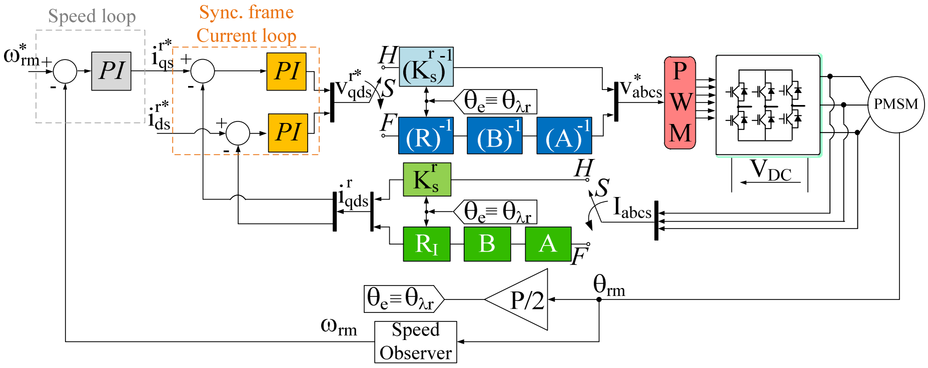

Figure 1.37 Fault tolerant control block diagram for FOC of PMSM.

Figure 1.37 shows the complete block diagram for a PMSM which include the matrices for the vector control or FOC in normal operations and that one for the control under an open phase fault. Naturally the position of the selector S is defined by an appropriate fault detection algorithm as well as the different parameter values.

Simulation tests can provide similar results as that one before showed for the IM.

1.3 Conclusions

In this chapter a State-of-the-Art-Review has been presented, starting from the definition of multi-drive systems and their applications; different topologies have been analyzed highlighting their pros and cons with respect to the concept of reliability improvement. This objective can be achieved modifying the standard drive topologies with additional circuital elements allowing to overcome the faulty conditions, sometimes with reduced performance, also in case of fault of one or more drive components. Many power converter structures and techniques have been reviewed together with the modeling and control referred in particular for three phase IM and PMSM.

1.4 References

[1] Shumei Cui; Shouliang Han; Chan C.C. "Overview of Multi-machine Drive Systems for Electric and Hybrid Electric Vehicles", Transportation Electrification Asia-Pacific (ITEC Asia-Pacific), 2014 IEEE Conference and Expo, pp. : 1-6, Aug. 31, 2014 – Sept. 3, 2014.

[2] Kerkman, R.J. "Twenty years of PWM AC drives: when secondary issues become primary concerns", Industrial Electronics, Control, and Instrumentation, 1996., Proceedings of the 1996 IEEE IECON 22nd International Conference on, vol.: 1, pp.: 57-63.

[3] Consoli, A.; Cacciato, M.; Gennaro, F.; Scarcella, G.; Testa, A. "Common Mode current elimination in multi-drive industrial systems", Industry Applications Conference, 1999. Thirty-Fourth IAS Annual Meeting. Conference Record of the 1999 IEEE, vol.: 3, pp.: 1851-1857.

[4] Levi, E.; Jones, M.; Vukosavic, S.N. "Even-phase multi-motor vector controlled drive with single inverter supply and series connection of stator windings", Electric Power Applications, IEE Proceedings, 2003, vol.: 150, Issue: 5, pp.: 580-590.

[5] Dujic, D.; Jones, M.; Vukosavic, S.N.; Levi, E. "A General PWM Method for a (2n + 1)-Leg Inverter Supplying n Three-Phase Machines," Industrial Electronics, IEEE Transactions on, 2009, vol.:56, Issue: 10, pp.: 4107-4118.

[6] Pulvirenti, M.; Scarcella, G.; Scelba, G.; Cacciato, M.; Testa, A. "Fault-Tolerant AC Multi-drive System," Emerging and Selected Topics in Power Electronics, IEEE Journal of, 2014, vol.: 2, Issue: 2, pp.: 224-235.

[7] Chee-Shen Lim; Levi, E.; Jones, M.; Abd Rahim, N.; Wooi-Ping Hew "A Fault-Tolerant Two-Motor Drive With FCS-MP-Based Flux and Torque Control," Industrial Electronics, IEEE Transaction on, 2014, vol.: 61, Issue: 12, pp.: 6603-6614.

[8] Lyra, R.O.C.; Lipo, T.A. "Torque density improvement in a six-phase induction motor with third harmonic current injection," Industry Applications, IEEE Transactions on, 2002, vol.: 38, Issue: 5, pp.: 1351-1360.

[9] Zhao, Y.; Lipo, T.A. "Space vector PWM control of dual three-phase induction machine using vector space decomposition," Industry Applications, IEEE Transactions on, 1995, vol.: 31, Issue: 5, pp.: 1100-1109.

[10] Hyung-Min Ryu; Ji-Woong Kim; Seung-Ki Sul "Synchronous frame current control of multi-phase synchronous motor. Part I. Modeling and current control based on multiple d-q spaces concept under balanced condition" Industry Applications Conference, 2004. 39th IAS Annual Meeting. Conference Record of the 2004 IEEE, vol.: 1, pp.:63.

[11] Parsa, L. "On advantages of multi-phase machines", Industrial Electronics Society, 2005. IECON 2005. 31st Annual Conference of IEEE, pp.: 6.

[12] Parsa, L.; Taehyung Kim “Reducing Torque Pulsation of Multi-Phase Interior Permanent Magnet Machines”, Industry Applications Conference, 2006. 41st IAS Annual Meeting. Conference Record of the 2006 IEEE, vol.: 4, pp.: 1978-1983.

[13] Levi, E.; Jones, M.; Vukosavic, S.N.; Toliyat, H.A. “A novel concept of a multiphase, multi-motor vector controlled drive system supplied from a single voltage source inverter,” Power Electronics, IEEE Transactions on, 2004, vol.: 19, Issue: 2; pp.: 320-335.

[14] Jones, M.; Vukosavic, S.N.; Levi, E. “Parallel-Connected Multiphase Multi-drive Systems With Single Inverter Supply,” Industrial Electronics, IEEE Transactions on, 2009, vol.: 56, Issue: 6, pp.:2047-2057.

[15] Ledezma, E.; McGrath, B.; Munoz, A.; Lipo, T.A. “Dual AC-drive system with a reduced switch count,” Industry Applications, IEEE Transactions on, 2001, vol.: 37, Issue: 5, pp.: 1325-1333.

[16] Gui-Jia Su; Hsu, J.S. “A five-leg inverter for driving a traction motor and a compressor motor,” Power Electronics, IEEE Transactions on, 2006, vol.: 21, Issue: 3, pp.: 687-692.

[17] Gui-Jia Su; Lixin Tang; Xianghui Huang “Control of Two Permanent Magnet Machines Using a Five-Leg Inverter for Automotive Applications,” Industry Applications Conference, 2006. 41st IAS Annual Meeting. Conference Record of the 2006 IEEE, vol.: 3, pp.:1606-1612.

[18] Lixin Tang; Gui-Jia Su “High-Performance Control of Two Three-Phase Permanent-Magnet Synchronous Machines in an Integrated Drive for Automotive Applications,” Power Electronics, IEEE Transactions on, 2008, vol.: 23,Issue:6, pp.: 3047-3055.

[19] Oka, K.; Nozawa, Y.; Omata, R.; Suzuki, K.; Furuya, A.; Matsuse, K. “Characteristic Comparison between Five-Leg Inverter and Nine-Switch Inverter”, Power Conversion Conference - Nagoya, 2007. PCC '07, 2007, pp.:279-283.

[20] Rajambal, K.; Rajarajan, B.; Khan, A.U. “Design analysis and implementation of nine switch inverter for the independent control of two AC motors”, Power Electronics (IICPE), 2010 India International Conference on, 2011, pp.: 1-6.

[21] Jingwei Zhu; Ertugrul, N.; Wen Liang Soong “Fault remedial strategies in a fault-tolerant brushless permanent magnet AC motor drive with redundancy”, Power Electronics and Motion Control Conference, 2009. IPEMC '09. IEEE 6th International, pp.:423-427.

[22] Arash H. Isfahani, Farid Ahmadi “Mechanical coupled BLDC motors for energy saving in submarine application” Przegląd Elektrotechniczny, 2011.

[23] Yu-Seok Jeong; Seung-Ki Sul; Schulz, S.E.; Patel, N.R. “Fault detection and fault-tolerant control of interior permanent-magnet motor drive system for electric vehicle,” Industry Applications, IEEE Transactions on, 2005, vol.: 41, Issue: 1, pp.:46-51.

[24] Rui Wu; Blaabjerg, F.; Huai Wang; Liserre, M.; Iannuzzo, F. “Catastrophic failure and fault-tolerant design of IGBT power electronic converters - an overview”, Industrial Electronics Society, IECON 2013 - 39th Annual Conference of the IEEE, pp.: 507-513.

[25] Cruz, S.M.A.; Cardoso, A.J.M. “Stator winding fault diagnosis in three-phase synchronous and asynchronous motors, by the extended Park's vector approach,” Industry Applications, IEEE Transactions on, 2001, vol.: 37, Issue: 5, pp.: 1227-1233.

[26] Briz, F.; Degner, M.W.; Guerrero, J.M.; Garcia, P. “Stator Windings Fault Diagnostics of Induction Machines Operated From Inverters and Soft-Starters Using High-Frequency Negative-Sequence Currents,” Industry Applications, IEEE Transactions on 2009, vol.: 45,issue: 5, pp.: 1637-1646.

[27] Adabi, J.; Zare, F.; Ledwich, G.; Ghosh, A.; Lorenz, R.D. “Bearing damage analysis by calculation of capacitive coupling between inner and outer races of a ball bearing”,
Power Electronics and Motion Control Conference, 2008. EPE-PEMC 2008. 13th, pp.: 903-907.

[28] Akrad, A.; Hilairet, M.; Diallo, D. “Design of a Fault-Tolerant Controller Based on Observers for a PMSM Drive,” Industrial Electronics, IEEE Transactions on, 2011, vol.: 58, Issue:4, pp.:1416-1427.

[29] Najafabadi, T.A.; Salmasi, F.R.; Jabehdar-Maralani, P. “Detection and Isolation of Speed-, DC-Link Voltage-, and Current-Sensor Faults Based on an Adaptive Observer in Induction-Motor Drives,” Industrial Electronics, IEEE Transactions on, 2011, vol.: 58, Issue:5, pp.:1662-1672.

[30] Berriri, H.; Naouar, M.W.; Slama-Belkhodja, I. “Easy and Fast Sensor Fault Detection and Isolation Algorithm for Electrical Drives,” Power Electronics, IEEE Transactions on, 2012, vol.: 27, Issue:2, pp.: 490-499.

[31] Foo, G.H.B.; Xinan Zhang; Vilathgamuwa, D.M. “A Sensor Fault Detection and Isolation Method in Interior Permanent-Magnet Synchronous Motor Drives Based on an Extended Kalman Filter,” Industrial Electronics, IEEE Transactions on, 2013, vol.:60, Issue:8, pp.: 3485-3495.

[32] Gilsu Choi; Jahns, T.M. “Interior permanent magnet synchronous machine rotor demagnetization characteristics under fault conditions”, Energy Conversion Congress and Exposition (ECCE), 2013 IEEE, pp.: 2500-2507.

[33] Jen-Ren Fu; Lipo, T.A. “A strategy to isolate the switching device fault of a current regulated motor drive” Industry Applications Society Annual Meeting, 1993, Conference Record of the 1993 IEEE, vol.: 2, pp.: 1015-1020.

[34] Bolognani, S.; Zordan, M.; Zigliotto, M. “Experimental fault-tolerant control of a PMSM drive,” Industrial Electronics, IEEE Transactions on, 2000, vol.: 47, Issue:5, pp.: 1134-1141.

[35] Welchko, B.A.; Lipo, T.A.; Jahns, T.M.; Schulz, S.E. “Fault tolerant three-phase AC motor drive topologies: a comparison of features, cost, and limitations,” Power Electronics, IEEE Transactions on, 2004, vol.: 19, Issue: 4, pp.: 1108-1116.

[36] Errabelli, R.R.; Mutschler, P. “Fault-Tolerant Voltage Source Inverter for Permanent Magnet Drives,” Power Electronics, IEEE Transactions on, 2012, vol.:27, Issue: 2, pp.:500-508.

[37] Jacobina, C.B.; de Araujo Ribeiro, R.L.; Lima, A.M.N.; da Silva, E.R.C. “Fault-tolerant reversible AC motor drive system,” Industry Applications, IEEE Transactions on, 2003, vol.: 39, Issue: 4, pp.: 1077-1084.

[38] Tian-Hua Liu; Jen-Ren Fu; Lipo, T.A. “A strategy for improving reliability of field-oriented controlled induction motor drives,” Industry Applications, IEEE Transactions on, 1993, vol.: 29, Issue: 5, pp.: 910-918.

[39] Jen-Ren Fu; Lipo, T.A. “Disturbance free operation of a multiphase current regulated motor drive with an opened phase,” Industry Applications, IEEE Transactions on, 1994, vol.: 30, Issue:5, pp.: 1267-1274.

[40] Zhao, Y.; Lipo, T.A. “An approach to modeling and field-oriented control of a three phase induction machine with structural imbalance”, Applied Power Electronics Conference and Exposition, 1996. APEC '96. Conference Proceedings 1996., Eleventh Annual, vol.:1, pp.: 380-386.

[41] Zhao, Y.; Lipo, T.A. “Modeling and control of a multi-phase induction machine with structural unbalance. Part I. Machine modeling and Multi-Dimensional Current Reguation,” Energy Conversion, IEEE Transactions on, 1996, vol.:11, Issue:3, pp.: 570-577.

[42] Zhao, Y.; Lipo, T.A. “Modeling and control of a multi-phase induction machine with structural unbalance. Part II. Field-Oriented Control and Experimental Verification,” Energy Conversion, IEEE Transactions on, 1996, vol.:11, Issue:3, pp.: 578-584.

[43] Hyung-Min Ryu; Ji-Woong Kim; Seung-Ki Sul “Synchronous frame current control of multi-phase synchronous motor - part II asymmetric fault condition due to open phases” Industry Applications Conference, 2004. 39th IAS Annual Meeting. Conference Record of the 2004 IEEE, vol.: 1, pp.: 275.

[44] Bianchi, N.; Bolognani, S.; Pré, M.D. “Strategies for the Fault-Tolerant Current Control of a Five-Phase Permanent-Magnet Motor,” Industry Applications, IEEE Transactions on, 2007, vol.: 43, Issue: 4, pp.: 960-970.

[45] Gaeta, A.; Scelba, G.; Consoli, A. “Modeling and Control of Three-Phase PMSMs Under Open-Phase Fault,” Industry Applications, IEEE Transactions on, 2013, vol. 49, Issue: 1, pp.: 74-83.

[46] P.C. Krause, O. Wasynczuk, S.D. Sudhoff, “ Analysis of Electric Machinery and Drive Systems”, second edition, IEEE press.

[47] A. Consoli, lecture notes from the course “ Dynamic of Electric Machine”, University of Catania, 2010.

[48] G. Scarcella, lecture notes from the course “Control of Electric Drives”, University of Catania, 2011.

[49] D.W. Novotny, T.A. Lipo, “Vector Control and Dynamics of AC Drives”, Oxford Science Publications.

[50] R.D. Lorenz, lecture notes from the course ME 746 “Dynamics of Controlled Systems”, University of Wisconsin, Madison, 2014.

[51] T. R Rowan and R.L. Kerman, “A new synchronous current regulator and an analysis of current-regulated PWM inverters,” Industry Applications, IEEE Transaction on, 1986, vol.: IA-22, Issue:4, pp.: 678-690.

Chapter 2 Fault tolerant Multi-Drive System

A proposed Fault Tolerant Multi-Drive System (FT MDS) is presented in this chapter, highlighting different caveats regarding the common mode voltage, the dc link utilization, the modulation strategy and the power losses. Simulation and experimental results have been conducted for a FT MDS composed of IM independently controlled and after with two IM mechanically coupled. It is also assumed that all the types of fault can be isolated and handled as open circuit.

2.1 Fault Tolerant Multi-Drive System

MDS can be employed in many types of applications and as already discussed in Chapter 1 a unique configuration for all the processes does not exist, but a standard and simple MDS topology that can be easily utilized consists of "n" two - level, three - leg inverters that feed three phase ac machines with a common dc bus as shown in Chapter 1, Figure 1.5. The aim of this type of system is to control independently each electrical motor and although this objective can be accomplished with other structures reducing the number of components and also the cost and sharing more elements, the degrees of freedom in case of fault are reduced too, causing in many cases the stop of all the drives. The degrees of freedom provided by the adopted topology can be exploited during one or more faults of the drives. Each three-phase inverter is modified adopting the structure proposed in [1],[2],[3], to isolate the faulty leg or phase of a drive, and as mentioned in [4] a three phase ac motor can work supplying only two phases with two independent currents. Hence, because the third phase is lost, the neutral point of the stator windings has to be connected providing an emergency current path. Usually the neutral point is connected to the midpoint of the dc-link capacitors bank [4], causing ripple on the DC bus voltage; the topology represented in Figure 2.1, [5], can provide the emergency current path for the faulty drives exploiting the remaining healthy drives; this goal is achieved by using additional switches, indicated as SW_1, SW_2, SW_n; depending on the system requirements, they can be semiconductor devices or simple electromechanical relays.

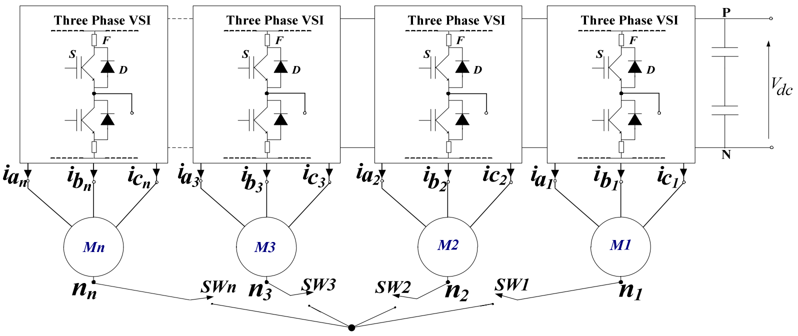

Figure 2.1 Fault tolerant Multi-drive topology.

During normal operations, when all the drives are healthy, these additional switches are turned off and act as an open circuit; instead, when a fault occurs in one or more drives, the faulty inverter component or motor phase will be isolated, some or all of the additional switches are turned on and the neutral points of the faulty and healthy machines are connected together.

Considering a MDS with "n" three phase drives with the proposed "cooperative" strategies, the system is tolerant to "n-1" faulty drives with a single fault and all the drives operating independently.

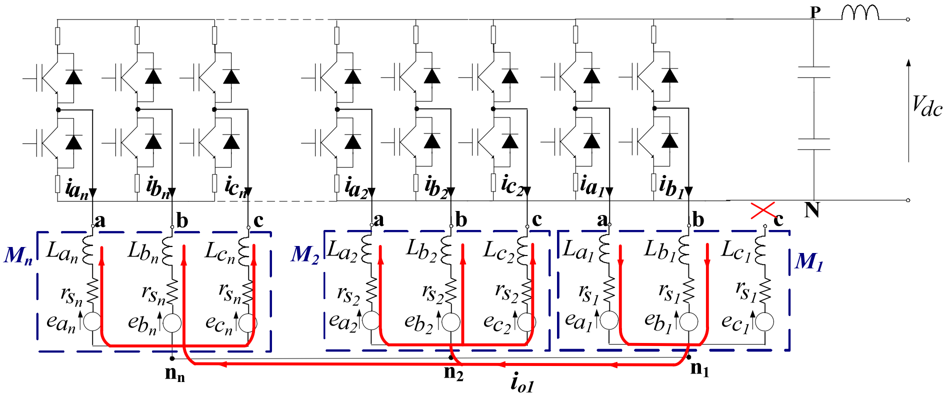

Figure 2.2 Sharing current strategy in case of a single faulted drive.

Figure 2.2 shows a MDS with a single open phase fault in one drive; in particular, the stator phase "c" of M_1 is disconnected from the inverter leg and the red line represents the neutral current obtained as the sum of the currents of the two healthy phases of the faulty unit; the neutral current is indicated as i_{o1}, and it flows through the neutral point connections in the stator windings of the healthy drives.

As this neutral current represents a zero sequence current in the healthy drives, it does not affect their control; therefore, torque and flux are still controlled respectively by the q and d stator current components whatever the ac motor is; consequently, the amount of neutral current flowing in the healthy stator windings is identified as a zero sequence current component and it will affect the zero sequence current circuit, constituted by the stator resistance and the leakage inductance [6].

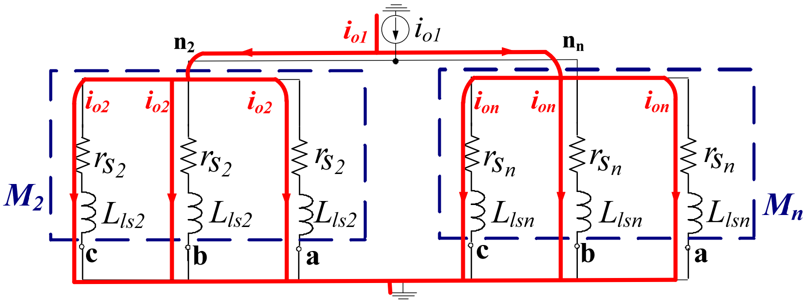

Figure 2.3 Sharing current strategy in case of a single faulted drive.

The zero sequence current circuit of each healthy machine results parallel connected, as can be seen in Figure 2.3, therefore, the per-phase zero sequence current amplitude I_{oj} will be shared among the healthy drives following the general current divider rule:

$$I_{oj} = \frac{1}{3} I_{o1} \left(\frac{\frac{1}{\bar{Z}_j}}{\frac{1}{\bar{Z}_1} + \frac{1}{\bar{Z}_j} + \frac{1}{\bar{Z}_n}} \right) \qquad (2.1.1)$$

I_{oj} is the amplitude of the per-phase current in each stator winding; I_{o1} is the amplitude of the neutral current or zero sequence current produced by the faulty drive; $\bar{Z}_j$ is the stator phase impedance of the zero sequence axis circuit for the j-th drive $\bar{Z}_j = R_s + j\, X_{ls}$.

If the "n-1" healthy drives, exploited as feedback path for the faulty current, have the same characteristics hence the same $\bar{Z}_j$, the per-phase current I_{oj} can be directly expressed as:

$$I_{oj} = \frac{1}{3(n\text{-}1)} I_{o1} \qquad (2.1.2)$$

The amplitude of the neutral current is given by the sum of the currents of the two healthy phases of the faulty drive; as discussed in [4], the mmf in a faulty drive is equal to that one during healthy operation, by applying two currents with an increased amplitude of $\sqrt{3}$ and shifted by 60 electrical degrees.

At steady state:

$$\begin{cases} i_{is}\,(t) = I_f \cos(\omega t) \\ i_{js}\,(t) = I_f \cos(\omega t - \pi/3) \end{cases}$$

$$\bar{I}_{is} = I_f; \qquad \bar{I}_{js} = I_f\, e^{j\frac{\pi}{3}} = \cos(\tfrac{\pi}{3}) + j \sin\tfrac{\pi}{3} = \tfrac{1}{2} I_f + j\tfrac{\sqrt{3}}{2} I_f \qquad (2.1.3)$$

$$I_{o1} = \left|\bar{I}_{o1}\right| = \sqrt{\bar{I}_{is} + \bar{I}_{js}} = \sqrt{\left(\tfrac{3}{2} I_f\right)^2 + \left(\tfrac{\sqrt{3}}{2} I_f\right)^2} = \sqrt{3}\, I_f \qquad (2.1.4)$$

If the rms amplitude of the current I_f in the faulty drive is equal to the rated value, indicated as I_{fn}, the neutral current will be at least $\sqrt{3} I_{fn}$. This current is flowing in the stator windings of the healthy drives and will be superimposed on each phase current; this increment, indicated as ΔI, will cause an additional copper power losses ΔP_{cu} in the healthy drive.

Considering the general equation (2.1.1) and assuming:

$$k_j = \left(\frac{\frac{1}{\bar{Z}_j}}{\frac{1}{\bar{Z}_1} + \frac{1}{\bar{Z}_j} + \frac{1}{\bar{Z}_n}} \right) \qquad (2.1.5)$$

can be obtained:

$$\Delta P_{cuj} = R_{sj}\, \Delta I_j^2 = R_{sj} \left(\frac{1}{3} k_j\, I_{o1} \right)^2 = R_{sj} \left(\frac{\sqrt{3}}{3} k_j\, I_f \right)^2 = R_{sj} \left(\frac{1}{\sqrt{3}} k_j\, I_f \right)^2 \qquad (2.1.6)$$

In the worst case, in each phase of the healthy machine, the copper losses increase of

$$\Delta P_{cujM} = R_{sj} \left(\frac{1}{\sqrt{3}} k_j\, I_{fn} \right)^2 \qquad (2.1.7)$$

In addition, the rated current of the healthy drives represent a physical boundary as the additional amount of the faulty current has to be considered, thus yielding to an avoidable torque reduction. By assuming I_{nj} the rated current of the j-th healthy drive, for a PMSM, it is possible to consider that the amplitude of the stator phase current is used only to control the torque (it is set $i_{ds} = 0$) and thus:

$$\frac{\Delta T_e}{T_{en}} = \frac{1}{3} k_j \frac{I_{o1}}{I_{nj}} \qquad (2.1.8)$$

The torque reduction depends on the ratio I_{o1}/I_{nj} and the factor k_j; hence, if the MDS is constituted by n ac machines with different power ratings different values of the phase impedance $\bar{Z}_j$ need to be considered. As $\bar{Z}_j$ is higher in small power motors they allow the flow of a less percentage of I_{o1}, with respect to higher rated power drives. Moreover, in the management of the current flow it is necessary to consider the overload capability of drives for a short period.

If the MDS consists of “n” drives with the same power ratings the equation (2.1.8) can be simplified as :

$$\frac{\Delta T_e}{T_{en}} = \frac{1}{3(n-1)} \frac{I_{o1}}{I_n} \qquad (2.1.9)$$

Table 2.1 shows the torque reduction on the healthy machines for MDS composed of a different number of PMSM drives and different values of the ratio I_{o1}/I_n; it can be noted that increasing the number of the drives, the torque reduction becomes very small, and for instance in a MDS with 4 drives the reduction on each one, when $I_{o1}/I_n = 100\%$ is about 11%

A similar consideration can be made for the IM but should be noted that a portion of the stator phase current vector controls the torque while the other controls the flux; therefore, the previous relation should be applied considering only the stator current component inherently to the torque production.

Table 2.1 Toque Capability reduction (%) of healthy PMSM drives under a Fault Condition.

n	I_{o1}/I_n						
	10(%)	20(%)	30(%)	40(%)	50(%)	70(%)	100(%)
2	3.34	6.67	10	13.34	16.67	23.34	33.34
3	1.67	3.34	5	6.67	8.34	11.67	16.66
4	1.11	2.22	3.34	4.44	5.55	7.78	11.12
5	0.83	1.67	2.5	3.34	4.17	5.84	8.34
6	0.67	1.34	2	2.67	3.34	4.67	6.67
7	0.56	1.11	1.67	2.22	2.78	3.89	5.56

Another issue that has to be considered is the additional voltage drop ΔV_o on the stator windings of the j-th healthy machine, due to the additional zero sequence current. It is given by:

$$\Delta V_o = R_{sj} i_{oj} + L_{sj} \frac{d}{dt} i_{oj} \qquad (2.1.10)$$

This additional voltage drop, depending on the drive operative condition could be considered small but in general not negligible and will affect the healthy drives voltage capability; hence an amount of the dc-link voltage is used to sustain this voltage drop and the remaining part is used to synthesize the fundamental voltage required by the control implemented in the healthy drive.

The modulation strategies adopted to generate the gate signal for the power converter, for a healthy three phase drive without neutral point connection are, in general, SVM or S-PWM with third harmonic injection [7], [8], that allow a constant switching frequency and increase the dc-bus utilization with respect to a standard S-PWM respectively of 15% and 13.4%. During post fault operation with the proposed MDS configuration, the connection of the neutral point allows the circulation of the neutral current of the faulty drives in healthy drives as well as the circulation of all low order harmonics due to the additional injection of harmonic voltages, yielding to torque and current ripples and additional losses; therefore, when the MDS is configured to work under one or more faulty drives, a standard S-PWM is adopted for both faulty and healthy drives. By the way, the analyzed FT configuration of Figure 2.1, also with a standard S-PWM, operates with higher voltage limits compared to other FT schemes, in which the neutral point of the stator winding is connected to the midpoint of DC-link capacitors, in the latter case the motor neutral point is locked to Vdc/2.

2.2 Common Mode Voltage analysis

The common mode voltage (CMV), can be defined as the voltage between the negative rail of the dc-bus and the neutral point of the stator windings of an electrical machine and it is a common issue in all drives. It is generated by the PWM [9], [11], and potentially can create many troubles, such as induced currents on the chassis, on the shaft and on the ball bearings, causing electromagnetic interference and a fast reduction of the life span of the last mechanical parts of the motor [10]. Different methods are addressed to mitigate this effect: in an active way such as [12]-[19] suggesting different modulation strategies, or in a passive way, adopting filters [20], [21]. It is clear that the active methods are preferred because generally they are based on software modification that in general does not require an increment of the drive costs.

During normal operation, when all the drives are healthy, the additional switches SW_1, SW_2, SW_n shown in Figure 2.2, are kept open and the CMV can be expressed with the classical relations used for single drive and here reported for simplicity.

Applying the Kirchhoff voltage law and considering the voltage and flux equations in the stationary frame, it can be obtained:

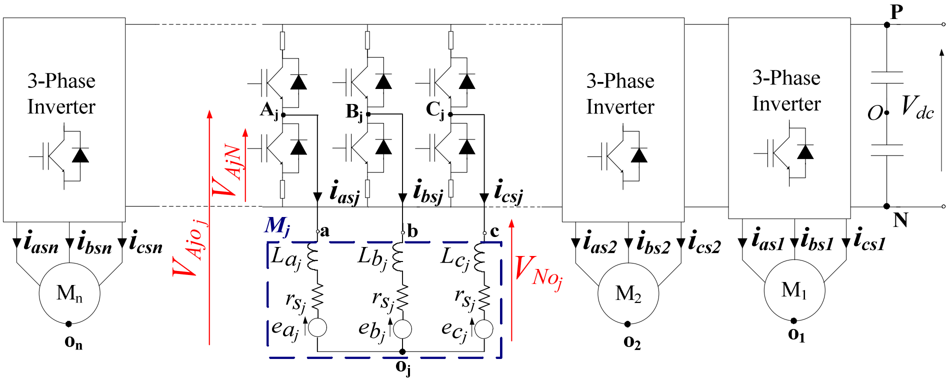

Figure 2.4 MDS with all drives working in healthy conditions.

$$\begin{cases} \mathbf{V}_{ABCjoj} = \mathbf{r}_s \, \mathbf{i}_{abcsj} + p \, \lambda_{abcsj} \\ \mathbf{V}'_{abcrj} = \mathbf{r}'_r \, \mathbf{i}'_{abcrj} + p \, \lambda'_{abcrj} = 0 \end{cases} \tag{2.2.1}$$

$$\begin{bmatrix} \lambda_{abcsj} \\ \lambda'_{abcrj} \end{bmatrix} = \begin{bmatrix} \mathbf{L}_s & \mathbf{L}'_{sr} \\ (\mathbf{L}'_{sr})^T & \mathbf{L}'_r \end{bmatrix} \begin{bmatrix} \mathbf{i}_{abcsj} \\ \mathbf{i}'_{abcrj} \end{bmatrix} \tag{2.2.2}$$

$$\begin{cases} V_{Ajoj} = V_{AjN} + V_{Noj} = R_j i_{asj} + p\lambda_{asj} \\ V_{Bjoj} = V_{BjN} + V_{Noj} = R_j i_{bsj} + p\lambda_{bsj} \\ V_{Cjoj} = V_{CjN} + V_{Noj} = R_j i_{csj} + p\lambda_{csj} \end{cases} \tag{2.2.3}$$

The index “j”, j = 1, 2 ,3,…n, represent the j-th, drive under test. By summing the previous three equations, it can be noted that the three-phase voltages V_{Ajoj}, V_{Bjoj}, V_{Cjoj} as well as the currents, i_{asj}, i_{bsj}, i_{csj} and fluxes, λ_{asj}, λ_{bsj}, λ_{csj} are defined as symmetrical and balanced positive sequences, and therefore their sum is equal to zero.

$$0 = V_{Ajoj} + V_{Bjoj} + V_{Cjoj} = 3\, V_{Noj} + V_{AjN} + V_{BjN} + V_{CjN}$$

$$V_{Noj} = -\frac{1}{3}\left(V_{AjN} + V_{BjN} + V_{CjN} \right) \qquad (2.2.4)$$

The voltages V_{AjN}, V_{BjN}, V_{CjN} are defined by the eight, inverter’s switch configurations.

Table 2.2 Common mode voltage.

States	000	100	110	010	011	001	101	111
V_{Noj}	0	$-1/3\ V_{dc}$	$-2/3\ V_{dc}$	$-1/3\ V_{dc}$	$-2/3\ V_{dc}$	$-1/3\ V_{dc}$	$-2/3\ V_{dc}$	$-V_{dc}$

As shown in Figure 2.2, in case of fault in one drive, the additional switches are turned on to provide a path for the zero sequence current through the stator windings of the healthy drives. This connection modifies the CMV which is unique for the whole system, and it contains, in addition to the high frequency term, low frequency terms as well.

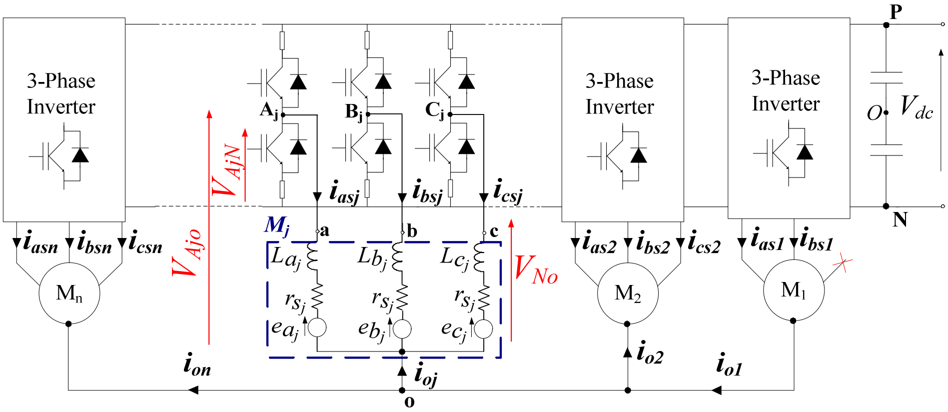

Figure 2.5 MDS with one drive working in fault conditions with all the neutral point connected together.

The expression of the CMV is provided for the MDS of Figure 2.5, in which there is only one faulty drive and hereafter it will be generalized as “m” faulty drives with a single open phase fault. By assuming the MDS of Figure 2.5 is composed by IMs with different characteristics.

$$
\begin{cases}
v_{A1o} = v_{A1N} + v_{No} \\
v_{B1o} = v_{B1N} + v_{No} \\
v_{C1o} = p\lambda_{cs1} \\
v_{A2o} = v_{A2N} + v_{No} \\
v_{B2o} = v_{B2N} + v_{No} \\
v_{C2o} = v_{C2N} + v_{No} \\
\quad . \\
\quad . \\
v_{Ano} = v_{AnN} + v_{No} \\
v_{Bno} = v_{BnN} + v_{No} \\
v_{Cno} = v_{CnN} + v_{No}
\end{cases}
\qquad (2.2.5)
$$

Summing all the equations of (2.2.5) the following expression is obtained:

$$v_{A1o} + v_{B1o} + v_{C1o} + v_{A2o} + v_{B2o} + v_{C2o} + \ldots + v_{Ano} + v_{Bno} + v_{Cno} =$$

$$= v_{A1N} + v_{B1N} + p\lambda_{cs1} + v_{A2N} + v_{B2N} + v_{C2N} + \ldots + v_{AnN} + v_{BnN} + \qquad (2.2.6)$$

$$+ v_{CnN} + (3n\text{-}1)\, v_{No}$$

For the faulty drive we get:

$$i_{as1} + i_{bs1} = i_{o1} \text{ and } i_{c1s} = 0 \qquad (2.2.7)$$

while the rotor currents are still balanced hence their sum is 0.

For the voltages:

$$v_{A1o} + v_{B1o} + v_{C1o} = R_{s1}\, i_{as1} + R_{s1}\, i_{bs1} + p\,\lambda_{as1} + p\,\lambda_{bs1} + p\,\lambda_{cs1} =$$

$$R_{s1}\,(i_{as1} + i_{bs1}) + pL_{ls1}(i_{as1} + i_{bs1}) + pL_{ms1}[i_{as1} + i_{bs1} - \frac{1}{2}(2i_{as1} + 2i_{bs1})]$$

$$= R_{s1}\, i_{01} + L_{ls1}\, pi_{01}$$

$$v_{A1o} + v_{B1o} + v_{C1o} = R_{s1}\, i_{01} + L_{ls1}\, pi_{01} \qquad (2.2.8)$$

In the healthy machine, the phase currents are related to the zero sequence components i_{oj} by applying the relationships (2.2.9) and (2.2.10) which can be derived by applying the Kirchhoff current law at the point “o”:

$$i_{as2} + i_{bs2} + i_{cs2} = -\, i_{o2} \qquad (2.2.9)$$

$$i_{asn} + i_{bsn} + i_{csn} = -\, i_{on} \qquad (2.2.10)$$

Also in this case the sum of the rotor currents on each healthy drive is equal to zero, therefore the previous voltage equation (2.2.6) can be rewritten as:

$$
\begin{aligned}
& V_{A2o} + V_{B2o} + V_{C2o} = R_{s2}\, i_{as2} + R_{s2}\, i_{bs2} + R_{s2}\, i_{cs2} + p\,\lambda_{as2} + p\,\lambda_{bs2} + p\,\lambda_{cs2} = \\
& R_{s2}\,(i_{as2} + i_{bs2} + i_{cs2}) + pL_{ls2}(i_{as2} + i_{bs2} + i_{cs2}) + pL_{ms2}[i_{as2} + i_{bs2} + i_{cs2} + \\
& - \frac{1}{2}(2i_{as2} + 2\, i_{bs2} + 2\, i_{cs2})] = - R_{s2}\, i_{02} - L_{ls2}\, pi_{02}
\end{aligned}
$$

$$
V_{A2o} + V_{B2o} + V_{C2o} = - R_{s2}\, i_{02} - L_{ls2}\, pi_{02} \tag{2.2.11}
$$

For the generic n-th healthy drive can be obtained:

$$
V_{Ano} + V_{Bno} + V_{Cno} = - R_{sn}\, i_{on} - L_{lsn}\, pi_{0n} \tag{2.2.12}
$$

Substituting (2.2.8), (2.2.11) and (2.2.12) in (2.2.6), the expression of the zero sequence voltage for the proposed MDS topology is determined:

$$
\begin{aligned}
V_{No} = & - \frac{1}{(3n-1)} \Big[V_{A1N} + V_{B1N} + p\lambda_{cs1} + V_{A2N} + V_{B2N} + V_{C2N} + \dots \\
& + V_{AnN} + V_{BnN} + V_{CnN} \Big] + \frac{1}{(3n-1)} \Big[R_{s1}\, i_{o1} + L_{ls1}\, pi_{o1} - R_{s2}\, i_{o2} + \\
& - L_{ls2}\, pi_{o2} \dots - R_{sn}\, i_{on} - L_{lsn}\, pi_{on} \Big]
\end{aligned}
\tag{2.2.13}
$$

The zero sequence currents of the healthy drives are obtained applying the relation (2.1.1) without $\frac{1}{3}$, and k_j is defined in (2.1.5).

$$
i_{oj} = k_j\, i_{o1} \tag{2.2.14}
$$

$$
\begin{aligned}
V_{No} = & - \frac{1}{(3n-1)} \Big[V_{A1N} + V_{B1N} + p\lambda_{cs1} + V_{A2N} + V_{B2N} + V_{C2N} + \dots + \\
& V_{AnN} + V_{BnN} + V_{CnN} \Big] + \frac{1}{(3n-1)} \Big[(R_{s1} - k_2\, R_{s2} + \dots - k_n\, R_{sn})\, i_{o1} \\
& + (L_{ls1} - k_2\, L_{ls2} \dots - k_n\, L_{lsn}) pi_{o1} \Big]
\end{aligned}
\tag{2.2.15}
$$

The equation (2.2.15) can be generalized in case of “m” drives with a single fault and at least one drive have to operate in healthy conditions.

The zero sequence current shared among the healthy drives will be given, in this case, summing the zero sequence currents generated by each faulty drive:

$$
i_{oj} = k_j\, (i_{o1} + i_{o2} + \dots + i_{om})
$$

$$
\begin{aligned}
V_{No} = & - \frac{1}{(3n-m)} \Big[V_{X1N} + V_{Y1N} + p\,\lambda_{ks1} \dots + V_{WmN} + V_{ZmN} + p\lambda_{k_m s1} + \\
& + V_{AjN} + V_{BjN} + V_{CjN} + \dots + V_{AnN} + V_{BnN} + V_{CnN} \Big] + \\
& + \frac{1}{(3n-m)} \Big[R_{s1}\, i_{o1} + \dots + R_{sm}\, i_{om} - (k_j\, R_{sj} + \dots + k_n\, R_{sn})\, (i_{o1} + \dots + i_{om}) \\
& + L_{ls1}\, pi_{01} + \dots + L_{lsm}\, pi_{0m} - (k_j\, L_{lsj} + \dots + k_n\, L_{lsn}) p(i_{o1} + \dots + i_{om}) \Big]
\end{aligned}
\tag{2.2.16}
$$

$$(X, Y), (W, Z) = \begin{cases} B, C \text{ fault stator phase A} \\ A, C \text{ fault stator phase B} \\ A, B \text{ fault stator phase C} \end{cases}$$

k and k_m represent the fault stator phase A, B or C.

A more compact and general expression for an MDS with “n” different drives, with “m” drives affected by a single phase fault can be written as:

$$\begin{aligned} V_{No} = -\frac{1}{(3n-m)}\Bigg\{ & \left[\sum_{q=1,2\ldots}^{3n-m} V_{kqN} \right]_{k=A,B,C} + \left[\sum_{q=1,2\ldots}^{m} p\lambda_{Msq} \right]_{M=A \text{ or } B \text{ or } C} + \\ & - \left[\sum_{h=1,2\ldots m}^{m} R_{sh} i_{0h} - \sum_{g=m+1,m+2\ldots}^{n-m} R_{sg} k_g \left(\sum_{h=1,2\ldots m}^{m} i_{0h} \right) \right] + \\ & - \left[\sum_{h=1,2\ldots m}^{m} L_{lsh} i_{0h} - \sum_{g=m+1,m+2\ldots m}^{n-m} L_{lsg} k_g \, p \left(\sum_{h=1,2\ldots}^{m} i_{0h} \right) \right] \Bigg\} \end{aligned} \tag{2.2.17}$$

In detail:

V_{kqN} represents the voltage between the midpoint of the healthy legs and the negative rail N of the DC bus.

$p\lambda_{Msq}$ represents the voltage related to the induced flux on the faulty leg of the faulty drives.

$R_{sh}\, i_{0h}$; $L_{lsh}\, p\, i_{0h}$ are the voltage drops produced by the zero sequence currents that flow on the stator resistances and the leakage inductances of the faulty drives.

$R_{sg}k_g \left(\sum_{h=1,2\ldots m}^{m} i_{0h} \right)$; $L_{lsg}k_g p \left(\sum_{h=1,2\ldots m}^{m} i_{0h} \right)$ are the voltage drops caused by the sum of the zero sequence currents that flow on the stator resistances and the leakage inductances of the “n-m” healthy drives taking into account the factor k_g .

During a fault, the CMV contains, in addition to the high frequency component also a low frequency term, one term is related to the rate of change of the induced flux on the faulty phase of the faulty drive due to the mutual coupling, while the other term is related to the stator resistance and leakage inductance of the faulty drives and the stator resistance and the leakage inductance of the healthy drives multiplied by the respectively amount of the zero sequence current.

If all the drives have the same characteristics the relation (2.2.17) can be simplified in (2.2.18):

$$
\begin{aligned}
V_{No} = -\frac{1}{(3n-m)}\Bigg\{ & \left[\sum_{q=1,2\ldots}^{3n-m} V_{kqN}\right]_{k=A,B,C} + \left[\sum_{q=1,2\ldots}^{m} p\lambda_{Msq}\right]_{\substack{M=A \text{ or } B \\ \text{or } C}} + \\
& - R_s\left[\sum_{h=1,2\ldots m}^{m} i_{0h} - \sum_{g=m+1,m+2\ldots}^{n-m} \frac{1}{(n-m)_g}\left(\sum_{h=1,2\ldots m}^{m} i_{0h}\right)\right] + \\
& - L_{ls}\left[\sum_{h=1,2\ldots m}^{m} i_{0h} - \sum_{g=m+1,m+2\ldots m}^{n-m} \frac{1}{(n-m)_g}\, p\left(\sum_{h=1,2\ldots}^{m} i_{0h}\right)\right]\Bigg]\Bigg\}
\end{aligned}
\qquad (2.2.18)
$$

With simple consideration from the previous relation (2.2.18), when R_s, L_{ls} are perfectly equal (ideal condition) a component of the low frequency term is perfectly balanced and the CMV is defined by (2.2.19):

$$
V_{No} = -\frac{1}{(3n-m)}\left\{\left[\sum_{q=1,2\ldots}^{3n-m} V_{kqN}\right]_{k=A,B,\ldots} + \left[\sum_{q=1,2\ldots}^{m} p\lambda_{Msq}\right]_{M=A \text{ or } B \text{ or } C}\right\} \qquad (2.2.19)
$$

This relation has been carried out in the case of MDS equipped only with IM, but it can be verified also for MDS with only PMSM or more in general for MDS with both IM and PMSM, using the appropriate equations, under the assumption of linear model, (magnetic saturation or second order effect not included). Only the stator resistance and the leakage inductance will be included in the CMV expression and the induced flux on the faulty phase of the faulty drive.

2.3 Numerical simulations and experimental results

In this paragraph simulations and experimental results to verify the capability and performance of the FT-MDS configuration are presented. A FT-MDS consisting of three 1.1kW and a 3kW IM, whose parameters are reported in Table 2.3, is investigated.

Table 2.3 Technical specifications of the considered induction motors.

Motor Specifications	IM_1, IM_2, IM_4	IM_3
Rated Power [kW]	1.1	3
Rated Voltage [V]	400	400
Rated frequency [Hz]	50	50
Rated speed [rpm]	1440	1430
Rated current [A]	3	6.9
R_s, R_r [Ω]	8, 7.1	2, 1.66
L_{ls}, L_{lr} [H]	0.0234, 0.0234	0.0105, 0.0105
L_{ms} [H]	0.534	0.171
Rotor Inertia [Kgm^2]	0.0089	0.014

The simulation test that is reported in Figure 2.6 has been carried out with all drives operating independently under IFOCs and IM_1 is affected by a single open phase "c" fault. The Figure shows: mechanical speeds, electromagnetic torques, phase currents and their module, and also the module of the neutral current. IM_1 is running at constant speed with 30% of load, the two healthy phase currents are producing a neutral current I_{01} of 6 A; IM_2, IM_3, IM_4 are working at different conditions with different speeds and load torques. Initially, a speed step from 120 to 50 rad/s is applied to IM_3 operating under the 75% of the rated torque; this is followed by a first load step from 0 to 6Nm (80% of rated torque) on IM_2 running at constant speed 10rad/s, and soon after a second load step from 6 to 9 Nm (120 % of rated torque) is applied to the last motor; IM_4 is working at constant speed 40 rad/s and under a torque load equal to 80% of the rated torque. The phase currents of all the healthy drives, used as feedback current path for the neutral current of the faulty machine, are modulated by each zero sequence current, given by the equation (2.1.1). It is clearly visible that faulty condition and thus the zero sequence current does not affect the drive control. Moreover, as can be seen from Figure 2.7, the zero sequence current is independent from the speed and load transients; this property confirms its relation only with the zero sequence circuit, composed of the stator resistance and the leakage inductance. As IM_3 has the phase impedance smaller than IM_2 and IM_4, in accordance with Kirchhoff current law, a significant zero sequence current is flowing through this drive, while an equal amount of this current, smaller than that of IM_3 is flowing through IM_2 and IM_4, since they have the same impedance.

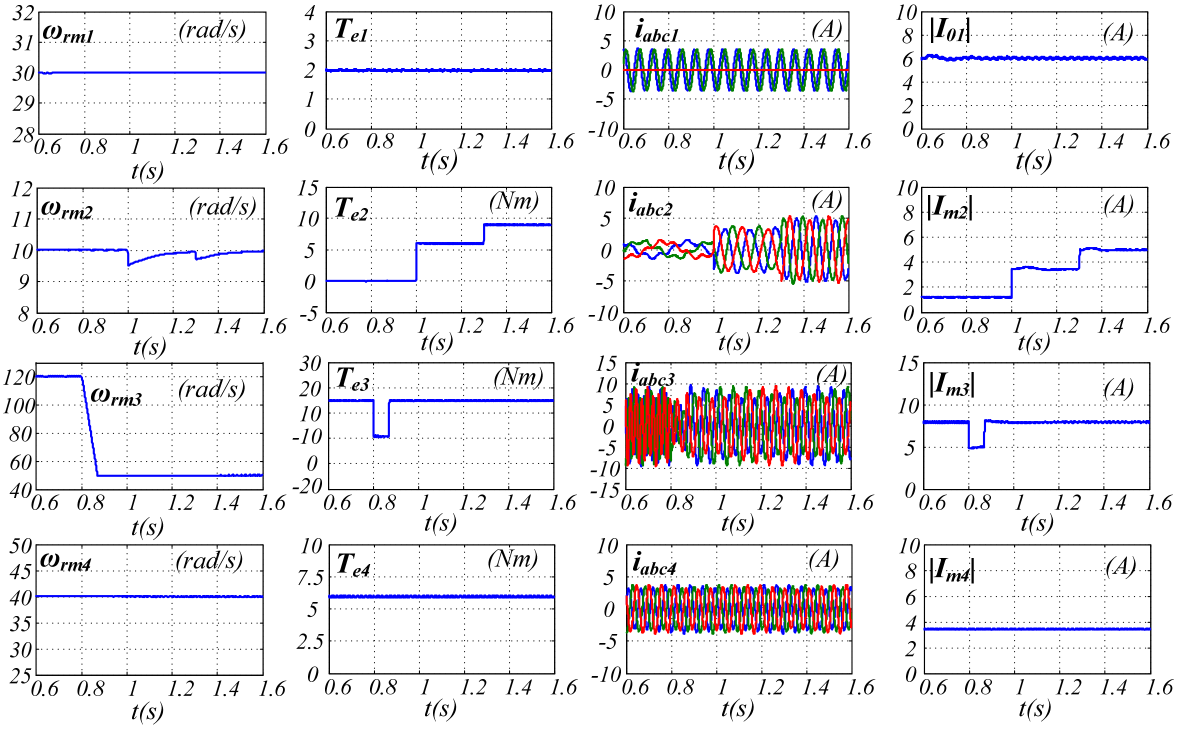

Figure 2.6 MDS with one drive operating with an open phase fault and three drives healthy used as feedback current path for the neutral current.

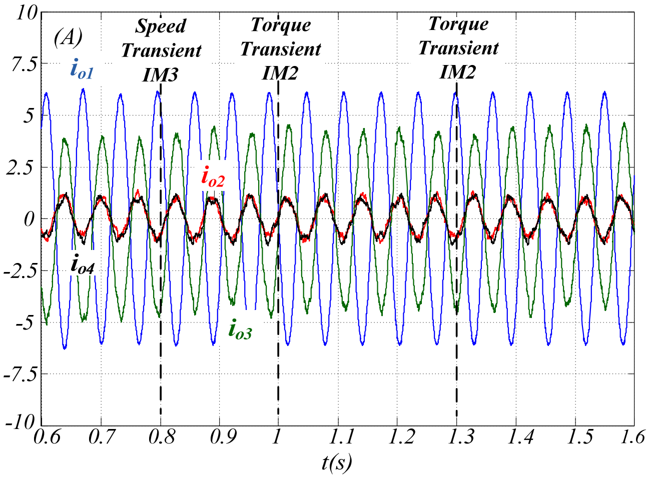

Figure 2.7 Zero sequence currents flowing in each motor.

Experimental results have been performed to validate the simulation analysis with a FT-MDS consisting of three IM drives, whose parameters have been already reported in Table 2.3, arranged as shown in the block diagram of Figure 2.8.

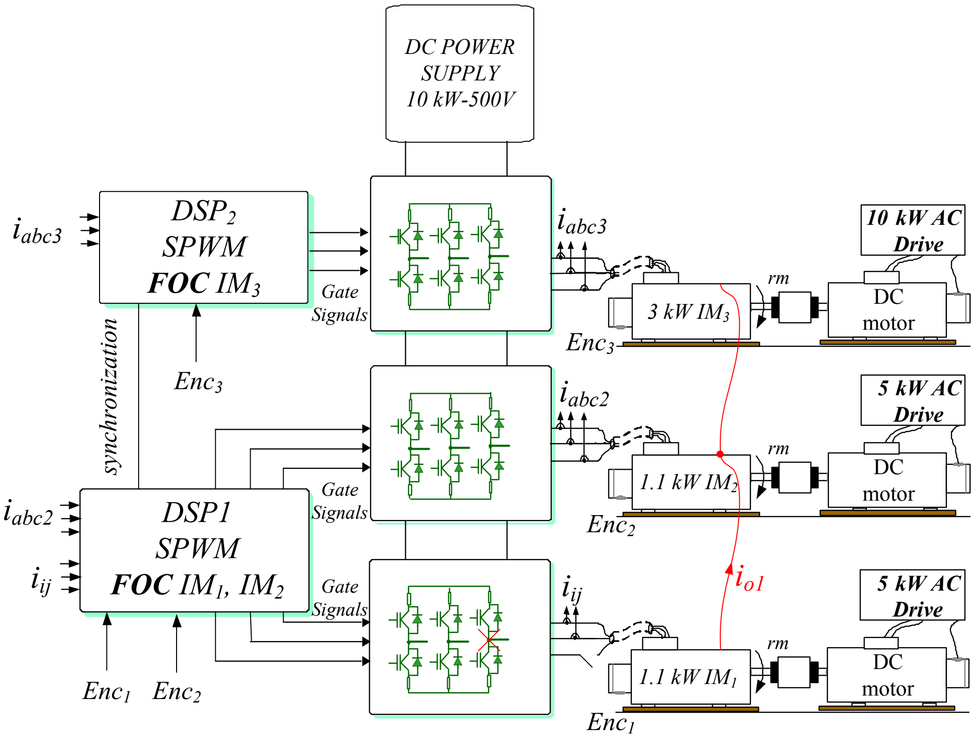

Figure 2.8 MDS Experimental Setup.

Figure 2.9 shows the steady state behavior at no load of the FT-MDS: the upper picture shows the two “a” phase currents of the healthy drives IM_2 and IM_3, which result distorted by the zero sequence current outgoing from the faulty drive IM_1, given by the sum of its two healthy phase currents; nevertheless, the ripple shown on i_{q_IM2}, $\Delta\omega_{rm\_IM2}$ and i_{q_IM3}, $\Delta\omega_{rm\_IM3}$ is quite negligible, confirming that the zero sequence currents do not affect the field orientation.

Figure 2.10 has been performed to evaluate the effect of the zero sequence currents during speed transient of the healthy drives, IM_2 and IM_3. For this test all the machines work at no load, therefore IM_1 is running at 50 rad/s, while IM_2 performs a speed variation from -30 rad/s to 30 rad/s, followed by a speed variation on IM_3 from 40 rad/s to – 40 rad/s. As can be noted from the experimental results, the zero sequence currents i_{o2} and i_{o3} remain quite constant during all the transients; this confirms that their amplitude is only related to the zero sequence axis phase impedance Z_j.

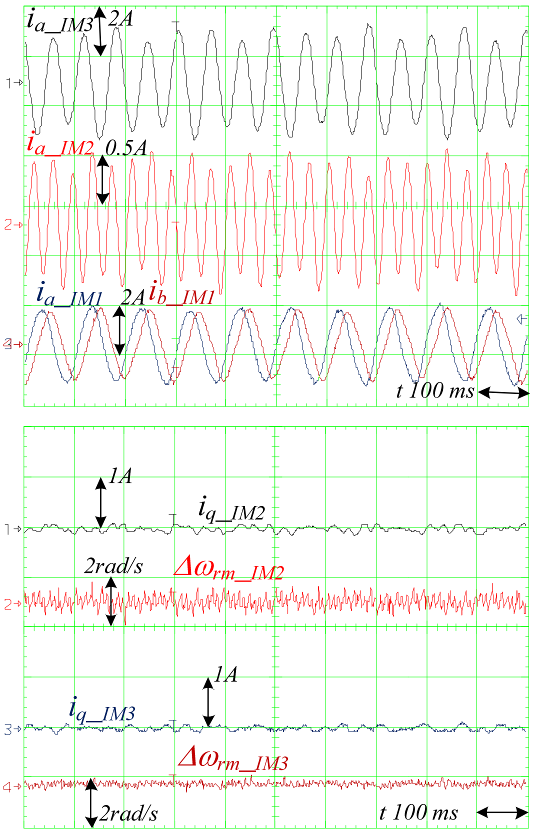

Figure 2.9 Steady state test at no load, $\omega_{rm\_IM_1}$=30rad/s, $\omega_{rm\_IM_2}$=80rad/s , and $\omega_{rm\_IM_3}$=50rad/s.

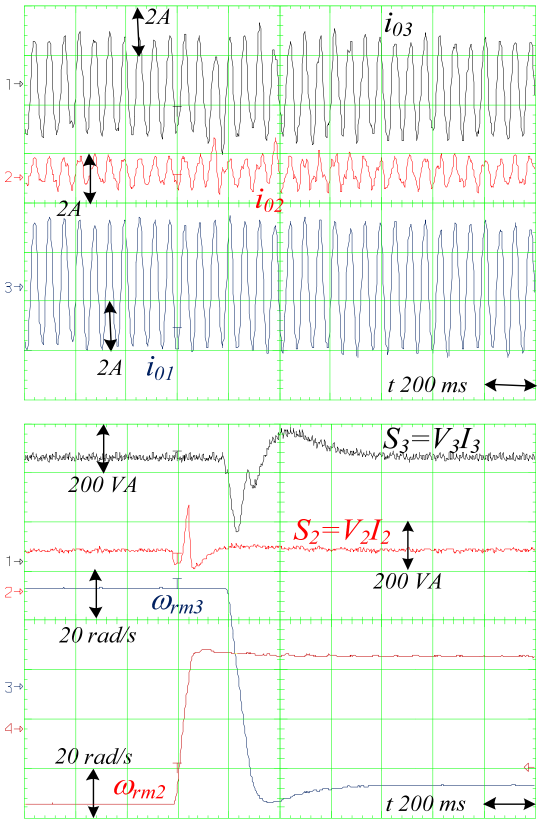

Figure 2.10 First method: Speed transients occurring at IM_2: $\omega_{rm\_IM_2}$=-30/30 rad/s and IM3: $\omega_{rm\_IM_3}$=40/-40 rad/s, while IM1operates at $\omega_{rm\_IM_1}$=50 rad/s.

2.4 MDS with motors mechanically coupled

In some applications it could be required that two or more motors are mechanically coupled powering a single mechanical shaft, as in Figure 2.11. This mechanical coupling can be more or less stiff depending on the component employed that can be e.g.: gear wheels, chains or belt and pulley.

In the following an MDS, with two drives composed of two identical IMs rigidly coupled, is analyzed. This configuration increases the fault tolerant capability with respect to an MDS without mechanical coupling, because it is able to work also in the following conditions:

1) One drive is affected by a single fault and the other is healthy;
2) Both drives are affected by a single fault;
3) One drive is affected by a single fault while the other is operating under a double fault.

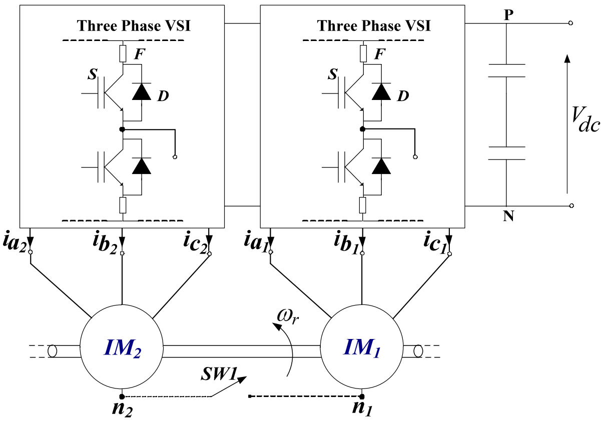

Figure 2.11 MDS with two motors mechanically coupled to the same shaft.

In normal conditions, without faults, both machines run at the same speed and the electromagnetic torque T_e is provided in equal part by the two drives, $T_e = T_{e1} + T_{e2}$. The IFOC is implemented in both drives, and the torque current components are equal, $i_{q1}^{*r} = i_{q2}^{*r}$. the field orientation is guaranteed by the relation (2.4.1) and in this case the angular position of the rotor flux is equal for both machines. Hence, the stator currents have the same frequency.

$$\theta_{\lambda r1} = \theta_{\lambda r2} = \int\left(\omega_{re} + \frac{1}{\tau_r}\frac{i_{q\,fbk}^{r}}{i_{dfbk}^{r}}\right)dt \tag{2.4.1}$$

ω_r is the rotor speed, τ_r is the rotor time constant, i_{qfbk}^{r} and i_{dfbk}^{r} are the q-d feedback current components of each drive. When the operative condition 1) is verified, the MDS is reconfigured isolating the faulty leg and connecting together the neutral points of the two machines, as shown in

Figure 2.12. IM$_2$ is faulty and the neutral current i_{o2} has to flow in the healthy drive stator windings.

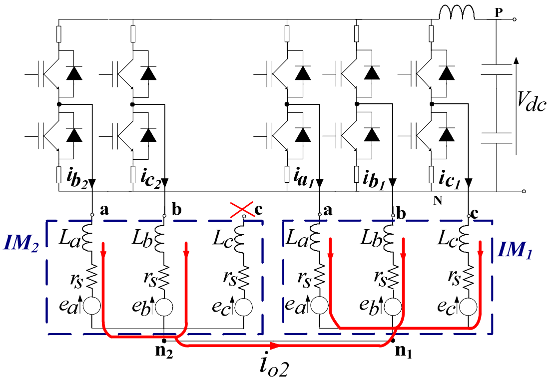

Figure 2.12 Single open phase fault on IM$_2$.

In the simulation results shown in Figure 2.13 the rotational speed is kept constant at 50rad/s, the phase currents of the healthy drive are modulated by the neutral current outgoing from the faulty one, while the electromagnetic torque T_{e1} and T_{e2} and the mechanical speed present a negligible ripple.

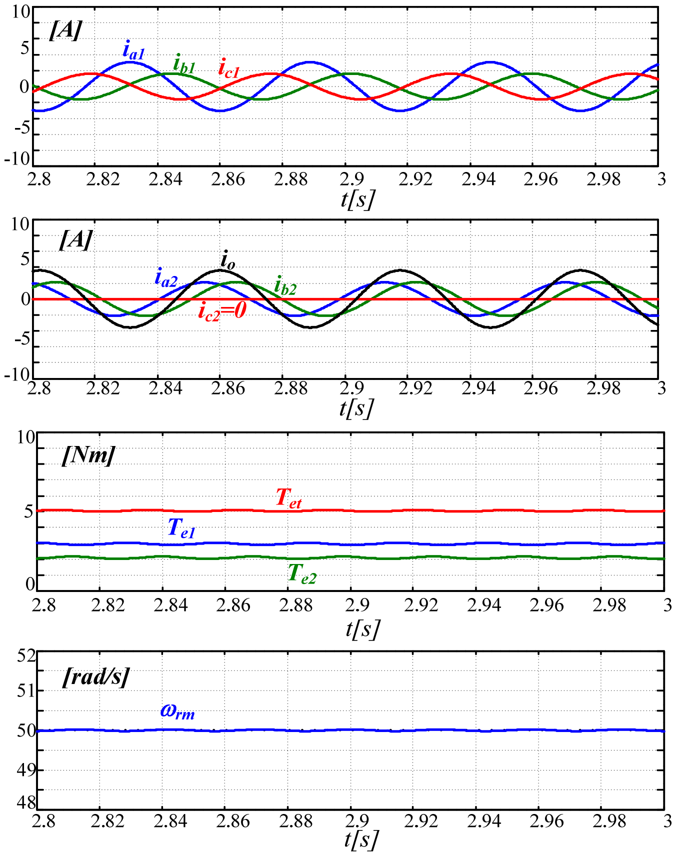

Figure 2.13 Single open phase fault.

When the operative condition 2) is verified the field orientation can still be achieved because the machine works at the same rotational speed ω_r, $i^{*r}_{q1} = i^{*r}_{q2}$ and $i^{*r}_{d1} = i^{*r}_{d2}$ hence the two neutral currents have the same amplitude but opposite phase:

$$i_{a1} + i_{b1} = i_{o1} = - i_{o2} = - (i_{b2} + i_{c2})$$

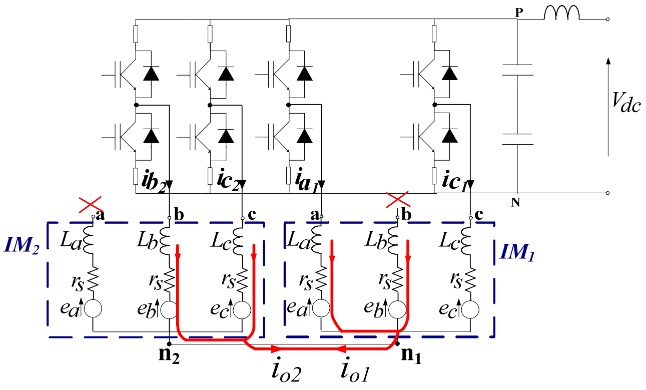

Figure 2.14 Two single open phase faults on IM_1 and IM_2.

The system is reconfigured as shown in Figure 2.14 while the simulation results are presented in Figure 2.15, and they have been performed in the same way as for the operative condition 1), but now the electromagnetic torque is equally shared between the two drives.

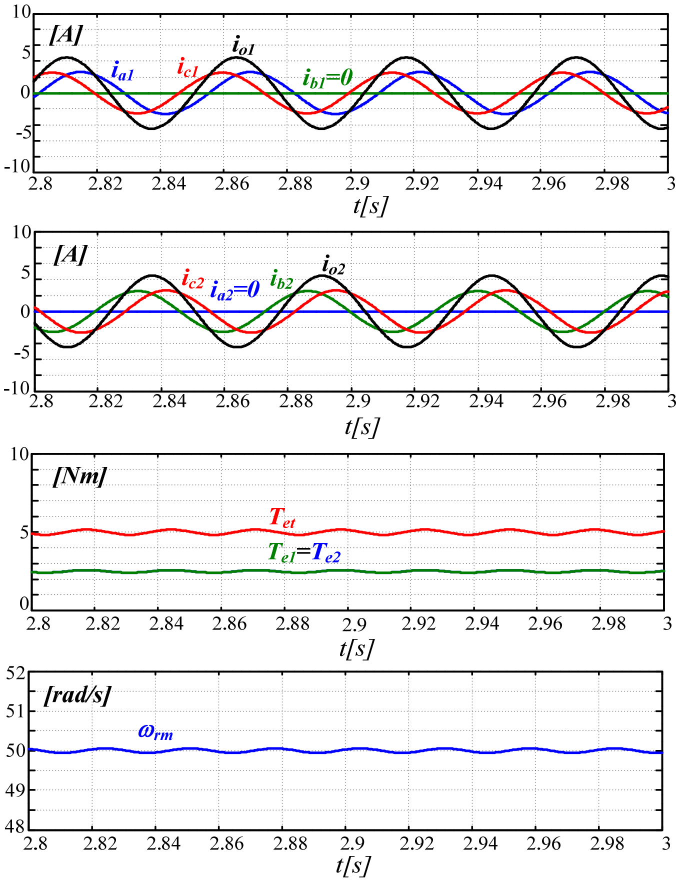

Figure 2.15 Two single open phase faults.

If i_{o1} and i_{o2} have not an opposite phase the field orientation cannot be correctly achieved and a complete loss of control can occur, as it is not possible to apply two independent currents shifted by 60° on the faulty drive. This drawback is overcome by imposing $\theta_{\lambda r1} = \theta_{\lambda r2}$. A similar undesirable effect is verified if the mechanical coupling is not perfectly stiff or the rotor time constant of the two motors is slightly different.

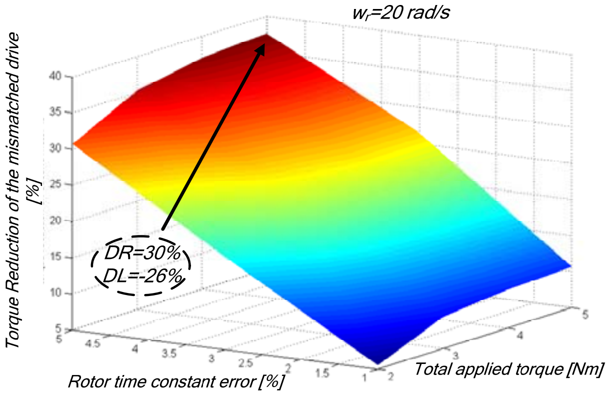

Figure 2.16 Torque reduction caused by the deviation from the correct field orientation.

Figure 2.16 represents the torque losses as function of the percentage error of the rotor time constant and the total applied torque, imposing the previous operative condition 2); this picture is obtained assuming the motor operating at 20 rad/s. As can be noted, a torque reduction of 25%-35% can be achieved with a rotor time constant just 4% different from the rated value.

The operative condition 3), can also be tolerated by the MDS which is still able to operate, although with a reduced torque capability since only one drive is working. In this case the drive with two faults is exclusively used to provide a current path for the other drive, as indicated in Figure 2.17.

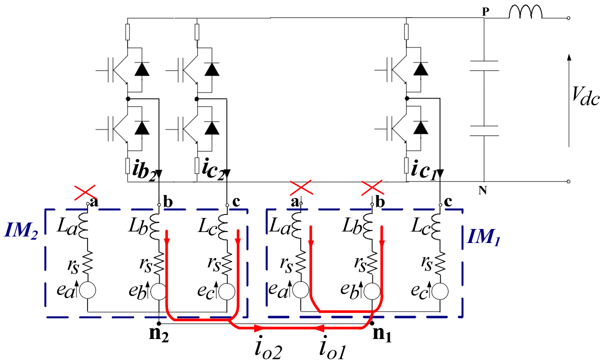

Figure 2.17 Single open phase fault in IM_1 and two open phase faults in IM_2.

As clearly shown in Figure 2.18, the phase current of the only healthy phase of IM_1 is equal to the neutral current i_{o2}, and the phase currents i_{b2} and i_{c2} are shifted by 60°, thus the total electromagnetic torque is almost provided by IM_2 but in this case both torque and speed present larger ripple with respect to the other cases.

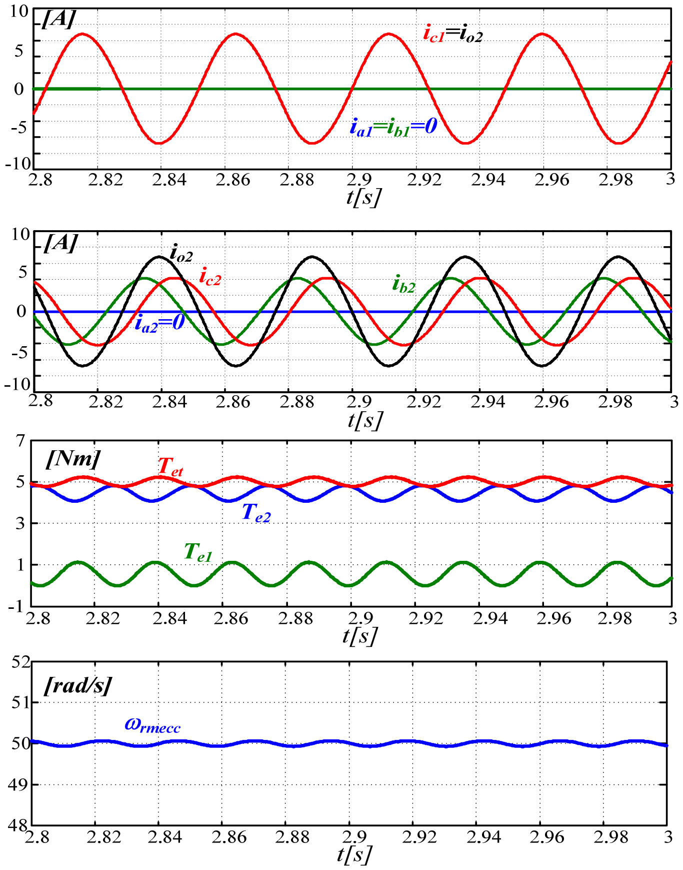

Figure 2.18 Single open phase fault in IM_2 and two open phase faults in IM_1.

2.4.1 Experimental results for mechanically coupled MDS

Theoretical aspects and simulation results have been evaluated with an experimental test bench. Two IMs have been mechanically coupled through two pulleys and a belt, for the tests of Figure 2.19, Figure 2.20 and Figure 2.21; the machines' parameters of IM_1 and IM_2 are indicated in Table 2.3. The S-PWM is used for both inverters to avoid additional harmonics circulation, as already discussed in the paragraph 2.1. IFOCs for the healthy and faulty drives have been implemented in a DSP board, dSpace 1104.

The magnetizing flux levels of the motors have been kept constant at the rated value, for all the tests.

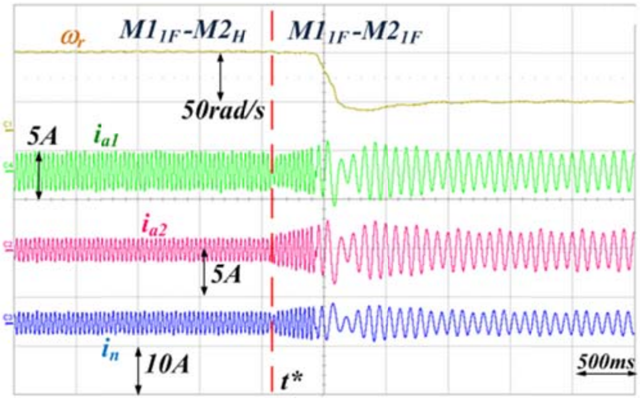

Figure 2.19 Speed Transient 80 rad/s — 30 rad/s: IM_1 operates with an open phase, while IM_2 initially operates in healthy conditions and after the instant time t^* works with an open phase.

Figure 2.19 displays the dynamic behavior of the MDS during a faulty condition. One drive, IM_1 is working under a single open phase fault, while the other is initially healthy, as reported in the pictures' label "M_{1F} - M_{2H}"; at the time instant t^* an open phase suddenly occurs on the stator winding of IM_2, and the new configuration is indicated with the label "M_{1F} - M_{2F}".

It is worth noting that the system is still working with both drives affected by a single open phase fault and that the phase current amplitude of IM_2 is increased in faulty operation mode with respect to the initial condition to balance the required load. A speed transient is applied to the drives from 80 to 30 rad/s showing a good command tracking also in this abnormal working condition.

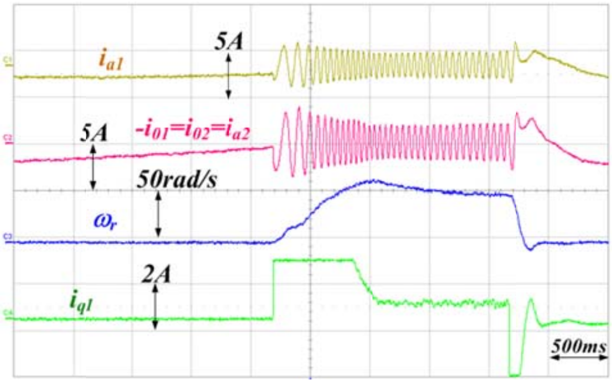

Figure 2.20 Speed Transient 0 rad/s — 50 rad/s — 0 rad/s: IM_1 operates with an open phase while IM_2 works with two open phases.

In particular, Figure 2.20 shows a speed transient with IM_1 operating under an open phase fault while IM_2 is affected by two faulty phases. Hence, its healthy phase “a” is used to provide a current path for the neutral current of IM_1. Although the dynamic is limited compared to the previous cases, because of a reduced torque capability, the stability of the system is not compromised also at very low speed.

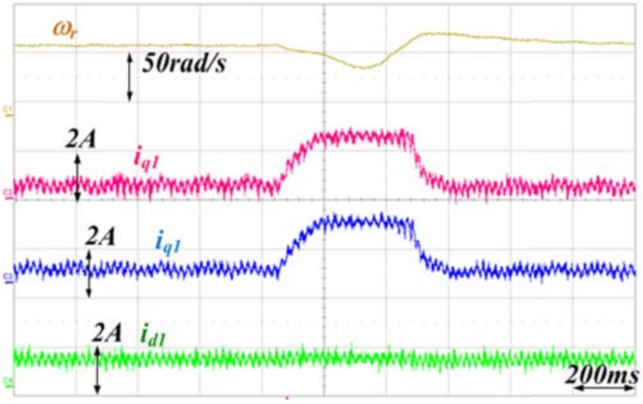

Figure 2.21 Load transient T_{total_load}=100% T_{en}, ω_r=70 rad/s. The two motors are operating under single open phase fault in each motor and controlled by imposing $\theta_{\lambda r1} = \theta_{\lambda r2}$.

Figure 2.21 shows the MDS behavior under the application of a load step. The total load applied is equal to the rated torque and both drives are operating under a single open phase fault. The speed is kept constant at 70 rad/s and a quite limited transient happens when the torque load is applied. In addition, it can be noted that the two feedback current torque components are defining an equal torque production while the superimposed ripple can be caused by an imperfect balance of motor phase impedances. The current flux component of IM_1 is also shown and it is decoupled by the q-axis current component.

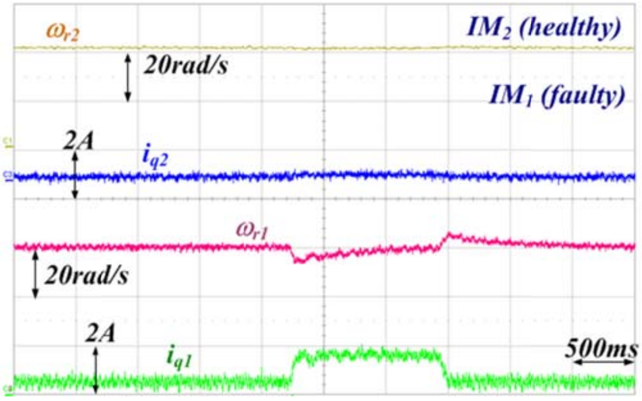

Figure 2.22 Load transient in the faulty motor IM_1, T_{load} =50% T_{en}. IM_2 spins at ω_{r2}=40 rad/s at no load, while IM_1 spins at ω_{r1}=60 rad/s.

Figure 2.22 shows the experimental test obtained with IM_1 working under an open phase fault while IM_2 is healthy; the two machines are not mechanically coupled and independently controlled. This test evaluates the effects on the healthy drive when a torque load is applied on the faulty one. The two motors IM_1 and IM_2 are running respectively at: 60 rad/s and 40 rad/s, the two torque current components are shown in the pictures; it is clear that the torque load which is equal to 50% of the rated one on the faulty unit, does not produce appreciable effects on the healthy drive.

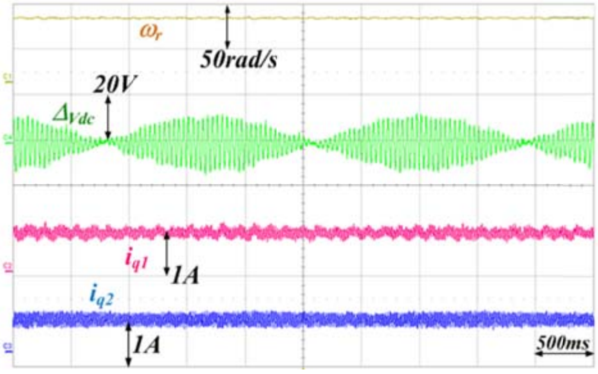

Figure 2.23 Steady state test, ω_r=80 rad/s. DC bus ripple measurement with MDS under a single open phase fault in both drives; the neutral points of both electrical machines are directly connected to the middle point of the DC bus and the motors are independently controlled $\theta_{\lambda r1} \neq \theta_{\lambda r2}$.

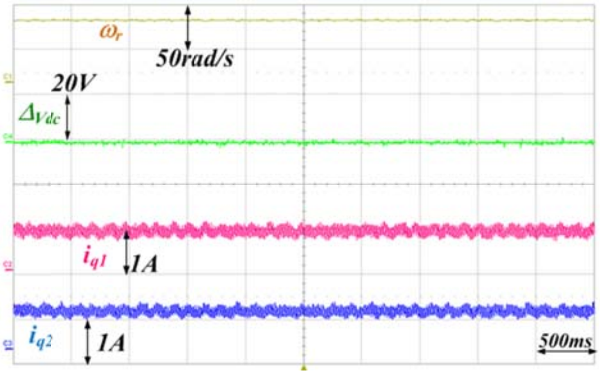

Figure 2.24 Steady state test, ω_r=80 rad/s. DC bus ripple measurement with MDS under a single open phase fault in both drives; the neutral points of both electrical machines are connected to each other and isolated from the DC bus; in addition, the two motors are controlled imposing that $\theta_{\lambda r1} = \theta_{\lambda r2}$.

Figure 2.23 and Figure 2.24 show the effect of the faulty operations on the DC bus voltage. Mechanical speed, DC bus voltage ripple and the two torque current components are reported in both pictures. Figure 2.23 displays the result obtained applying a standard FT-MDS configuration where the neutral point is connected to the middle point of the DC bus. Both drives are independently controlled, $\theta_{\lambda r1} \neq \theta_{\lambda r2}$, with a single open phase failure, operating at 80 rad/s without torque load, it can be noted that a huge ripple affects the DC bus voltage due to the neutral current flowing on the capacitor bank. On the contrary, Figure 2.24 highlights the results obtained with the proposed FT-MDS topology with the neutral point of the two machines connected together and isolated from the DC bus; also in this case both drives operate with a single phase fault but they are controlled imposing $\theta_{\lambda r1} = \theta_{\lambda r2}$ and running at 80rad/s. It can be noted that ΔV_{dc} is almost negligible compared to the one shown in Figure 2.23.

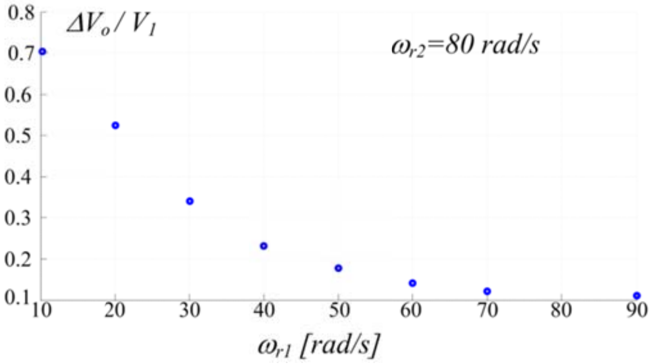

Figure 2.25 Ratio between ΔV_o and V_1 at different ω_{r1}.

The evaluation of the voltage drop ΔV_o produced by the neutral current i_{o1} in the stator windings of the healthy drive has been performed with no load steady state tests. In this case IM_2 is operating under a single phase fault, at a constant speed, while the healthy drive IM_1 is running at different speeds. Measuring the amplitude of the fundamental stator voltage component V_1 and the amplitude of the voltage drop ΔV_o on the healthy drive, the ratio $\Delta V_o/V_1$ is calculated for each speed combination, as shown in Figure 2.25. When the difference between the rotational speed of the two motors is small, ΔV_o becomes negligible, this means that the effect of the faulty current on the healthy drive is weak.

Figure 2.26 shows the harmonic spectrum of the phase voltage of IM_1 and IM_2 running respectively at ω_{r1} = 80 rad/s and ω_{r2} = 90 rad/s. As can be noted the spectrum of IM_2 has only its fundamental frequency, instead that one of IM_1 has its fundamental voltage harmonic and the additional harmonic related to ΔV_o at the same frequency of the faulty drive.

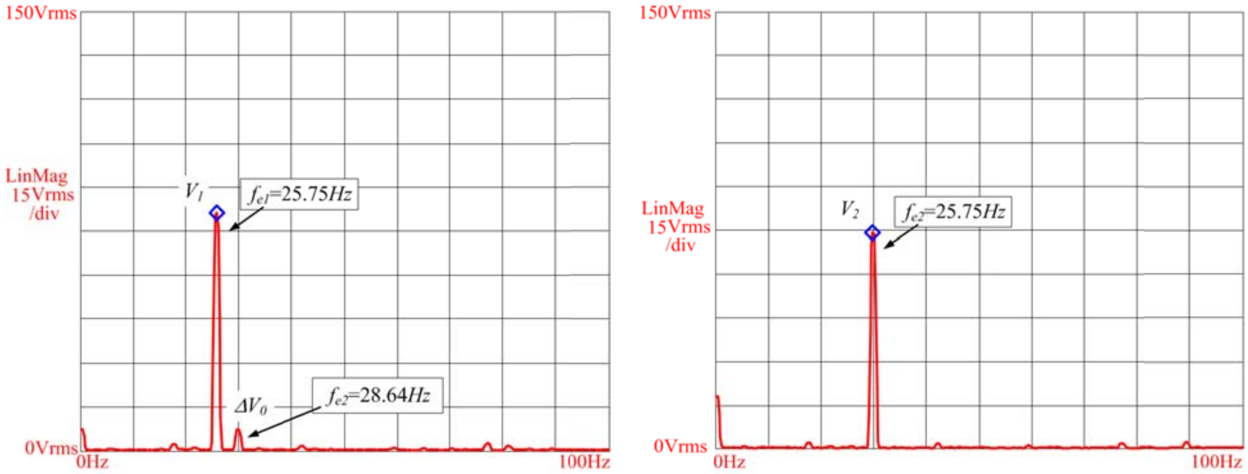

A) Phase voltage measured in IM_1.

B) Phase voltage measured in IM_2.

Figure 2.26 Frequency spectrum of voltage phases of the two motors running under a single fault.

2.5 Conclusions

In this chapter a novel fault tolerant MDS has been presented for three phase drives. Thanks to a cooperative control strategy in case of fault in one or more drives, they can still operate only with two phases, after the application of a proper control, capable of imposing two independent currents shifted by 60° electrical to each other. This can be accomplished with the connection of the neutral point of the stator winding of the faulty units with the neutral point of the stator windings of the healthy drives; in this way a significant improvement of the system’s reliability is guaranteed without significant increment of the cost.

Moreover, the configuration with two drives mechanically coupled has also been investigated and the effectiveness of the fault tolerant approach has been evaluated for different types of faults.

Simulation and experimental tests have confirmed the preliminary considerations and simulations tests.

2.6 References

[1] Jen-Ren Fu; Lipo, T.A. “A strategy to isolate the switching device fault of a current regulated motor drive” Industry Applications Society Annual Meeting, 1993, Conference Record of the 1993 IEEE, vol.: 2, pp.: 1015-1020.

[2] Bolognani, S.; Zordan, M.; Zigliotto, M. “Experimental fault-tolerant control of a PMSM drive,” Industrial Electronics, IEEE Transactions on, 2000, vol.: 47, Issue:5, pp.: 1134-1141.

[3] Welchko, B.A.; Lipo, T.A.; Jahns, T.M.; Schulz, S.E. “Fault tolerant three-phase AC motor drive topologies: a comparison of features, cost, and limitations,” Power Electronics, IEEE Transactions on, 2004, vol.: 19, Issue: 4, pp.: 1108-1116.

[4] Tian-Hua Liu; Jen-Ren Fu; Lipo, T.A. “A strategy for improving reliability of field-oriented controlled induction motor drives,” Industry Applications, IEEE Transactions on, 1993, vol.: 29, Issue: 5, pp.: 910-918.

[5] Pulvirenti, M.; Scarcella, G.; Scelba, G.; Cacciato, M.; Testa, A. “Fault-Tolerant AC Multi-drive System,” Emerging and Selected Topics in Power Electronics, IEEE Journal of, 2014, vol.: 2, Issue: 2, pp.: 224-235.

[6] P.C. Krause, O. Wasynczuk, S.D. Sudhoff, “ Analysis of Electric Machinery and Drive Systems”, second edition, IEEE press.

[7] Ned Mohan, Tore M. Undeland, William P. Robbins, “Power Electronics: Converters, Applications, and Design” Wiley, , 3rd Edition 2003.

[8] Panaitescu, R.C.; Mohan, N. “A simple space-vector PWM algorithm for VSI-fed AC motor drives ”, Applied Power Electronics Conference and Exposition, 2002. APEC 2002. Seventeenth Annual IEEE, vol.:1, pp.: 72-75.

[9] Kerkman, R.J. “Twenty years of PWM AC drives: when secondary issues become primary concerns”, Industrial Electronics, Control, and Instrumentation, 1996., Proceedings of the 1996 IEEE IECON 22nd International Conference on, vol.: 1, pp.: 57-63.

[10] Adabi, J.; Zare, F.; Ledwich, G.; Ghosh, A.; Lorenz, R.D. “Bearing damage analysis by calculation of capacitive coupling between inner and outer races of a ball bearing”, Power Electronics and Motion Control Conference, 2008. EPE-PEMC 2008. 13th, pp.: 903-907.

[11] Cacciato, M.; Consoli, A.; Scarcella, G.; Testa, A. “Effects of PWM techniques on common mode currents in induction motor drives”, Industrial Electronics, 1997. ISIE '97., Proceedings of the IEEE International Symposium on, vol.: 1, pp.:SS2121-SS217.

[12] Cacciato, M.; Consoli, A.; Scarcella, G.; Scelba, G.; Testa, A. “A novel space-vector modulation technique for common mode emissions reduction”, Electrical Machines and Power Electronics, 2007. ACEMP '07. International Aegean Conference on, pp.: 199-204.

[13] Pulvirenti, M.; Scarcella, G.; Scelba, G.; Cacciato, M. “Space vector modulation technique for common mode currents reduction in six phase AC drives”, Power Electronics and Applications (EPE), 2013 15th European Conference on, pp.: 1-10.

[14] Dae-Woong Chung; Joohn-Sheok Kim; Seung-Ki Sul “Unified voltage modulation technique for real-time three-phase power conversion,” Industry Applications, IEEE Transactions on, 1998, vol.: 34, Issue:2, pp.: 374-380.

[15] Mutoh, N.; Kanesaki, M.; Nakashima, J.; Ogata, M. “A new method to control common mode currents focusing on common mode current paths produced in motor drive systems”, Industry Applications Conference, 2003. 38th IAS Annual Meeting. Conference Record of the, vol.: 1, pp.: 459-466.

[16] Iimori, K.; Yamamoto, K.; Jyosui, S. “Suppressing of common mode voltage on ac motor with changing ground point of DC link in PWM inverter”, Power Electronics Conference (IPEC), 2010 International, pp.: 2488-2492.

[17] Tallam, R.M.; Leggate, D.; Kirschnik, D.W.; Lukaszewski, R.A. “PWM scheme to reduce the common-mode current generated by an AC drive at low modulation index”, Energy Conversion Congress and Exposition (ECCE), 2011 IEEE.

[18] Adabi, J.; Boora, A.A.; Zare, F.; Nami, A.; Ghosh, A.; Blaabjerg, F. “Common-mode voltage reduction in a motor drive system with a power factor correction”, Power Electronics, IET, 2012, vol.:5, Issue: 3, pp.. 366-375.

[19] Ali, S.M.; Reddy, V.V.; Kalavathi, M.S. “Simplified active zero state PWM algorithms for vector controlled induction motor drives for reduced common mode voltage
” Recent Advances and Innovations in Engineering (ICRAIE), 2014, pp: 1-7.

[20] Xu Dianguo; Gao Qiang; Wang Wei “Design of a Passive Filter to Reduce Common-Mode and Differential-Mode Voltage Generated by Voltage-Source PWM Inverter”, IEEE Industrial Electronics, IECON 2006 - 32nd Annual Conference on pp.:2483-2487.

[21] Jettanasen, C. “Passive common-mode EMI filter adapted to an adjustable-speed AC motor drive”, IPEC, 2010 Conference Proceedings, pp.: 1025-1030.

Chapter 3 Fault tolerant Wind Power Systems

The concepts of reliability discussed in the previous chapters can be straightforwardly applied to distributed generation units (DGU) adopting at least rotating and stationary electrical machines.

In this chapter the Fault Tolerant Multi-Drive System (FT-MDS) configuration analyzed in Chapter 2 is suitable re-adopted to get a Fault Tolerant - Wind Power System (FT - WPS). In case of fault, using a very limited number of additional components and after an appropriate reconfiguration, the system is still able to deliver power to the grid.

3.1 Introduction

The production of energy from renewable sources has increased in the last few years, especially the wind energy systems and their market have grown [1], [2].

Many topologies of wind turbines are available and one of the elements that characterize the system is the type of electrical machine applied to carry out the transformation from mechanical energy, produced by the blade rotation induced by the wind, in to electrical energy. The type of the generator is chosen as a function of different constraints such as: minimization of the energy cost, and the type of connections that will be made; many research activities such as [3], [4] and [5] present a comparison among different types of generators.

Grid connected wind generation systems have to respect grid standards in order to provide active support to the stability of the whole systemic grid [6]; moreover, fault ride-through (FRT) capability is required [7].

A standard Wind Energy Conversion System (WECS) for small-medium power is realized connecting the electric generator to the grid through two controlled power converters connected in “back to back” configuration, in addition the grid side converter (GSC) can be connected to the grid by means of a transformer. A passive filter is also connected between the GSC and the transformer to eliminate higher order harmonics. The back to back converter can be realized with a standard two level three-phase voltage source inverter (VSI) but depending on the wind turbine power rating and the grid voltage level also different converters can be used, such as multilevel converters [12].

There are two more common electrical machines employed in variable speed WPS: permanent magnet synchronous machine (PMSM) [8], [9], thanks to its higher efficiency and torque density, and the Doubly Fed Induction Machine (DFIM) [13]. The last is an IM with wound rotor; in this case, the back to back converter connects the grid and the rotor circuit, while the stator circuit is steadily connected to the grid. DFIM coupled with a back to back converter allows the use of the rotor side converter with about 20% of the rated stator power [14]. Both PMSM and DFIM based wind power configurations, thanks to the controlled power converters can precisely regulate the phase shift between voltage and current working at unity power factor [15] with a bidirectional power flow. DFIM is more sensitive to grid imbalance due to its stator windings directly connected to the grid.

The full controlled power converter connected to the generator allows variable speed operations in order to maximize the energy extracted from WPS, implementing a Maximum Power Point Tracking (MPPT) algorithm.

The wind turbine and the generator shaft can be coupled with a gear box distinguishing low speed shaft and high speed shaft turbines. The presence of the gear box increases the maintenance cost and reduces the efficiency; hence, in many case it is removed by adopting electrical machines with high number of poles and low rated speed [8], whose typical range is 20-200 r/min, depending on the machine's rated power. In the latter case a direct drive configuration is performed and the wind turbine rotor is connected to the generator shaft.

Figure 3.1, Figure 3.2, Figure 3.3 show different configuration of variable speed WPS [3].

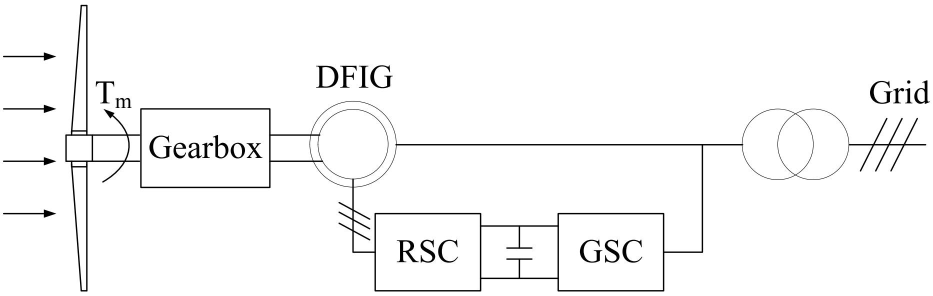

Figure 3.1 Standard configuration of WPS based on DFIG.

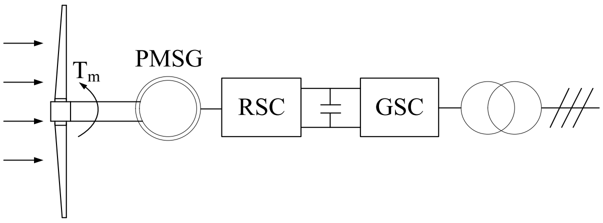

Figure 3.2 Standard configuration of WPS based on PMSG.

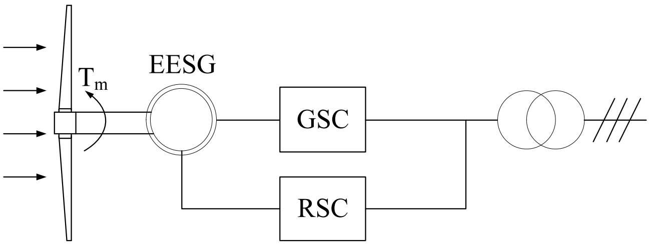

Figure 3.3 Configuration of WPS based on the Electrically excited synchronous generator.

3.1.1 Fault Tolerant Wind Power Systems

A WPS can be upset by different types of faults [16], causing, in the worst case, its shutdown or disconnection from the grid; therefore, causing loss of incoming and grid instability. A wind turbine is composed of many components and fundamentally can be seen as a system consisting of a mechanical part and an electrical one. Typical elements that can be affected by faults on the mechanical system are [17], [18] [19], [20], [21]:

- Drive train;
- Pitch control;
- Yaw control;

while the faults in the electrical system can occur in [22], [23], [24], [25]:

- Power converter;
- Currents, voltages, position sensors;
- DC link capacitor bank;

The requirements of wind energy production for the highest number of hours is becoming more and more necessary; hence, it is fundamental that WPS must be fault tolerant. Different actions can be accomplished to satisfy this requirement but a good evaluation about the type of faults, their frequency and their effects, needs to be made including that a WPS can be installed in remote area and it is not easy to repair or substitute rapidly the faulty elements; after, considering also the desirable reliability level and the ratio between cost and benefit, different opportunities can be considered.

It has been verified that the electrical components are more affected by faults with respect to the mechanical ones [23], nevertheless different fault tolerant controls are implemented to compensate also faults on the mechanical systems; many activities are devoted to compensate faults on the pitch control system, such as oil pressure reduction, guaranteeing the dynamic response of the WPS. In [17], active and passive fault-tolerant linear parameter-varying controllers, also discussed in [18], are formulated to compensate the non-linearities in the aerodynamic model or variations in the pitch system dynamics. In [19] a model predictive control is implemented and a Kalman Filter is designed to estimate the system states and many fault parameters. In [20] the authors propose a fuzzy model reference adaptive control to overcome both model uncertainty and actuator fault in the generator/converter. In [21] it is presented a fault tolerant observer which estimates the rotor, generator, and wind speed to overcome fault on the hydraulic system for the pitch control. On the other hand for the electrical systems, fault tolerant can be achieved with different approaches considering the power level of the WPS and the type of the generator; nevertheless some configurations already analyzed in Chapter 1 can be widely exploited, for example the use of redundant converter components or modified converter legs, are the most conventional approaches to implement a fault tolerant WPS [26], [27], [28].

In [29] the authors propose a fault tolerant control strategy for a squirrel cage induction generator (SCIG) based WPS, against inter-turn fault on the stator windings, that can be generated by moisture in the isolation, overheating, vibrations but also by the PWM voltages at the winding terminal that can have very high dv/dt. Fundamentally, a model predictive tracking controller is proposed to control the flux modulation preventing the fault propagation, without a strong degradation on the power delivered to the grid; although this is proposed for SCIG the method can be applied also for other types of generator, the block diagram of the control is reported in Figure 3.4.

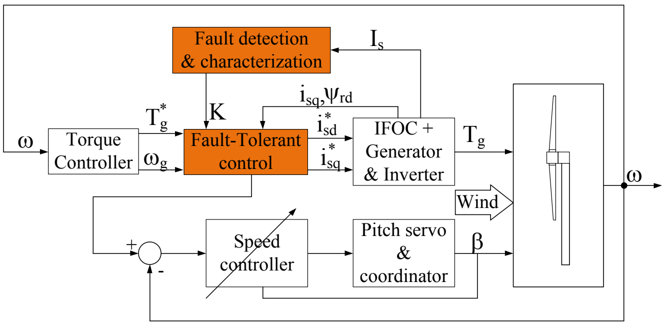

Figure 3.4 Control system of wind turbine with fault-tolerant control strategy.

In [30] the authors analyze the back to back configuration for WPS; compared to the standard two level three-phase converters that are usually parallel connected to deliver high power and increasing also the reliability in case of fault of one module; they propose a back to back configuration realized by multi-level converter for high power applications, Figure 3.5, that can work directly on medium voltage; the most widely used topology is the three level (3L) neutral-point clamped (NPC). This topology reaching a power rating up to 9MVA can be exploited for high power WPS, where just a single converter is enough to satisfy the power required. The last power converter structure can be suitably modified even including additional legs in order to mitigate faulty situations.

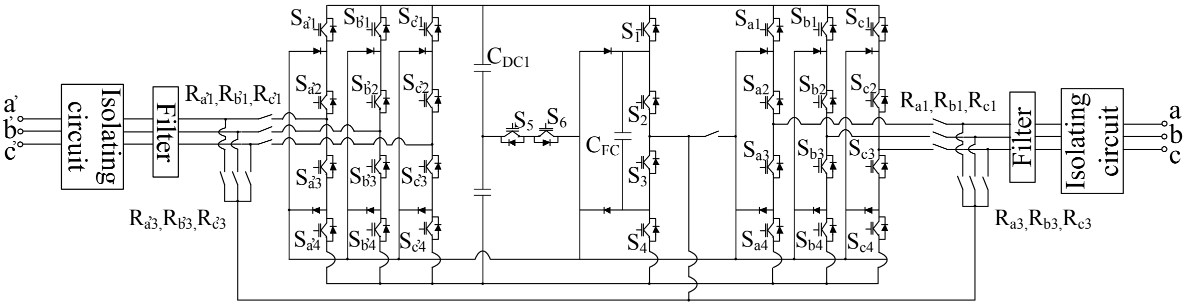

Figure 3.5 Fault- tolerant back-to-back converter topology with redundant 3L-FC-based leg for NP voltage balancing in normal operation mode and for substitution of a faulty leg on generator or grid side in fault operation mode.

The effects of different faults for a direct drive PMSG WPS, with a back to back converter based on two level three-phase inverter are presented in [23]. The rms currents of the grid and of the PMSG, total waveform distortion (TWD) index, power factor, electromagnetic torque and global drive efficiency are presented in case of: single fault in the grid side converter, single fault in the generator side converter, single fault in both converters, double fault in the generator side converter and finally a single fault in the grid side converter together with a double fault in the PMSG side-converter. The results obtained lead to the conclusion that the faults in one converter do not influence the variables on the other converter side, and it has also been verified that a fault on the grid side converter has more negative effect than a fault on the generator side converter.

In [24] the authors investigate the effects of faults on sensors employed in a PMSG based WPS. A matrix converter controls the PMSG and delivers power to the grid. As different sensors are used to measure currents and voltages to realize the control loop necessary to handle the system, erroneous information caused by a sensor failure leads to performance degradation and instability of the whole system. The authors implement a fault tolerant control (FTC) defining also a fault detection and isolation (FDI) algorithm necessary to detect and isolate the faulty sensor. The FDI algorithm is based on a neural network (NN) observer which takes into account the system non-linearity. After suitable training, the NN observer provides the correct signal substituting that coming from the faulty sensor, as shown in Figure 3.6

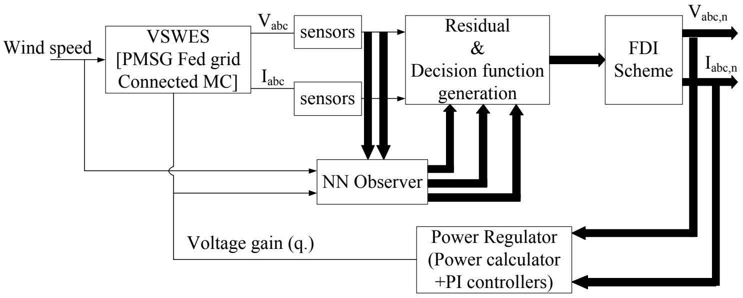

Figure 3.6 Schematic diagram of FTC in VSWES with power regulation loop.

More specific fault tolerant structures are presented for PMSG and DFIG rely on the hardware topology.

The authors, in [31] present a fault-tolerant PMSG based WPS employing new direct control techniques. For post fault operation a direct power control (DPC) of four-switch three-phase converter and direct torque control (DTC) for three-switch three-phase rectifier are proposed.

Reconfigurations to handle only open-circuit faults are triggered by a reliable fault diagnostic method without requiring additional measurements. The design of a fault tolerant drive has to consider a tradeoff between post-fault performance and cost increase.

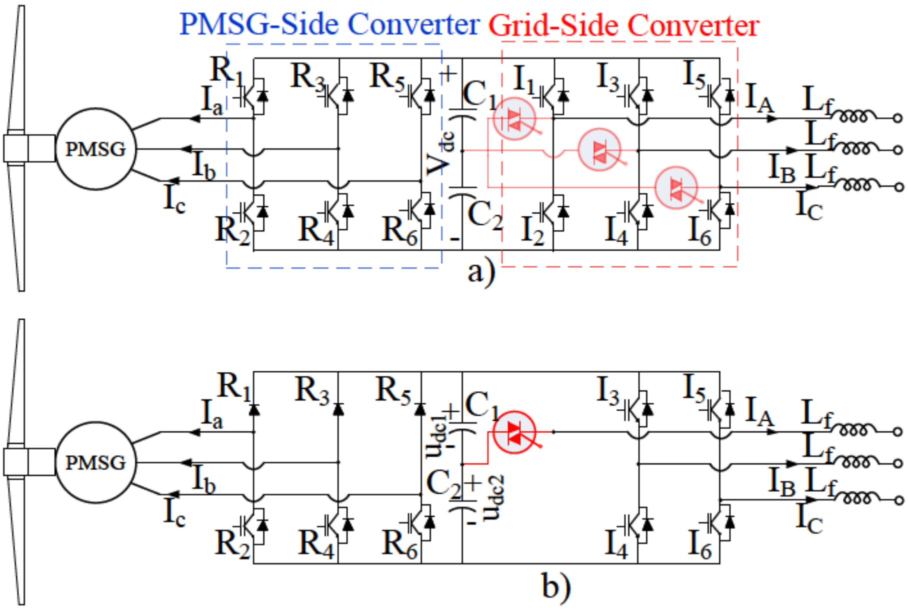

Figure 3.7 Fault-tolerant converter topologies: a) under normal operating conditions; b) After fault occurrences in power switches R_1 and I_1.

A different fault tolerant topology is obtained by including additional TRIACs which remain open under normal operating conditions, as shown in Figure 3.7 a) and they are used to reconfigure the circuit topology of the grid-side converter, in case of fault on this side; after the isolation of the faulty leg, the grid phase is connected through the triac to the dc bus middle point and the dc bus voltage reference has to be twice with respect to normal operations.

For a fault on the generator side there is no need for hardware reconfiguration but only a software reconfiguration which fundamentally inhibits the control signals of the three upper or bottom power devices depending on where the faulty component is situated.

Figure 3.7 b) shows the post fault topology when a fault occurs in both converters.

For post fault operations the DPC is again used to control independently active and reactive powers by selecting the optimum voltage vector in a switching table that must be suitably modified; similarly also the switching table for DTC algorithm is modified to properly control the generator reducing the torque oscillation.

The same authors in [32] present another fault tolerant PMSG based WPS also in this case able to handle power switch open-circuit, considering a different configuration system where also a transformer is included as shown in Figure 3.8 a).

This topology requires three relays and one TRIAC for the fault isolation and converter reconfiguration in the grid-side converter.

If a fault occurs on the grid side converter, the faulty leg is isolated and to properly control the transformer, the neutral point is connected to a PMSG phase hence the inverter leg is shared and used to create a closed path for the neutral current. If the rated power is to be reached the shared leg needs to be designed with a rated current four times higher than the other legs. To avoid this oversizing the maximum power is reduced to 58% of the rated value that can be delivered to the grid.

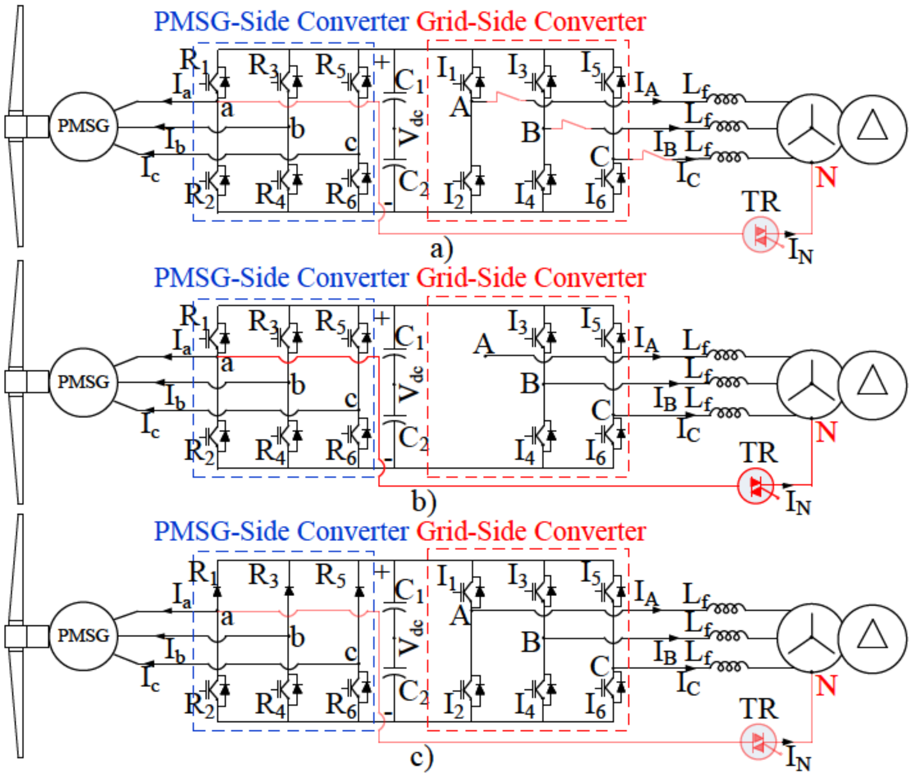

Figure 3.8 Fault-tolerant converter topologies: a) under normal operating conditions (two SSTC); b) after a fault in I_1 or I_2 (five- leg converter); c) after a fault in R_1, R_3or R_5 (TSTPR and SSTC).

The post fault operation for the generator side is equal to that one presented in [31] and previously discussed, where only open switch faults are tolerated and the system is reconfigured as shown in Figure 3.8 b and c. In this case a dc bus voltage twice as high with respect to normal operation is not required.

The converter is not able to tolerate simultaneous open circuit faults in the two converter sides.

It is not necessary to oversize any component hence the cost of the system does not increase if a reduction of the operating range during post fault operation is acceptable.

In [33] the authors are proposing a fault tolerant PMSG based WPS similar to that one presented in [32] but in this case the main goal is the reduction of additional components to obtain a fault tolerant system, Figure 3.9 a). Considering only the case of open-switch of the power converter, in case of fault on the grid side converter the faulty leg is isolated and the transformer is fed with the remaining two healthy phases and the neutral point is connected to the middle point of the capacitor bank through the additional TRIAC; fundamentally the post fault operation requires, due to this connection, the increasing of the dc link voltage. A fault on the generator side is managed as already discussed in [31] and [32]. With respect to [32] in this case a single fault in both converters is tolerated and Figure 3.9 b) shows the post fault configuration topology. Different control strategies are presented for both control units to guarantee high performances also during post fault operations.

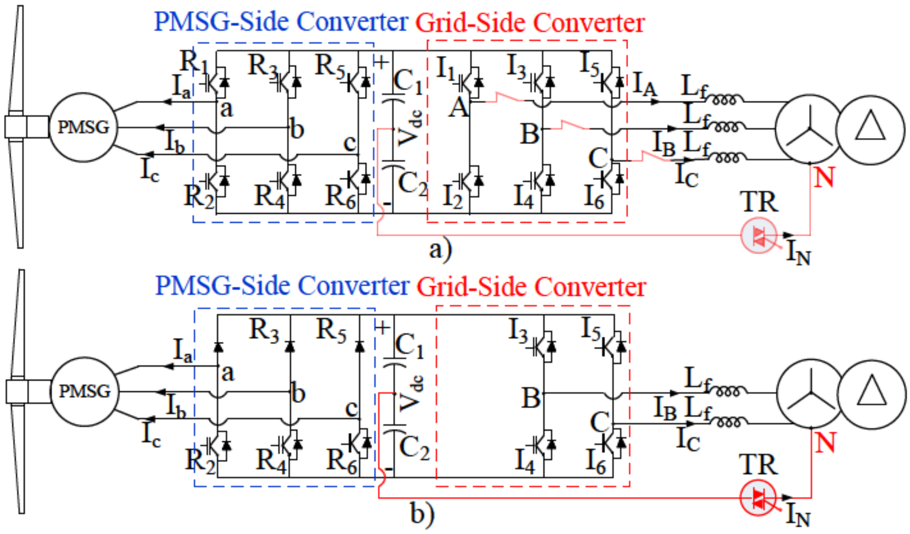

Figure 3.9 Fault-tolerant converter topologies: a) under normal operating conditions and b) after fault on R_1 and I_1.

For DFIG fault tolerant topologies are presented in [34] and [35], in particular [34] proposes a back to back configuration with an additional leg as shown in Figure 3.10, defining the so-called redundant topology configuration, which in case of fault on the GSD or in the RSC can replace the damaged leg avoiding performance reduction during post fault operation. Also this configuration can handle only a single fault in the GSC or in the RSC.

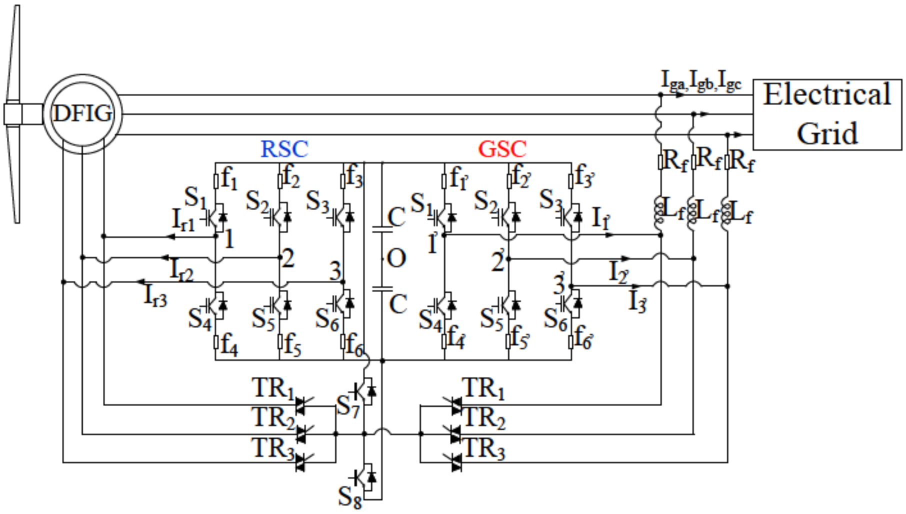

Figure 3.10 Fault tolerant WECS topology with DFIG.

In [35] a FT converter topology without redundancy is proposed, as shown in Figure 3.11. In this case when a fault occurs on the RSC or in the GSC the faulty leg is isolated. In particular, in case of an open switch fault, the control signal is disabled, while in case of short circuit in addition to the control signal disabling, the fuses are activated to isolate physically the leg from the dc link; after this, the suitable TRIAC is activated and a leg of the RSC or of the GSD is shared, realizing a five leg converter. In this case, for the post-fault operation, different control algorithms that the authors implement with five LUTs are required. In post-fault operation to obtain the same power capability as in normal condition, the DC bus voltage level will depend on the slip of the DFIG.

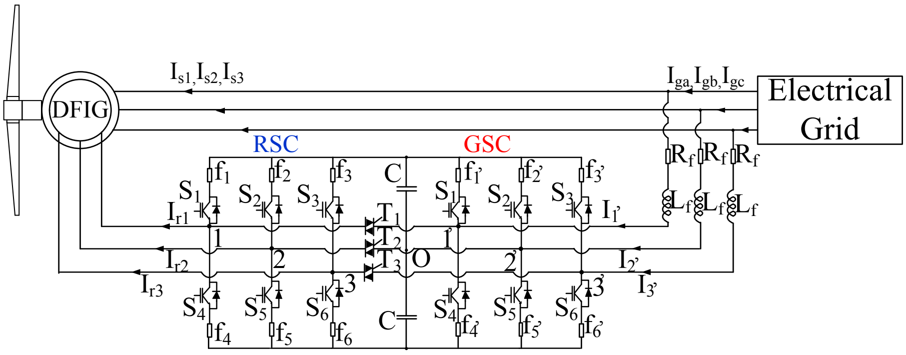

Figure 3.11 Fault tolerant topology without redundancy.

An alternative FT WPS based on PMSG, studied in this section [36] is presented in Figure 3.12: with respect to other FT WPS with similar arrangement, only to additional switches SW1 and SW2 are required to reconfigure the system after a fault event occurs in a single leg of the two inverters or a single open phase in the generator or in the transformer.

In normal operating conditions, when the system is healthy, these switches are turned off, working as an open circuit, to avoid flowing of zero sequence current; on the contrary, when a fault occurs, a fault detection algorithm is used to identify and isolate the damaged part similarly to the topologies analyzed in Chapter 1, and soon after SW1 and SW2 are turned on. As already discussed, three phase drives can still work after a fault only with two phases if they are supplied by two independent currents suitably phase shifted. In the latter case, the sum of these two currents will produce a neutral current that can flow through the path realized with SW1 and SW2, connecting the neutral point of the generator, the filter and the transformer.

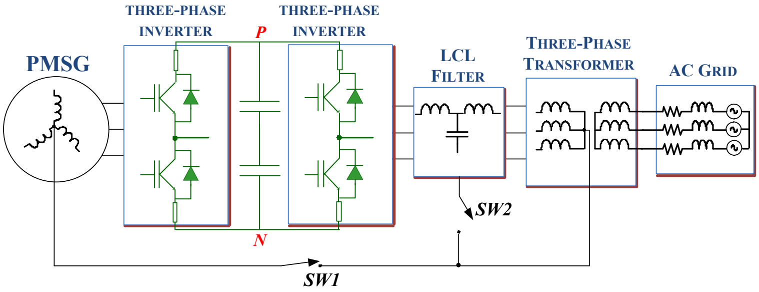

Figure 3.12 Block diagram of the proposed FTWPS.

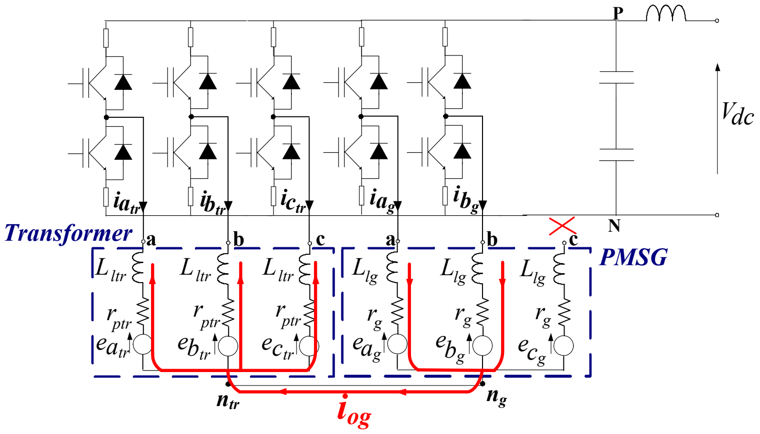

Figure 3.13 Schematic representation of the FTWPS operating with an open phase fault in the generator.

Figure 3.13 highlights the post fault converter configuration when a fault affects the generator side, in this representation the LCL filter is omitted because it has a higher impedance and in the following it will be verified that all the neutral current flows through the transformer. Moreover, the isolated leg is not reported. The neutral current, indicated with “i_{og}”, generated by the two healthy phases of the PMSG is flowing in the three-phase stator windings of the transformer; a similar configuration can be obtained if a fault occurs in the transformer side, in this case the neutral current will be indicated with “i_{otr}”.

Considering the case reported in Figure 3.13, the neutral current, i_{og}, is considered as a zero sequence current from the transformer side and looking at the qd0 transformer model, the zero sequence circuit of primary and secondary are not mutually coupled, therefore, this additional current on the primary windings does not produce effect on the transformer control depending only on q and d axis and also i_{og} does not induce any current on the secondary windings connected to the grid.

In different transformer configurations a zero sequence current circulation could be possible [37] hence should be considered to avoid any undesired effect.

Similar considerations can be made if a fault occurs on the transformer side and the neutral current i_{otr} flows through the PMSG stator windings and in this case it does not affect torque and flux controls.

The great benefit of this configuration is the capability of energy production in presence of fault and this is allowed with minimal additional hardware and inexpensive algorithm control that can be included on the DSP board together with the standard algorithm. The fault tolerant control for the PMSG can be done as presented in [38] and reviewed in Chapter 1 without any other hardware modification; similar consideration can be made for the control of the transformer side where the active and reactive power control, PQ control [8] can be performed modifying the reference frame transformations [39] of the inner current loop.

3.2 Functionality and operating limits

3.2.1 Wind Turbine Model

When the wind meets the blades of the turbine its energy produces the rotation of the shaft at the speed $\omega_r(t)$, the power extractable from the wind depends on the wind speed, $v_w(t)$, the air density, ρ, and the swept area, A. The power effectively transferred from the swept area to the rotor transformed in real mechanical power, P_m is function of the power coefficient $C_p(\lambda(t),\beta(t))$; this coefficient is function of the pitch angle $\beta(t)$ and the tip speed ratio $\lambda(t)$. It can be noted that P_m is proportional to the cubic of the wind speed [9].

$$P_m = \frac{1}{2}\rho A C_p(\lambda(t),\beta(t))\, v_w^3(t) \qquad (3.2.1.1)$$

Figure 3.14 represents a block diagram of a wind turbine [17].

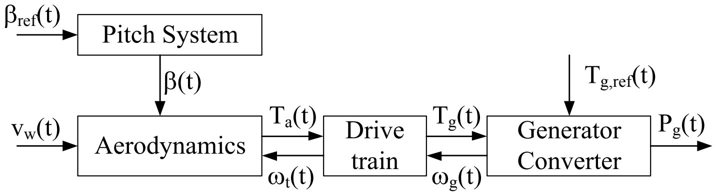

Figure 3.14 Block diagram of the wind turbine model.

The pitch angle $\beta(t)$ allows to change the area of the blade swept by the wind and it can be modified by electric or hydraulic systems; that can be modeled as second order system with its natural frequency ω_n and damping ratio ξ [18].

$$\ddot{\beta}(t) = -2\xi\omega_n\dot{\beta}(t) - \omega_n^2\beta(t) + \omega_n^2\beta_{ref}(t - t_d) \qquad (3.2.1.2)$$

in this case t_d is used to model a time delay.

Figure 3.15, shows the behavior of the power coefficient $C_p(\lambda(t),\beta(t))$, while Figure 3.16 shows the captured wind power with respect to the turbine speed, as a function of the wind speed.

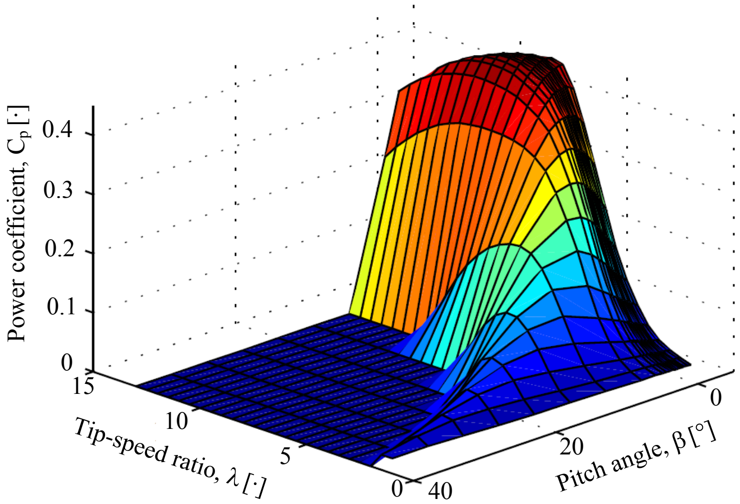

Figure 3.15 Representation of the power coefficient, Cp, [17].

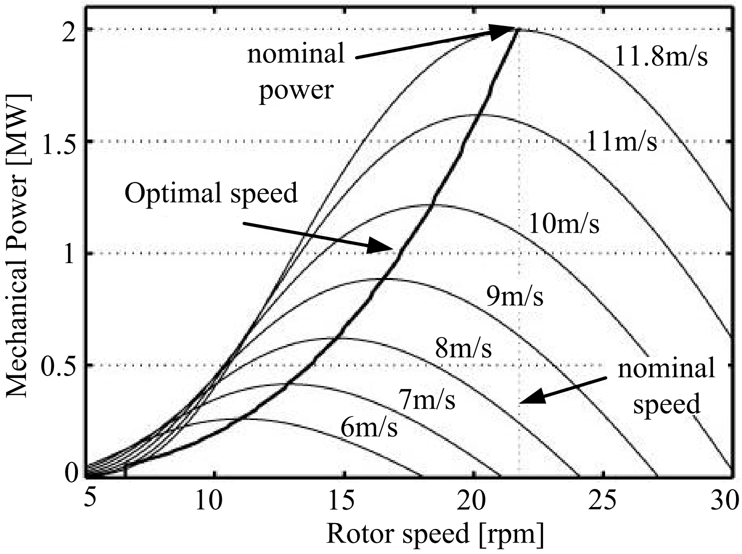

Figure 3.16 Power- Speed characteristics of a wind turbine.

The tip speed ratio λ(t) is calculated dividing the speed of the turbine at the tip of a blade and the wind velocity $v_W(t)$.

$$\lambda(t) = \frac{\omega_r(t)R}{v_W(t)} \tag{3.2.1.3}$$

R is the turbine radius.

The energy production is improved extracting the maximum power from the wind, thus implementing a maximum power point tracking (MPPT) algorithm like the ones described in [10], [11] where the optimal tip speed ratio λ_{opt} is tracked as well as the maximum power coefficient C_{p_max}, defining equations:(3.2.1.4) and (3.2.1.5).

$$\lambda_{opt} = \frac{\omega_{r\_opt} R}{v_w} \qquad (3.2.1.4)$$

$$P_{m\_max} = \frac{1}{2} \rho A C_{p\_max} \left(\frac{\omega_{r\_opt} R}{\lambda_{opt}} \right)^3 \qquad (3.2.1.5)$$

It is obvious to consider that the maximum power (3.2.1.5) cannot be higher than the rated power of the generator.

The rated power of the generator will be reached at the rated wind velocity, therefore for higher wind speeds the output power is limited to this edge by continuously modifying the pitch angle of the blades, causing a reduction of the power coefficient C_p, as shown in Figure 3.15. Small speed transients can be accepted due to the slow dynamic of the pitch control system.

If the wind speed increases too much, over a cut –off value, ($v_{cut\text{-}off}$) the turbine is shut down to prevent structural damage, in addition, also if the wind speed is too low, under the cut-in value, ($v_{cut\text{-}in}$) the turbine is turned-off because the power is too low.

The aforementioned control strategies can be resumed with Figure 3.17: when the wind speed is between $v_{cut\text{-}in}$ and v_{rated} the speed generator changes to extract the maximum power. The optimal reference speed is calculated according to equation (3.2.1.5); this value is applied as input of a controller which provides the correct torque command or the relative stator current, in terms of "qd0" component, proportional to the electromagnetic torque provided by the generator; when the wind speed is between v_{rated} and $v_{cut\text{-}off}$, the generator power will be kept roughly constant at its rated value, thus the pitch angle will be adjusted to reduce the power extracted from the turbine. Before $v_{cut\text{-}in}$ or over $v_{cut\text{-}off}$ the wind turbine is shut down for economic or safety reasons.

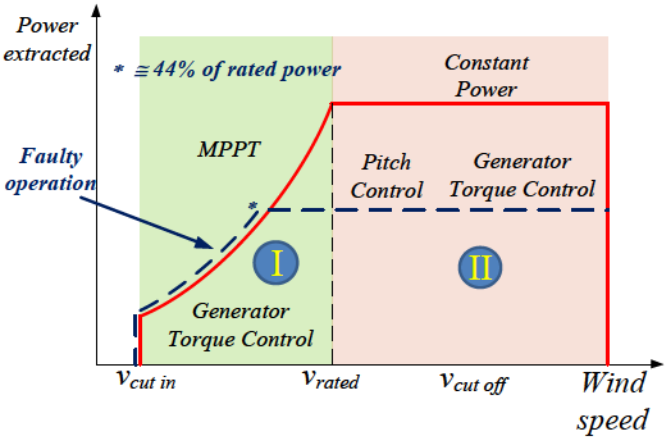

Figure 3.17 Control regions of the WPS.

Taking into account that usually the rated voltages and currents of the PMSG and transformer are comparable to avoid intermediate conversion stage, during fault operations the power capability of the whole system is clearly reduced, if a fault affects the PMSG or its relative converter, the drive will work only with two phases, a similar approach is adopted for the transformer and its converter. As already shown in Figure 3.13 where the PMSG operates with an open phase fault, the neutral current i_{og} flows through the transformer and it is equally split in its primary windings. The per phase amount of i_{og} is identify with ΔI_{tr} and will affect the current capability of the transformer. It is possible to quantify ΔI_{tr} assuming that the faulted generator is working at the rated current I_n and the currents flowing in the two healthy phases are 60° phase shifted, can be obtained:

$$\Delta I_{tr} = \frac{1}{3} I_{og} = \frac{1}{3}\left| \bar{I}_n + \bar{I}_n e^{j\frac{\pi}{3}} \right| = \frac{1}{3}\sqrt{3} I_n = \frac{1}{\sqrt{3}} I_n \cong 0.58\, I_n \tag{3.2.1.6}$$

where I_{og} is the amplitude of the neutral current i_{og}.

In this condition the maximum breaking torque produced by the generator is reduced to 58% T_{en}, as verified in [38]. The torque reduction will affect the operative wind speed range; in fact, considering the turbine aerodynamic equation, the torque produced by the turbine can be written exploiting (3.2.1.5), considering that the MPPT defines an optimum value of the tip speed ratio:

$$T = \frac{1}{2}\rho A C_p \frac{R}{\lambda_{opt}} v_w^2 \tag{3.2.1.7}$$

During the faulty operation the maximum torque is achieved at a reduced wind speed by a factor γ.

$$\frac{0.58 T_n}{T_n} = \frac{\frac{1}{2}\rho A C_p \frac{R}{\lambda_{opt}} (\gamma v_w)^2}{\frac{1}{2}\rho A C_p \frac{R}{\lambda_{opt}} v_w^2} \rightarrow \gamma^2 = 0.58 \rightarrow \gamma \cong 0.76 \tag{3.2.1.8}$$

Although the wind speed range is limited to 76% of the rated value this corresponds to the control region where statistically the WPS operate for the higher number of hours and extract a significant amount of energy.

The total extracted power is obtained as:

$$P_{nfault} = 0.76\omega_{rmn}\, 0.58 T_n = 0.441 P_n \tag{3.2.1.9}$$

Another important issue regards the currents flowing in the primary windings of the transformer which can be overloaded under certain conditions. The current of the transformer is related to the power delivered by the generator, considering that the voltage on the primary side of the transformer is imposed by the grid, it can be assumed that the power is related only to current variations, therefore $0.441P_n$ defines a transformer current of about $44\%I_n$ considering the previous assumption that the PMSG and transformer have the same rated current, but it is necessary to add the term ΔI_{tr} due to i_{og}, obtaining (3.2.1.10).

$$I_{tr} \cong 0.44I_n + \Delta I_{tr} = 1.02I_n \qquad (3.2.1.10)$$

Equation (3.2.1.10) leads to a very small overload of the transformer only when the faulted PMSG deliver the rated power P_{nfault} this condition is not permanent hence this overload can be easily tolerated for short periods.

These considerations can be extended if a fault occurs on the grid side system and the transformer primary side operates only with two phases. Assuming that the same MMF with respect to normal operation, need to be generated on the transformer, the two healthy phase currents should be shifted by 60° and increased in amplitude by $\sqrt{3}$ this allows delivery to the grid of the same power as in normal conditions. If the transformer cannot be overloaded the power delivered to the grid is reduced to 58% equivalent to $(1/\sqrt{3})\ P_n$, but the whole power of the WPS is affected also by the limitations induced to the PMSG. In this case a neutral current i_{otr} produced by the sum of the healthy phases of the transformer flows through the stator windings of the PMSG defining a quantity equal to ΔI_g.

$$\Delta I_g = \frac{1}{3} I_{otr} = \frac{1}{3}\left|\bar{I}_{tr} + \bar{I}_{tr}\, e^{j\frac{\pi}{3}}\right| = \frac{1}{\sqrt{3}} I_{tr} \qquad (3.2.1.11)$$

The torque current component I_g is limited to:

$$I_g = I_n - \Delta I_g \qquad (3.2.1.12)$$

knowing that the electromagnetic torque is proportional to the torque current component, the following ratio can be written:

$$\frac{T}{T_n} = \frac{I_g}{I_n} \qquad (3.2.1.13)$$

From the aerodynamic equation it is also true:

$$\frac{T}{T_n} = \frac{v_w^2}{v_{wn}^2} = \frac{\omega_r^2}{\omega_{rn}^2} = \frac{I_g}{I_n}$$

$$\frac{v_w}{v_{wn}} = \frac{\omega_r}{\omega_{rn}} = \sqrt{\frac{I_g}{I_n}} \qquad (3.2.1.14)$$

In terms of power:

$$\frac{P_g}{P_n} = \frac{T\omega}{T_n\omega_n} = \frac{I_g}{I_n}\sqrt{\frac{I_g}{I_n}} = \left(\frac{I_g}{I_n}\right)^{\frac{3}{2}}$$

$$\left(\frac{P_g}{P_n}\right)^{\frac{2}{3}} = \frac{I_g}{I_n} \qquad (3.2.1.15)$$

Substituting equation (3.2.1.12)

$$\left(\frac{P_g}{P_n}\right)^{\frac{2}{3}} = \frac{I_g}{I_n} = 1 - \frac{\Delta I_g}{I_n} = 1 - \frac{I_{tr}}{\sqrt{3}I_n} \qquad (3.2.1.16)$$

If the WPS is operating at unity power factor and assuming negligible the losses of the converters the equation (3.2.1.16) can be approximated in (3.2.1.17)

$$\left(\frac{P_g}{P_n}\right)^{\frac{2}{3}} = 1 - \frac{\Delta I_g}{I_n} = 1 - \frac{P_{tr}}{P_n} \qquad (3.2.1.17)$$

Where

$$P_{tr} = \sqrt{3}V_n\frac{1}{\sqrt{3}}I_{tr} = V_n\, I_{tr}$$

$$P_n = \sqrt{3}V_nI_{tr} \qquad (3.2.1.18)$$

At steady state $P_g = P_{tr} = P$, hence substituting in (3.2.1.17)

$$\left(\frac{P}{P_n}\right)^{\frac{2}{3}} = 1 - \frac{P}{P_n} \qquad (3.2.1.19)$$

The equation (3.2.1.19) is verified when $P/P_n = 0.43$ this relation defines a quite similar power reduction estimated in case of a single fault on the PMSG.

To sum up, if a fault occurs on the generator side or on the grid side the WPS can deliver 43 % of its rated power to the AC grid.

Another aspect needs to be considered: the neutral currents i_{og} or i_{otr} produced respectively when the PMSG or the transformer works only with two healthy phases, yields an additional voltage drop ΔV which is related to the phase resistance and the leakage inductance of the healthy drive used as feedback current path, i. e. the parameters of the zero sequence circuit of the PMSG or the transformer model. Although ΔV does not affect the control of the system, will reduce the DC bus voltage dedicated to generate the fundamental voltage. An experimental result carried out with the PMSG under an open phase fault shows that this voltage drop can reach 10% of the phase voltage of the transformer when the PMSG runs at high rotational speeds.

$$\Delta V = -\frac{1}{3} r_{ptr}\, i_{og} - \frac{1}{3} L_{lptr}\frac{d}{dt} i_{og} \quad \text{per phase voltage drop in case of PMSG fault} \qquad (3.2.1.20)$$

$$\Delta V = -\frac{1}{3} r_{g}\, i_{otr} - \frac{1}{3} L_{lg}\frac{d}{dt} i_{otr} \quad \text{per phase voltage drop in case of transformer fault} \qquad (3.2.1.21)$$

In addition, as discussed for fault tolerant MDS [40] also for this FT-WPS , during post fault operation, modulation techniques such as Space Vector Modulations (SVM) or S-PWM with third harmonic injection cannot be used because the neutral connection allows the circulation of large third harmonic currents, this drawback is overcome using a standard S-PWM in both inverters, leading to a further DC bus voltage utilization reduction equal to 15% compared to SVM.

Although standard S-PWM is adopted, during a fault on the transformer, a quite small third harmonic current is presented on the generator depending on the rotational speed ω_{rm}, due to the MMF distribution. This third harmonic current component can be balanced with a suitable third harmonic voltage, as will be shown with the experimental result, whose amplitude can be 10% of the fundamental voltage. The maximum value of the phase voltage V_{max} in both drives can be reduced up to 30% with respect to normal operative conditions. This drawback can be partially compensated increasing the reference voltage of the dc bus control loop performed by the grid side converter.

However, these voltage drops, could be negligible, in case of fault of the PMSG because it will work at a lower speed than the nominal value hence also the phase voltage will be almost reduced, instead it must be considered that the drive connected to the grid requires full voltage DC bus capability.

3.2.2 Generator Side Converter Control

A three phase fully controlled converter is applied to control the PMSM and to achieve a good dynamic behavior a vector control very similar to that implemented in Chapter 1, paragraph 1.2.2 D, has been exploited for this fault tolerant system as shown on Figure 3.18. The equations are reported in terms of qd0 variables and the qd0 reference frame that allows to achieve the vector control of the machine is that one rotating synchronously with the rotor magnet flux.

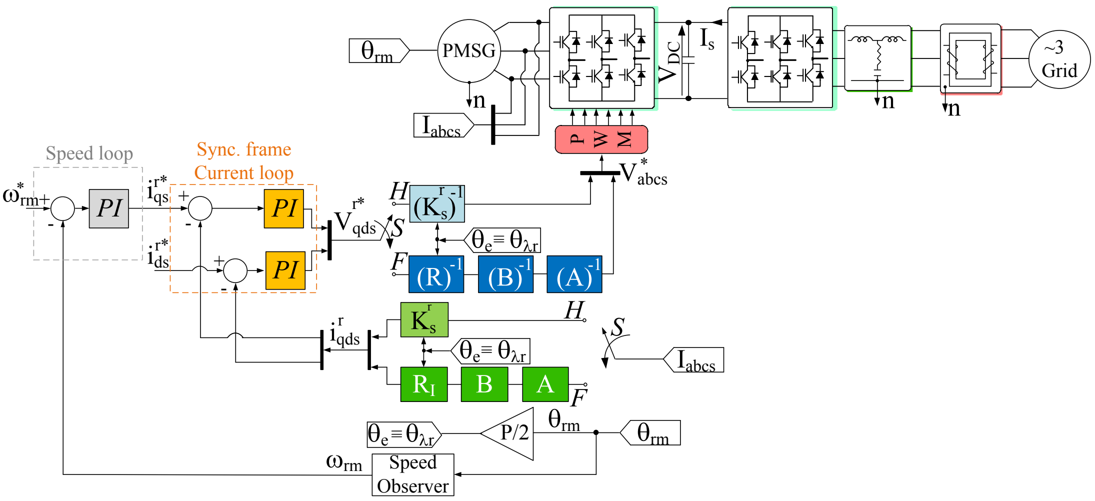

Figure 3.18 Block diagram for the fault tolerant control of the PMSG Converter.

The equations are reported adopting the motor convention, for the generator convention the " - " sign needs to be considered for the current, in addition the machine model considered includes a rotor saliency hence a different q and d inductance values are indicated. The electromagnetic torque consists of two contributions: a torque component provided only by the product between the permanent magnet and the stator current component i^r_{qs}, called "Excitation torque", and the other component proportional to the difference $(L_d - L_q)$ times $i^r_{ds} i^r_{qs}$, called "Reluctance torque".

In the simulation results shown after the d stator current component i^r_{ds} will be set to zero therefore the total torque is defined by the excitation torque component. To improve the efficiency of the drive the i^r_{ds} value can be adjusted adopting the MTPA strategy, but at this moment this is not the goal of this study.

$$\begin{cases} v_{qs}^{r} = R_g\, i_{qs}^{r} + p\, \lambda_{qs}^{r} + \omega_r\, \lambda_{ds}^{r} \\ v_{ds}^{r} = R_g\, i_{ds}^{r} + p\, \lambda_{ds}^{r} - \omega_r\, \lambda_{qs}^{r} \\ \lambda_{qs}^{r} = L_q\, i_{qs}^{r} \\ \lambda_{ds}^{r} = L_d\, i_{ds}^{r} + \lambda_m \\ \lambda_{0s} = L_{ls}\, i_{0s} \end{cases} \qquad (3.2.2.1)$$

$$T_e = \frac{3}{2}\frac{P}{2}\left[\lambda_m\, i_{qs}^{r} + (L_d - L_q)\, i_{ds}^{r}\, i_{qs}^{r}\right] \qquad (3.2.2.2)$$

Assuming $i_{ds}^{r}=0$

$$T_e = \frac{3}{2}\frac{P}{2}\left[\lambda_m\, i_{qs}^{r}\right]$$

The tuning of the current loop and the speed loop can be done according to the method reported in the Appendix.

3.2.3 Grid Side Converter Control

The grid side converter is controlled to keep constant the DC-link voltage [13] and at the same time to regulate the flows of active, P, and reactive, Q, power delivered to the grid. The expression of these powers can be obtained applying the matrix transformation presented in Chapter 1, Paragraph 1.2.1 C, for healthy conditions, in an arbitrary rotating qd0 reference frame attaining (3.2.3.1):

$$P = \frac{3}{2}\left(V_q I_q + V_d I_d\right) \qquad Q = \frac{3}{2}\left(V_q I_d - V_d I_q\right) \qquad (3.2.3.1)$$

As the voltage amplitude is imposed by the grid, a decoupled control of P and Q can be achieved if the qd0 reference frame is rotating at the grid pulsation ω_e and aligning the d-axis with the grid voltage, this condition is equivalent to set $V_q=0$. Hence the active and reactive power will be proportional only to the q and d current components.

$$P = \frac{3}{2} V_d I_d \qquad Q = -\frac{3}{2} V_d I_q \qquad (3.2.3.2)$$

If we assume that the WPS delivers to the grid only active power, the current component I_q can be imposed to zero, in the following analysis inverter losses are neglected and only fundamental voltage harmonic is considered. Equation (3.2.3.3) can be obtained from a power balancing:

$$V_{DC}\, I_s = \frac{3}{2} V_d\, I_d \tag{3.2.3.3}$$

where I_s is the DC bus current as shown in Figure 3.18 and Figure 3.19.

Considering that the fundamental voltage can be expressed as function of the modulation index of the grid side converter, m_g and the DC bus voltage, V_{DC} as reported in (3.2.3.4).

$$Vd = \frac{m_g}{2\sqrt{2}} V_{dc} \tag{3.2.3.4}$$

$$I_s = \frac{3}{4\sqrt{2}}\, m_g\, I_d \tag{3.2.3.5}$$

Equations (3.2.3.3) - (3.2.3.5) demonstrate that the DC-link voltage can be controlled by I_d, therefore the additional loop for the DC-link voltage is used to provide the d-axis current reference that control the active power.

Figure 3.19 shows the control of the grid side converter including the transformation matrices for healthy and faulty operative conditions. The transformation matrices K_s^e and $(K_s^e)^{-1}$ are adopted during normal operations, instead during a fault on the primary side of the transformer T_s^s, T_s^e and $(T_s^s)^{-1}$, $(T_e^s)^{-1}$ will be adopted, in this way the current loop structure is similar to that of Figure 1.34 for IM. The outer loop is used to control the DC bus voltage generating a d-axis reference current with a PI controller, while the q-axis reference current can be set directly to 0 or can be provided realizing a control loop on the reactive power Q.

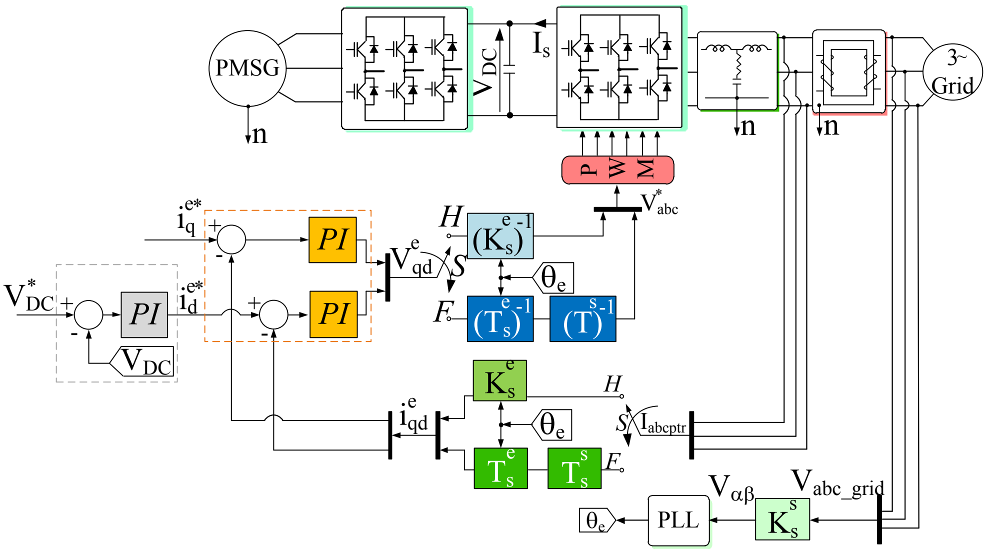

Figure 3.19 Block diagram for the fault tolerant control of the Grid- side converter.

The correct synchronous reference frame can be determined estimating the grid voltage vector angle, by means of PLL.

A. Modeling of the grid side circuit in phase variables

The modeling of the grid side circuit has been made assuming that the system is healthy and balanced, thus the single phase equivalent circuit in phase variables can be adopted as shown in Figure 3.20.

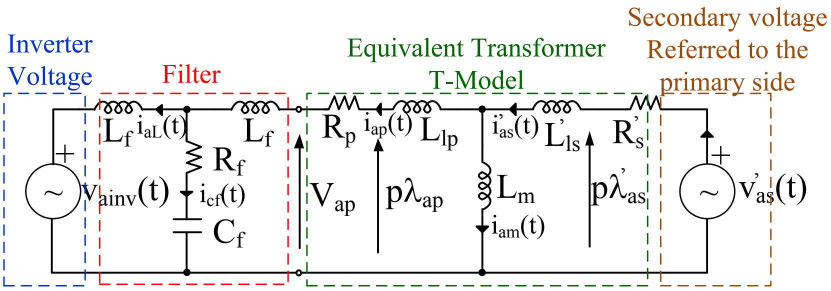

Figure 3.20 Single phase equivalent circuit relative to the phase "a" of the system: inverter, filter and transformer.

The equation in a complex form is:

$$\mathbf{v}_{abcinv} = -\mathbf{L}_f \left(p\, \mathbf{i}_{abcL} + p\, \mathbf{i}_{abcp}\right) + \mathbf{v}_{abcp} \qquad (3.2.3.6)$$

$(\mathbf{v}_{abcinv})^T = \left[\, v_{ainv} \;\; v_{binv} \;\; v_{cinv} \,\right]$ $\qquad (\mathbf{v}_{abcp})^T = \left[\, v_{ap} \;\; v_{bp} \;\; v_{cp} \,\right]$

$(\mathbf{i}_{abcp})^T = \left[\, i_{ap} \;\; i_{bp} \;\; i_{cp} \,\right]$ $\qquad (\mathbf{i}_{abcL})^T = \left[\, v_{aL} \;\; v_{bL} \;\; v_{cL} \,\right]$

$$\mathbf{L}_f = \begin{bmatrix} L_f & 0 & 0 \\ 0 & L_f & 0 \\ 0 & 0 & L_f \end{bmatrix}$$

$\mathbf{v}_{abcinv}$ is the vector of the fundamental equivalent voltage generated by the inverter;

$\mathbf{v}_{abcp}$ is the vector of the voltage at the primary side of the transformer;

$\mathbf{i}_{abcp}$ is the vector of the currents flowing at the primary side of the transformer;

$\mathbf{i}_{abcL}$ is the vector of the currents flowing along the filter inductance matrix $\mathbf{L}_f$;

The model of the transformer is that one with the secondary parameters, indicated with the subscript "s", referred to the primary side, indicated with the superscript "'", defining the so called "T" model.

$$\begin{cases} \mathbf{v}_{abcp} = -\mathbf{r}_p\, \mathbf{i}_{abcs} + p\, \boldsymbol{\lambda}_{abcp} \\ \mathbf{v}'_{abcs} = \mathbf{r}'_s\, \mathbf{i}'_{abcs} + p\, \boldsymbol{\lambda}'_{abcs} \end{cases} \qquad (3.2.3.7)$$

$$\begin{bmatrix} \lambda_{abcp} \\ \lambda'_{abcs} \end{bmatrix} = \begin{bmatrix} \mathbf{L_p} & \mathbf{L'_{ps}} \\ (\mathbf{L'_{ps}})^T & \mathbf{L'_s} \end{bmatrix} \begin{bmatrix} -\mathbf{i}_{abcp} \\ \mathbf{i}'_{abcs} \end{bmatrix} \qquad (3.2.3.8)$$

$$\mathbf{r_p} = \begin{bmatrix} R_p & 0 & 0 \\ 0 & R_p & 0 \\ 0 & 0 & R_p \end{bmatrix} \quad \mathbf{r'_s} = \begin{bmatrix} R'_s & 0 & 0 \\ 0 & R'_s & 0 \\ 0 & 0 & R'_s \end{bmatrix}$$

$$\mathbf{L_p} = \begin{bmatrix} L_{lp} + L_m & -\frac{1}{2}L_m & -\frac{1}{2}L_m \\ -\frac{1}{2}L_m & L_{lp} + L_m & -\frac{1}{2}L_m \\ -\frac{1}{2}L_m & -\frac{1}{2}L_m & L_{lp} + L_m \end{bmatrix}$$

$$\mathbf{L'_s} = \begin{bmatrix} L'_{ls} + L_m & -\frac{1}{2}L_m & -\frac{1}{2}L_m \\ -\frac{1}{2}L_m & L'_{ls} + L_m & -\frac{1}{2}L_m \\ -\frac{1}{2}L_m & -\frac{1}{2}L_m & L'_{ls} + L_m \end{bmatrix}$$

$$\mathbf{L'_{ps}} = \begin{bmatrix} L_m & -\frac{1}{2}L_m & -\frac{1}{2}L_m \\ -\frac{1}{2}L_m & L_m & -\frac{1}{2}L_m \\ -\frac{1}{2}L_m & -\frac{1}{2}L_m & L_m \end{bmatrix}$$

B. Modeling of the grid side circuit in the qd0 reference frame

Applying the transformation matrix $\mathbf{K_X}$ and $\mathbf{K_X^{-1}}$, below reported for simplicity, from the equations (3.2.3.6) can be obtained equation (3.2.3.9). For the decoupled control of the power it is assumed that the qd0 reference frame is synchronously rotating with the grid voltage, $\gamma_X = \theta - \theta_X = \theta_e$.

$$\mathbf{K_X} = \frac{2}{3} \begin{bmatrix} \cos\gamma_X & \cos\left(\gamma_X - \frac{2\pi}{3}\right) & \cos\left(\gamma_X + \frac{2\pi}{3}\right) \\ \sin\gamma_X & \sin\left(\gamma_X - \frac{2\pi}{3}\right) & \sin\left(\gamma_X + \frac{2\pi}{3}\right) \\ \frac{1}{2} & \frac{1}{2} & \frac{1}{2} \end{bmatrix}$$

$$\mathbf{K}_X^{-1} = \begin{bmatrix} \cos\gamma_X & \sin\gamma_X & 1 \\ \cos\left(\gamma_X - \frac{2\pi}{3}\right) & \sin\left(\gamma_X - \frac{2\pi}{3}\right) & 1 \\ \cos\left(\gamma_X + \frac{2\pi}{3}\right) & \sin\left(\gamma_X + \frac{2\pi}{3}\right) & 1 \end{bmatrix}$$

$$\mathbf{v}_{qd0inv} = -\mathbf{L}_f\,(p\,\mathbf{i}_{qd0L} + \mathbf{W}_r\,\mathbf{i}_{qd0L} + p\,\mathbf{i}_{qd0p} + \mathbf{W}_r\,\mathbf{i}_{qd0p}) + \mathbf{v}_{qd0p} \qquad (3.2.3.9)$$

$$(\mathbf{v}_{qd0inv})^T = \begin{bmatrix} v_{qinv} & v_{dinv} & v_{0inv} \end{bmatrix} \qquad (\mathbf{v}_{qd0p})^T = \begin{bmatrix} v_{qp} & v_{dp} & v_{0p} \end{bmatrix}$$

$$(\mathbf{i}_{qd0L})^T = \begin{bmatrix} i_{qL} & i_{dL} & i_{0L} \end{bmatrix} \qquad (\mathbf{i}_{qd0p})^T = \begin{bmatrix} i_{qL} & i_{dL} & i_{0L} \end{bmatrix}$$

$$\mathbf{W}_r = \begin{bmatrix} 0 & \omega_e & 0 \\ -\omega_e & 0 & 0 \\ 0 & 0 & 0 \end{bmatrix}$$

The vector “$\mathbf{v}_{qd0p}$” represents the voltages at the transformer terminals connected to the filter and is obtained applying $\mathbf{K}_X$ and $\mathbf{K}_X^{-1}$ at the transformer equations (3.2.3.7) and (3.2.3.8), achieving (3.2.3.10) and (3.2.3.11).

$$\begin{cases} \mathbf{v}_{qd0p} = -\mathbf{r}_p\,\mathbf{i}_{qd0p} + p\,\boldsymbol{\lambda}_{qd0p} + \mathbf{W}_r\,\boldsymbol{\lambda}_{qd0p} \\ \mathbf{v}'_{qd0s} = \mathbf{r}'_s\,\mathbf{i}'_{qd0s} + p\,\boldsymbol{\lambda}'_{qd0s} + \mathbf{W}_r\,\boldsymbol{\lambda}'_{qd0s} \end{cases} \qquad (3.2.3.10)$$

$$\begin{bmatrix} \boldsymbol{\lambda}_{qd0p} \\ \boldsymbol{\lambda}'_{qd0s} \end{bmatrix} = \begin{bmatrix} \mathbf{L}_{pqd0} & \mathbf{L}'_{psqd0} \\ (\mathbf{L}'_{psqd0})^T & \mathbf{L}'_{sqd0} \end{bmatrix} \begin{bmatrix} -\mathbf{i}_{qd0p} \\ \mathbf{i}'_{qd0s} \end{bmatrix} \qquad (3.2.3.11)$$

The inductance matrices: $\mathbf{L}_{pqd0}$, $\mathbf{L}'_{psqd0}$, $(\mathbf{L}'_{psqd0})^T$ and $\mathbf{L}'_{sqd0}$) are expressed as below reported:

$$\mathbf{L}_{pqd0} = \begin{bmatrix} L_{lp}+L_M & 0 & 0 \\ 0 & L_{lp}+L_M & 0 \\ 0 & 0 & L_{lp} \end{bmatrix}$$

$$\mathbf{L}'_{psqd0} = (\mathbf{L}'_{psqd0})^T = \begin{bmatrix} L_M & 0 & 0 \\ 0 & L_M & 0 \\ 0 & 0 & 0 \end{bmatrix}$$

$$\mathbf{L}'_{sqd0} = \begin{bmatrix} L'_{ls}+L_M & 0 & 0 \\ 0 & L'_{ls}+L_M & 0 \\ 0 & 0 & L'_{ls} \end{bmatrix}$$

$$L_M = \frac{3}{2}L_m$$

Taking in to account the equation (3.2.3.9) and substituting the equations of the transformer (3.2.3.10) can be obtained (3.2.3.12):

$$\begin{aligned} \mathbf{v}_{qd0inv} = &-\mathbf{L}_f\,(p\,\mathbf{i}_{qd0L} + \mathbf{W}_r\,\mathbf{i}_{qd0L} + p\,\mathbf{i}_{qd0p} + \mathbf{W}_r\,\mathbf{i}_{qd0p}) - \mathbf{r}_p\,\mathbf{i}_{qd0p} + \\ &+ p\,\boldsymbol{\lambda}_{qd0p} + \mathbf{W}_r\,\boldsymbol{\lambda}_{qd0p} \end{aligned} \tag{3.2.3.12}$$

Substituting also the expression of the derivative of the flux in terms of currents and remembering that the zero sequence components of the electrical variables are steadily zero because we are assuming to operate with balanced systems, the last equations can be omitted from the following expressions:

$$\begin{aligned} v_{qinv} = &-L_f\,(p\,i_{qL} + \omega_e\,i_{dL} + p\,i_{qp} + \omega_e\,i_{dp}) - R_p\,i_{qp} - L_p\,p\,i_{qp} + \\ &+ L_M\,p\,i_{qs} + \omega_e\,\lambda_{dp} \end{aligned} \tag{3.2.3.13}$$

$$\begin{aligned} v_{dinv} = &-L_f\,(p\,i_{dL} - \omega_e\,i_{qL} + p\,i_{dp} - \omega_e\,i_{qp}) - R_p\,i_{dp} - L_p\,p\,i_{dp} + \\ &+ L_M\,p\,i_{ds} - \omega_e\,\lambda_{qp} \end{aligned} \tag{3.2.3.14}$$

Solving respectively for $p\,i_{qp}$ and $p\,i_{dp}$, the final expression are:

$$\begin{aligned} (L_f + L_p)pi_{qp} = &- v_{qinv} - R_pi_{qp} - L_f\,p\,i_{qL} - L_f\,\omega_e\,i_{dL} - L_f\,\omega_e\,i_{dp} + \\ &+ \omega_e\,\lambda_{dp} + L_M\,p\,i_{qs} \end{aligned} \tag{3.2.3.15}$$

$$\begin{aligned} (L_f + L_p)pi_{dp} = &- v_{dinv} - R_pi_{dp} - L_f\,p\,i_{dL} + L_f\,\omega_e\,i_{qL} + L_f\,\omega_e\,i_{qp} + \\ &- \omega_e\,\lambda_{qp} + L_M\,p\,i_{ds} \end{aligned} \tag{3.2.3.16}$$

The controller tuning is performed considering the perfect decoupling of all the terms in order to obtain a classical first order RL circuit, as shown with Figure 3.21 and Figure 3.22, where the equations (3.2.3.15) and(3.2.3.16) are expressed in Laplace domain considering the initial conditions set to 0.

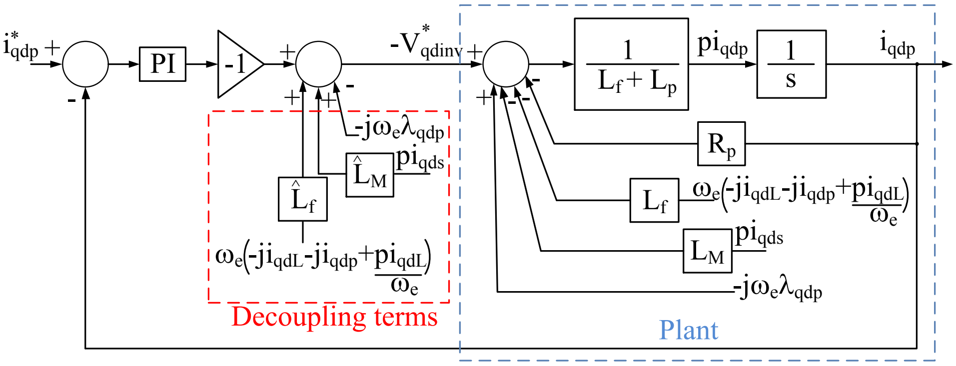

Figure 3.21 Block diagram for the representation of equation(3.2.3.15) and (3.2.3.16) in complex notation.

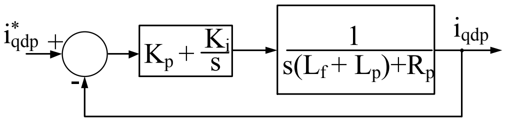

Figure 3.22 Equivalent representation of Figure 3.21 considering a perfect decoupling of cross-coupled terms.

From Figure 3.22 the closed loop transfer function of the system can easily be obtained and determine the value of K_p and K_i.

$$K_p = (L_f+L_p)(P_1 + P_2)-R_p \tag{3.2.3.17}$$

$$K_i = (L_f+L_p)P_1P_2 \tag{3.2.3.18}$$

P_1 and P_2 are the poles associated to the desired frequency $P_1=2\pi f_1$ and $P_2=2\pi f_2$ usually can be set $f_2 = (5\div 10)\ f_1$.

For a more precise tuning process it is important to consider that the entire system is simulated in a discrete domain and implemented using digital controllers, hence the model should be referred in the Z domain; in addition, also the inverter has to be included in the model and could be seen as a “Latch” interface [41].

C. LCL Filter Design

The design of the line filter considered in the configuration reported in Figure 3.19, results almost complex including also the transformer, that is the “load” of the filter on the transfer function. Hence, a simplified transfer function of the filter considered at no load has been used to design L_f, C_f and R_f

$$\frac{V_{ap}}{V_{ainv}} = \frac{sC_f R_f + 1}{s^2\ C_f L_f + s\ C_f R_f + 1} \tag{3.2.3.19}$$

Solving the denominator of the transfer function by imposing the desired poles, functions of the cut-off frequencies, f_{1f} and f_{2f}, we obtain:

$$L_f = \frac{1}{P_{1f} P_{2f} C_f}$$

$$R_f = (P_{1f} + P_{2f})L_f$$

With $C_f = 4.7\mu F$ and $P_{1f} = 2\ \pi\ f_{1f}$ and $P_{2f} = 2\ \pi\ f_{2f}$ with $f_{1f} = 300$ and $f_{2f} = 3000$ are obtained: $L_f = 6mH$; $R_f = 124\ \Omega$

D. Modeling of the grid side circuit with an open phase fault in phase and qd0 variables

When a fault occurs on a phase or an inverter leg it will be isolated hence the converter, the filter and the transformer will work only with two phases. The equation (3.2.3.6) that describes the healthy system will be modified as reported in (3.2.3.20) in a complex form.

$$\mathbf{v}_{ijinv} = -\mathbf{L}_{ff}\,(p\ \mathbf{i}_{ijL} + p\ \mathbf{i}_{ijp}) + \mathbf{v}_{ijp} \tag{3.2.3.20}$$

$(\mathbf{v}_{ijinv})^T = [\ v_{iinv}\ \ v_{jinv}\ ]$ $\quad (\mathbf{v}_{ijp})^T = [\ v_{ip}\ \ v_{jp}\ ]$

$(\mathbf{i}_{ijp})^T = [\ i_{ip}\ \ i_{jp}\ ]$ $\quad (\mathbf{i}_{ijL})^T = [\ v_{iL}\ \ v_{jL}\ ]$

$$\mathbf{L}_{ff} = \begin{bmatrix} L_f & 0 \\ 0 & L_f \end{bmatrix}$$

$$(i, j) = \begin{cases} \text{b,c fault primary side phase a} \\ \text{a,c fault primary side phase b} \\ \text{a,b fault primary side phase c} \end{cases}$$

For the transformer, also in this case, all the quantities indicated with the subscript “p” are of the primary side while that one indicated with the subscript “s” are of the secondary side.

For simplicity, for equations (3.2.3.21) and (3.2.3.22) it is assumed that the currents go in the primary and secondary side of the transformer, setting the positive sign.

$$\begin{cases} \mathbf{v}_{ijp} = \mathbf{r}_{pf}\,\mathbf{i}_{ijp} + p\ \boldsymbol{\lambda}_{ijp} \\ \mathbf{v}'_{abcs} = \mathbf{r}'_s\,\mathbf{i}'_{abcs} + p\ \boldsymbol{\lambda}'_{abcs} \end{cases} \tag{3.2.3.21}$$

$$\begin{bmatrix} \boldsymbol{\lambda}_{ijp} \\ \boldsymbol{\lambda}'_{abcs} \end{bmatrix} = \begin{bmatrix} \mathbf{L}_{pf} & \mathbf{L}'_{psf} \\ (\mathbf{L}'_{psf})^T & \mathbf{L}'_s \end{bmatrix} \begin{bmatrix} \mathbf{i}_{ijp} \\ \mathbf{i}'_{abcs} \end{bmatrix} \tag{3.2.3.22}$$

The secondary side variables have been referred to the primary side, this is indicated with the superscript “'”.

$$\mathbf{r}_{pf} = R_p \begin{bmatrix} 1 & 0 \\ 0 & 1 \end{bmatrix}$$

$$\mathbf{L}_{pf} = \begin{bmatrix} L_{lp} + L_m & -\frac{1}{2} L_m \\ -\frac{1}{2} L_m & L_{lp} + L_m \end{bmatrix}$$

$$\mathbf{L}'_{psf} = L_m \begin{bmatrix} \cos(\alpha) & \cos(\beta) & \cos(\gamma) \\ \cos(\delta) & \cos(\phi) & \cos(\rho) \end{bmatrix}$$

$$\begin{array}{c} (\alpha,\beta,\gamma) \\ (\delta,\phi,\rho) \end{array} = \begin{cases} \begin{array}{l} \frac{2\pi}{3}, 0, \frac{2\pi}{3} \\ \frac{2\pi}{3}, \frac{2\pi}{3}, 0 \end{array} & \text{fault primary side phase a} \\ \begin{array}{l} 0, \frac{2\pi}{3}, \frac{2\pi}{3} \\ \frac{2\pi}{3}, \frac{2\pi}{3}, 0 \end{array} & \text{fault primary side phase b} \\ \begin{array}{l} 0, \frac{2\pi}{3}, \frac{2\pi}{3} \\ \frac{2\pi}{3}, 0, \frac{2\pi}{3} \end{array} & \text{fault primary side phase c} \end{cases} \qquad (3.2.3.23)$$

The inductance matrix $\mathbf{L}'_s$ is not changing because the secondary side is healthy.

The qd0 model is obtained following the same approach discussed in Chapter 1, Paragraph 1.2.1 E. adopting the convention $f_d + jf_q$.

The qd0 transformation of equation (3.2.3.20) is almost simple since it does not contain cross-coupled terms and can be written as follow, on a stationary reference frame with the matrix T^s_s:

$$\mathbf{v}^s_{dqinv} = -T^s_s \mathbf{L}_{ff} \left[p\left((T^s_s)^{-1}\, \mathbf{i}^s_{dqL}\right) + p\left((T^s_s)^{-1}\, \mathbf{i}^s_{dqp}\right))\right] + T^s_s\,(T^s_s)^{-1}\,\mathbf{v}^s_{dqp} \qquad (3.2.3.24)$$

The transformation matrix T^s_s is obtained from a set of eigenvectors associated to the eigenvalues of the matrix $\mathbf{L}_{pf}$ keeping out the leakage inductance.

For fault of phase a and c:

$$T_s^s = \frac{\sqrt{2}}{2}\begin{bmatrix} 1 & -1 \\ 1 & 1 \end{bmatrix}$$

$$(T_s^s)^{-1} = \frac{\sqrt{2}}{2}\begin{bmatrix} 1 & 1 \\ -1 & 1 \end{bmatrix} \qquad (3.2.3.25)$$

For fault of phase b:

$$T_s^s = (T_s^s)^{-1} = \frac{\sqrt{2}}{2}\begin{bmatrix} -1 & 1 \\ 1 & 1 \end{bmatrix} \qquad (3.2.3.26)$$

Equation (3.2.3.24) since T_s^s contains constant terms, becomes:

$$\mathbf{v}_{dqinv}^s = -T_s^s \mathbf{L}_{ff} (T_s^s)^{-1} (p\, \mathbf{i}_{dqL}^s + p\, \mathbf{i}_{dqp}^s) + \mathbf{v}_{dqp}^s \qquad (3.2.3.27)$$

$$\mathbf{T}_s^s\, \mathbf{L}_{ff}\, (\mathbf{T}_s^s)^{-1} = L_f \begin{bmatrix} 1 & 0 \\ 0 & 1 \end{bmatrix} = \mathbf{L}_{ff}$$

Now the attention is given to the modeling of the transformer, where the primary side equations will be transformed with T_s^s while the secondary side equations, since they describe a balanced three-phase system, will be transformed with the standard transformation matrix K_s^s.

$$K_s^s = \sqrt{\frac{2}{3}}\begin{bmatrix} 1 & -\frac{1}{2} & -\frac{1}{2} \\ 0 & \frac{\sqrt{3}}{2} & -\frac{\sqrt{3}}{2} \\ \frac{1}{\sqrt{2}} & \frac{1}{\sqrt{2}} & \frac{1}{\sqrt{2}} \end{bmatrix}$$

$$(3.2.3.28)$$

$$(K_s^s)^{-1} = \sqrt{\frac{2}{3}}\begin{bmatrix} 1 & 0 & \frac{1}{\sqrt{2}} \\ -\frac{1}{2} & \frac{\sqrt{3}}{2} & \frac{1}{\sqrt{2}} \\ -\frac{1}{2} & -\frac{\sqrt{3}}{2} & \frac{1}{\sqrt{2}} \end{bmatrix}$$

The constant gain $\sqrt{\frac{2}{3}}$ allows to have a so called “power invariant” transformation.

$$\begin{cases} \mathbf{v}^{s}_{dqp} = \mathbf{T}^{s}_{s}\, \mathbf{r}_{pf}\, (\mathbf{T}^{s}_{s})^{-1}\, \mathbf{i}^{s}_{dqp} + \mathbf{T}^{s}_{s}\, p\left[\, (\mathbf{T}^{s}_{s})^{-1}\, \lambda^{s}_{dqp} \right] \\ \mathbf{v}'^{s1}_{dqs} = \mathbf{K}^{s}_{s}\, \mathbf{r}'_{s}\, (\mathbf{K}^{s}_{s})^{-1}\, \mathbf{i}'^{s1}_{dqs} + \mathbf{K}^{s}_{s}\, p\left[\, (\mathbf{K}^{s}_{s})^{-1}\, \lambda'^{s1}_{dqs} \right] \end{cases} \qquad (3.2.3.29)$$

$$\begin{bmatrix} \lambda^{s}_{dqp} \\ \lambda'^{s1}_{dqs} \end{bmatrix} = \begin{bmatrix} \mathbf{T}^{s}_{s}\mathbf{L}_{pf}(\mathbf{T}^{s}_{s})^{-1} & \mathbf{T}^{s}_{s}\mathbf{L}'_{psf}\,(\mathbf{K}^{s}_{s})^{-1} \\ \mathbf{K}^{s}_{s}\,(\mathbf{L}'_{psf})^{T}\,(\mathbf{T}^{s}_{s})^{-1} & \mathbf{K}^{s}_{s}\,\mathbf{L}'_{s}\,(\mathbf{K}^{s}_{s})^{-1} \end{bmatrix} \begin{bmatrix} \mathbf{i}^{s}_{dqp} \\ \mathbf{i}'^{s1}_{d\,qs} \end{bmatrix} \qquad (3.2.3.30)$$

The equations (3.2.3.29) and (3.2.3.30) are below verified neglecting the 0-axis, that could be included for the secondary side:

$$\mathbf{T}^{s}_{s}\, \mathbf{r}_{pf}\, (\mathbf{T}^{s}_{s})^{-1} = R_{p} \begin{bmatrix} 1 & 0 \\ 0 & 1 \end{bmatrix} = \mathbf{r}_{pf}$$

$$\mathbf{T}^{s}_{s}\, p\left[\, (\mathbf{T}^{s}_{s})^{-1}\, \lambda^{s}_{dqs} \right] = p\, \lambda^{s}_{dqs}$$

$$\mathbf{K}^{s}_{s}\, \mathbf{r}'_{s}\, (\mathbf{K}^{s}_{s})^{-1} = R'_{s} \begin{bmatrix} 1 & 0 \\ 0 & 1 \end{bmatrix} = \mathbf{r}'_{s}$$

$$\mathbf{K}^{s}_{s}\, p\left[\, (\mathbf{K}^{s}_{s})^{-1}\, \lambda'^{r}_{dqs} \right] = p\, \lambda'^{r}_{dqs}$$

$$\mathbf{L}_{pp} = \mathbf{T}^{s}_{s}\, \mathbf{L}_{pf}\, (\mathbf{T}^{s}_{s})^{-1} = \begin{bmatrix} Ll_{p} + \frac{3}{2}L_{m} & 0 \\ 0 & Ll_{p} + \frac{1}{2}L_{m} \end{bmatrix}$$

$$\mathbf{L}_{psf} = \mathbf{T}^{s}_{s}\, \mathbf{L}'_{psf}\, (\mathbf{K}^{s}_{s})^{-1} = \begin{bmatrix} 0 & \frac{3}{2}L_{m} \\ -\frac{\sqrt{3}}{2}L_{m} & 0 \end{bmatrix}$$ fault on phase a

$$\mathbf{K}^{s}_{s}\, (\mathbf{L}'_{psf})^{T}\, (\mathbf{T}^{s}_{s})^{-1} = (\mathbf{L}_{psf})^{T}$$

$$\mathbf{L}_{psf} = \mathbf{T}^{s}_{s}\, \mathbf{L}'_{psf}\, (\mathbf{K}^{s}_{s})^{-1} = \begin{bmatrix} -\frac{3\sqrt{3}}{4}L_{m} & -\frac{3}{4}L_{m} \\ \frac{\sqrt{3}}{4}L_{m} & -\frac{3}{4}L_{m} \end{bmatrix}$$ fault on phase b

$$\mathbf{K}^{s}_{s}\, (\mathbf{L}'_{psf})^{T}\, (\mathbf{T}^{s}_{s})^{-1} = (\mathbf{L}_{psf})^{T}$$

$$\mathbf{L}_{psf} = \mathbf{T}^{s}_{s}\, \mathbf{L}'_{psf}\, (\mathbf{K}^{s}_{s})^{-1} = \begin{bmatrix} \frac{3\sqrt{3}}{4}L_{m} & -\frac{3}{4}L_{m} \\ \frac{\sqrt{3}}{4}L_{m} & \frac{3}{4}L_{m} \end{bmatrix}$$ fault on phase c

$$\mathbf{K}_s^s\,(\mathbf{L}'_{psf})^T\,(\mathbf{T}_s^s)^{-1} = (\mathbf{L}_{psf})^T$$

$$\mathbf{L}_{ss} = \mathbf{K}_s^s\,\mathbf{L}'_s\,(\mathbf{K}_s^s)^{-1} = \begin{bmatrix} Ll_s + \frac{3}{2}L_m & 0 \\ 0 & Ll_s + \frac{3}{2}L_m \end{bmatrix}$$

Then, the secondary side variables refer to the stationary reference frame of the primary side by exploiting the following K_s^p matrix, because the matrices $\mathbf{L}_{psf}$ are not diagonals:

$$\mathbf{v}'^{s}_{dqs} = K_s^p\,\mathbf{v}'^{s1}_{dqs}$$

$$\mathbf{i}'^{s}_{dqs} = K_s^p\,\mathbf{i}'^{s1}_{dqs}$$

$$K_s^p = \begin{bmatrix} \cos(\alpha) & -\sin(\alpha) \\ \sin(\alpha) & \cos(\alpha) \end{bmatrix} \qquad (K_s^p)^{-1} = \begin{bmatrix} \cos(\alpha) & \sin(\alpha) \\ -\sin(\alpha) & \cos(\alpha) \end{bmatrix} \tag{3.2.3.31}$$

$$\alpha = \begin{cases} -\frac{\pi}{2} & \text{phase a-fault} \\ \frac{5\pi}{6} & \text{phase b-fault} \\ \frac{\pi}{6} & \text{phase c-fault} \end{cases} \tag{3.2.3.32}$$

$$\begin{cases} \mathbf{v}^{s}_{dqp} = \mathbf{r}_{pf}\,\mathbf{i}^{s}_{dqp} + p\,\lambda^{s}_{dqp} \\ \mathbf{v}'^{s}_{dqs} = \mathbf{K}_s^p\,\mathbf{r}'_s\,(\mathbf{K}_s^p)^{-1}\,\mathbf{i}'^{s}_{dqs} + \mathbf{K}_s^p\,p\left[\,(\mathbf{K}_s^p)^{-1}\lambda'^{s}_{dqs}\,\right] \end{cases} \tag{3.2.3.33}$$

$$\begin{bmatrix} \lambda^{s}_{dqp} \\ \lambda'^{r}_{dqs} \end{bmatrix} = \begin{bmatrix} \mathbf{L}_{pp} & \mathbf{L}_{psf}\,(\mathbf{K}_s^p)^{-1} \\ \mathbf{K}_s^p\,(\mathbf{L}_{psf})^T & \mathbf{K}_s^p\,\mathbf{L}_{ss}\,(\mathbf{K}_s^p)^{-1} \end{bmatrix} \begin{bmatrix} \mathbf{i}^{s}_{dqp} \\ \mathbf{i}'^{s}_{dqs} \end{bmatrix} \tag{3.2.3.34}$$

$$\mathbf{K}_s^p\,\mathbf{r}'_s\,(\mathbf{K}_s^p)^{-1} = \mathbf{r}'_s$$

$$\mathbf{K}_s^p\,p\left[\,(\mathbf{K}_s^p)^{-1}\lambda'^{s}_{dqs}\,\right] = p\,\lambda'^{s}_{dqs}$$

$$\mathbf{L}_{psf}\,(\mathbf{K}_s^p)^{-1} = \mathbf{K}_s^p\,(\mathbf{L}_{psf})^T = \begin{bmatrix} \frac{3}{2} L_{ms} & 0 \\ 0 & \frac{\sqrt{3}}{2} L_{ms} \end{bmatrix} \quad \text{for faults on phases: a,b or c.}$$

$$\mathbf{K}_s^p\,\mathbf{L}_{ss}\,(\mathbf{K}_s^p)^{-1} = \mathbf{L}_{ss}$$

To sum up, the final model on a dq stationary frame is reported below in scalar form

$$\begin{cases} v_{dp}^{s} = R_p\, i_{dp}^{s} + p\, \lambda_{dp}^{s} \\ v_{qp}^{s} = R_p\, i_{qp}^{s} + p\, \lambda_{qs}^{s} \\ v_{ds}^{\prime s} = R_s^{\prime}\, i_{ds}^{\prime s} + p\, \lambda_{ds}^{\prime s} \\ v_{qs}^{\prime s} = R_s^{\prime}\, i_{qs}^{\prime s} + p\, \lambda_{qs}^{\prime s} \end{cases} \tag{3.2.3.35}$$

$$\begin{cases} \lambda_{dp}^{s} = L_{lp}\, i_{dp}^{s} + M_d(i_{dp}^{s} + i_{ds}^{\prime s}) = L_d\, i_{dp}^{s} + M_d\, i_{ds}^{\prime s} \\ \lambda_{qp}^{s} = L_{lp}\, i_{qp}^{s} + M_q(\frac{i_{qp}^{s}}{\sqrt{3}} + i_{qs}^{\prime s}) = L_q\, i_{qp}^{s} + M_q\, i_{qs}^{\prime s} \\ \lambda_{ds}^{\prime s} = L_{ls}^{\prime}\, i_{ds}^{\prime s} + M_d(i_{ds}^{\prime s} + i_{dp}^{s}) = L_s^{\prime}\, i_{ds}^{\prime s} + M_d\, i_{dp}^{s} \\ \lambda_{qs}^{\prime s} = L_{ls}^{\prime}\, i_{qs}^{\prime s} + L_M(i_{qs}^{\prime s} + \sqrt{3}\frac{i_{qp}^{s}}{3}) = L_s^{\prime}\, i_{qs}^{\prime s} + M_q\, i_{qp}^{s} \end{cases} \tag{3.2.3.36}$$

$$L_d = L_{lp} + \frac{3}{2} L_m$$

$$L_q = L_{lp} + \frac{1}{2} L_m$$

$$L_s^{\prime} = L_{ls}^{\prime} + \frac{3}{2} L_m$$

$$M_d = L_M = \frac{3}{2} L_m$$

$$M_q = \frac{\sqrt{3}}{2} L_m$$

The aforementioned model looks like that one presented for IM under an open phase fault in Chapter 1.

The independent control of active and reactive power can be obtained also when the transformer works under unbalanced conditions, hence also in this case if the d-axis is aligned with the grid voltage, it is possible to realize a decoupled control of P and Q. The rotation matrix to transform the primary side current components, $\mathbf{i}^{s}_{dqp}$ from the stationary frame to the rotating frame synchronous with the grid voltage and vice versa are reported in (3.2.3.37) and (3.2.3.38).

$$\mathbf{i}^{e}_{dqp} = \mathbf{K}^{e}_{s}\,\mathbf{i}^{s}_{dqp}$$

$$(\mathbf{i}^{s}_{dqp})^{-1} = (\mathbf{K}^{e}_{s})^{-1}\,\mathbf{i}^{e}_{dqp}$$

$$\mathbf{K}^{e}_{s} = \begin{bmatrix} \sqrt{\frac{M_d}{M_q}}\cos(\theta_e) & \sqrt{\frac{M_q}{M_d}}\sin(\theta_e) \\ -\sqrt{\frac{M_d}{M_q}}\sin(\theta_e) & \sqrt{\frac{M_q}{M_d}}\cos(\theta_e) \end{bmatrix} \qquad (3.2.3.37)$$

$$(\mathbf{K}^{e}_{s})^{-1} = \begin{bmatrix} \sqrt{\frac{M_q}{M_d}}\cos(\theta_e) & -\sqrt{\frac{M_q}{M_d}}\sin(\theta_e) \\ \sqrt{\frac{M_d}{M_q}}\sin(\theta_e) & \sqrt{\frac{M_d}{M_q}}\cos(\theta_e) \end{bmatrix} \qquad (3.2.3.38)$$

At the end of this procedure, a representation similar to that of Figure 3.21 can be obtained, hence the same approach for the tuning of the current regulators can be followed considering the modeling process just proposed.

3.3 Simulation and experimental results

Simulations results of the proposed FT-WPS are presented in this section; the system simulated is composed of a 3kW three-phase PMSG, a 5kVA three-phase transformer with voltage ratio equal to 220V/380V and a capacitor bank of 3mF. The two electrical machines are the same as that used for the experimental test and their parameters are reported in Table 3.1 and Table 3.2.

Table 3.1 Generator Parameters.

Number of phases	3	Rated Current	6.4A
Pole Pairs	3	R_g	2.1Ω
Rated Voltage	345V	L_q	0.045H
Max Speed	3000rpm	L_d	0.028H
BEMF	84V/krpm	J	0.00105kgm^2

Table 3.2 Transformer Parameters.

Number of phases	3	R_p	0.71Ω
Rated power	5000VA	R_s'	0.5Ω
Rated primary voltage	220V	$L_{lp}=L_{ls}'$	0.00113H
Rated secondary voltage	380V	L_m	1.8H

Figure 3.23 and Figure 3.24 show the behavior of the whole system in case of normal operative conditions, i.e. all components are healthy. In addition, the SVM with a switching frequency of 10kHz is used for both the Generator side and Grid side converters, the additional switches are kept open and the neutral point of the stator windings of PMSG, transformer and of the filter are isolated. The sample frequency of the simulation is set to 1MHz.

Figure 3.23 shows the dynamic performances of the Generator Side system where the PMSG is controlled as indicated in Figure 3.18, the inner current loop has been tuned for 400Hz while the speed outer loop for 10Hz; at the beginning, because the capacitor bank has an initial voltage of 800V, the PMSG starts following a speed ramp profile from stand-still to 20rad/s at no load working as a motor, at 0.1s a torque step of -5Nm, 25% of the rated torque, is applied and the PMSG starts to work as a generator delivering power to the grid. The load step is then followed by a speed step at 0.2s from 20 to 100 rad/s and at the end of the simulation another torque step equal to -10Nm, 50% of the rated torque, is applied. The previous speed and torque command are used to evaluate the performances of the PMSG and as expected it is possible to note the decoupled control of the qd axis current components, leading to decoupled torque and flux controls; in this case the flux current component, is set to 0 and the air-gap flux is primarily provided by the permanent magnet.

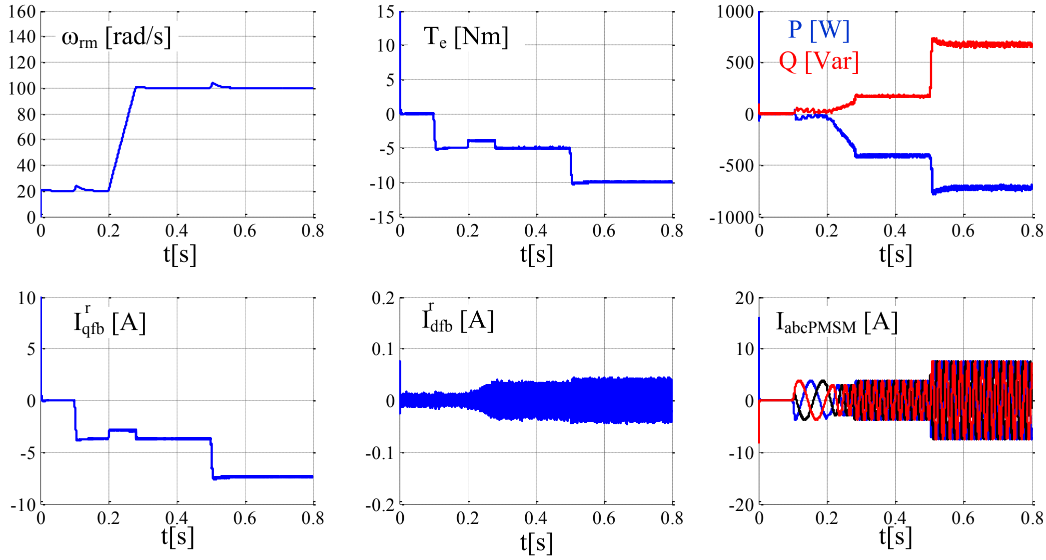

Figure 3.23 Performance evaluation of the PMSG control in healthy condition.

Figure 3.24 shows the Grid side system behavior during the PMSG operative condition of Figure 3.23; the grid side converter is controlled as shown in Figure 3.19, hence the dc bus voltage is kept constant at 800V thanks to the voltage loop exploited also to deliver the active power to the grid, using the d-axis current, while the q-axis current is directly set to zero although it can be used with an additional control loop to control the reactive power.

The phase currents are measured after the LCL filter at the primary side of the transformer and in addition, also the secondary currents are shown in this figure and their transient behavior is due to the direct connection to an ideal-three phase grid.

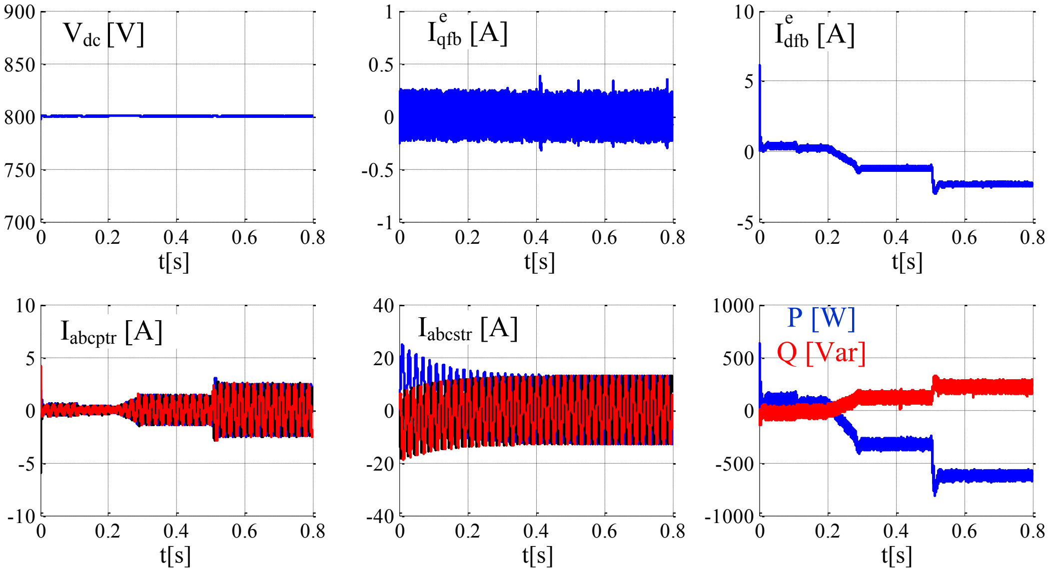

Figure 3.24 Performance evaluation of the Grid Side system control.

Figure 3.25 and Figure 3.26 show the results obtained with the PMSG working with a fault on the phase c; the neutral point of the PMSG stator windings is connected directly to the neutral point of the primary windings of the transformer and the neutral point of the filter. Figure 3.25 shows the rotor speed, the electromagnetic torque, the d-axis current component and the phase currents, one of these, I_{cPMSM}=0 while the other two are shifted by 60°.

Figure 3.26 shows the voltage on the dc-link capacitor bank that is kept constant at the required value, the phase currents at the primary side of the transformer that are modulated by the neutral current produced by the faulty PMSG, and the currents at the secondary side of the transformer that are not influenced by I_{og}; this last one is also shown together with the neutral current flowing on the filter, $I_{ofilter}$, and on the transformer, I_{otr}. As before discussed, the impedance of the transformer is lower than that one of the filter, hence all the neutral current I_{og} is flowing through the transformer windings.

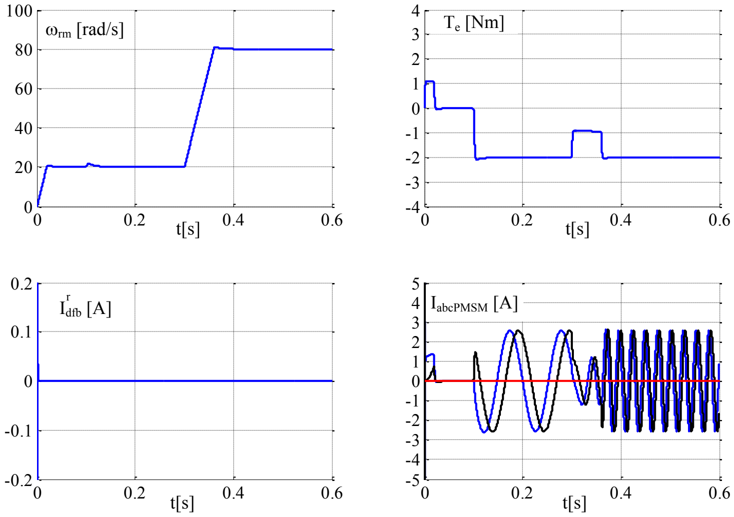

Figure 3.25 Performance evaluation of the PMSG control under phase c fault.

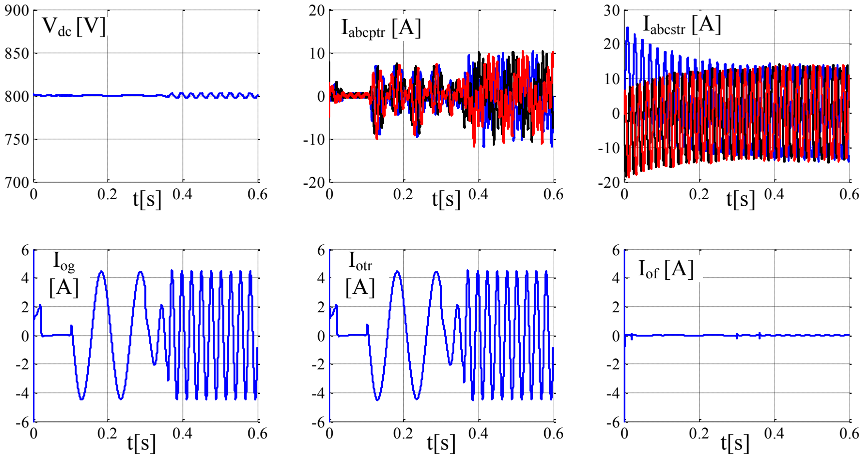

Figure 3.26 Performance evaluation of the Grid side system under phase c fault on the PMSM.

After these numerical simulations, some experiments have been conducted with the system setup shown in Figure 3.27, consisting of two back to back connected three-phase inverters supplied by a common DC bus limited to 300V. For some tests an external DC bus has been used. The fault tolerant control algorithms for the PMSG as well as for the transformer side converters have been implemented on a single DSP board.

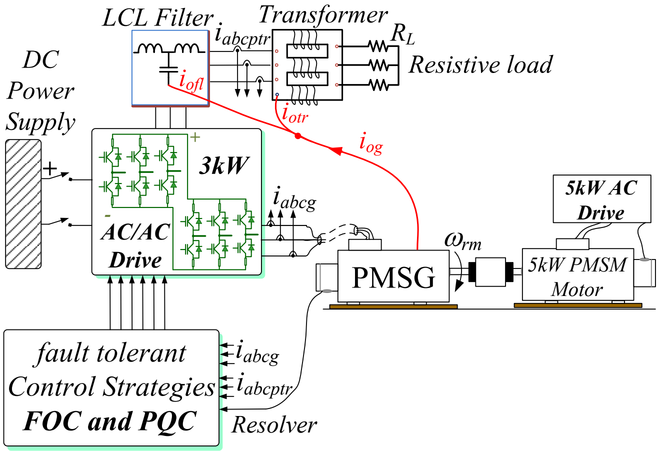

Figure 3.27 Block diagram of the experimental setup.

The modulation strategy is the S-PWM to avoid additional third harmonic components circulation due to the connection of the generator, transformer and LCL filter neutral points . For the following tests the secondary side of the transformer is connected to a variable resistive load.

The test reported in Figure 3.28 has been conducted to verify the presence of a third harmonic current due to the connection of the neutral points although the PMSG was healthy, while the transformer converter was modulating at 0.5. The PMSG works without load to emphasize the distortion of the phase currents as shown in Figure 3.28 a), while Figure 3.28 b) shows the benefit obtained thanks to the compensation of the third harmonic current. The compensation has been performed summing a suitable zero sequence voltage to the voltage reference provided by the vector control, PI current regulators; Figure 3.29 shows the ratio between the third harmonic voltage V_3 required for the compensation and the fundamental voltage V_1 at different rotational speed; in addition, also the phase of V_3 is reported, this test has been performed also at different load conditions obtaining almost similar results to that one here shown in case of maximum load. It can be observed from Figure 3.29 a) that at high rotational speed the amplitude of the additional voltage is about 10% of the fundamental one.

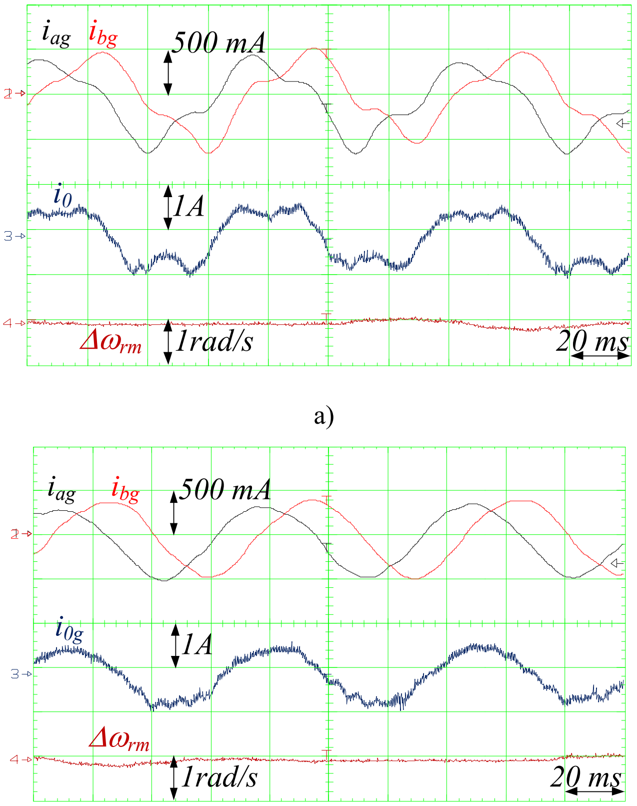

a)

b)

Figure 3.28 Steady state tests with ω_{rm}=30 rad/s: phase currents, i_{og} and rotational speed ripple in the PMSG without a) and with b) third harmonic compensation.

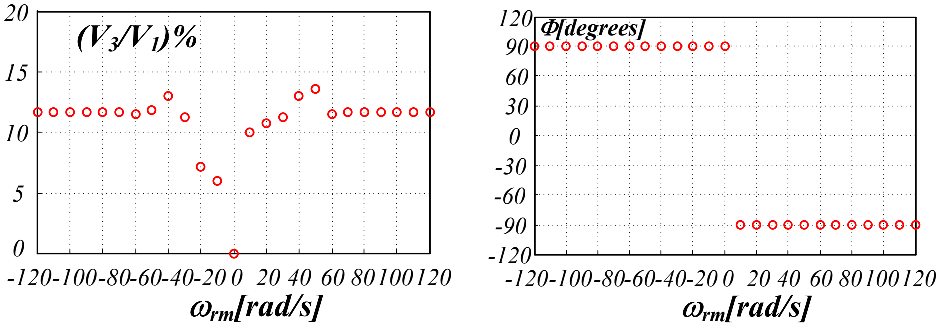

a) b)

Figure 3.29 Steady state tests: a)amplitude ratio V_3/V_1 and b) phase shift of the third harmonic compensation voltages.

Figure 3.30 is carried out with the PMSG operating with phase c fault, running at 50 rad/s with 50% of the rated load, while the transformer is fed on the primary side with a fundamental line to line voltage V_{LL} = 135V and frequency corresponding to the rated magnetizing flux and the secondary side is connected to a symmetrical resistive load of 20Ω. The waveforms shown represent the neutral currents that are flowing from the faulty generator to the transformer and the filter; as expected and already seen in simulation, the filter impedance is higher than that one of the transformer hence almost all the neutral current is flowing on the transformer windings. The effect of the neutral current on the transformer is verified with the results reported in Figure 3.31, as already known, and proved for a MDS, this current affects only the zero sequence circuit and because the primary and the secondary transformer zero sequence circuits are not coupled, the secondary side will be not affected by this current. For this test the PMSG is running at 30 rad/s and the external power supply is used to keep constant the DC bus voltage at 300V while the transformer is supplied at zero voltage setting a modulation index of 0.5.

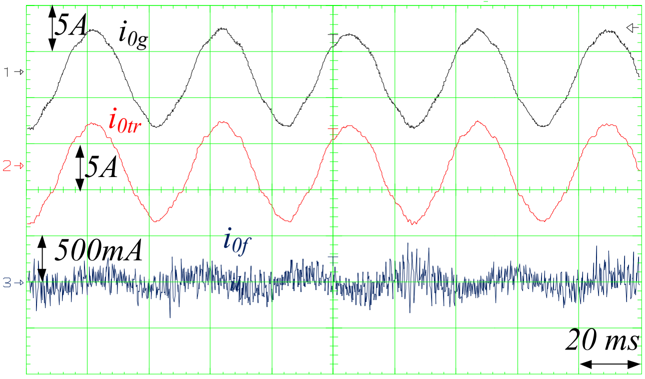

Figure 3.30 Steady state test with the generator operating under an open phase: comparison of the zero sequence crurrent flowing through the transformer i_{otr} and filter i_{of}.

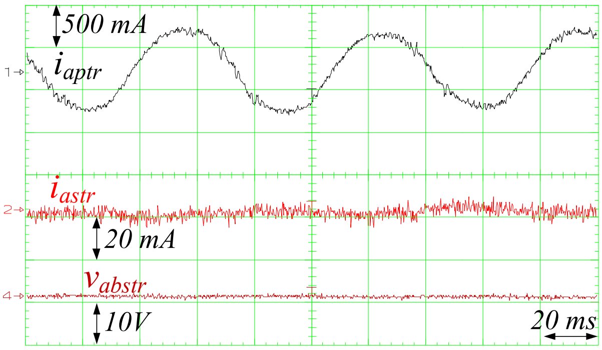

Figure 3.31 Steady state test with the generator operating under an open phase fault: transformer phase current at the primary winding i_{aptr}, phase current i_{astr} and phase-to-phase voltage v_{abstr} at the secondary winding.

Figure 3.32 shows a speed transient test of the faulted PMSG from -30 rad/s to 30 rad/s at 50% of the rated load while the transformer is supplied by the inverter with a modulation index of 0.5. Although a wind turbine probably never performs a speed transient from negative to positive speed with this dynamic, this test is presented to validate the performance of the faulty drive affected by a torque capability reduction due to the fault, and also in this case the variation of i_{og} produces negligible effect on the secondary windings of the transformer.

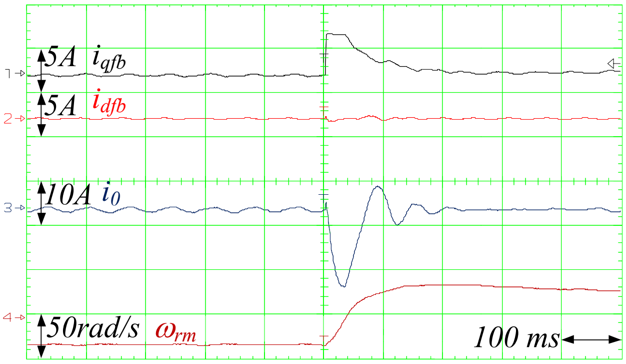

a)

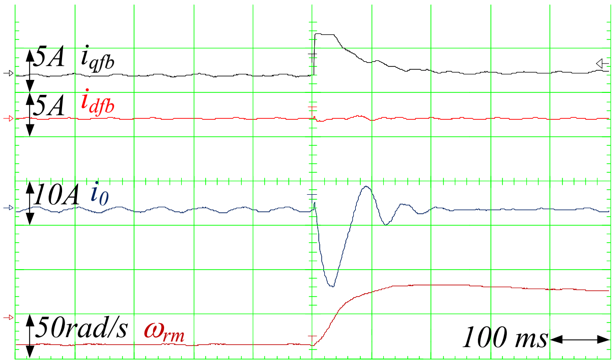

b)

Figure 3.32 Speed transient ω_{rm} = [- 30 rad/s to 30 rad/s] in the PMSG, performed at 50% of rated load, with the generator operating under an open phase fault wihile the transformer is healthy operating.

The following experimental results are obtained with the transformer affected by an open phase on the primary side, in particular the c phase is kept open, while the PMSG is healthy and controlled with a standard VC. The neutral points are always connected together as already done for the previous tests.

Figure 3.33. and Figure 3.34 are obtained with the faulty transformer operating at 50% of the rated power and rated flux, Figure 3.33 shows the healthy phase currents i_{aptr} and i_{bptr} on the primary side and line to line voltages v_{abstr} and v_{bcstr} on the secondary side; the PMSG is running at 70 rad/s. The fault tolerant control algorithm applied for the transformer maintains the two primary currents shifted by 60° while the line to line voltage at secondary windings are still shifted by 120° as in case of healthy conditions.

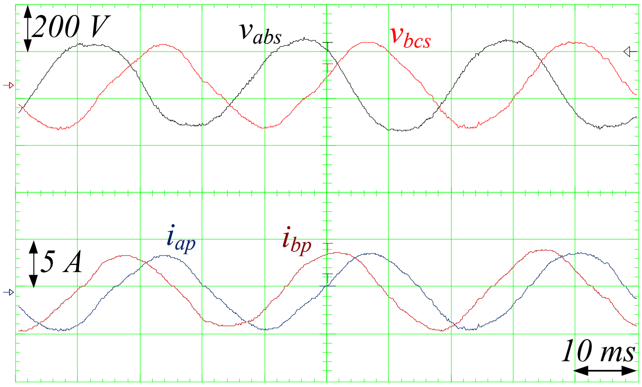

Figure 3.33 Steady state test with transformer operating in faulty conditions, at 50% of the rated load: Line to line voltages v_{abstr}, v_{bcstr} at the secondary windings and phase currents i_{aptr}, i_{bptr} at the primary windings.

Figure 3.34 is carried out with the PMSG running at 70 rad/s at 50% of the rated torque, the neutral current produced by the faulty transformer i_{otr} is flowing in the PMSG stator windings and as can be seen from Figure 3.34 a) it is modulating the PMSG phase currents but this does not affect the control of the generator as can be seen from the negligible speed ripple. Figure 3.34 b) shows the line to line voltage v_{abptr} of the primary windings and the three-phase currents i_{astr}, i_{bstr} and i_{cstr} measured at the secondary side; they are slightly distorted due to an imperfect third harmonic compensation.

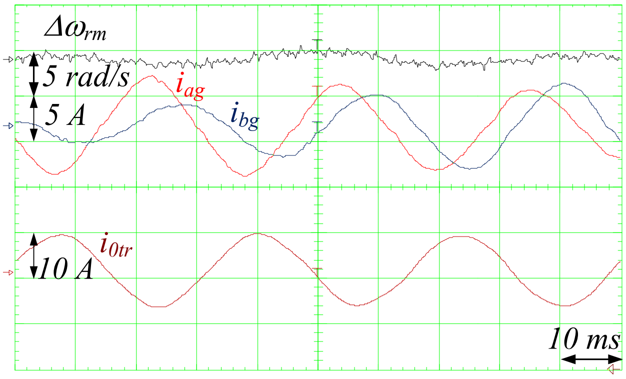

a)

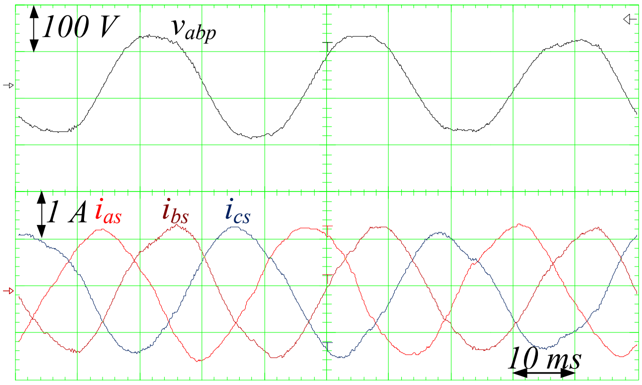

b)

Figure 3.34 Steady state test with transformer operating under an open phase and with the healthy generator working at 50% of rated load.

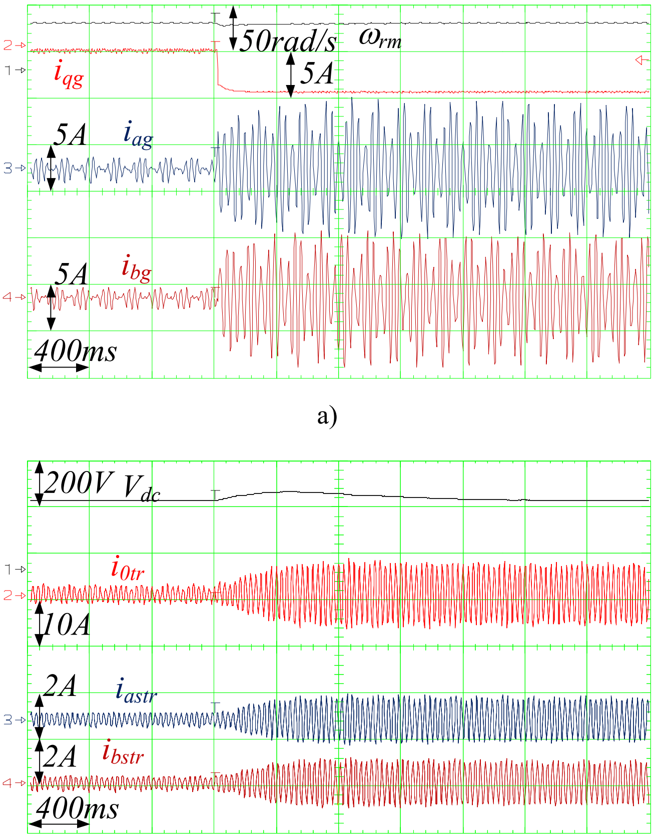

a)

b)

Figure 3.35 Load transient with transformer operating under open phase fault: rotational speed, torque current component i_{qg}, phase currents of PMSG i_{ag} and i_{bg} a); DC bus voltage, i_{otr}, phase currents i_{astr} and i_{bstr} b).

Figure 3.35 shows the system dynamic when a load transient from 10% to 80% of the rated torque is applied to the healthy PMSG. In this case an external 5kW PMSM works as prime mover and it is speed controlled setting a velocity of 50 rad/s, while the PQ control maintains the DC bus at 300V. Figure 3.35 a) depicts the rotational speed, the torque current component i_{qg} and the phase currents i_{ag} and i_{bg} of the generator, while Figure 3.35 b) displays the dc bus voltage, the neutral current i_{otr} and the phase currents i_{astr} and i_{bstr} of the secondary windings of the transformer. The generator phase currents are, also in this case, modulated by i_{otr} without generate interference with the control of the whole system.

The last test highlights the effects on the phase voltage of the healthy transformer due to the neutral current i_{og} produced when the PMSG is faulty. This current creates a voltage drop ΔV related to the phase resistance and the leakage inductance of the equivalent zero sequence circuit of the transformer primary windings. Figure 3.36 a) shows the amplitude of the fundamental voltage V_{aptr} and the voltage drop ΔV, when the faulty generator is working at different speeds, and the healthy transformer is working at 30Hz. Figure 3.36 b) shows the amplitude of the phase voltage V_{aptr} and the common mode voltage V_{Nn} measured between the neutral point of the transformer and the negative rail of the DC bus. This test verifies that the zero sequence current has a very low impact on the dc bus voltage utilization by the healthy drive, primarily dedicated to generate the fundamental voltage required by its control.

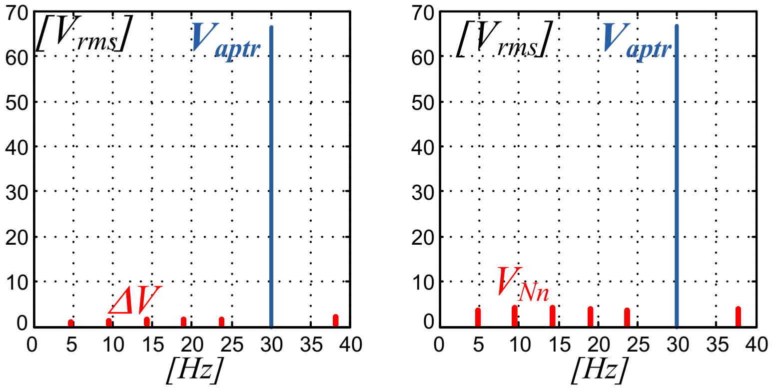

a) b)

Figure 3.36 Harmonic spectrum of the phase voltage in the transformer and harmonic spectrum of V_{nN}: PMSG is controlled at different rotational speeds $\omega_{rm} = 20 \div 80$ rad/s, while the transformer is operating at $f_e = 30$Hz and $V_{ab\_rms} = 135$ V.

3.4 Conclusions.

The content of this chapter has been pointed out on the application of a fault tolerant control strategy for a wind power system. The cooperation among the drives, which constitute the system, is exploited in case of fault of one of them. In this FT-WPS, where there are two three-phase drives, when a fault occurs in the generator side or in the transformer side, it can be isolated and the faulty unit can still operate with an open phase and the healthy one is exploited as feedback current path necessary to control properly the faulty drive. The proposed FT-WPS requires a very limited number of additional components and a simple post fault reconfiguration, in addition only a suitable selection of matrix transformation set ensures the vector control in every case of fault of the generator or the transformer, without other changes in the control loops. Simulations and experimental results have confirmed the theoretical analysis.

3.5 References.

[1] Mozina, C.J. “Impact of Smart Grids and Green Power Generation on Distribution Systems” IEEE Transactions on Industry Applications, 2013, vol. 49, Issue: 3, pp.: 1079-1090.

[2] Alsayed, M.; Cacciato, M.; Scarcella, G.; Scelba, G. “Multicriteria Optimal Sizing of Photovoltaic-Wind Turbine Grid Connected Systems” IEEE Transactions on Energy Conversion, 2013, vol. 28, Issue: 2, pp.: 370–379.

[3] Li, H. ; Chen, Z. “Overview of different wind generator systems and their comparisons”, 2008, IET Renewable Power Generation, vol.: 2,Issue: 2, pp.: 123–138.

[4] Ahuja, H. ; Bhuvaneswari, G. ; Balasubramanian, R. “Performance comparison of DFIG and PMSG based WECS”, 2011, IET Conference on Renewable Power Generation (RPG 2011), pp.:1–6.

[5] Polinder, H. ; Ferreira, J.A. ; Jensen, B.B. ; Abrahamsen, A.B. ; Atallah, K. ; McMahon, R.A. “Trends in Wind Turbine Generator Systems”, 2013, IEEE Journal of Emerging and Selected Topics in Power Electronics, vol.: 1, Issue: 3, pp.: 174-185.

[6] Altın, M. ; G ksu, O. ; Teodorescu, R. ; Rodriguez, P. ;Jensen, B.-B. ; Helle, L. “Overview of recent grid codes for wind power integration”, 2010, 12th International Conference on Optimization of Electrical and Electronic Equipment (OPTIM), pp.: 1152 – 1160.

[7] Rahmann, C. ; Haubrich, H.-J. ; Moser, A. ; Palma-Behnke, R.; Vargas, L. ; Salles, M.B.C. “Justified Fault-Ride-Through Requirements for Wind Turbines in Power Systems”, 2011, IEEE Transactions on Power Systems, Vol.: 26 ,no.: 3, pp.: 1555 – 1563.

[8] Chinchilla, M.; Arnaltes, S.; Burgos, J.C. “Control of permanent-magnet generators applied to variable-speed wind-energy systems connected to the grid,” Energy Conversion, IEEE Transactions on, 2006, vol.: 21, Issue:1, pp.: 130-135.

[9] Xibo Yuan; Yongdong Li “Control of variable pitch and variable speed direct-drive wind turbines in weak grid systems with active power balance,” Renewable Power Generation, IET, 2014, vol.: 8, Issue:2, pp.: 119-131.

[10] Hamadi, A.; Rahmani, S.; Ndtoungou, A.; Al-Haddad, K.; Kanaan, H.Y. “A new Maximum Power Point Tracking with indirect current control for a three-phase grid-connected inverter used in PMSG-based wind power generation systems”, IECON 2012 - 38th Annual Conference on IEEE Industrial Electronics Society, pp.: 916-923.

[11] Xia, Y.; Ahmed, K. H.; Williams, B. W. “Wind turbine power coefficient analysis of a new maximum power point tracking technique” IEEE Transactions on Industrial Electronics, Mar. 2013, vol. 60, n°. 3, pp.: 1122–1132. (MPPT)

[12] Frede Blaabjerg; Ke Ma "Future on Power Electronics for Wind Turbine Systems" IEEE Journal of Emerging and Selected topics in power electronics, September 2013, vol. 1, Issue:3, pp.: 139 – 152.

[13] Pena, R. ; Clare, J.C. ; Asher, G.M. "Doubly fed induction generator using back-to-back PWM converters and its application to variable-speed wind-energy generation", 1996, IEE Proceedings - Electric Power Applications, vol.: 143, Issue: 3, pp.: 231 – 241.

[14] Yazhou Lei; Mullane, A.; Lightbody, G.; Yacamini, R. "Modeling of the wind turbine with a doubly fed induction generator for grid integration studies," Energy Conversion, IEEE Transactions on, 2006, vol.: 21, Issue: 1, pp.: 257-264.

[15] Kayikci, M. ; Milanovic, J.V. "Reactive Power Control Strategies for DFIG-Based Plants", 2007, IEEE Transactions on Energy Conversion, Vol.: 22, Issue: 2, pp.: 389 – 396.

[16] Polinder, H.; Lendenmann, H.; Chin, R.; Arshad, W.M. "Fault Tolerant Generator Systems for Wind Turbines" IEMDC '09. IEEE International Electric Machines and Drives Conference, 2009, pp.: 675 – 681.

[17] Sloth, C.; Esbensen, T.; Stoustrup, J. "Active and passive fault-tolerant LPV control of wind turbines", American Control Conference (ACC), 2010, pp.: 4640-4646.

[18] Sloth, C.; Esbensen, T.; Stoustrup, J.; "Robust and fault-tolerant linear parameter-varying control of wind turbine," Mechatronics ,2011, vol.:21, Issue:4, pp.:645-659.

[19] Yang, Xiaoke; Maciejowski, Jan "Fault-tolerant model predictive control of a wind turbine benchmark", 8th IFAC Symposium on Fault Detection, Supervision and Safety of Technical Processes, 2012, vol.: 8, Issue: 1, pp.: 337-342.

[20] Badihi, H.; Youmin Z.; Hong, H. "Model Reference Adaptative Fault-Tolerant Control for a Wind Turbine agianst Actuator Faults" COntrl and Fault-Tolerant Systems (SysTol), 2013 Conference on, pp.: 498-503.

[21] Jain, T.; Yame, J.J.; Sauter, D. "A novel trajectory-based active fault-tolerant control: Application to a Wind Turbine system", Control Applications (CCA), 2013 IEEE International Conference on, pp.: 164-169.

[22] Karimi, S.; Gaillard, A.; Poure, P.; Saadate, S. "Current Sensor Fault-Tolerant Control for WECS With DFIG," Industrial Electronics, IEEE Transactions on, 2009, vol.: 56, Issue: 11, pp.: 4660-4670.

[23] Estima, Jorge O.; Fernandes, Jose L.J.; Marques Cardoso, A.J. "Faulty operation analysis of permanent magnet synchronous generator drives for wind turbine applications", Power Electronics, Machines and Drives (PEMD 2010), 5th IET International Conference on, pp.: 1-6.

[24] Rajendran, S.; Govindarajan, U.; Senthilvadivelu, S.; Uandai, S.B. “Intelligent sensor fault-tolerant control for variable speed wind electrical systems”, Power Electronics, IET, 2013, vol.: 6, Issue:7, pp.: 1308-1319.

[25] Freire, N.M.A.; Estima, J.O.; Cardoso, A.J.M. “A New Approach for Current Sensor Fault Diagnosis in PMSG Drives for Wind Energy Conversion Systems,” Industry Applications, IEEE Transactions on, 2014, vol.: 50, Issue: 2, pp.:1206-1214.

[26] Jen-Ren Fu; Lipo, T.A. “A strategy to isolate the switching device fault of a current regulated motor drive” Industry Applications Society Annual Meeting, 1993, Conference Record of the 1993 IEEE, vol.: 2, pp.: 1015-1020.

[27] Bolognani, S.; Zordan, M.; Zigliotto, M. “Experimental fault-tolerant control of a PMSM drive,” Industrial Electronics, IEEE Transactions on, 2000, vol.: 47, Issue:5, pp.: 1134-1141.

[28] Welchko, B.A.; Lipo, T.A.; Jahns, T.M.; Schulz, S.E. “Fault tolerant three-phase AC motor drive topologies: a comparison of features, cost, and limitations,” Power Electronics, IEEE Transactions on, 2004, vol.: 19, Issue: 4, pp.: 1108-1116.

[29] Lesic, V.; Vasak, M.; Peric, N.; Joksimovic, G.; Wolbank, T.M. “Optimal flux magnitude tracking with application to fault-tolerant control of wind turbine generators”, Control Conference (ECC), 2013 European, pp.: 466-471.

[30] Boettcher, M.; Reese, J.; Fuchs, F.W. “Reliability comparison of fault-tolerant 3L-NPC based converter topologies for application in wind turbine systems”, Industrial Electronics Society, IECON 2013 - 39th Annual Conference of the IEEE, pp.: 1223-1229.

[31] Nuno M. A. Freire, António J. Marques Cardoso, “A Fault-Tolerant Direct Controlled PMSG Drive for Wind Energy Conversion Systems”, Industrial Electronics, IEEE Transactions on, 2004, vol.: 61, Issue: 2, pp.: 821-834.

[32] Freire, N.M.A.; Cardoso, A.J.M. “Fault-Tolerant PMSG Drive With Reduced DC-Link Ratings for Wind Turbine Applications,” Emerging and Selected Topics in Power Electronics, IEEE Journal of, 2014, vol.: 2, Issue: 1, pp.: 26-34.

[33] Freire, N.M.A.; Marques Cardoso, A.J. “A Fault-Tolerant PMSG Drive for Wind Turbine Applications With Minimal Increase of the Hardware Requirements,” Industry Applications, IEEE Transactions on,2014, vol.: 50, Issue: 3, pp.:2039-2049.

[34] Shahbazi, M.; Zolghadri, M.R.; Poure, P.; Saadate, S. “Wind energy conversion system based on DFIG with open switch fault tolerant six-legs AC-DC-AC converter”, Industrial Technology (ICIT), 2013 IEEE International Conference on, 2013, pp.: 1656-1661.

[35] Gaillard, A.; Poure, P.; Saadate, S. “Reconfigurable control and converter topology for wind energy conversion systems with switch failure fault tolerance capability”, Energy Conversion Congress and Exposition, 2009. ECCE 2009. IEEE, pp.: 390-397.

[36] Scarcella, G.; Scelba, G.; Pulvirenti, M.; Gaeta, A. “A fault-tolerant power conversion topology for PMSG based Wind Power Systems”, Electrical Machines (ICEM), 2014 International Conference on, pp.: 1688-1696.

[37] Yu Zhang; Yong Kang; Jian Chen “The Zero-Sequence Circulating Currents between Parallel Three-Phase Inverters with Three Pole Transformers and Reactors” APEC Applied Power Electronics Conference and Exposition, 2006, Twenty-First Annual IEEE.

[38] Gaeta, A.; Scelba, G.; Consoli, A. “Modeling and Control of Three-Phase PMSMs Under Open-Phase Fault” IEEE Transactions on Industry Applications, 2013, vol. 49, n° 1. pp. 74 – 83.

[39] Zhao, Y.; Lipo, T.A. “An approach to modeling and field-oriented control of a three phase induction machine with structural imbalance” proc. of APEC 96, March 3-7, 1996, San Jose, California, (USA), pp.: 380 – 386.

[40] Pulvirenti, M.; Scarcella, G.; Scelba, G.; Cacciato, M.; Testa, A. “Fault-Tolerant AC Multi-drive System,” Emerging and Selected Topics in Power Electronics, IEEE Journal of, 2014, vol.: 2, Issue: 2, pp.: 224-235.

[41] R.D. Lorenz, lecture notes from the course ME 601/547 “Physics Based Modeling for computer control”, University of Wisconsin, Madison, 2014.

Chapter 4 Current sharing strategies for Fault Tolerant AC Multi-Drive System

Previous chapters have shown that fault of one drive can be supported by the healthy ones realizing a sort of cooperative control, and post fault operations are possible without severe performance losses. In case of one or more faults occurring to the three-phase drives composing the MDS, the faulty units can still work using only two phases because they exploit the closed path for the neutral current provided by the healthy drives, without introducing additional components. The aim of Chapter 4 is to analyze some viable solutions of sharing the neutral current outgoing from the faulty units among the healthy drives. Three different methods will be examined and validated by simulations and experimental tests.

4.1 Current sharing control strategies

The FT-MDS considered for this analysis is presented in Figure 4.1, as already seen in Chapter 1, where a common DC link supplies "n" VSIs controlling independently "n" ac machines. Although in the following analysis we are considering IM drives, it can be easily extended to synchronous motor drives. Additional switches SW$_1$,… SW$_n$ are kept off working as open circuit during normal operation while in case of fault affecting one or more motor drives, they are turned on, connecting the stator winding neutral point of the faulty units with the neutral points of some or all of the healthy drive stator windings.

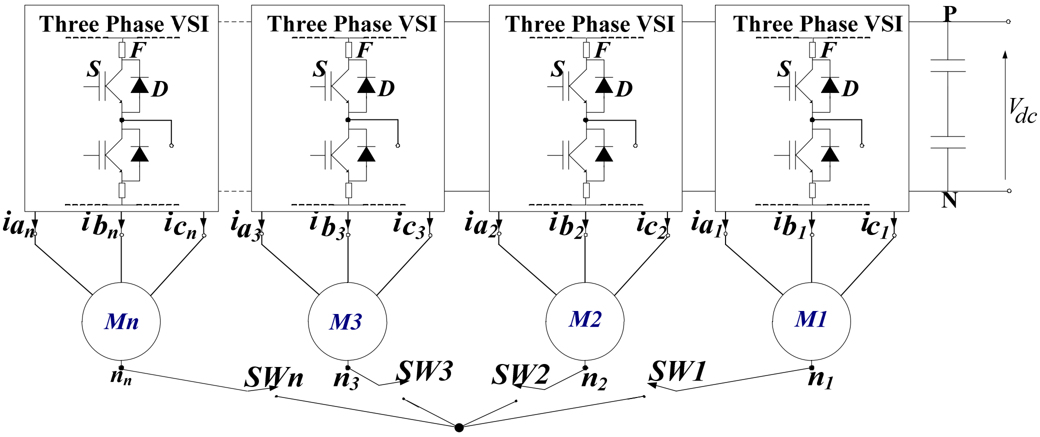

Figure 4.1 Fault tolerant Multi-drive topology.

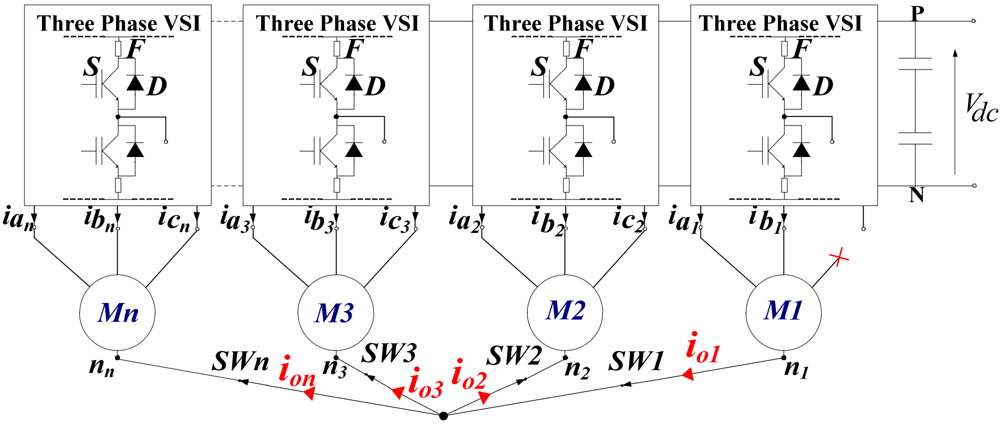

Figure 4.2 Post fault configuration of the MDS.

Figure 4.2 displays the post-fault configuration in case of fault on drive M_1, the neutral current i_{o1} flows through all the n-1 healthy drives.

Hereafter, the analysis is focused on defining some control strategies devoted to the sharing of the neutral currents produced by the faulty units among the healthy drives. This choice can have significant impact on the performance and continuity of service of the application.

The **First** analyzed **current sharing method** consists in allowing that i_{o1}, the neutral current produced by the faulty drives is naturally split among the healthy machines.

As highlighted in the previous Chapters, the neutral current of the faulty machine affects only the zero sequence circuit of the healthy machine, thus the current i_{oj}, of the j-th healthy drive, can be simply expressed using the current divider rule.

$$\bar{I}_{oj} = \frac{1}{3} I_{o1}\left(\frac{1/\bar{Z}_j}{1/\bar{Z}_1 + 1/\bar{Z}_2 + \dots 1/\bar{Z}_j + \dots 1/\bar{Z}_n}\right) \qquad (4.1.1)$$

Z_j is the zero-sequence axis phase impedance of the machine IM_j consisting of the stator resistance r_{sj} and the stator leakage inductance L_{lsj}, while I_{o1} is the amplitude of i_{o1}.

According to (4.1.1) it can be noted that induction machines with high power have a smaller phase impedance than machines with low power, as is shown on Figure 4.3, thus a significant amount of the neutral current i_{o1} will flow on the machine with the smallest phase impedance.

Although this method is very simple and does not require any kind of control, the neutral current could yield to overcurrents in the healthy machines when they operate at rated current; hence, the following sharing methods investigate the possibility to impose i_{oj} in each healthy unit, avoiding any drawback related to uncontrolled sharing current.

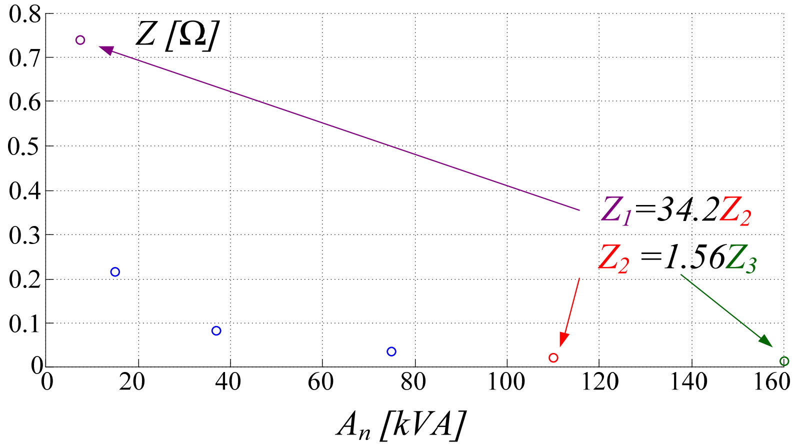

Figure 4.3 Per-phase impedance versus motor rated power.

The **Second current sharing method** overcomes the problem of possible overcurrent exploiting an additional zero-sequence closed loop current control in each healthy drive. Figure 4.4 shows the block diagram of the proposed technique.

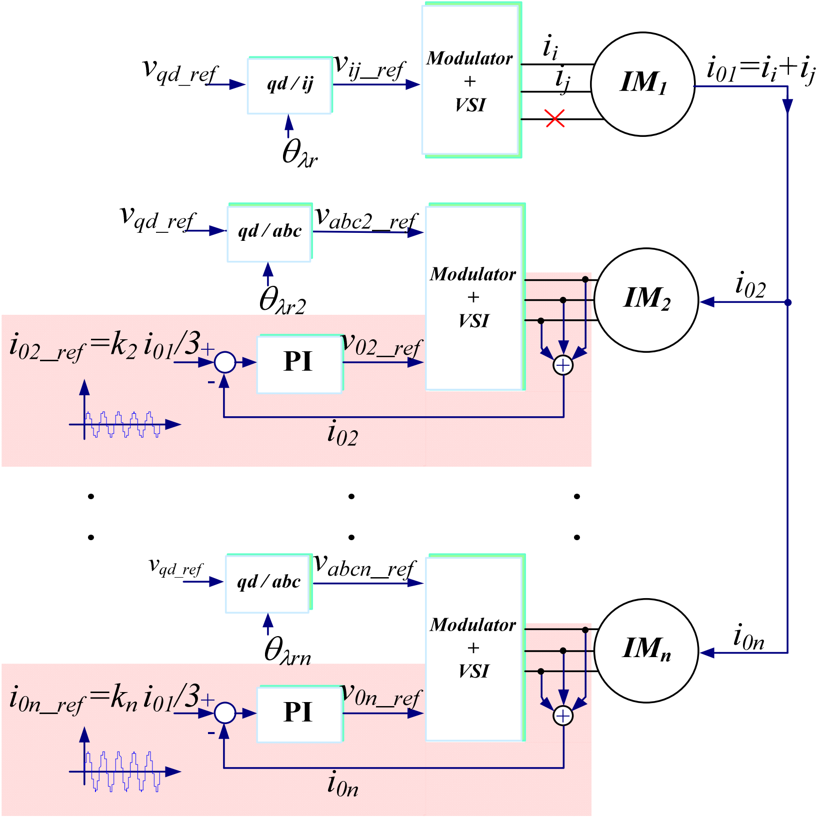

Figure 4.4 Additional zero-sequence control loops.

The feedback current i_{oj} is obtained summing together and dividing by three the actual phase currents of each healthy drive, while the zero sequence reference currents, i_{oj_ref}, are obtained applying to i_{o1} a suitable sharing factor k_j. The current controller output is the zero sequence voltage v_{oj_ref} which is superimposed on the voltage reference provided by the drive control system.

The sharing factor k_j is calculated considering the rated current and the operating condition of healthy drives. In case of a single open phase fault the flow chart of Figure 4.5 provides a possible calculation procedure of k_j . The main objective of this process is to assign a small sharing factor to drives that are operating under high loads, thus with current amplitudes close to the rated values. In practice, initially a load factor α_i, defined as the ratio between the actual current amplitude I_j and the rated current I_{nj} is calculated for each healthy drive. Then, if the load factor of one or more healthy drives is lower than one, sharing factors are obtained according to the equation (4.1.2).

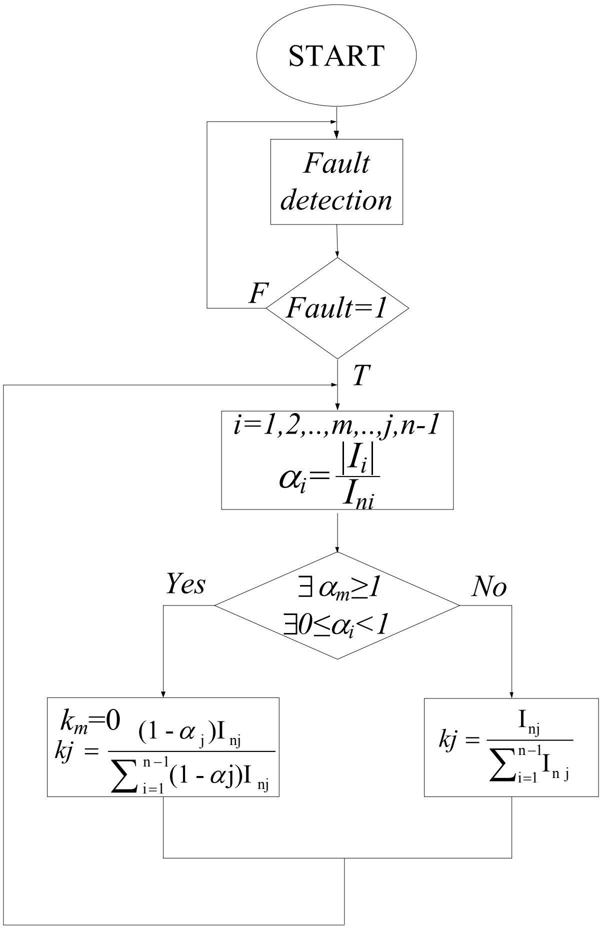

Figure 4.5 Flowchart used in the second and third current-sharing methods.

$$k_j = \frac{(1-\alpha_j)I_{nj}}{\sum\limits_{i}^{n-1} [(1-\alpha_j)I_{ni}]} \qquad (4.1.2)$$

Otherwise, if all the healthy drives have a load factor equal or higher than 1 the sharing factor is computed according to (4.1.3), which takes into account the overload capability of each healthy drive and will be proportional to the rated current.

$$k_j = \frac{I_{nj}}{\sum_{i}^{n-1} I_{ni}} \qquad (4.1.3)$$

Both previous cases have to respect the condition (4.1.4).

$$\sum_{i}^{n-1} k_i = 1 \qquad (4.1.4)$$

A representation of the sharing factor k_j is provided with Figure 4.6; it is obtained considering a MDS with three IM, whose parameters are reported in Table 4.1. For this test IM_1 operates under a single open phase fault, and the load factors of IM_2 and $IM_3$are always lower than one and suitably modified to compute the sharing factor k_2 and k_3. The latter underlines a non-linear behavior as can be clearly seen from the waveforms.

Table 4.1 Technical specification of the considered induction motors.

Motor Specifications	IM_1, IM_2, IM_4	IM_3
Rated Power [kW]	1.1	3
Rated Voltage [V]	400	400
Rated frequency [Hz]	50	50
Rated speed [rpm]	1440	1430
Rated current [A]	3	6.9
R_s, R_r [Ω]	8, 7.1	2, 1.66
L_{ls}, L_{lr} [H]	0.0234, 0.0234	0.0105, 0.0105
L_{ms} [H]	0.534	0.171
Rotor Inertia [Kgm^2]	0.0089	0.014

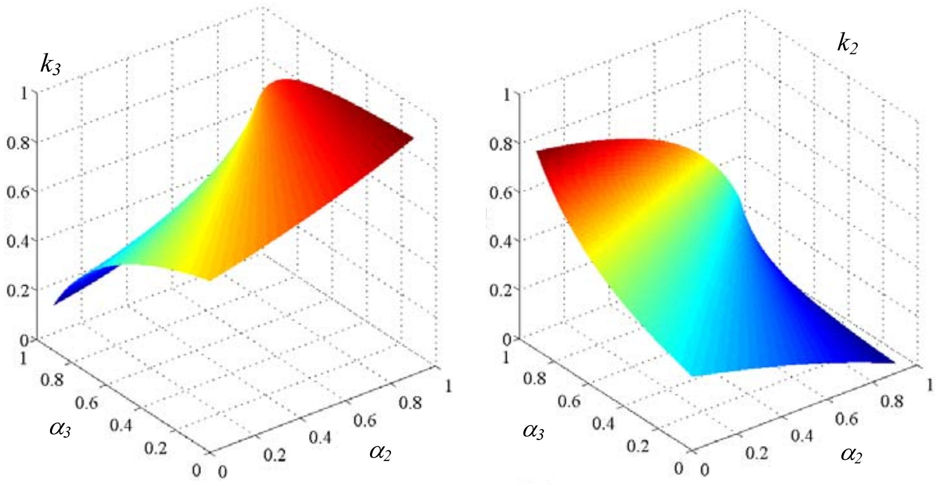

Figure 4.6 Sharing coefficient k_2 and k_3 computed at different α_2 and α_3.

The last current sharing method indicated as **Third current sharing method**, is a tradeoff among the previous two. It allows to avoid overcurrents in healthy drives due to the flow of i_{o1} and does not require additional control loop, because the controller in this case is model-based, hence the reference voltage v_{oj_ref} to generate the desired i_{oj} is computed considering the equation of the zero sequence circuit on the base of the sharing factors previously defined, the equation (4.1.6) is obtained:

$$i_{oj} = k_j \frac{i_{o1}}{3} \tag{4.1.5}$$

$$v_{oj\_ref} = \hat{r}_{sj}\, i_{oj} + \hat{L}_{lsj} \frac{d\, i_{oj}}{dt} \tag{4.1.6}$$

with i_{oj} calculated with (4.1.5).

Compared to the second current sharing method, this one does not suffer the regulator dynamic but it is affected by the machine parameters and their estimated values can deviate from the real ones; moreover, the derivate operation included in (4.1.6) introduces noise, that can be mitigated by a low-pass filter. Figure 4.7 shows the schematic block diagram.

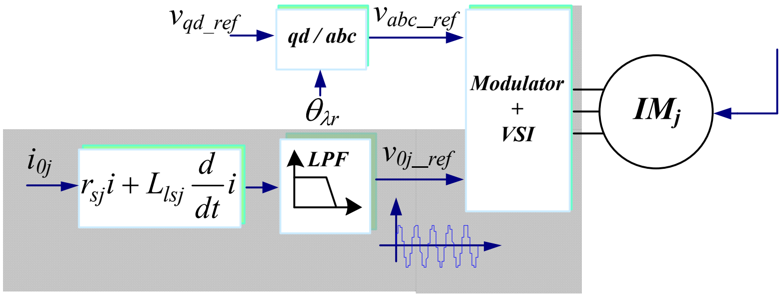

Figure 4.7 Block diagram for the implementation of the Third current sharing method.

Although these three methods and the relative block diagrams are proposed considering a single drive fault, they can be extended for MDS with more drives affected by a single fault, and these methods are always applicable when there are at least two healthy drives.

4.2 Losses and performance evaluation reduction

The zero sequence current flowing on the healthy machine generates additional joule losses on their stator windings according to (4.2.1)

$$P_{Js} (i_{o2}, i_{o3},\dots i_{on}) = 3\ r_{s2} i_{o2}^{2} + 3\ r_{s3} i_{o2}^{3} + \dots + 3\ r_{sn} i_{on}^{2} \qquad (4.2.1)$$

The last relationship can be minimized considering the constraint defined by the Kirchhoff' s current law:

$$g (i_{o1}, i_{o2},\dots i_{on}) = 0 \rightarrow g (i_{o1}, i_{o2},\dots i_{on}) = i_{o2} + i_{o3} + \dots i_{on} - i_{o1} \qquad (4.2.2)$$

Applying the method of Lagrange multipliers equations (4.2.1) and (4.2.2) can be solved and the results achieved are equal to those that can be carried out applying the current divider rule.

Figure 4.8, shows the results obtained with the same MDS configuration considered for the test reported in Figure 4.6; in particular, Figure 4.8 depicts the loci of the minimum power losses with respect to different operative conditions. IM_1 operates again under a single open phase fault establishing a neutral current of 6A that is shared between IM_2 and IM_3; the four pictures are obtained keeping constant the load factor of one drive and changing the load conditions of the other one. In each case the black rhombus represents the minimum power losses obtained applying the current divider rule equivalent to the application of the first current sharing method. Different results are obtained applying the second or the third current sharing method where power losses are expressed through equation (4.2.3):

$$P_{Js} = 3\ r_{s2} (k_2\ i_{o1})^2 + 3\ r_{s3} (k_3\ i_{o1})^2 \qquad (4.2.3)$$

The sharing factors are obtained applying the relation(4.1.2) and it is worth noting that, for a given load condition of the faulty drive, the additional power losses depend on the actual load conditions of both healthy drives, and their stator resistances..

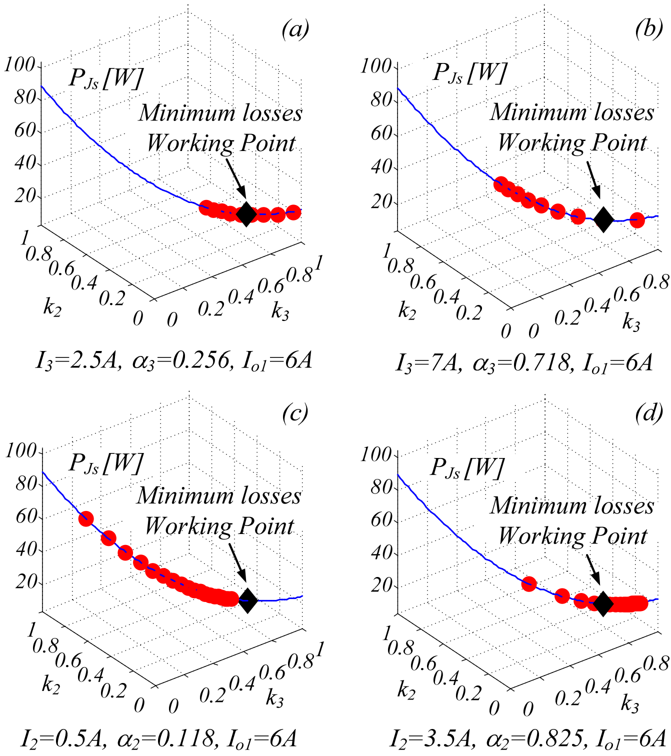

I_3=2.5A, α_3=0.256, I_{o1}=6A

I_3=7A, α_3=0.718, I_{o1}=6A

I_2=0.5A, α_2=0.118, I_{o1}=6A

I_2=3.5A, α_2=0.825, I_{o1}=6A

Figure 4.8 Additional losses P_{js} obtained by implementing the first (black rhombus) and second/third current-sharing methods (red dots).

From the aforementioned drawbacks, it can be deduced that the higher the number of drives that constitute the MDS and are used as feedback current path in case of fault of one or more drives the lower will be the additional power losses, the dc bus voltage and the torque reduction, keeping in mind also that post fault operations, in general, are temporary and extraordinary conditions.

4.3 Simulation results

In this section the three current sharing methods are evaluated with some simulations developed for a MDS consisting of three 1.1kW IM and one 3kW IM drives whose parameters are reported in Table 4.1, already shown.

All the motors are controlled independently and IM_1 is working under a single open phase fault. Different speed and load transient are applied to each drive and the effect of the zero sequence currents on the healthy drives is evaluated.

Figure 4.9 shows the MDS performances when the first current sharing method is applied; in particular, the rotational speeds, torques, phase currents, the neutral current amplitude of the faulty drive IM_1 and the phase current amplitude of the healthy drives are reported. As can be noted, although the phase currents of the healthy drives are modulated, torques and speeds are not distorted, following their commanded reference signals.

Figure 4.11 shows the neutral current of the faulty unit and its split quantities among the healthy drives IM_2, IM_3, IM_4, that do not change also during speed and load transients.

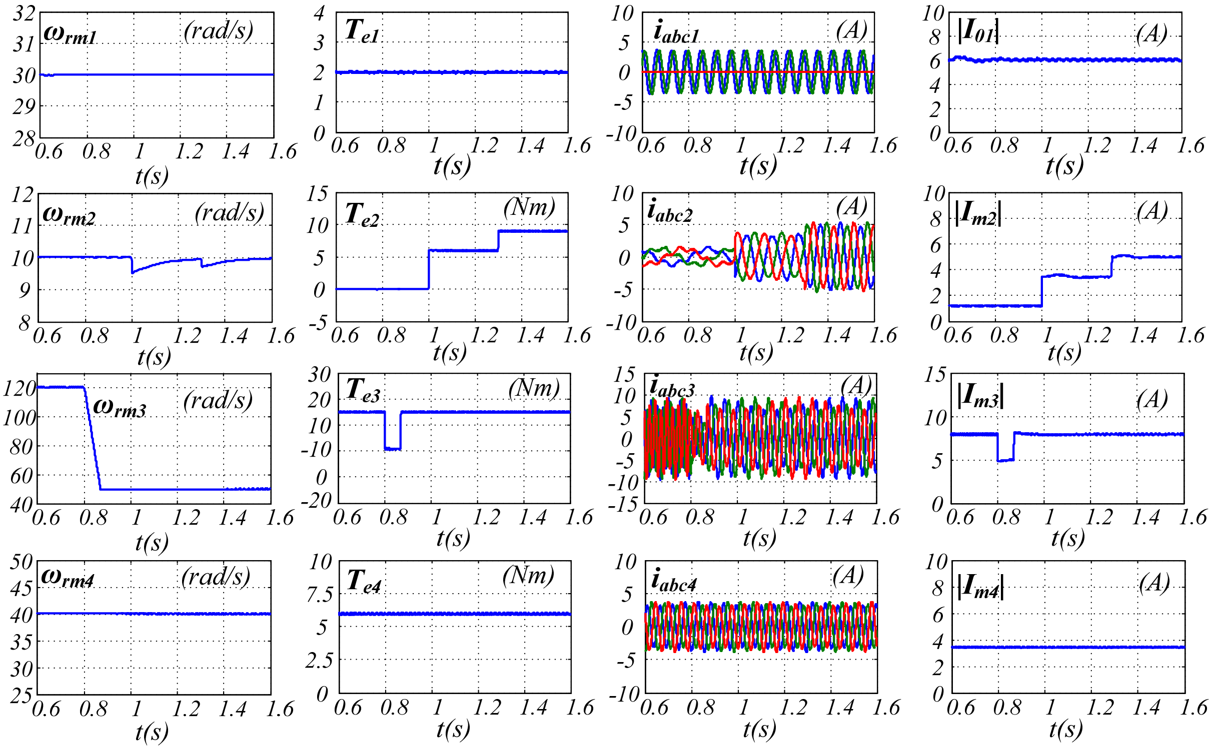

Figure 4.9 Current sharing strategy based on the first method.

The same tests have been performed applying the second current sharing method, hence the additional current loop to control the zero sequence currents have been implemented as well as the computation of the sharing factor k_j. The results of the simulations are displayed in Figure 4.10, also in this case torques and speeds of the healthy drives are not affected by the zero sequence currents similarly to the previous test, but on the contrary, the zero sequence current amplitudes are modulated by the sharing factors as clearly visible in Figure 4.12; depending on the load condition of the healthy drives, the zero sequence current is defined on the basis of its current capability α_j, as can be clearly seen at the beginning from 0.6s to 0.8s where IM$_2$ is operating at no load, thus its current capability is higher than that of IM$_3$ and IM$_4$. In fact, a significant amount of the neutral current is flowing through IM$_2$, followed by IM$_3$ while the smallest quantity is flowing through IM$_4$; in the simulation interval between 0.8s and 1s the speed transient on IM$_3$ produces a short transient but at steady state the same zero sequence current distribution is obtained on IM$_2$, IM$_3$, IM$_4$. When a torque load is applied on IM$_2$ its current capability is reduced, hereafter the load factor α_2 increases and the zero sequence current is reduced as shown in the graph from 1s to 1.3s; after 1.3s the torque is increased over the rated value hence the sharing factor k$_2$ is set to zero and only the other two healthy drives are used as feedback current path for the neutral current.

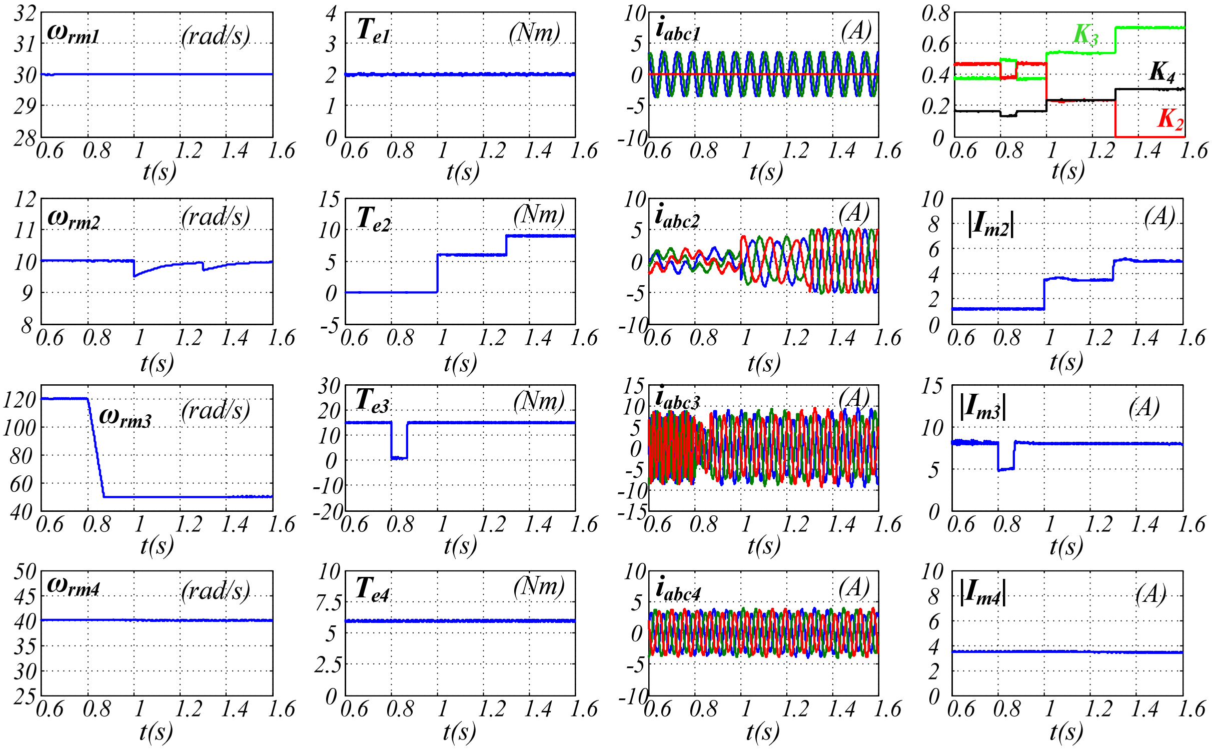

Figure 4.10 Current sharing strategy based on the second method.

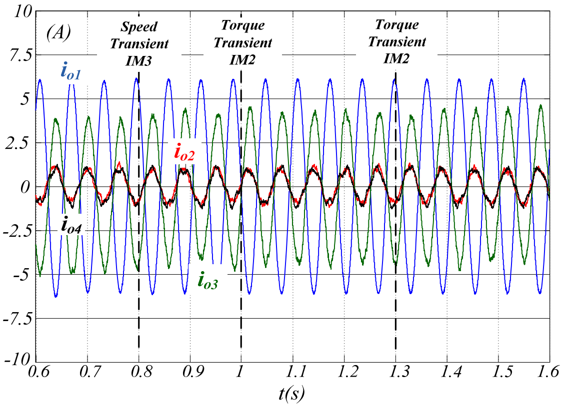

Figure 4.11 Zero-sequence currents flowing in each motor when applying the first method.

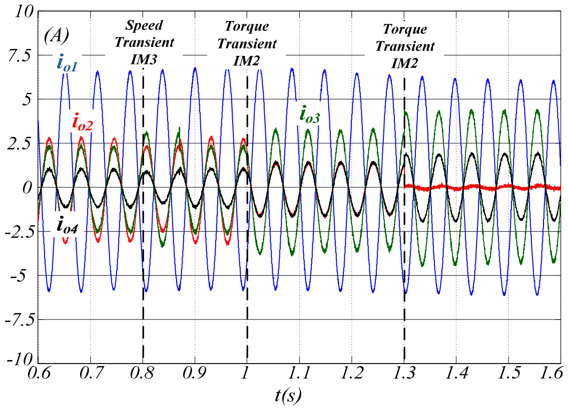

Figure 4.12 Zero-sequence currents flowing in each motor when applying the second method.

The third current sharing method has been tested applying the same speed and torque load transient, as reported in Figure 4.13, and although the drive performance is very similar to the results already shown with the first and second current sharing methods, the zero sequence current waveforms are reported in Figure 4.14 and Figure 4.15. In the first one the model based controller has the same parameters as the machine hence the waveforms are very close to that one of Figure 4.12, while in the second case a mismatching on the resistance is introduced and $\hat{r}_{s3}$, the estimated value, is 50% higher than the real value r_{s3}; in the last part of the simulation from 1.2s to 1.6s the value of i_{o2} is not exactly zero although the sharing factor $k_2 = 0$ due to a wrong generation of the voltage v_{o3_ref}

.

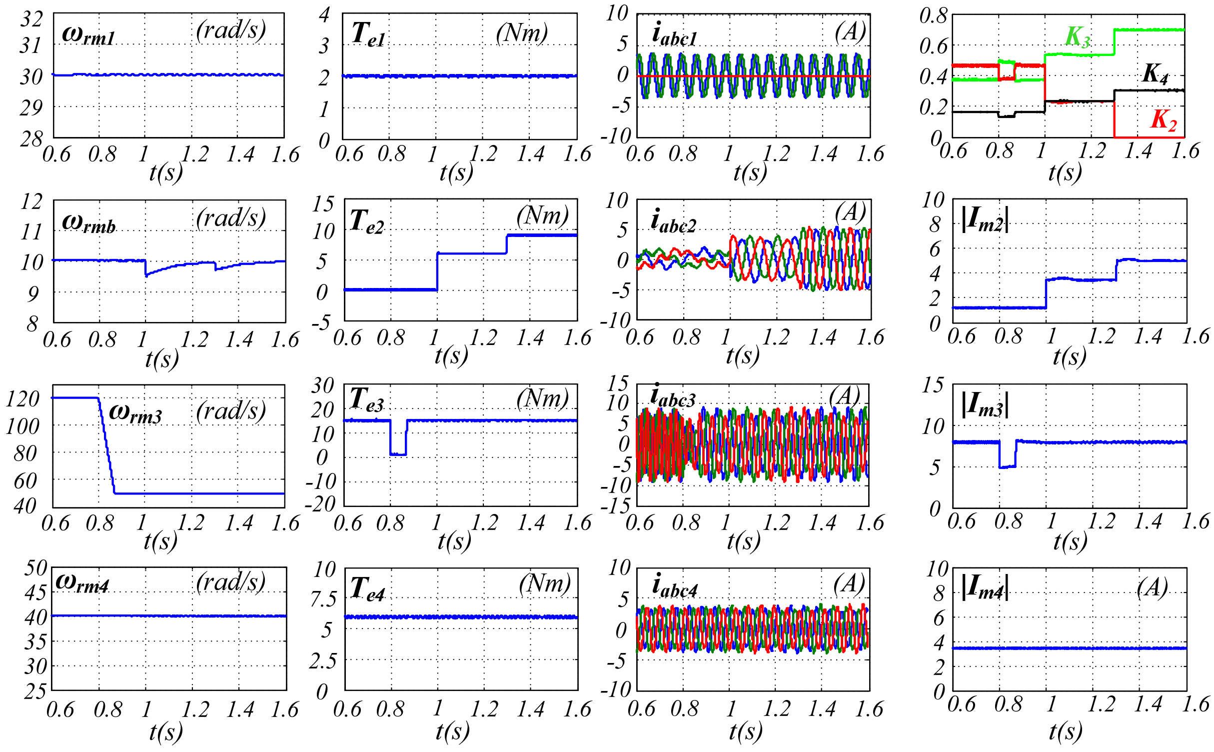

Figure 4.13 Current sharing strategy based on the third method.

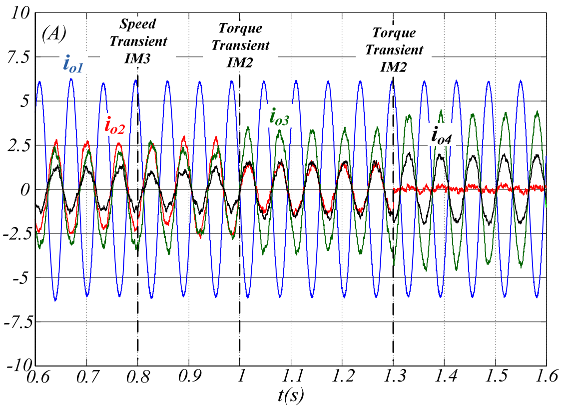

Figure 4.14 Zero-sequence currents flowing in each motor when applying the third method.

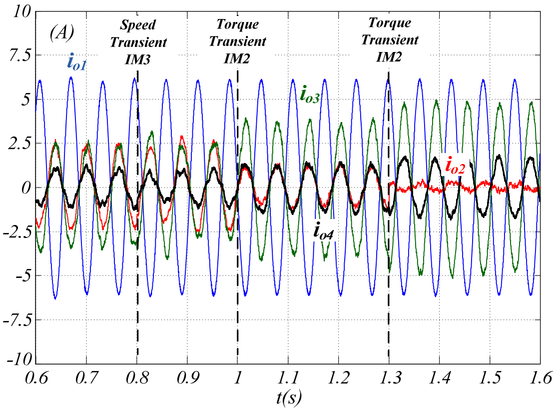

Figure 4.15 Zero-sequence currents flowing in each motor when applying the third method $\hat{r}_{s3}$ =1.5r_{s3}.

4.4 Experimental results

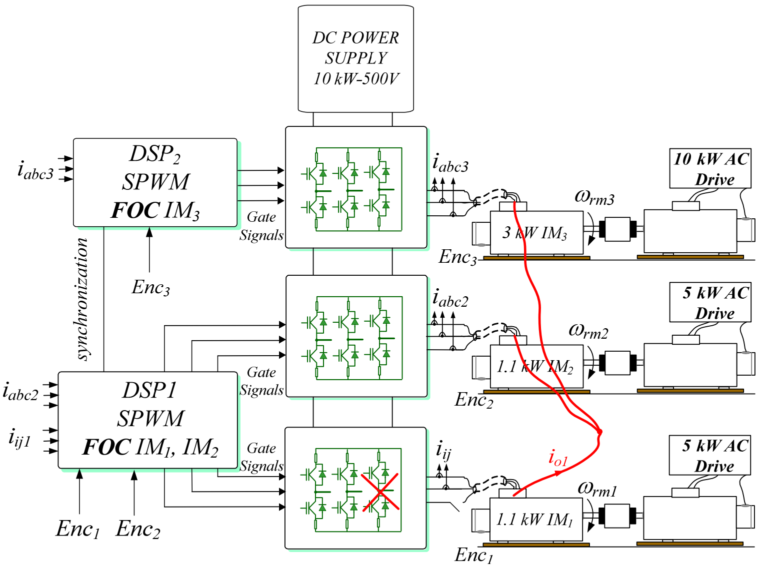

Figure 4.16 Experimental setup.

The three current sharing methods have been evaluated also with experimental tests performed on a MDS with three IMs: IM_1, IM_2, IM_3 whose parameters are listed in Table 4.1. The block diagram of the experimental setup is shown in Figure 4.16, a common DC bus supplies the power converters while in two DSP boards are implemented the VC and the sharing algorithms; the standard S-PWM is used to generate the gate signals of the inverter power devices.

IM_1 operates under a single open phase fault while IM_2 and IM_3 are healthy and independently controlled, moreover, the neutral point of the stator windings of IM_1, IM_2, IM_3 are connected together.

Due to the necessary connection of the neutral points, a small third harmonic current can flow whose amplitude depends on IM design, therefore this current is mitigated adding a third harmonic voltage V_3 on the stator voltage of healthy drives whose amplitude is adjusted offline.

Figure 4.17 shows the amplitude ratio V_3/V_1 and the phase of V_3, where V_1 is the amplitude of the fundamental voltage, as can be noted this additional voltage has a very small amplitude compared to the fundamental one especially at high rotational speed.

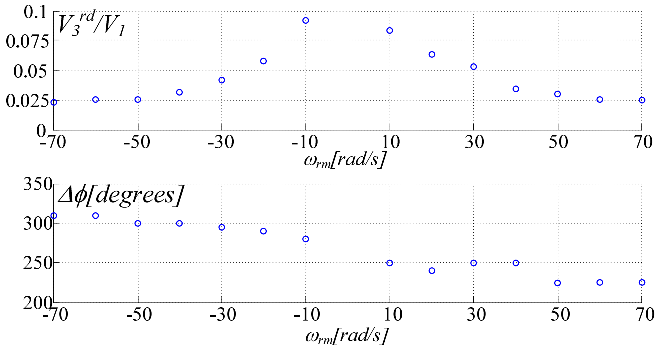

Figure 4.17 Amplitude ratio and phase of the voltages used to compensate the third-harmonic currents flowing in IM_3.

The results of a steady state test applying the first current sharing method are shown in Figure 4.18, where the two phase currents of the faulty drive IM_1 and the “a” phase currents of the healthy drives IM_2 and IM_3 are depicted; although these two currents are distorted due to the zero sequence currents, the ripples on the torque current components i_{q_M2} and i_{q_M3} and on the speed $\Delta\omega_{rm\_M2}$ and $\Delta\omega_{rm\_M3}$ are very small, confirming that the zero sequence current does not affect the field orientation control implemented on IM_2 and IM_3.

Figure 4.18 Steady-state test at no load, by using the first, method: $\omega_{rm_IM1} = 30$rad/s, $\omega_{rm_IM2} = 80$rad/s and $\omega_{rm_IM3} = 50$rad/s.

Figure 4.19 shows a transient test performed with the first current sharing method to evaluate the effects of speed variations on the zero sequence current. For this test IM_1 runs at 50 rad/s while on IM_2 a speed step from -30 to 30 rad/s is applied followed by another speed step on IM_3 from 40 to -40 rad/s; in addition, all the machines operate without mechanical load. The zero sequence currents, i_{o2} and i_{o3} flowing on IM_2 and IM_3 are almost constant during the test, this confirms that the amplitude of the zero sequence currents flowing on the healthy drives depends only on the zero-sequence circuit phase impedance, in this case, respectively Z_2 and Z_3.

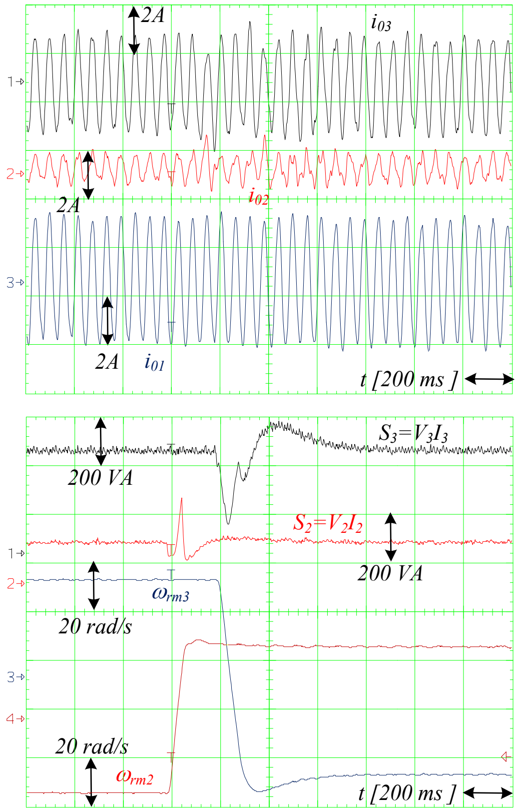

Figure 4.19 First method: speed transients occurring at: IM$_2$: ω_{rm_IM2} = -30/30rad/s and IM$_3$ ω_{rm_IM3} = -40/40rad/s, whereas IM$_1$ operates at ω_{rm_IM1} = 50rad/s.

The following tests have been carried out applying the other two current sharing methods, controlling the zero sequence current.

Figure 4.20 highlights the differences between the first sharing current method and the third one while the drives operate at steady state at no load. In this case, with the third method, the sharing factors k_2 and k_3 are freely imposed, in order to force a considerable amount of the neutral current i_{o1} to flow through the smaller drive. As can be noted the control of the zero sequence current amplitude does not affect the apparent power and the rotational speed of the healthy drives.

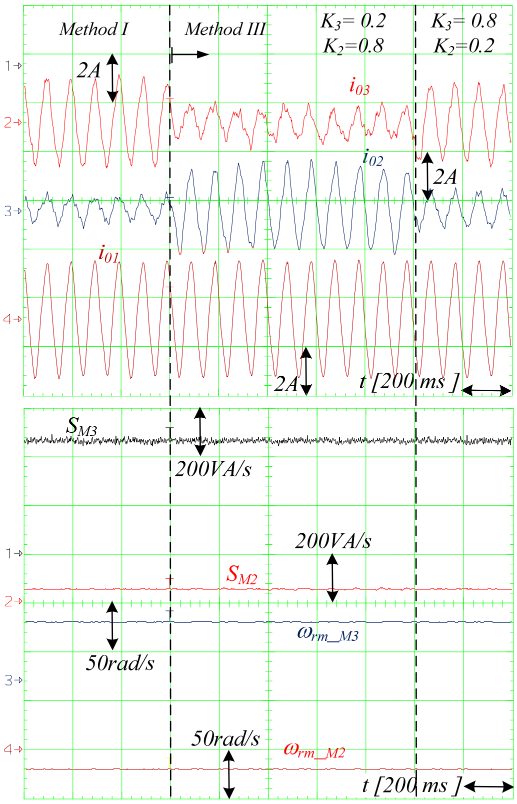

Figure 4.20 Steady-state test at no load by using the first and third methods: ω_{rm_IM1} = 30rad/s, ω_{rm_IM2} = 20rad/s and ω_{rm_IM3} = 60rad/s.

A similar test has been performed to evaluate the second current sharing method realizing a closed loop control on the zero sequence currents of the healthy drives; Figure 4.21 shows the results obtained with this method and it is possible to observe that there is a residual third harmonic current on the healthy machine when its sharing factor is set to zero due to an imperfect third harmonic compensation, and in addition a negligible increment of the ripple on the speed of IM_2, that is the smallest healthy machine, is generated when it operates at high sharing factor value.

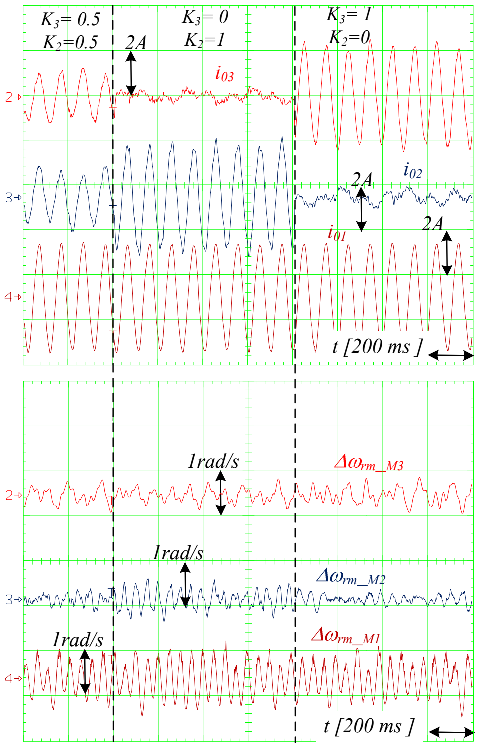

Figure 4.21 Steady-state test at no load by using the second method: ω_{rm_IM1} = 30rad/s, ω_{rm_IM2} = 20rad/s and ω_{rm_IM3} = 60rad/s.

Another test for a better evaluation of the speed ripple of the three drives is shown in Figure 4.22 with the faulty drive operating at rated load while the second current sharing method control the zero sequence current on the healthy drives setting k_2=k_2=0.5 also in these conditions the speed ripple is almost moderate on each drive.

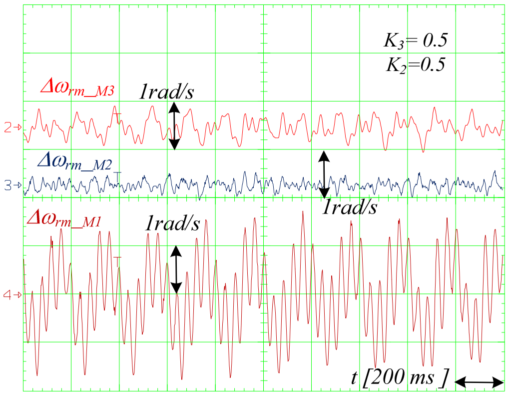

Figure 4.22 Steady-state test with the faulty motor operating at rated load, by using the second method: ω_{rm_IM1} = 30rad/s, ω_{rm_IM2} = 20rad/s and ω_{rm_IM3} = 60rad/s.

The last test is shown in Figure 4.23 where a load transient is applied on IM_3 while the second current sharing method is performed on the zero sequence current control and the sharing factors are calculated according to the flow chart of Figure 4.5 At the beginning, IM_2 and IM_3 run at no load and i_{o1} is shared in even parts, when the rated load is applied on IM_3 the sharing factors are automatically updated and a large amount of i_{o1} is transferred to IM_2 which has a higher capability to accept the additional zero sequence current, avoiding in this way overcurrent on IM_3.

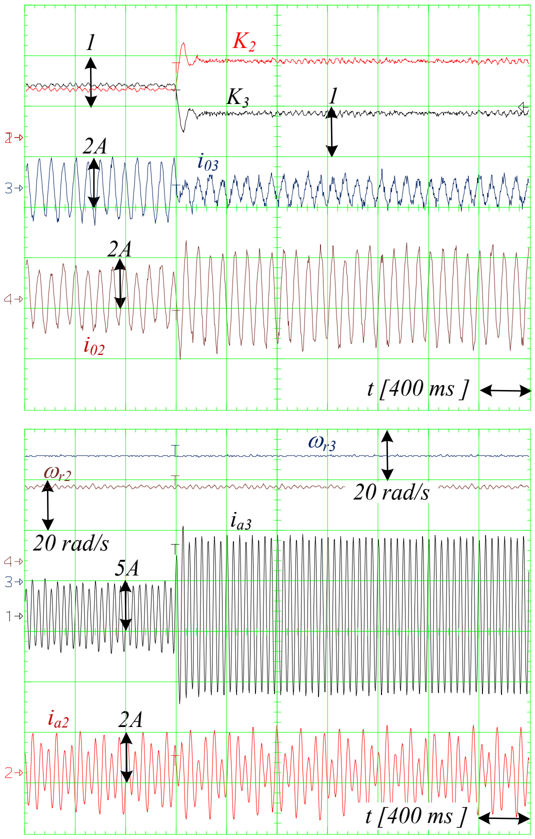

Figure 4.23 Load step occurring at IM_2 with the second method: $\omega_{rm\_IM1} = 30rad/s$, $\omega_{rm\_IM2} = 50rad/s$ and f_{e_M3}=20Hz.

4.5 Conclusions

In this chapter a particular issue related to the proposed FT-MDS topology has been analyzed. In fact, the utilization of the healthy drives as feedback current path for the neutral current, produced by one or more faulty drives, could lead to overcurrents in healthy drives, depending on their load conditions. To overcome this problem, some current sharing methods have been proposed and investigated to manage the zero sequence current on the healthy drives. These current sharing strategies have been validated by means of simulations and experimental tests.

Chapter 5 Fault-Tolerant Mechanical Control Variables Estimation in AC Multi-Drive Systems Using Binary Hall-Effect Sensors

In this chapter application of fault tolerant concept is extended to ac motor drive, where the sensor position is determined exploiting Hall effect sensors; the last are positioned inside the machines and used to reconstruct the rotor position. This information can be used to select the suitable state of the converter power devices. An incorrect signal provided by the Hall effect sensors may lead to an incorrect rotor position, therefore to a wrong firing sequence of the converter switches, causing instability of the drives that in some cases have to be turned off. The reliability improvement and a significant stop reduction of the drive during fault on the hall effect sensors for position detection can be extremely enhanced, by implementing a suitable compensation technique as will be shown in the next paragraphs. Even though this approach can be used for any type of ac machine hereafter it will be focused on a BLDC machine with trapezoidal back-emf.

5.1 Single drives with binary Hall-Effect sensors rotor position feedback

The application of field oriented control for ac drive requires the knowledge of the rotor position; usually optical encoder (incremental or absolute) or electromagnetic resolver, which have high resolution, are employed. Their precision is counterbalanced by high costs that in some applications could be higher than the entire drive and also their presence increases the motor size and the space necessary for the drive installation. Moreover, the reliability of the system can be affected by a fault on this external position sensor.

Although many self-sensing techniques have been developed to use the motor itself as position sensor, based fundamentally on the back-EMF estimation [1]-[9] or on the high frequency signal injection [10]-[13], [22], [23] they do not allow good dynamic performance and control of the drive on its entire operating region, therefore, a good tradeoff can be reached adopting low cost hall effect sensors, which are positioned inside the machine and provide discrete absolute position information. Usually three or more hall effect sensors can be mounted in two configurations [28]: the first one is inside the stator slots while the second one is on a printed circuit board outside the motor; the angular position of the rotor is detected since the permanent magnets positioned on it produce alternatively a positive and negative magnet field for the first configuration, while in the second one there is an independent magnetic field source that mirrors the rotor magnets; each sensor output generates a digital high level signal for 180 electrical degrees and a low level signal for the other 180 electrical degrees; in this way, during normal conditions, it is not possible that contemporarily all these sensors produce, at the same time, a high or a low level signal. Considering the case of three hall effect position sensors displaced by 120 electrical degrees to each other, it is possible to have $2^3 = 8$ logic combinations where the states 000 and 111 are excluded while the remaining six are used to identify the rotor position in an absolute way.

The application of this type of position sensors has been extensively evaluated for PMSM with sinusoidal [16], [17], [15], [18] and trapezoidal back-emf [19]. In the latter case, PMSM with trapezoidal back-emf also called Brushless DC Motors (BLDC) have been more involved in the use of hall effect position sensors, although they are synchronous machine their behavior is quite similar to DC machines but their windings are electronically commutated.

To be more precise, considering a three phase BLDC machine the stator windings are distributed in order to have a back-emf with a trapezoidal shape, the maximum torque will be produced only when the stator and the rotor flux are orthogonally. Hence, with a properly firing sequence, based on the rotor position information provided by the hall effect position sensors, the current will flow on each phase only during the flat region of the back-emf and only two phases will be supplied every 60° electrical degrees. Although the sequence commutation leads only on the hall effect position sensor states and does not depend on the machine's parameters, an inevitable torque ripple will occur due to the quantized nature of the signals especially at low rotational speed. Moreover, external speed and position loop could not work properly. In general, the speed loop is based on the average speed as feedback signal, calculated by measuring the time between two consecutive hall effect sensor transitions. This information would not be appropriate during sharply acceleration or deceleration transients.

Certainly, the improving of PMSM control both with sinusoidal and trapezoidal back-emf can be obtained exploiting the quantized information produced by the hall effect position sensors to generate a high resolution speed and position signals.

The simplest solution is presented in [15] where the general definition of the angular position is approximated with the Zero-th order term of the Taylor series expansion [16].

Considering the six active states provided by three hall effect position sensors, they can be reported on an orthogonal plane defining six sectors, each of them has an amplitude of 60° degrees. Inside a sector "k" the rotor angular position θ_{re} can be defined with (5.1) and ω_{re} is the instantaneous electrical angular rotor speed. θ_k is the initial angle of the sector k and t_k is the time when the magnetic axis enters in this sector.

$$\theta_{re}(t) = \int_{t_k}^{t} \omega_{re}(t)dt + \theta_k \tag{5.1}$$

Equation (5.1) can be approximated with (5.2).

$$\hat{\theta}_o(t) = \theta_k + \hat{\omega}_{ok}(t-t_k) \tag{5.2}$$

The angular position expressed in (5.2) needs to be bounded considering the limits of the sector k, that can be generally expressed as (5.3):

$$\theta_k \le \hat{\theta}_o(t) \le \theta_k + \pi/3 \tag{5.3}$$

$\hat{\omega}_{ok}$ is the angular rotor speed inside each sector and if it is considered constant, it is equivalent to the average speed and can be expressed with (5.4):

$$\omega_{re}(t) \cong \hat{\omega}_{ok} = \frac{\frac{\pi}{3}}{\Delta t_{k-1}} \tag{5.4}$$

Δt_{k-1} is the time taken by the rotor's magnetic axis to cross the entire previous sector k-1.

The aforementioned approach will be called Zero-Order-Algorithm (ZOA).

The authors in [16] propose also the position approximation with the first-order term of the Taylor expansion defining a First-order Algorithm (5.5) - (5.8), hence:

$$\omega_{re}(t) \cong \hat{\omega}_{1k}(t) = \hat{\omega}_{ok} + \hat{\omega}_{1k}^{(1)}(t - t_k) \tag{5.5}$$

The derivative term $\hat{\omega}_{1k}^{(1)}$ can be expressed as:

$$\hat{\omega}_{1k}^{(1)} = \frac{\hat{\omega}_{ok} - \hat{\omega}_{o(k-1)}}{\Delta t_{k-1}} \tag{5.6}$$

$$\theta_{re}(t) \cong \hat{\theta}_1(t) = \theta_k + \hat{\omega}_{ok}(t - t_k) + \frac{\hat{\omega}_{1k}^{(1)}}{2}(t - t_k)^2 \tag{5.7}$$

$$\theta_k \le \hat{\theta}_1(t) \le \theta_k + \pi/3 \tag{5.8}$$

It is clear that considering more terms of the Taylor series expansion the computational efforts will considerably increase.

Different techniques are based on state filters, PLL structures and observers.

A first solution proposed in [18] is based on a hybrid observer exploiting a differential equation (5.9) of a rotating vector to estimate a high resolution position. The block diagram of this method is presented in Figure 5.1.

$$\frac{d}{dt}\begin{bmatrix}\cos\theta_{re}\\ \sin\theta_{re}\end{bmatrix}=\begin{bmatrix}0 & -\omega_{re}\\ \omega_{re} & 0\end{bmatrix}\begin{bmatrix}\cos\theta_{re}\\ \sin\theta_{re}\end{bmatrix} \tag{5.9}$$

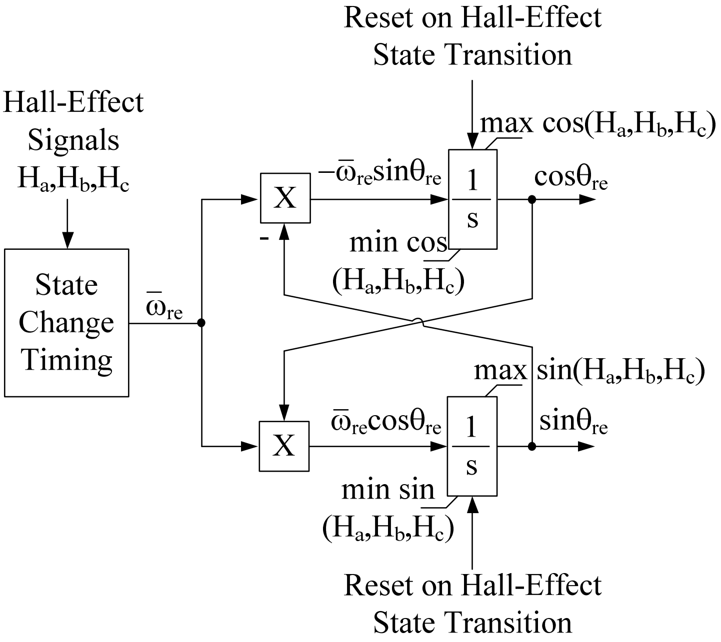

Figure 5.1 Hybrid Observer block diagram.

In [14], [16], [17], [20] the authors use a Vector Tracking Observer (VTO) to estimate the high resolution position and velocity; this observer is based on the Luenberger Style Observer (LSO) proposed in [21] and used for self-sensing techniques such as [22], [23]. The VTO has two inputs: the first one is the rotating vector generated by the hall effect position sensors containing the rotor position information, and the second one is the torque feed-forward generated by the speed loop controller and applied to the mechanical model inside the observer. The last contribution is useful to provide the position and velocity information above the observer bandwidth, this structure has intrinsically zero lead or lag on position and velocity tracking.

Another technique presented in [24] is based on the back-emf estimation, using a suitable regulator where a non-linear equation is implemented, it can guarantee the convergence of the algorithm to the desired equilibrium point. The estimated position will be obtained with the estimated speed integration but thanks to the hall effect position sensors the initial position is not arbitrary.

The authors of [25] propose the rotor position and velocity estimation of a PMSM with sinusoidal back-emf, using the back-emf of the machine model estimated on a reference frame synchronous to the rotor and exploiting also the information of three hall effect position sensors in order to establish the initial rotor position and reset the error on the rotor position estimation every 60 electrical degrees. In addition, the authors have implemented a Space vector modulation technique and they have reduced the mathematical operations and the total execution time exploiting the sector identification provided by the Hall effect positions sensors and the position with the estimation algorithm proposed.

Until now these are the principal structures and techniques employed to estimate a high resolution position and velocity from the quantized signal generated by the hall effect position sensors, under two fundamental assumptions: the first one is that the sensors are perfectly positioned while the second one is that no fault affects the sensors.

In case of misalignment of the sensors as shown on Figure 5.2, that often happens for medium and low precision BLDC, although the estimated rotor position could be close to the real one at steady state, the average velocity will be affected by a significant error especially using the ZOA, leading to a degradation in the drive performance and increasing the torque ripple independently on the load conditions, due to unequal conduction intervals among the motor phases.

The signals provided by the Hall effect sensors in case of misalignment and the estimated position obtained with the ZOA are illustrated in Figure 5.3.

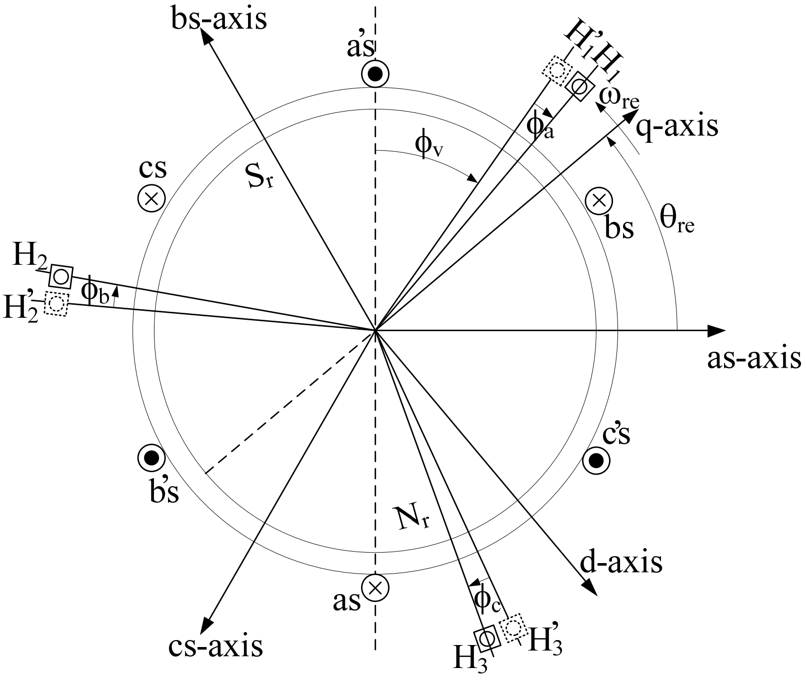

Figure 5.2 Cross section of a BLDC machine with misplaced Hall sensors [26].

The authors of [26] investigate the effects of the hall effect position sensors misalignment on phase current and electromagnetic torque for three BLDC motors and present an offline method to determine the real position of the hall sensors with respect to the ideal one, using a prime mover to run the BLDC rotor. Fundamentally, they consider that the zero crossing of the line-to-line back-emf is independent of sensor positioning, hence the misplacement angle for each sensor can be measured by comparing the line – to line back-emf and Hall sensor signal.

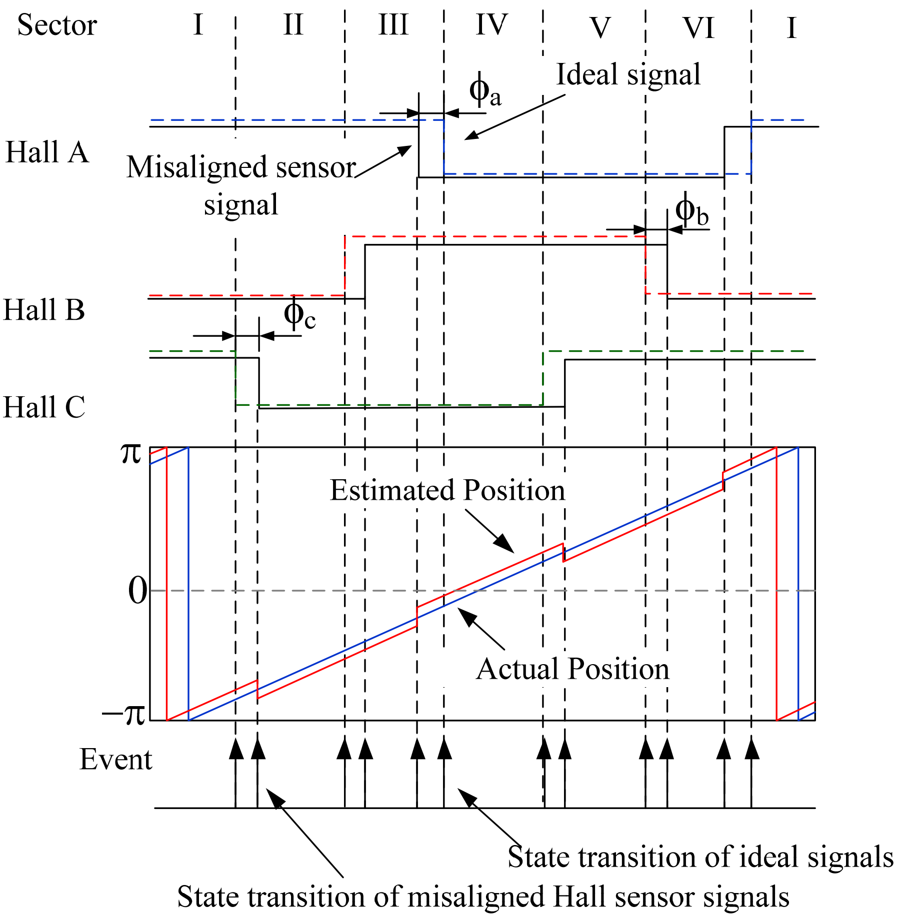

Figure 5.3 Actual and ideal Hall sensor output signals and resultant position estimate [29].

The authors in [27] propose a filtering technique to approximate the ideal hall effect position sensor signals, modifying the signals of the actual sensors.

In particular, the proposed method works by finding an interval duration $\tau(n)$, corresponding to $\theta_{re}(n)$; when $\tau(n)$ is known, it is used for estimating the correct timings for inverter states transitions. In case of misalignment $\tau(n)$ is not uniform and phase currents and torque waveform present undesirable harmonics. The method suggested by the authors consists in removing these additional harmonics, filtering the original Hall sensor signals.

In [28] the authors investigate the effects of the hall effect position sensors misplacement evaluating also the drive efficiency reduction and propose the estimation of the misplacement with an on-line method based on the back-emf of the silent phase.

The authors in [29] apply the VTO to estimate high resolution position and velocity, taking into account also a compensation for a misalignment of the hall effect position sensors. The authors estimate the back-emf with a stator electrical model and apply this signal to the first input of the VTO, the second input used as feed-forward in this case is not the commanded torque but the average speed calculated with the zero order algorithm as shown in Figure 5.4.

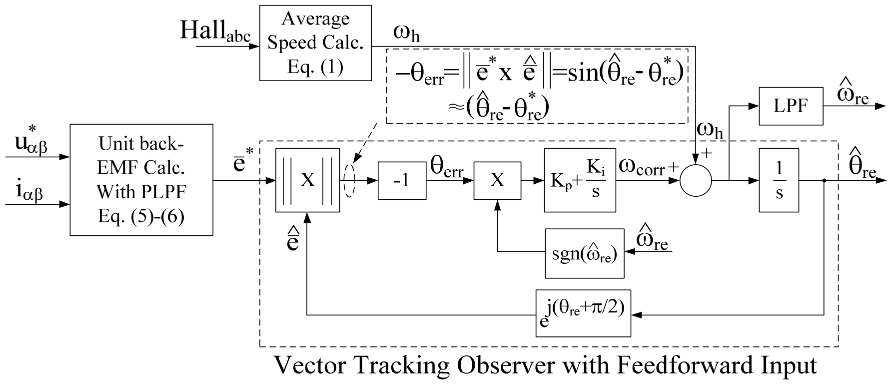

Figure 5.4 Vector tracking observer adopted in [29].

In Figure 5.4 the equations inside the block are below reported.

Eq. (1)

$$\omega_{re}(t) = \omega_h \cong \hat{\omega}_{ok} = \frac{\frac{\pi}{3}}{\Delta t_{k-1}}$$

Eq. (5)

$$\begin{bmatrix} (u^*_\alpha - R_s i_\alpha) - L_s \dfrac{i_\alpha(k) - i_\alpha(k-1)}{T_s} \\ \\ (u^*_\beta - R_s i_\beta) - L_s \dfrac{i_\beta(k) - i_\beta(k-1)}{T_s} \end{bmatrix} = \hat{\omega}_{re}\lambda_m \begin{bmatrix} -\sin\hat{\theta}_{re} \\ \\ \cos\hat{\theta}_{re} \end{bmatrix}$$

Eq. (6)

$$\bar{E}^*_f = \frac{\bar{E}^*}{\tau s + 1}(1+j\tau\hat{\omega}_{re})$$

Eq. 1 that provides ω_h has the same meaning as equation (5.4); Eq. 5 represents the model of a PMSM on the stationary frame $\alpha\beta$, in discrete time domain while Eq. 6 is the filtered reference back-emf vector, where $\hat{\omega}_{re}$ is the estimated rotor angular speed.

The authors in [30] propose a modified version of the hybrid observer defined in [18] to compensate misalignment and delay of the hall effect position sensors to reduce the torque ripple; in particular a routine to compensate the offset in placement of the sensors is provided and based on a look-up table while the compensation of hall effect position sensor delay is performed rearranging the control proposed in [31]. With this technique the authors limit the torque ripple from 1-2Nm to less than 30mNm compared to the rated torque of 13Nm.

The authors of [32] present a technique for high resolution position and velocity estimation adopting a modified structure of the VTO including also a compensation for a misalignment problem exploiting a flux observer. They suggest using as input for the VTO an interpolated angle instead of the discrete hall effect sensors signals, while for the position offset compensation a flux observer is used to estimate the electromagnetic torque that is compared to the commanded torque;

the error between these two quantities will be applied to a PI regulator which provides a signal proportional to the compensation angle θ_{offset}.

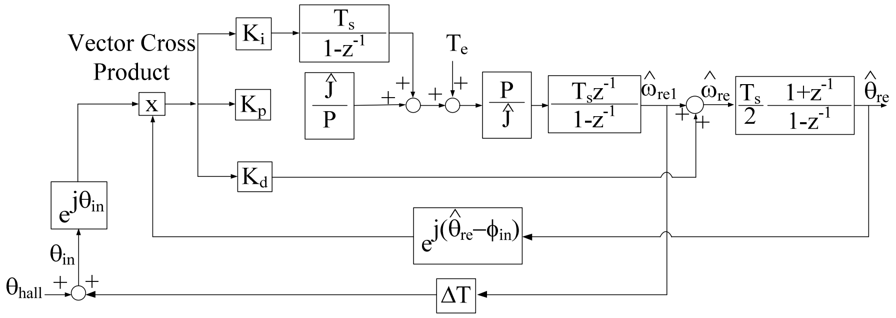

Figure 5.5 Vector feedback position observer [32].

The second assumption that could be not verified is related to possible faults in the hall effect position sensors which consist of an incorrect logical signal provided by the sensors during the rotor movement; for instance, it can provide a logical signal always high or low during the rotation period. This issue has been analyzed in very few research activities.

In [20] the authors propose an accurate analysis of all the possible types of faults on a drive with three hall effect position sensors. Single and double faults are investigated and a fault detection and identification strategy is presented considering the loci of the rotating vector $\mathbf{H}_{\alpha\beta}$ defined by the hall effect position sensors represented with a decomposition on the $\alpha\beta$ stationary frame. The authors adopt a VTO to estimate high resolution position and velocity as already done in [16] with the harmonic decoupling of the rotating vector $\mathbf{H}_{\alpha\beta}$, and for post fault operation they can estimate the correct position and velocity with a suitable modification of the decoupling terms of the rotating vector $\mathbf{H}_{\alpha\beta}$. Experimental tests have been conducted on an IM with IFOC.

In [33] the authors investigate the effect of faults on the hall effect position sensors in a BLDC drive by means of simulations, at the beginning they show the effects of the sensor H_A fault, for both cases $H_A=0$ and $H_A=1$, on: torque, current and line voltage; noting that each fault produces a particular and different effect. After this, a simple method for the fault diagnosis is presented, the fault detection is based on the value achieved by a flag signal and the maximum time for the fault detection is equal to the time for a complete electrical rotation of the rotor, while the sensor fault identification is performed applying a discrete Fourier transform on the line voltage for specific time interval and calculating the Spectral Energy Density (SED). With the errors obtained from the comparison of the SED in successive time intervals the faulty sensor will be identified. The fault compensation is realized exploiting the remaining two healthy sensors applying a suitable phase shift.

The line voltage used to detect and identify the fault position sensor will have noise and also it requires another sensor to perform its measurements; moreover, the authors generically claim to use a closed loop control on the speed to adjust the duty cycle of the PWM signal but they do not specify what algorithm or method is used to estimate the speed and also only single faults of hall effect position sensors are analyzed.

In [34] the authors analyze only single faults on the hall effect position sensors on a BLDC drive, the fault detection is obtained with a comparison between the hall sequence commutations stored on the DSP memory for normal conditions with the actual hall sequence commutations; in this way also the faulted sensor can be easily identified. The compensation for post fault operation is done using a counter to calculate the number of PWM cycles during the intervals that are no longer described as in normal conditions, in the paper the example of a fault on the sensor H_c is reported and the counter starts during the intervals from 120°-180° and from 300°-360°. This information is used to adjust the firing sequence of the power converter.

5.1.1 Model and control of a BLDC drive

The modeling of the BLDC has been proposed by [19], considering a three-phase BLDC, it has permanent magnets placed on the surface of the rotor while in the stator three windings, which are distributed in order to obtain a back-emf with a trapezoidal shape . The trapezoidal back-emf shape defines a non-sinusoidal variation of the motor inductances with the rotor angle hence the transformation of the equations on the qd0 reference frame is not necessary. Hence, both the model and its control will be performed in machine variables. The equations of the BLDC model are reported as follow in the next pages.

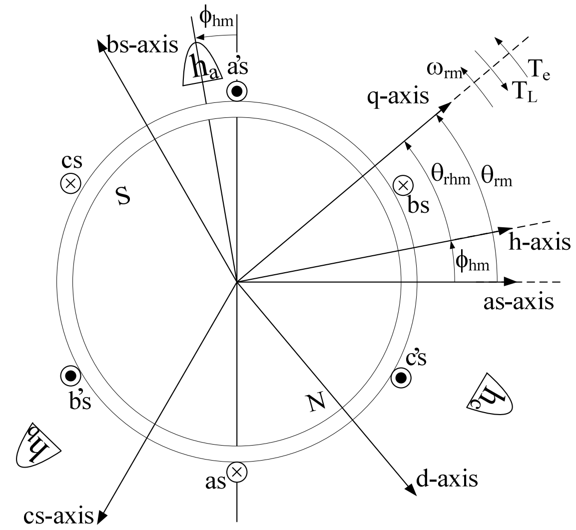

Figure 5.6 Permanent magnet synchronous machine [18].

$$\begin{cases} \mathbf{v}_{abcs} = \mathbf{r}_s\, \mathbf{i}_{abcs} + p\, \boldsymbol{\lambda}_{abcs} \\ \boldsymbol{\lambda}_{abcs} = \mathbf{L}_s\, \mathbf{i}_{abcs} + \boldsymbol{\lambda}_m^{'} \end{cases} \tag{5.1.1}$$

Since the inductance matrix is constant it is possible to write:

$$\mathbf{v}_{abcs} = \mathbf{r}_s\, \mathbf{i}_{abcs} + \mathbf{L}_s\, p\, \mathbf{i}_{abcs} + \mathbf{e}_{abcs} \tag{5.1.2}$$

$$\mathbf{e}_{abcs} = p\, \boldsymbol{\lambda}_m^{'} \tag{5.1.3}$$

$\boldsymbol{\lambda}_m^{'}$ is the permanent magnet flux linkages with the stator windings, which depends on the rotor position.

$\mathbf{e}_{abcs}$ is the back-emf.

$$\mathbf{r}_s = R_s \begin{bmatrix} 1 & 0 & 0 \\ 0 & 1 & 0 \\ 0 & 0 & 1 \end{bmatrix} \tag{5.1.4}$$

$$\mathbf{L}_s = \begin{bmatrix} L_{aa} & L_{ab} & L_{ac} \\ L_{ba} & L_{bb} & L_{bc} \\ L_{ca} & L_{cb} & L_{cc} \end{bmatrix} \tag{5.1.5}$$

Considering that the windings are balanced:

$$L_{aa}=L_{bb}=L_{cc}=L \tag{5.1.6}$$

$$L_{ab}=L_{ac}=L_{ba}=L_{bc}=L_{ac}=L_{ca}=M \tag{5.1.7}$$

The inductance matrix can be written as:

$$\mathbf{L}_s = \begin{bmatrix} L & M & M \\ M & L & M \\ M & M & L \end{bmatrix} \tag{5.1.8}$$

Finally remember that $i_a + i_b + i_c = 0$ the final form of $\mathbf{L}_s$ can be:

$$\mathbf{L}_s = \begin{bmatrix} L\text{-}M & 0 & 0 \\ 0 & L\text{-}M & 0 \\ 0 & 0 & L\text{-}M \end{bmatrix} \tag{5.1.9}$$

In scalar form the model equations are:

$$\begin{bmatrix} v_{as} \\ v_{bs} \\ v_{cs} \end{bmatrix} = \begin{bmatrix} R_s & 0 & 0 \\ 0 & R_s & 0 \\ 0 & 0 & R_s \end{bmatrix} \begin{bmatrix} i_{as} \\ i_{bs} \\ i_{cs} \end{bmatrix} + \begin{bmatrix} L\text{-}M & 0 & 0 \\ 0 & L\text{-}M & 0 \\ 0 & 0 & L\text{-}M \end{bmatrix} \begin{bmatrix} i_{as} \\ i_{bs} \\ i_{cs} \end{bmatrix} + \begin{bmatrix} e_a \\ e_b \\ e_c \end{bmatrix} \tag{5.1.10}$$

The back-emf can be expressed with the following expression:

$$e_a = \omega_{re}\,\lambda_m F(\theta_{re})$$

$$e_b = \omega_{re}\,\lambda_m F(\theta_{re} - \frac{2\pi}{3}) \qquad (5.1.11)$$

$$e_c = \omega_{re}\,\lambda_m F(\theta_{re} + \frac{2\pi}{3})$$

λ_m is the amplitude of the flux linkages established by the permanent magnet; ω_{re} is the electrical rotor speed. The function $F(\theta_{re})$ can be expressed with the relation(5.1.12) and the waveform of the back-emf and phase currents are represented in Figure 5.7.

$$F(\theta_{re}) = \begin{cases} \frac{6}{\pi}\theta_{re} & 0 \le \theta_{re} \le \frac{\pi}{6} \\ 1 & \frac{\pi}{6} \le \theta_{re} \le \frac{5\pi}{6} \\ 1 - \frac{6}{\pi}(\theta_{re} - \frac{5\pi}{6}) & \frac{5\pi}{6} \le \theta_{re} \le \frac{7\pi}{6} \\ -1 & \frac{7\pi}{6} \le \theta_{re} \le \frac{11\pi}{6} \\ -1 + \frac{6}{\pi}(\theta_{re} - \frac{11\pi}{6}) & \frac{11\pi}{6} \le \theta_{re} \le (2\pi) \end{cases} \qquad (5.1.12)$$

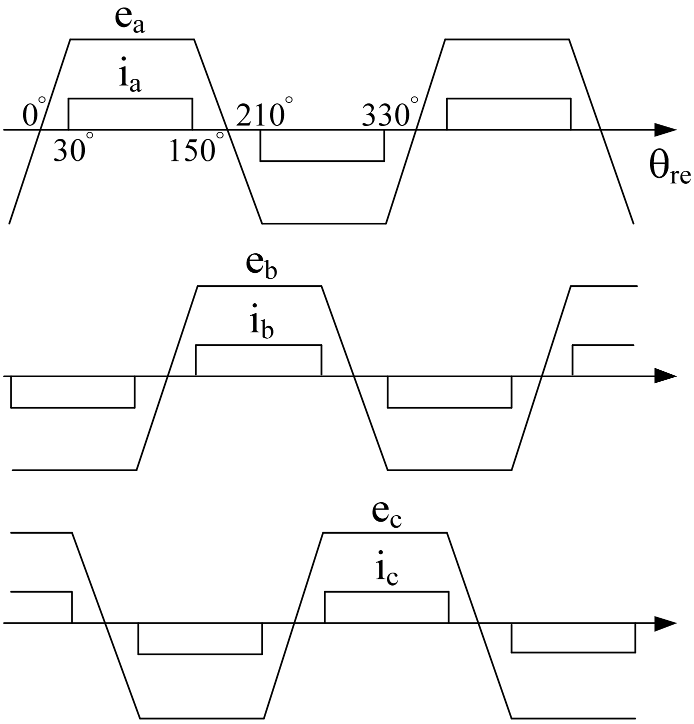

Figure 5.7 Typical back-emf and current waveform of a BLDC [19].

The electromagnetic torque can be expressed as (5.1.13):

$$T_e = (e_a\, i_{as} + e_b\, i_{bs} + e_c\, i_{cs}) / \omega_{re} = \lambda_m[\, F(\theta_{re})\, i_{as} + F(\theta_{re} - \frac{2\pi}{3})\, i_{bs} + F(\theta_{re} + \frac{2\pi}{3})\, i_{cs}] \qquad (5.1.13)$$

The model is completed adding the equation for the mechanical system:

$$T_e = T_L + J_p p\omega_{rm} + b_p\omega_{rm} \qquad (5.1.14)$$

Integrating (5.1.14) the mechanical speed and position will be obtained.

J_p is the total inertia of the rotor;

b_p is the physical viscous dumping.

p=d/dt

The electrical speed and position are obtained multiplying the mechanical quantities by the pole pairs P/2.

$$\begin{aligned} \omega_{re} &= \frac{P}{2}\,\omega_{rm} \\ \theta_{re} &= \frac{P}{2}\,\theta_{rm} \end{aligned} \qquad (5.1.15)$$

The control of the BLDC is realized in order to achieve the maximum torque; it can be reached only if the stator and the rotor flux vectors are orthogonal, if it is considered that the rotor flux is conventionally directed along the d-axis, the back-emf produced will be directed always on the q-axis, therefore exploiting the position information provided by the hall effect position sensors, it is possible to define the correct firing sequence in order to enable a current circulation during the 120° flat area of the back-emf. In this way the stator flux, generated by the corresponding stator current will be directed on the q-axis, and this will allow to extract the maximum torque. The current path is defined only by two active phases while the third one is not supplied, and from the last it could be possible to measure the back-emf; each 60° there is a commutation of the inverter power switches, and the firing sequence will be determined depending on the desired rotation.

It is important to note that for a BLDC the reference current will be not sinusoidal but it will be rectangular, while the feedback current in reality will not be exactly rectangular but trapezoidal due to the finite rise time and an inductance phase value that is not zero. The feedback current can be measured from the dc bus source or from the motor phases; in the latter case it is necessary to know the path of the current and measuring this quantity from the correct phase, according to the firing sequence of the power converter.

The modulation strategy adopted for simulation and experimental results is the PWM complementary switching, and in addition to the current loop also an external speed loop is realized as shown in Figure 5.8.

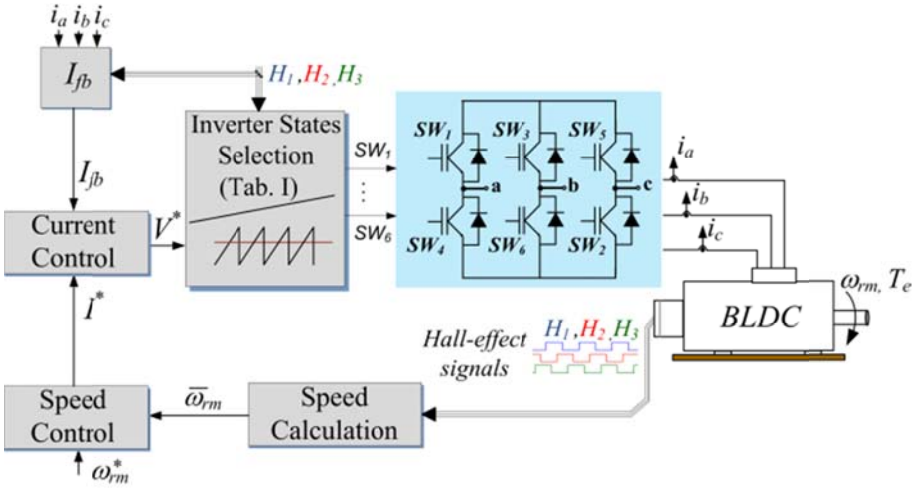

Figure 5.8 Control scheme of a standard speed controlled BLDC drive.

The commutation table is presented in Table 5.1.

Table 5.1 Power converter switches commutation table for counter clockwise rotation.

Position of PM magnetic axis	**Hall-effect sensors' states**	**Active switches**
$330° < \theta_{re} \leq 30°$	$H_1=1$, $H_2=0$, $H_3=0$	SW_3 and SW_2
$30° < \theta_{re} \leq 90°$	$H_1=1$, $H_2=1$, $H_3=0$	SW_3 and SW_4
$90° < \theta_{re} \leq 150°$	$H_1=0$, $H_2=1$, $H_3=0$	SW_5 and SW_4
$150° < \theta_{re} \leq 210°$	$H_1=0$, $H_2=1$, $H_3=1$	SW_5 and SW_6
$210° < \theta_{re} \leq 270°$	$H_1=0$, $H_2=0$, $H_3=1$	SW_1 and SW_6
$270° < \theta_{re} \leq 330°$	$H_1=1$, $H_2=0$, $H_3=1$	SW_1 and SW_2

The limitation on the application of Table 5.1 is clear in case of a fault on a hall effect position sensor, and it does not allow stable speed control of the drive as will be shown, due to the incorrect firing sequence of the power converter switches. The rotor velocity will be calculated and compared using three different observers: the Vector Tracking Observer (VTO), the Zero order algorithm (ZOA) and the Hybrid Observer (HO), that will be suitably modified to tolerate one or more faults of the hall effect position sensors and guarantee stable operation of the BLDC drive.

5.2 Hall effect position sensors fault types and compensation

Considering a single drive, during the rotation of the motor, the hall effect position sensors will provide three alternating logic signals that can be reported on a dq stationary frame indicated as αβ, with the axis orientation defined as $f_\alpha + j\, f_\beta$; the αβ component will define a vector $\overrightarrow{\mathbf{H}}_{\alpha\beta}$, rotating in a quantized fashion and moves from one direction to another every 60° , describing a hexagon locus, as shown in Figure 5.9. The transformation matrix is defined according to (5.2.2) where the signals provided by the Hall effect sensors H_1, H_2, H_3 are modified with(5.2.1) in order to be symmetrical with respect to zero.

$$\begin{bmatrix} H_a \\ H_b \\ H_c \end{bmatrix} = 2 \begin{bmatrix} H_1 \\ H_2 \\ H_3 \end{bmatrix} - 1 \tag{5.2.1}$$

$$\begin{bmatrix} H_\alpha \\ H_\beta \end{bmatrix} = \frac{\pi}{4} \begin{bmatrix} 1 & -\frac{1}{2} & -\frac{1}{2} \\ 0 & \frac{\sqrt{3}}{2} & -\frac{\sqrt{3}}{2} \end{bmatrix} \begin{bmatrix} H_a \\ H_b \\ H_c \end{bmatrix} \tag{5.2.2}$$

$$\theta_{\alpha\beta} = \operatorname{atan}\left(\frac{H_\beta}{H_\alpha}\right) \tag{5.2.3}$$

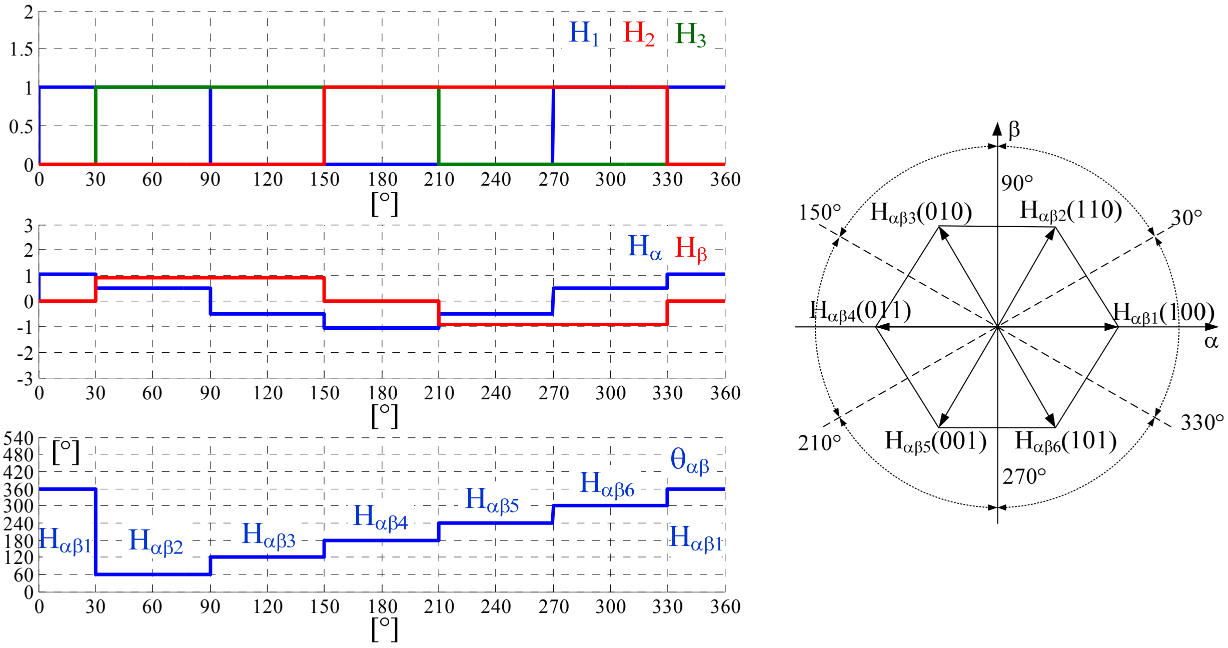

Figure 5.9 Hall effect sensors signals and vector representation on the αβ plane.

Figure 5.9 shows the hall sensor signals H_1, H_2, H_3 waveforms during a complete rotation and the position $\theta_{\alpha\beta}$ of the rotating vector $\vec{\mathbf{H}}_{\alpha\beta}$ and its locus on the αβ plane, during normal operations when all the sensors are healthy.

In case of a single fault, one of the three hall effect position sensors will keep its state constantly high or low. Under this condition, a total of six possible faults can arise. The effects of the fault will modify the locus of the vector $\vec{\mathbf{H}}_{\alpha\beta}$ and the zero vector will also appear, i.e. (000) or (111) depending on the fault type. Figure 5.10 reports the locus of $\vec{\mathbf{H}}_{\alpha\beta}$ when the sensor $H_1 = 1$, while Figure 5.11 represents the fault event of $H_1 = 0$, as can be noted in both cases the zero vector V_7 or V_0 appears. In this particular state all the switches of the power converters are kept open, moreover, the sector width is not constant as in normal case but two sectors are 60° wide and the other two are 120° wide. The different sectors width characterize also the other type of single hall position sensors faults but each fault can be distinguished from the others by the specific $\vec{\mathbf{H}}_{\alpha\beta}$ rhomboidal locus.

The major issues caused by a single fault can be associated to a wrong feedback current reconstruction if it is measured by the machines' phases, and also the average speed calculation will be incorrect because some sectors have a different length than 60°. These elements cause, without any doubts, instability of the drive control.

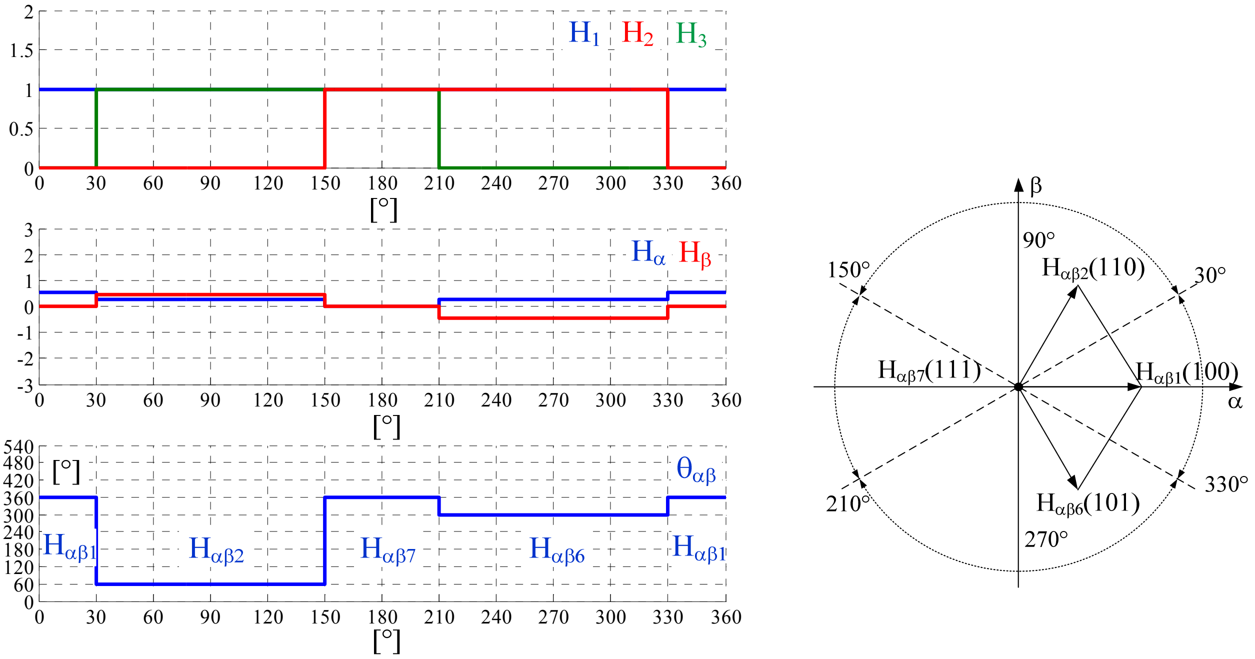

Figure 5.10 Single fault affects the Hall sensors signals with H_1=1 and representation on the αβ plane.

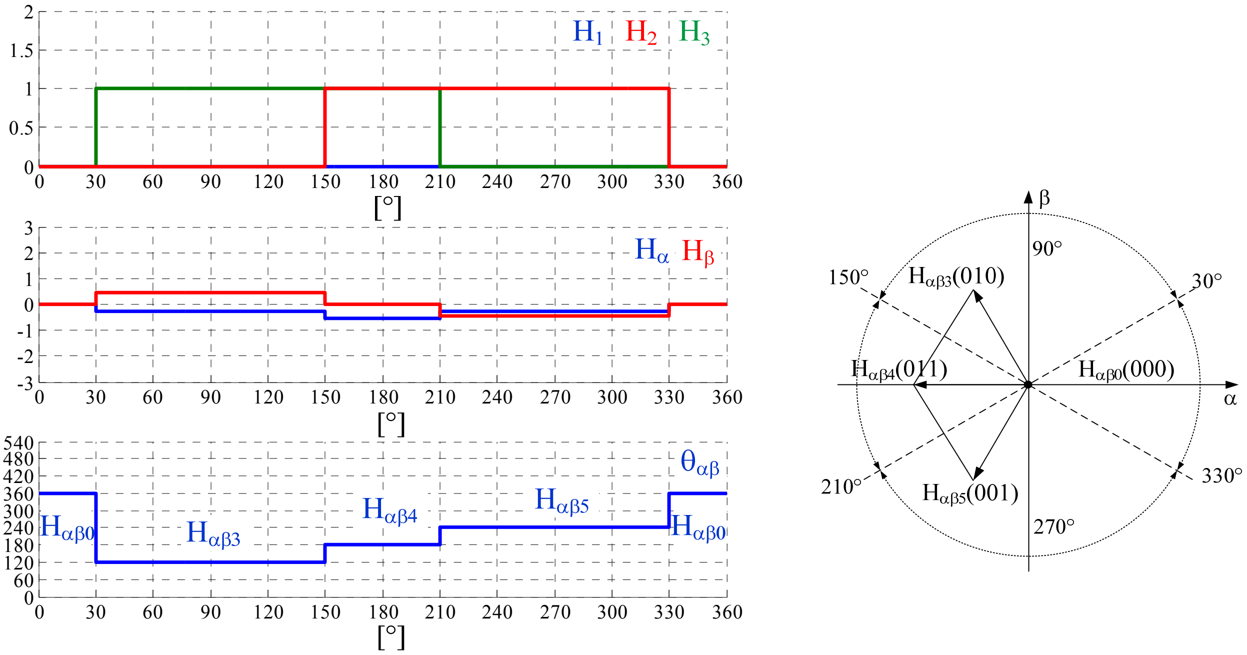

Figure 5.11 Single fault affects the Hall sensors signals with H_1=0 and representation on the αβ plane.

Similar considerations can be made in case of double faults, where two hall position sensors keep constant their states; a total of 12 possible faults exist. It will be useful to distinguish the case when both the faulty sensors keep the same state as reported in Figure 5.12 with $H_1 = H_3 = 1$ from the mixed cases as reported in Figure 5.13 with $H_2 = 1$ and $H_3 = 0$. Although each fault defines a particular $\vec{\mathbf{H}}_{\alpha\beta}$ locus, when both the sensors have the same state the zero vector, V_7 or V_0, will appear on the locus, while in the other cases it will not appear. The sector width in this case will be always 180° and with only one healthy sensor it is not possible to understand the rotor direction nor perform a startup.

Exploiting the information given by the $\vec{\mathbf{H}}_{\alpha\beta}$ locus, the fault detection can be implemented as suggested by [20], for a single fault after check for the presence of the zero vector it is necessary to wait for the next position of the vector $\vec{\mathbf{H}}_{\alpha\beta}$ in this way, the faulty sensor can be identified unequivocally within 360°. The identification of a double fault is more complex; moreover, it can be well performed only when the rotor is rotating in one direction, i.e. not during a speed reversal. When both sensors have the same state 0 or 1, as shown in Figure 5.12 the zero vector appears in the locus therefore an erroneous single fault detection could be made. This can be avoided considering after the single fault identification another sensor transition. The distinction from single fault to double fault will require in the worst case 480°, instead for a mixed double fault as that one presented in Figure 5.13 the identification is based on the fact that $\vec{\mathbf{H}}_{\alpha\beta}$ switches back and forth in only two positions, depending on the group of these two vectors. The double fault will be detected and identified unequivocally, after waiting for three sensor transitions and in the worst case it requires 540°.

It is worth noting that this procedure can be generically adopted for all types of drive equipped with hall effect position sensors.

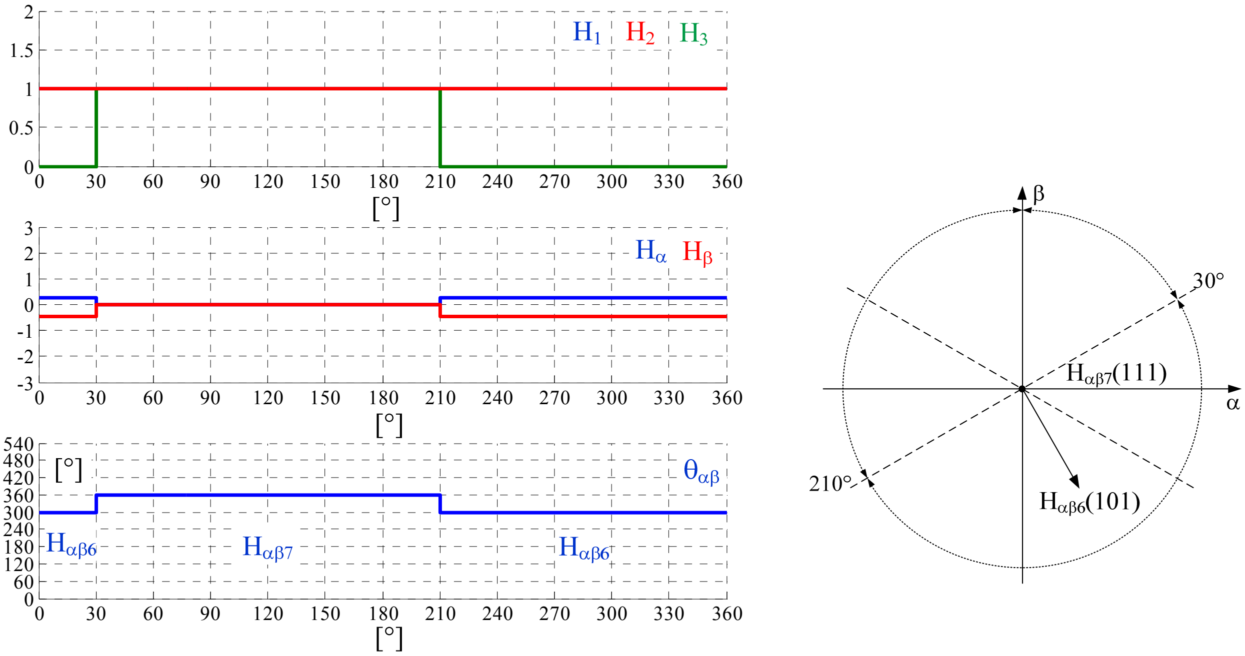

Figure 5.12 Double fault affects the Hall sensors signals with H_1=1 H_3=1and representation on the αβ plane.

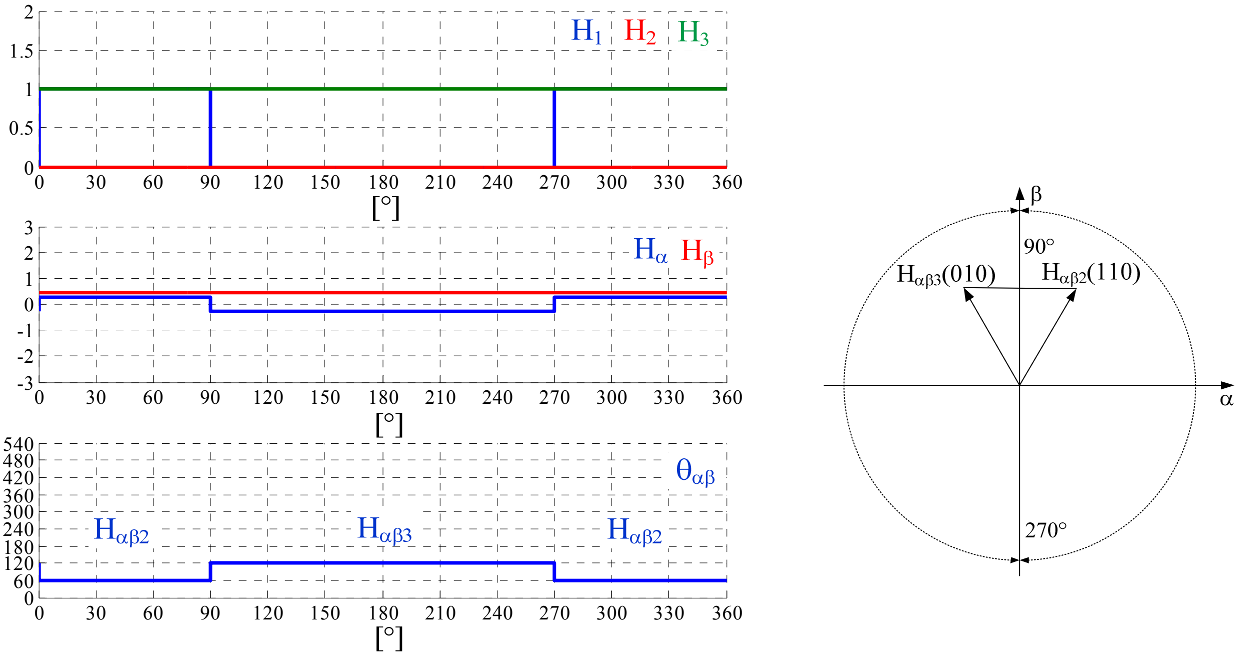

Figure 5.13 Double fault affects the Hall sensors signals with H_2=1 H_3=0 and representation on the αβ plane.

5.2.1 Fault compensation

As before discussed during one or more hall position sensors faults the switches power converter will be incorrectly turned on and off. In order to avoid the consequent instability in the drive three modified rotor position and speed estimation structures have been adopted: VTO, ZOA and HO.

A. Fault compensation for the Vector Tracking Observer

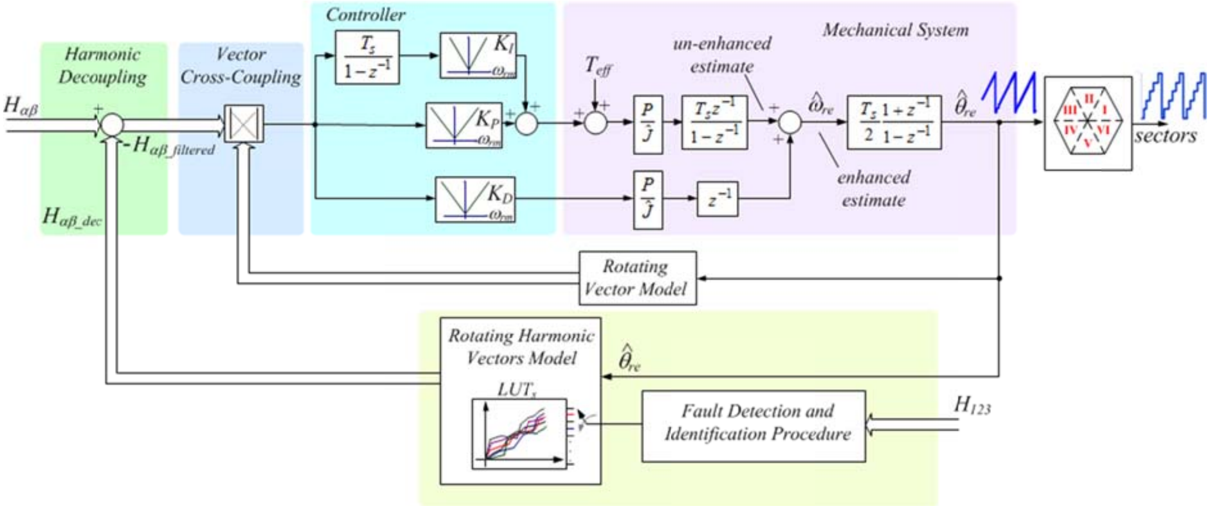

Figure 5.14 B lock diagram of the fault tolerant vector tracking observer with harmonic decoupling.

Figure 5.14 shows the block diagram of the VTO in the Z domain suitably modified to be adapted for a BLDC drive; six parts can be identified:

- the harmonic decoupling of the rotating vector $\vec{\mathbf{H}}_{\alpha\beta}$, that generates two sinusoidal signals shifted by 90°;
- the rotating harmonic vectors model that is realized by different look up tables, which store the high order harmonics;
- the vector cross product, using this “heterodyne” process can be obtained a signal proportional to ($\theta_{re} - \hat{\theta}_{re}$);
- a state controller composed of a proportional plus an integral action is applied to force the error ($\theta_{re} - \hat{\theta}_{re}$) to zero;
- the mechanical system including the torque command feed-forward, obtained considering the input torque latch interfaced;
- the high to low resolution conversion that is specific for the BLDC drive.

The harmonic decoupling is performed on the base of a Fourier series of the rotating vector $\vec{\mathbf{H}}_{\alpha\beta}$, composed of different harmonics, some of them defining the vector $\vec{\mathbf{H}}^{+}_{\alpha\beta}$ rotating in forward direction and others defining the vector $\vec{\mathbf{H}}^{-}_{\alpha\beta}$ rotating in reverse direction.

$$\vec{\mathbf{H}}_{\alpha\beta} = \vec{\mathbf{H}}^{+}_{\alpha\beta} + \mathrm{eq}\,\vec{\mathbf{H}}^{-}_{\alpha\beta} \tag{5.2.1.1}$$

$$\vec{\mathbf{H}}^{+}_{\alpha\beta} = e^{j(\theta_{re}-\frac{\pi}{6})} + \frac{1}{7}e^{j(7\theta_{re}-\frac{\pi}{6})} + \frac{1}{13}e^{j(13\theta_{re}-\frac{\pi}{6})} + \dots \tag{5.2.1.2}$$

$$\vec{\mathbf{H}}^{-}_{\alpha\beta} = -\frac{1}{5}e^{-j(5\theta_{re}+\frac{\pi}{6})} - \frac{1}{11}e^{-j(11\theta_{re}+\frac{\pi}{6})} + \dots \tag{5.2.1.3}$$

Since the components H_α and H_β, of the rotating vector $\vec{\mathbf{H}}_{\alpha\beta}$, are exactly known as we are operating with digital signals, their harmonic contents can be subtracted from the complete spectrum in order to carry out the fundamental one. $\vec{\mathbf{H}}_{\alpha\beta\_dec}$ is the vector of the harmonic sequence that will be subtracted from $\vec{\mathbf{H}}_{\alpha\beta}$.

$$\vec{\mathbf{H}}_{\alpha\beta\_dec} = \vec{\mathbf{H}}_{\alpha\beta} - e^{j(\theta - \pi/6)} \tag{5.2.1.4}$$

In case of a fault, the vector $\vec{\mathbf{H}}_{\alpha\beta}$ will has different high harmonics content but in a similar way as in normal operation this content can be eliminated using the suitable $\vec{\mathbf{H}}_{\alpha\beta\_dec}$ related to the type of fault. The harmonic decoupling sequence can be stored in look-up tables taking into account all the possible 18 type of faults.

$\vec{\mathbf{H}}_{\alpha\beta\_dec}$ can be obtained equivalently with the following procedure depicted in Figure 5.15.

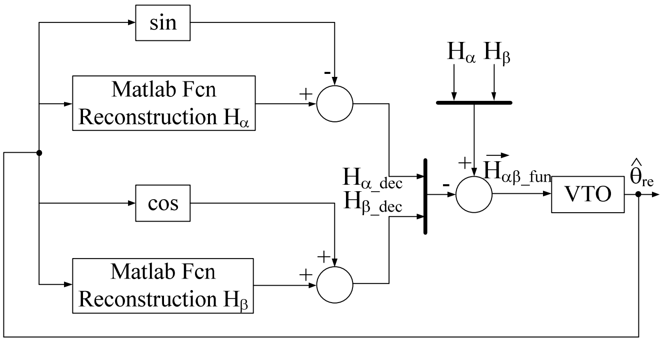

Figure 5.15 Alternative method for harmonics decoupling.

B. Fault compensation for the Zero Order Algorithm

The fault tolerant ZOA can be implemented according to the block diagram of Figure 5.16.

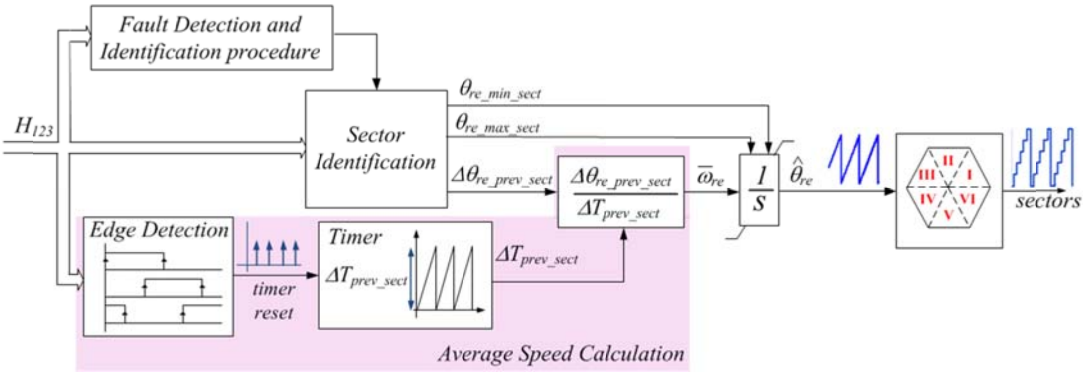

Figure 5.16 Block diagram of the fault tolerant ZOA.

This algorithm calculates the average velocity from the ratio between the width of the previous sector and time required to cross it. The time necessary to cross a sector can be calculated by detecting the edge of the hall signal while the sector width, as shown by the locus of Figure 5.9, is equal to π/3 during normal operation, but during fault this value is not constant any more but depends on the type of the fault and the sector.

Figure 5.17 and Figure 5.18 show the representation of the lower and upper sector boundaries, indicated with $\theta_{re\_min\_sect}$ and $\theta_{re\_max\_sect}$ and the sector width, $\Delta\theta_{re\_prev\_sect}$, in case of normal and faulty operation with $H_1=1$. These quantities are adopted to calculate properly the average velocity ω_{re}.

a) b) c)

Figure 5.17 ZOA setup in normal operation: a) $\theta_{re\_min\_sect}$ b) $\theta_{re\_max\_sect}$ c) $\Delta\theta_{re\_prev\_sect}$.

a) b) c)

Figure 5.18 ZOA setup for H1=1 fault,operation: a) $\theta_{re\_min\_sect}$ b) $\theta_{re\_max\_sect}$ c) $\Delta\theta_{re\_prev\_sect}$.

For all single and double faults, the appropriate values of: $\theta_{re\_min\_sect}$, $\theta_{re\_max\_sect}$ and $\Delta\theta_{re\_prev\_sect}$ can be evaluated with the expression (5.2.1.5), where the indexes: n, k and z assume the values reported in Table 5.2 for single faults and that one of Table 5.3 for double faults. The values of: $\theta_{re\_min\_sect}$, $\theta_{re\_max\_sect}$ and $\Delta\theta_{re\_prev\_sect}$ are valid for both positive and negative rotation but in the latter case $\theta_{re\_min\_sect}$ and $\theta_{re\_max\_sect}$ are swapped. In any operative conditions, the high resolution rotor position can be obtained from the numerical integration of the average velocity calculated with (5.4),.

$$\begin{aligned} \Delta\theta_{re\_prev\_sect} &= n\cdot 60^\circ \\ \theta_{re\_min\_sect} &= k\cdot 30^\circ \\ \theta_{re\_max\_sect} &= z\cdot 30^\circ \end{aligned} \tag{5.2.1.5}$$

Table 5.2 ZOA Setup for Single Faults.

	$H_1=1$				$H_2=1$				$H_3=1$		
	n	*k*	*z*		*n*	*k*	*z*		*n*	*k*	*z*
$\mathbf{H}_{\alpha\beta 1}$	2	11	1	$\mathbf{H}_{\alpha\beta 2}$	1	11	3	$\mathbf{H}_{\alpha\beta 4}$	1	3	7
$\mathbf{H}_{\alpha\beta 2}$	1	1	5	$\mathbf{H}_{\alpha\beta 3}$	2	3	5	$\mathbf{H}_{\alpha\beta 5}$	2	7	9
$\mathbf{H}_{\alpha\beta 6}$	1	7	11	$\mathbf{H}_{\alpha\beta 4}$	1	5	9	$\mathbf{H}_{\alpha\beta 6}$	1	9	1
$\mathbf{H}_{\alpha\beta 7}$	2	5	7	$\mathbf{H}_{\alpha\beta 7}$	2	9	11	$\mathbf{H}_{\alpha\beta 7}$	2	1	3
	$H_1=0$				$H_2=0$				$H_3=0$		
	n	*k*	*z*		*n*	*k*	*z*		*n*	*k*	*z*
$\mathbf{H}_{\alpha\beta 0}$	2	11	1	$\mathbf{H}_{\alpha\beta 0}$	2	3	5	$\mathbf{H}_{\alpha\beta 0}$	2	7	9
$\mathbf{H}_{\alpha\beta 3}$	1	1	5	$\mathbf{H}_{\alpha\beta 1}$	1	11	3	$\mathbf{H}_{\alpha\beta 1}$	1	9	1
$\mathbf{H}_{\alpha\beta 4}$	2	5	7	$\mathbf{H}_{\alpha\beta 5}$	1	5	9	$\mathbf{H}_{\alpha\beta 2}$	2	1	3
$\mathbf{H}_{\alpha\beta 5}$	1	7	11	$\mathbf{H}_{\alpha\beta 6}$	2	9	11	$\mathbf{H}_{\alpha\beta 3}$	1	3	7

Table 5.3 ZOA Setup for Double Faults.

H_1=1 H_2=1				**H_1=1 H_3=1**				**H_2=1 H_3=1**			
	n	*k*	*z*		*n*	*k*	*z*		*n*	*k*	*z*
$\mathbf{H}_{\alpha\beta 2}$	3	11	5	$\mathbf{H}_{\alpha\beta 6}$	3	7	1	$\mathbf{H}_{\alpha\beta 4}$	3	3	9
$\mathbf{H}_{\alpha\beta 7}$	3	5	11	$\mathbf{H}_{\alpha\beta 7}$	3	1	7	$\mathbf{H}_{\alpha\beta 7}$	3	9	3
$H_1=0\ H_2=0$				$H_1=0\ H_3=0$				$H_2=0\ H_3=0$			
	n	*k*	*z*		*n*	*k*	*z*		*n*	*k*	*z*
$\mathbf{H}_{\alpha\beta 0}$	3	5	11	$\mathbf{H}_{\alpha\beta 0}$	3	7	1	$\mathbf{H}_{\alpha\beta 0}$	3	3	9
$\mathbf{H}_{\alpha\beta 5}$	3	11	5	$\mathbf{H}_{\alpha\beta 3}$	3	1	7	$\mathbf{H}_{\alpha\beta 1}$	3	9	3
$H_1=1\ H_2=0$				$H_1=1\ H_3=0$				$H_2=1\ H_3=0$			
	n	*k*	*z*		*n*	*k*	*z*		*n*	*k*	*z*
$\mathbf{H}_{\alpha\beta 1}$	3	11	5	$\mathbf{H}_{\alpha\beta 1}$	3	7	1	$\mathbf{H}_{\alpha\beta 2}$	3	9	3
$\mathbf{H}_{\alpha\beta 6}$	3	5	11	$\mathbf{H}_{\alpha\beta 2}$	3	1	7	$\mathbf{H}_{\alpha\beta 3}$	3	3	9
$H_1=0\ H_2=1$				$H_1=0\ H_3=1$				$H_2=0\ H_3=1$			
	n	*k*	*z*		*n*	*k*	*z*		*n*	*k*	*z*
$\mathbf{H}_{\alpha\beta 3}$	3	11	5	$\mathbf{H}_{\alpha\beta 4}$	3	1	7	$\mathbf{H}_{\alpha\beta 5}$	3	3	9
$\mathbf{H}_{\alpha\beta 4}$	3	5	11	$\mathbf{H}_{\alpha\beta 5}$	3	7	1	$\mathbf{H}_{\alpha\beta 6}$	3	9	3

C. Fault compensation for the Hybrid Observer

The fault tolerant HO block diagram is presented in Figure 5.19.

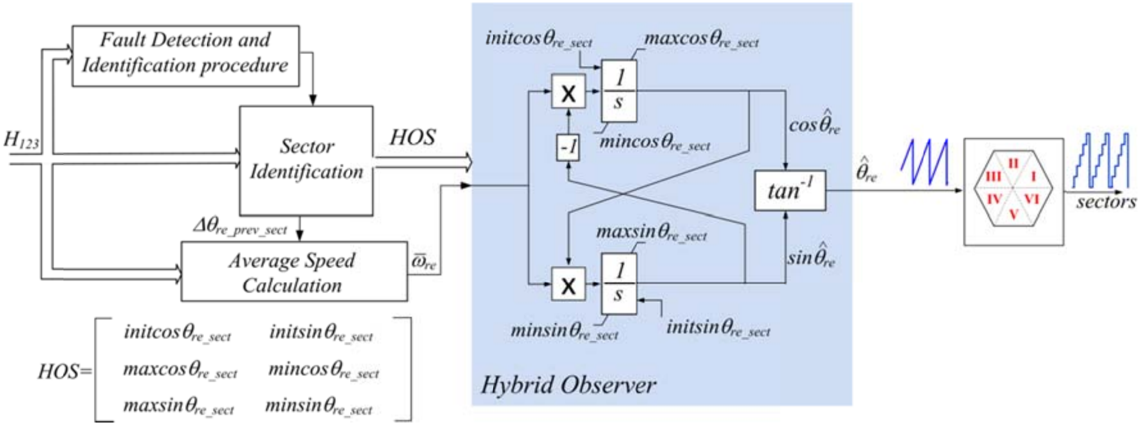

Figure 5.19 Block diagram of the fault tolerant Hybrid observer.

It is fundamentally based on the integration of the differential equation (5.9) below reported for simplicity.

$$\frac{d}{dt}\begin{bmatrix}\cos\theta_{re}\\ \sin\theta_{re}\end{bmatrix}=\begin{bmatrix}0 & -\omega_{re}\\ \omega_{re} & 0\end{bmatrix}\begin{bmatrix}\cos\theta_{re}\\ \sin\theta_{re}\end{bmatrix}$$

ω_{re} is the average velocity that can be obtained as already shown for the ZOA with equation (5.4), solving the differential equation, the components $\cos\hat{\theta}_{re}$ and $\sin\hat{\theta}_{re}$ are defined hence the estimated position can be obtained according to (5.2.1.6):

$$\hat{\theta}_{re}=\operatorname{atan}\left(\frac{\sin\hat{\theta}_{re}}{\cos\hat{\theta}_{re}}\right) \qquad (5.2.1.6)$$

The position estimated with (5.2.1.6) has a high resolution hence as is shown in the block diagram of Figure 5.19, it is quantized for BLDC commutation. Also in this HO the integration of the quantities $\cos\hat{\theta}_{re}$ and $\sin\hat{\theta}_{re}$ need to be initialized defining the following quantities: $\text{initcos}\theta_{re\_sect}$, $\text{initsin}\theta_{re\_sect}$ and the definitions of limit values: $\text{maxcos}\theta_{re\_sect}$, $\text{maxsin}\theta_{re\_sect}$, $\text{mincos}\theta_{re\_sect}$, $\text{minsin}\theta_{re\_sect}$, identified in the block diagram as Hybrid observer setup (HOS). Figure 5.20 shows two operating conditions for determining the initializations and the bound values of sin and cos functions, in case of normal and faulty operations; in the last case with $H_1 = 1$. During fault operations the sector width is not constant so it will be necessary consider the correct value of $\Delta\theta_{re\_prev}$ to calculate the average velocity. Moreover it will be necessary to change also the HOS, hence also these variables can be defined off-line and stored on a LUT for every 18 faults, but in this case with respect to the ZOA 7 variables against 3 have to be stored.

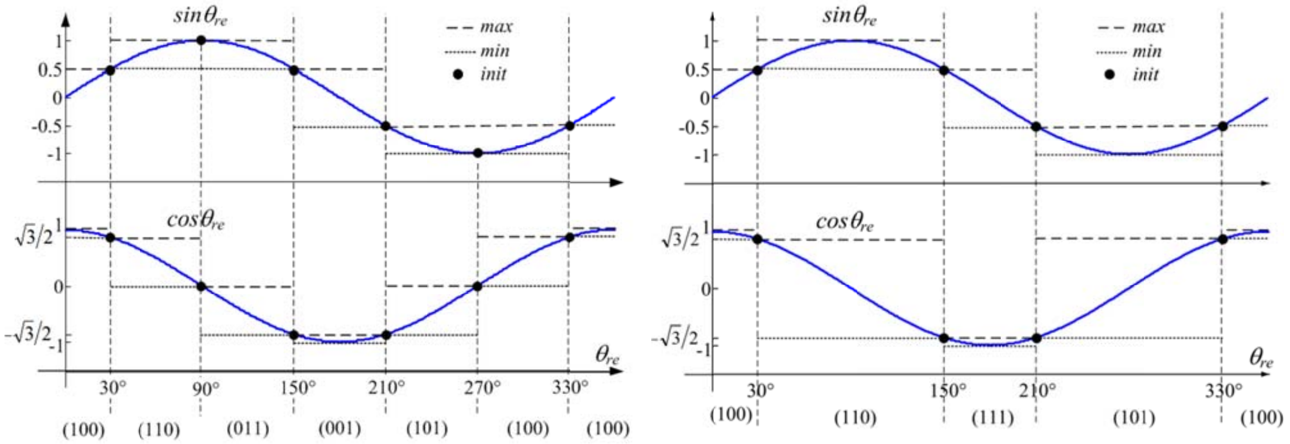

a)

b)

Figure 5.20 HOS for: a) normal operation, b) H_1=1 fault.

The following tables summarize the HOS in case of single and double faults, respectively Table 5.4 and Table 5.5, and equations (5.2.1.7) are used to calculate the HOS values, for positive and negative speed and only the index “r” needs to be changed considering the value “r_f” for forward direction and “r_r” for reverse direction.

$$\begin{aligned}
&\text{init}\cos\theta_{re\_sect}=\cos(r\cdot 30°)\\
&\text{max}\cos\theta_{re\_sect}=\cos(s\cdot 30°)\\
&\text{min}\cos\theta_{re\_sect}=\cos(t\cdot 30°)\\
&\text{init}\sin\theta_{re\_sect}=\sin(u\cdot 30°)\\
&\text{max}\sin\theta_{re\_sect}=\sin(v\cdot 30°)\\
&\text{min}\sin\theta_{re\_sect}=\sin(w\cdot 30°)
\end{aligned} \qquad (5.2.1.7)$$

Table 5.4 HO Setup for Single Faults.

$H_1=1$							**$H_2=1$**							**$H_3=1$**						
	r_f	r_r	s	t	u	v		r_f	r_r	s	t	u	v		r_f	r_r	s	t	u	v
$\mathbf{H_{\alpha\beta1}}$	11	1	0	1	1	11	$\mathbf{H_{\alpha\beta2}}$	11	3	0	3	3	11	$\mathbf{H_{\alpha\beta4}}$	3	7	3	6	3	7
$\mathbf{H_{\alpha\beta2}}$	1	5	1	5	3	5	$\mathbf{H_{\alpha\beta3}}$	3	5	3	5	3	5	$\mathbf{H_{\alpha\beta5}}$	7	9	9	7	7	9
$\mathbf{H_{\alpha\beta6}}$	7	11	11	7	9	11	$\mathbf{H_{\alpha\beta4}}$	5	9	9	6	5	9	$\mathbf{H_{\alpha\beta6}}$	9	1	0	9	1	9
$\mathbf{H_{\alpha\beta7}}$	5	7	7	6	5	7	$\mathbf{H_{\alpha\beta7}}$	9	11	11	9	11	9	$\mathbf{H_{\alpha\beta7}}$	1	3	1	3	3	1
$H_1=0$							**$H_2=0$**							**$H_3=0$**						
	r_f	r_r	s	t	u	v		r_f	r_r	s	t	u	v		r_f	r_r	s	t	u	v
$\mathbf{H_{\alpha\beta0}}$	11	1	0	1	1	11	$\mathbf{H_{\alpha\beta0}}$	3	5	3	5	3	5	$\mathbf{H_{\alpha\beta0}}$	7	9	9	7	7	9
$\mathbf{H_{\alpha\beta3}}$	1	5	1	5	3	5	$\mathbf{H_{\alpha\beta1}}$	11	3	0	3	3	11	$\mathbf{H_{\alpha\beta1}}$	9	1	0	9	1	9
$\mathbf{H_{\alpha\beta4}}$	5	7	7	6	5	7	$\mathbf{H_{\alpha\beta5}}$	5	9	9	6	5	9	$\mathbf{H_{\alpha\beta2}}$	1	3	1	3	3	1
$\mathbf{H_{\alpha\beta5}}$	7	11	11	7	9	11	$\mathbf{H_{\alpha\beta6}}$	9	11	11	9	11	9	$\mathbf{H_{\alpha\beta3}}$	3	7	3	6	3	7

Table 5.5 HO setup for double faults.

$H_1=1$ $H_2=1$							**$H_1=1$ $H_3=1$**							**$H_2=1$ $H_3=1$**						
	r_f	r_r	s	t	u	v		r_f	r_r	s	t	u	v		r_f	r_r	s	t	u	v
$\mathbf{H_{\alpha\beta2}}$	11	5	0	5	3	11	$\mathbf{H_{\alpha\beta6}}$	7	1	0	7	1	9	$\mathbf{H_{\alpha\beta4}}$	3	9	3	6	3	9
$\mathbf{H_{\alpha\beta7}}$	5	11	11	6	5	9	$\mathbf{H_{\alpha\beta7}}$	1	7	1	6	3	7	$\mathbf{H_{\alpha\beta7}}$	9	3	0	9	3	9
$H_1=0$ $H_2=0$							**$H_1=0$ $H_3=0$**							**$H_2=0$ $H_3=0$**						
	r_f	r_r	s	t	u	v		r_f	r_r	s	t	u	v		r_f	r_r	s	t	u	v
$\mathbf{H_{\alpha\beta0}}$	11	5	0	5	3	11	$\mathbf{H_{\alpha\beta0}}$	7	1	0	7	1	9	$\mathbf{H_{\alpha\beta0}}$	3	9	3	6	3	9
$\mathbf{H_{\alpha\beta5}}$	5	11	11	6	5	9	$\mathbf{H_{\alpha\beta3}}$	1	7	1	6	3	7	$\mathbf{H_{\alpha\beta1}}$	9	3	0	9	3	9
$H_1=1$ $H_2=0$							**$H_1=1$ $H_3=0$**							**$H_2=1$ $H_3=0$**						
	r_f	r_r	s	t	u	v		r_f	r_r	s	t	u	v		r_f	r_r	s	t	u	v
$\mathbf{H_{\alpha\beta1}}$	11	5	0	5	3	11	$\mathbf{H_{\alpha\beta1}}$	7	1	0	7	1	9	$\mathbf{H_{\alpha\beta2}}$	9	3	0	9	3	9
$\mathbf{H_{\alpha\beta6}}$	5	11	11	6	5	9	$\mathbf{H_{\alpha\beta2}}$	1	7	1	6	3	7	$\mathbf{H_{\alpha\beta3}}$	3	9	3	6	3	9
$H_1=0$ $H_2=1$							**$H_1=0$ $H_3=1$**							**$H_2=0$ $H_3=1$**						
	r_f	r_r	s	t	u	v		r_f	r_r	s	t	u	v		r_f	r_r	s	t	u	v
$\mathbf{H_{\alpha\beta3}}$	11	5	0	5	3	11	$\mathbf{H_{\alpha\beta4}}$	7	1	0	7	1	9	$\mathbf{H_{\alpha\beta5}}$	3	9	3	6	3	9
$\mathbf{H_{\alpha\beta4}}$	5	11	11	6	5	9	$\mathbf{H_{\alpha\beta5}}$	1	7	1	6	3	7	$\mathbf{H_{\alpha\beta6}}$	9	3	0	9	3	9

5.3 Simulation and experimental results

Simulation tests have been performed with a BLDC drive, whose parameters are listed in Table 5.6; a first simulation has been performed implementing only the current control loop while the mechanical speed has been fixed at 50 rad/s; at a certain instant a fault $H_1 = 1$ is applied, it can be noted in Figure 5.21 that the current waveforms as well as the torque present a significant ripple.

Table 5.6 BLDC machine's parameters.

Rated Power	2.3 kW
Rated Torque	7.6 Nm
Rated Speed	3000 rpm
Rotor Inertia	$1.05\ 10^{-3}$ kg m^2
Rated Voltage	345 V
Rated Current	5.4 A
Pole Pairs	3

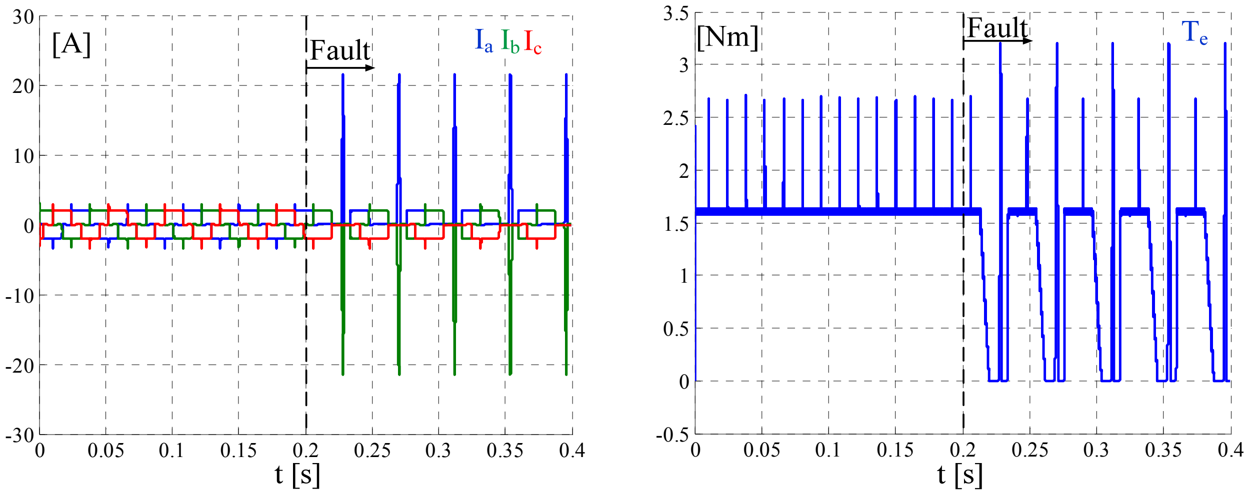

Figure 5.21 Fault H_1=1 on the BLDC drive under current control.

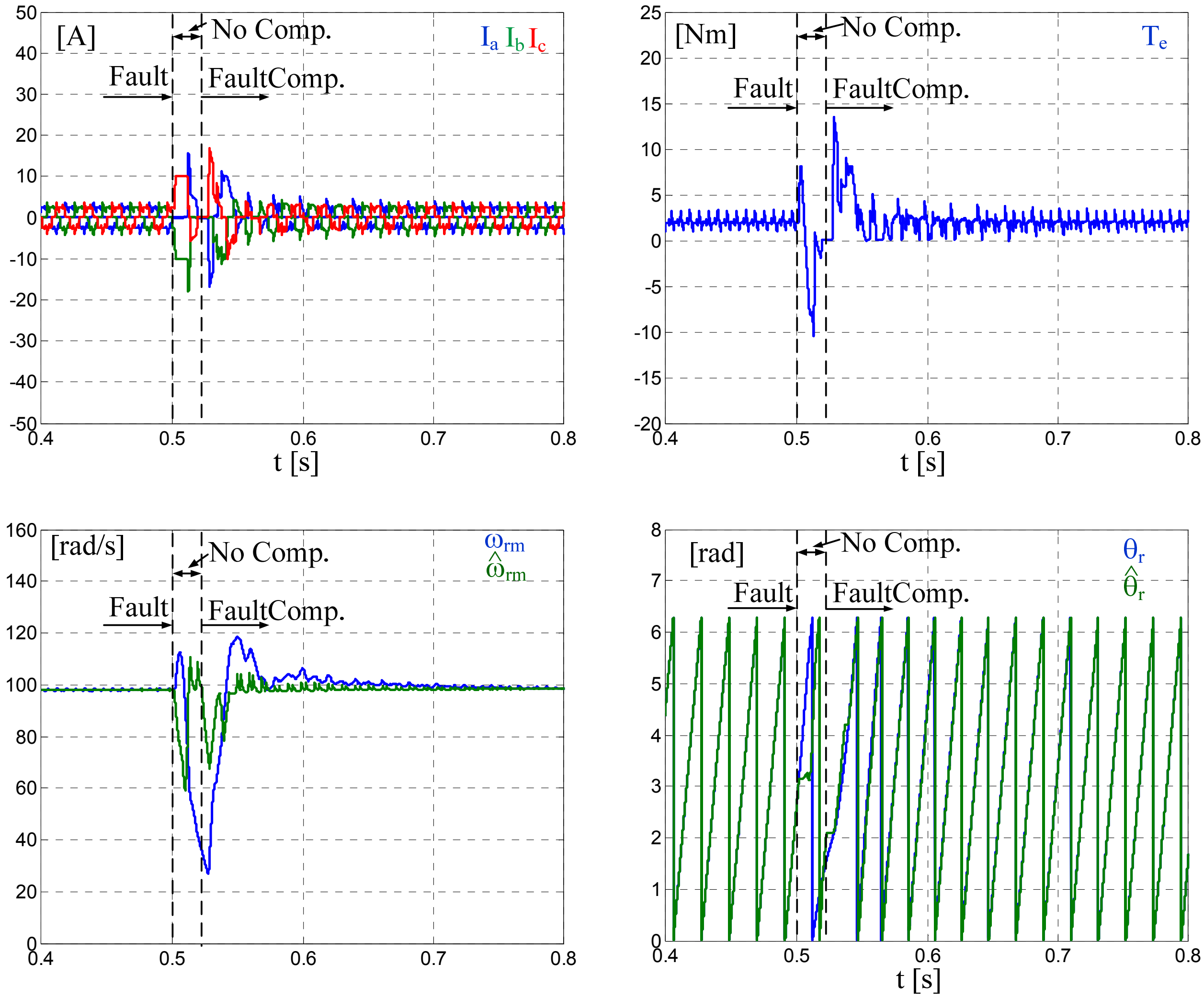

Figure 5.22 Hall effect position sensor fault H_1=1 on a BLDC using VTO to provide the speed feedback.

The simulation results of Figure 5.22 show the behavior of the BLDC with the fault tolerant VTO, its eigenvalues are positioned considering the bandwidth frequency of 80Hz-8 Hz -0.8 Hz. The drive is speed controlled and the unenhanced VTO velocity is used as feedback signal, it is running at 100 rad/s with a torque load of 2Nm, the sensor fault H_1=1 is applied and it is intentionally not compensated for 0.1s, during this transient period a strong ripple affect the torque hence speed and position are also influenced by the incorrect harmonic decoupling, although a larger controller bandwidth will improve the dynamic response, this reduces its filtering properties and more noise will be included on the speed.

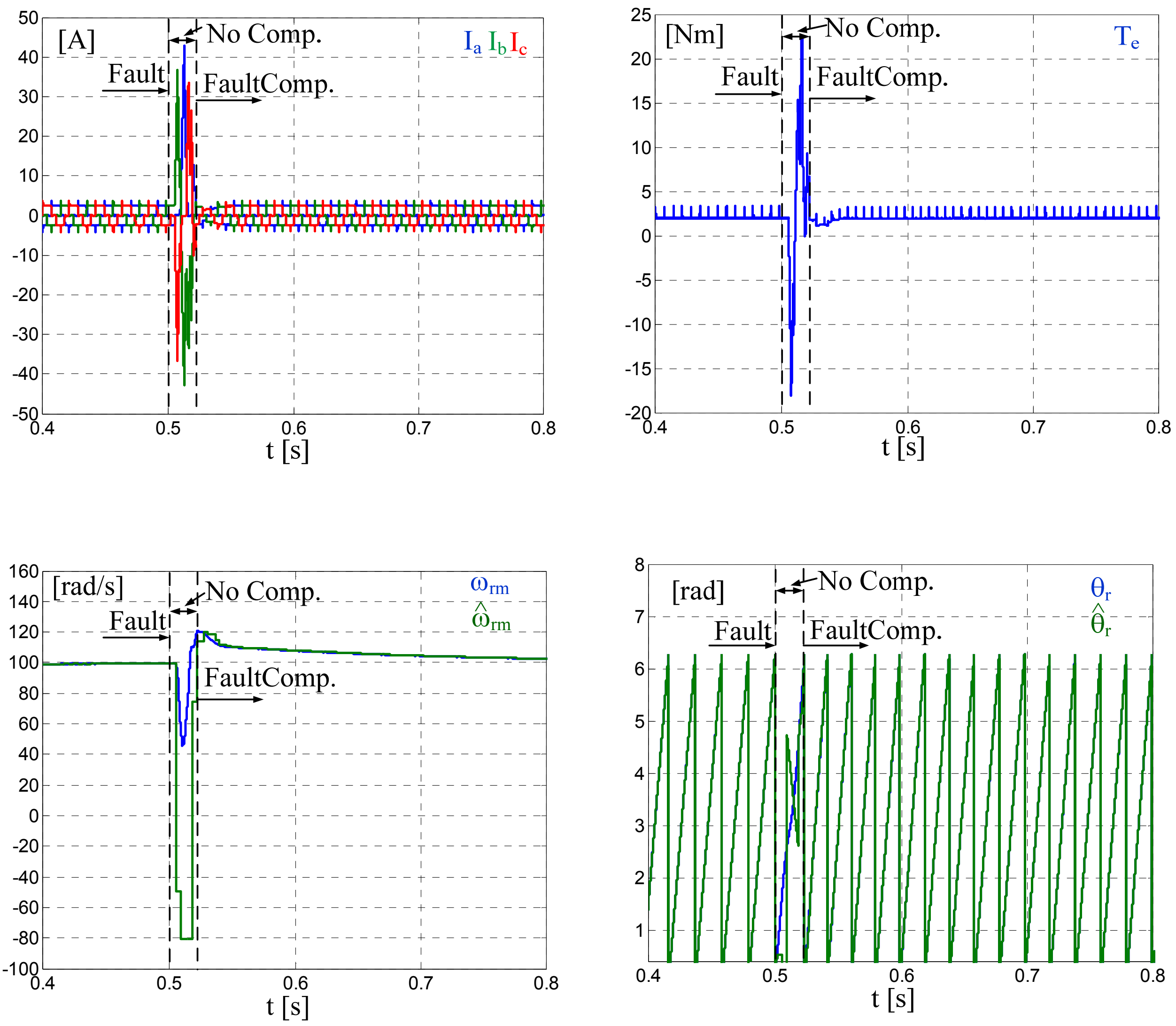

Figure 5.23 Hall effect position sensor fault $H_1=1$ on a BLDC using the ZOA.

The same test has been implemented using the ZOA, Figure 5.23, and the HO, Figure 5.24; both algorithms use the estimated average velocity as feedback in the speed loop and during the non-compensation of the fault it has an inappropriate value due to the incorrect application of equation to calculate the average speed, where the initial and boundary values are different with respect to the normal operative conditions. Soon after, the fault compensation is performed and the drive is again able to track the required speed and load.

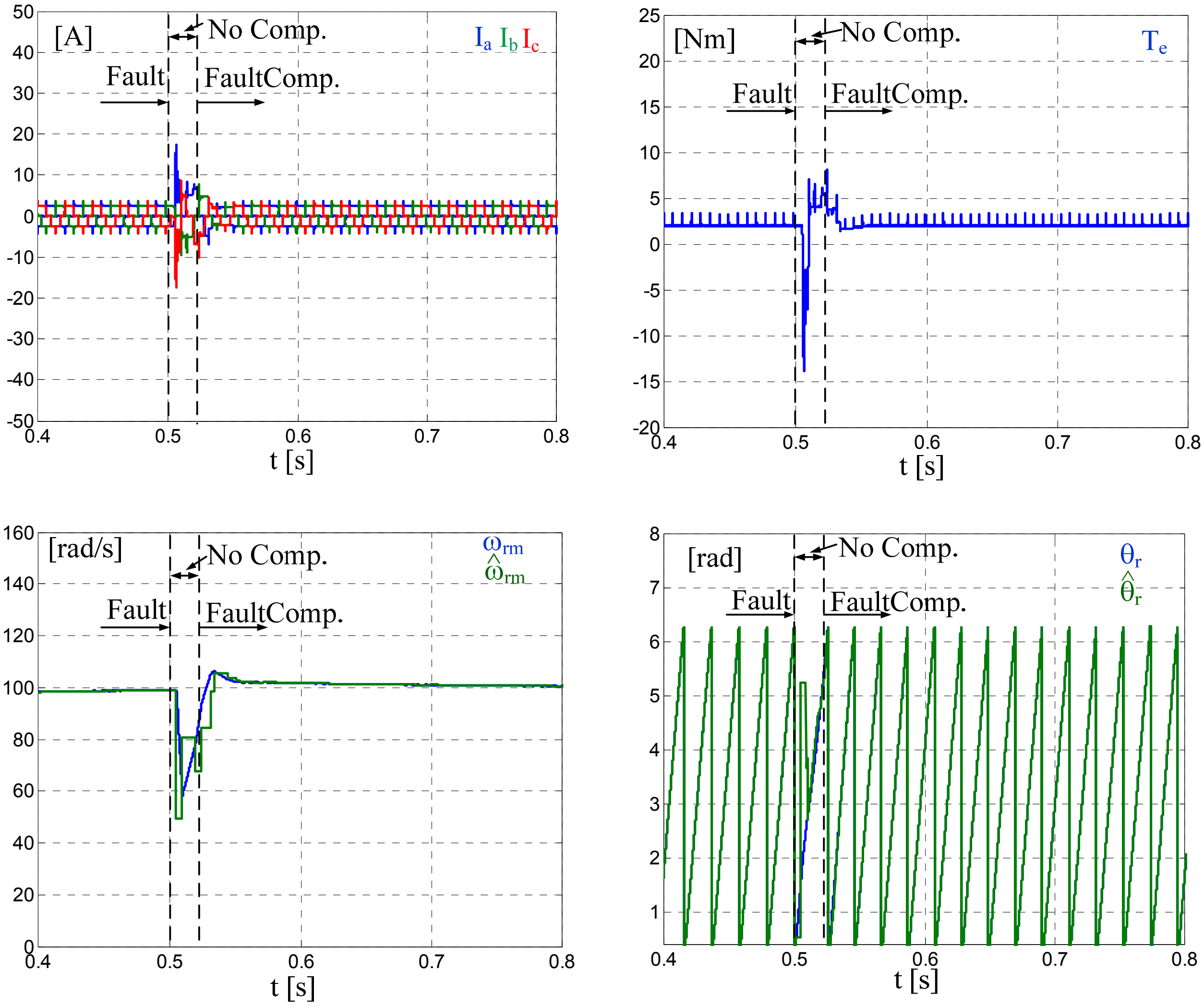

Figure 5.24 Hall effect position sensor fault H_1=1 on a BLDC using the HO.

The estimation velocity and position errors for VTO, ZOA and HO are reported in Figure 5.25, where it can be noted that all these algorithms are capable of estimating, properly the average velocity and position also with a hall effect position sensor fault.

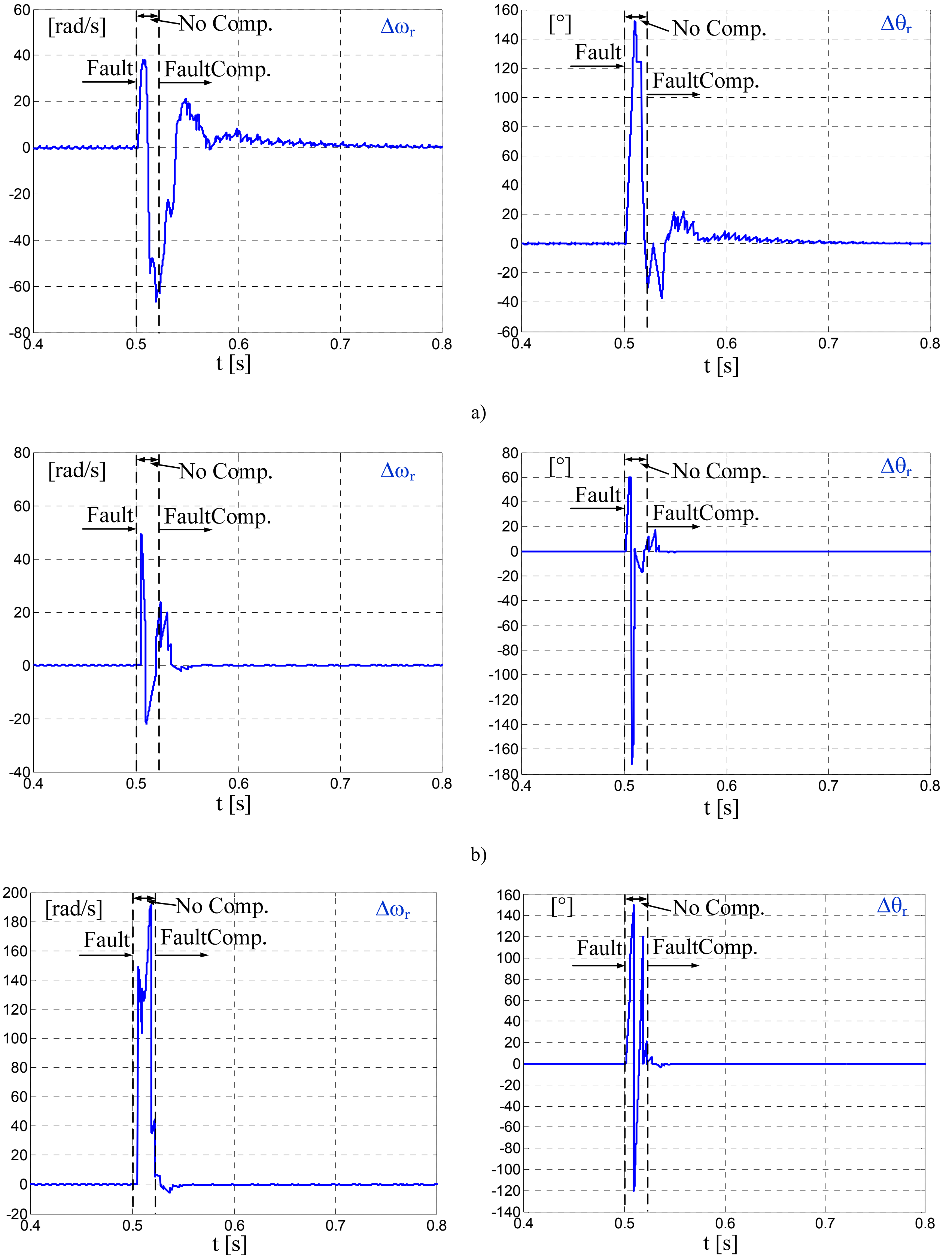

a)

b)

c)

Figure 5.25 Estimation position and velocity error with a)VTO, b)ZOA and c) HO.

The preliminary simulation results have been followed by different experimental tests; the block diagram of the test bench is reported in Figure 5.26, where a 450V DC bus feeds the three-phase converter connected to the stator windings of the BLDC machine whose parameters are reported in Table 5.6.

The drive control is based on standard PI regulators to realize the current and the speed loop, that have been tuned to achieve respectively 300Hz and 10Hz of bandwidth.

The VTO controller has been tuned to set the three eigenvalues considering the closed loop transfer function at the frequency of: 40, 4, 0.4 Hz at rated speed, these values are linearly reduced with the speed to reduce the harmonic decoupling errors [16]. All the control system is implemented with a dSpace 1104 development board, and all the routines are executed with a sample time of 100μs, the logic signals of the firing sequence are processed with an external board to implement the complementary switching modulation with a switching frequency of 10kHz.

An optical encoder with 2048 pulses per revolution is used to emulate the three Hall-effect position sensors whose sequence is included in a Matlab function according to Table 5.1; the measured position and estimated velocity are compared with the estimated position and velocity obtained from VTO, ZOA and HO.

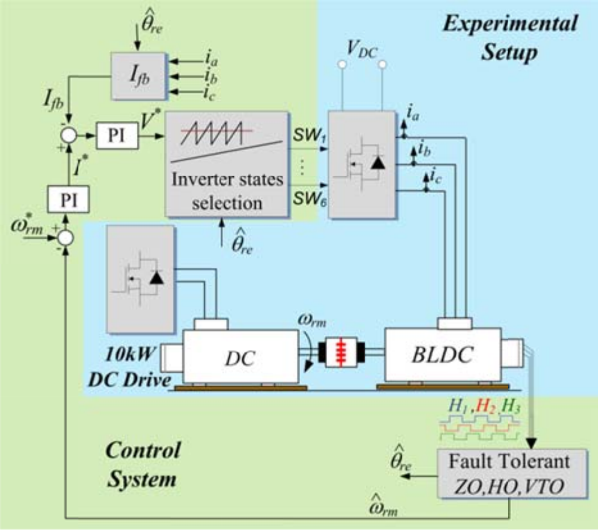

Figure 5.26 Block diagram of the experimental setup.

Figure 5.27 and Figure 5.28 show respectively a speed command tracking and a torque disturbance response with the three algorithms, during normal operative conditions with all the emulated hall position sensors working properly.

A trapezoidal speed profile with the reference values of: 20-100-20 rad/s is commanded at no load and Figure 5.27 depicts the mechanical speed ω_{rm}, the actual current I_{fb}, the mechanical speed estimation error $\Delta\omega_{rm}$ and the electrical position estimation error $\Delta\theta_{re}$. For the test with the VTO the unenhanced speed is used to realize the speed loop as a result of its filtered nature, while the average velocity $\bar{\omega}_{rm}$ is the feedback signal of the speed loop with the ZOA and HO test.

It is clearly shown that the VTO produces less ripple on the feedback current and in the estimated speed and position, thanks to its filtering properties, nevertheless, at low speed the estimation errors take more time to be reduced to zero compared with the ZOA and HO; both these two topologies introduce more noise on the feedback signals and have a very similar behavior because both utilize the average velocity $\bar{\omega}_{rm}$.

Figure 5.28 shows the same waveforms as Figure 5.27 but in this case the drive run at 20 rad/s and a 0.8 p. u. disturbance torque is applied, in this case thanks to the torque command feed-forward and using the estimation of the disturbance torque after its controller the VTO has the best performance compared to the ZOA and HO.

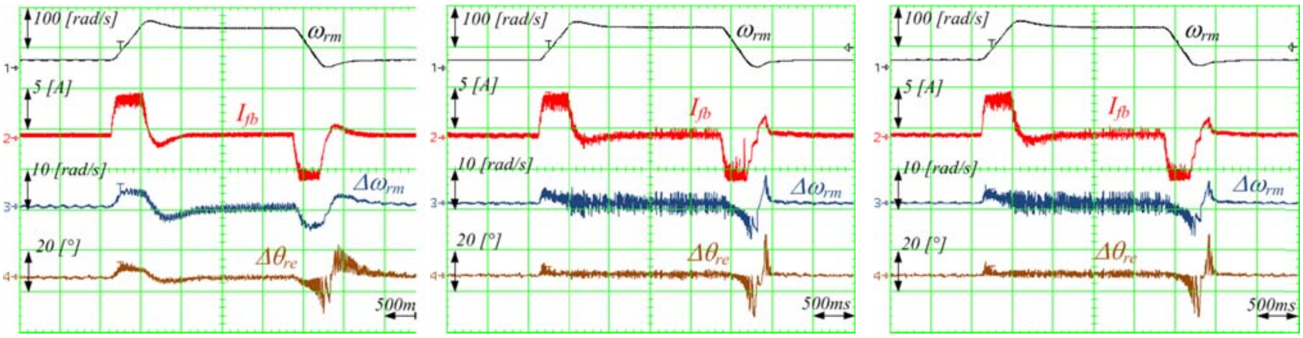

a) b) c)

Figure 5.27 No load, trapezoidal speed command tracking response: a) VTO b) ZOA c) HO.

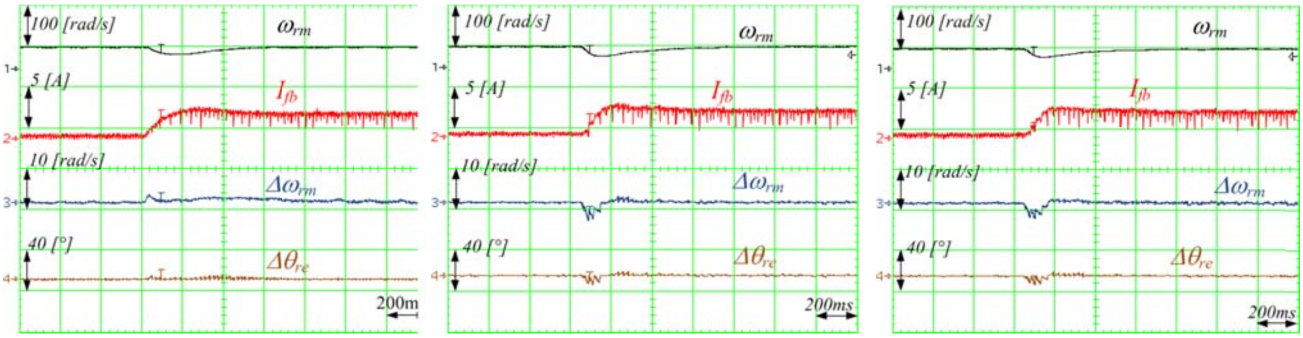

a) b) c)

Figure 5.28 Disturbance torque response: a) VTO b) ZOA c) HO.

Figure 5.29 shows the effect of the position sensors misalignment, a speed ramp profile has been applied from 20 to 100 rad/s, at no load, introducing an offset equal to +5° with respect to the standard position of H_2 and -5° on H_3 also in this case the filtering property of the VTO's controller produces a reduced ripple on the drive than the ZOA and HO.

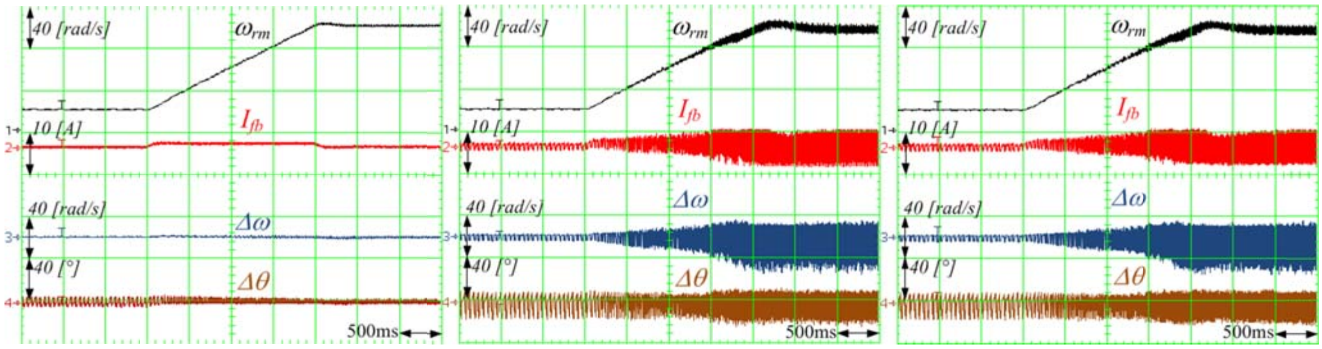

a) b) c)

Figure 5.29 Position sensors misalignment 120°+5° H_2 and -5° H_3: a) VTO b) ZOA c) HO.

The following experimental tests investigate the behavior of the VTO, ZOA and HO during faults. Figure 5.30 shows the effects on the system in case of a non-compensated single fault, for this test the speed control loop is implemented and the BLDC is rotating at 50 rad/s when a fault is emulated setting H_1=1.

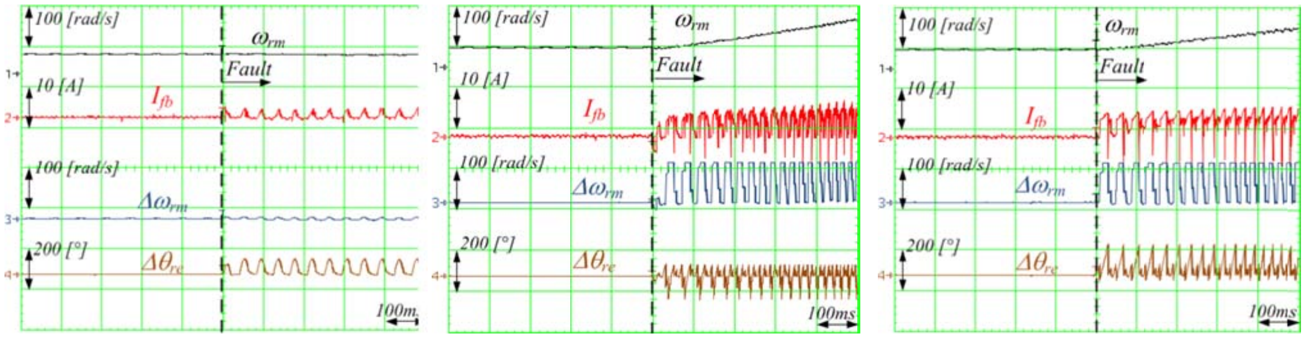

a) b) c)

Figure 5.30 Operation following a non compensated fault : a) VTO b) ZOA c) HO.

As can be noted, with the VTO, picture a), the drive is still stable although significant ripple is visible due to the incorrect harmonic decoupling of the rotating vector $\vec{\mathbf{H}}_{\alpha\beta}$, while with the ZOA and HO pictures b) and c) the drive becomes unstable, this is caused by a wrong calculation of the average velocity.

Figure 5.31 shows the results carried out implementing the fault detection, identification and compensation algorithm; a single fault H_1=1 is emulated and applied at the same instant with the VTO, ZOA and HO, in this case the angular width for the detection and identification is constant.

The drive operates at 20 rad/s with 0.6 p. u load, and the pictures show the mechanical velocity, the position estimation error and the current components I_α and I_β on the stationary frame, as can be noted with the VTO the effect of the fault during the non-compensated transient period is less visible with respect to the ZOA and HO but the reduced controller bandwidth and a finite number of higher order harmonic for the decoupling of $\overrightarrow{\mathbf{H}}_{\alpha\beta}$ introduces much more error on the estimated position visible on the position estimation error $\Delta\theta_{re}$ than that one obtained with the ZOA and HO.

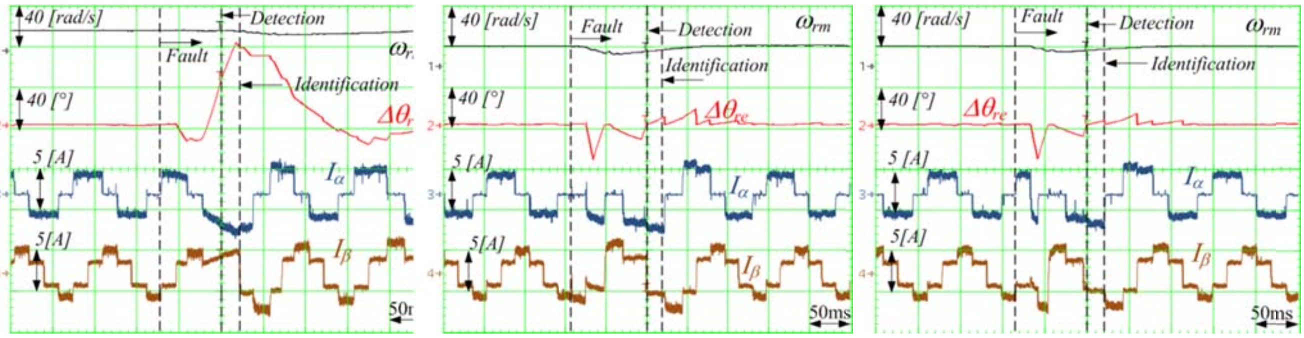

a) b) c)

Figure 5.31 Single fault compensation: a) VTO b) ZOA c) HO at 20 rad/s.

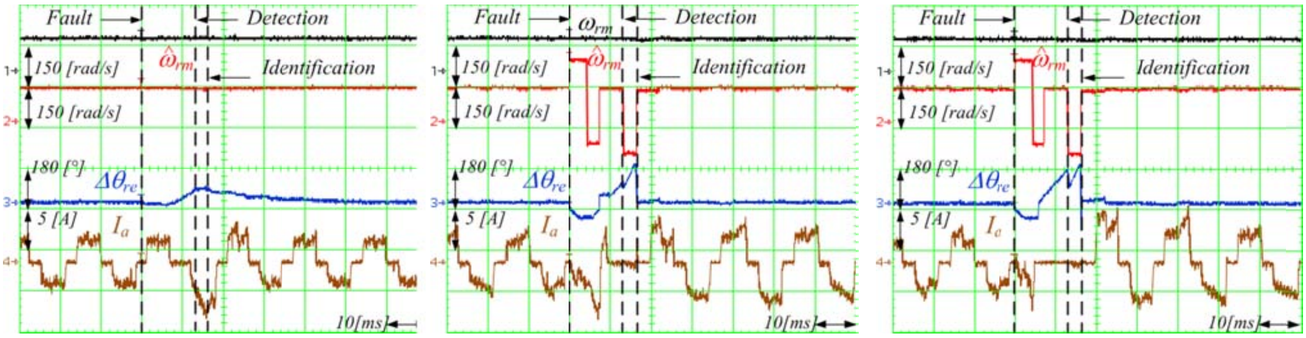

a) b) c)

Figure 5.32 Single fault compensation: a) VTO b) ZOA c) HO at 120 rad/s.

Figure 5.32 depicts the results obtained with the same setting applied to carry out Figure 5.31 but at high speed 120 rad/s, in this case since the controller bandwidth of the VTO is higher than the previous case, because it is speed dependent, the VTO shows a very limited effect on the estimated speed $\hat{\omega}_{rm}$ and on the position estimation error $\Delta\theta_{re}$, while for ZOA and the HO the wrong calculation of the average velocity during the non-compensated transient period produces a large position estimation error.

The effects of a double fault are examined with the results shown in Figure 5.33, a ramp speed profile is applied from 20 to 100 rad/s with 0.8 p. u load, both the faults H_1=1 and H_3=1 are applied at the same instant for the three algorithms; after a transient period the faults are compensated and the drive maintains a stable behavior but a different performance is visible, in fact, the first fault is applied at low speed and the position estimation error has the value of: 60° for the VTO, 20° for the ZOA and 15° for the HO; these results are consistent with those shown in Figure 5.31 where the VTO has the higher position estimation error due to a limited controller bandwidth while the non-compensated calculation of the average velocity in the ZOA and HO has a limited effect.

Instead, since the second fault is applied at high speed, the controller bandwidth of the VTO is higher, and the position estimation error becomes: 20° for the VTO, 60° for the ZOA and 70° for the HO, these results are in accordance with the tests of Figure 5.32.

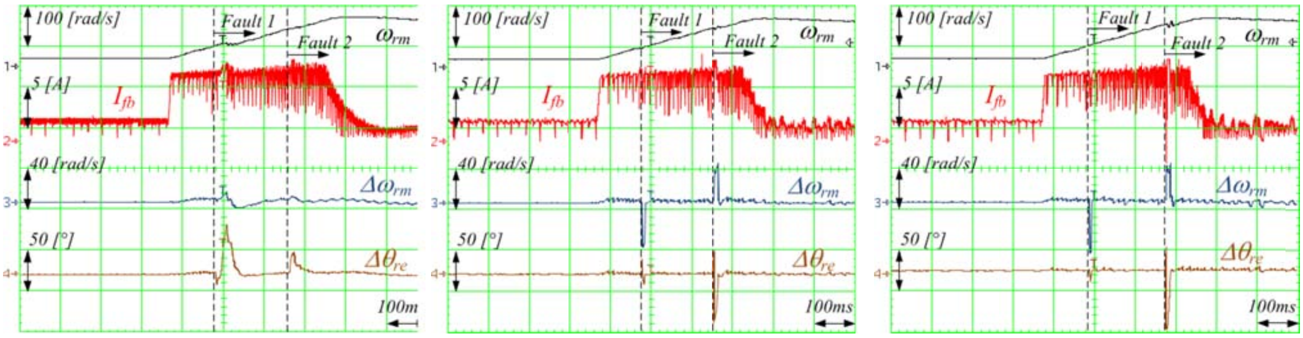

a) b) c)

Figure 5.33 Double fault compensation during speed transient: a) VTO b) ZOA c) HO.

Useful consideration can be made taking into account also the measured currents and their components on the αβ plane, some experimental tests have been conducted controlling the BLDC only with the current loop while the speed loop is enabled on the DC drive mechanically coupled to the BLDC as shown in Figure 5.26.

Figure 5.34 shows the locus of the current components during normal operations as can be expected it is hexagonal and 90° rotated in advance with respect to the hall position sensor locus because the last one represents also the quantized position of the PM rotor flux.

Figure 5.35 shows the current components locus when a single fault is applied setting H_1=1, since the locus of the hall effect position sensors is rhomboidal also the current locus is rhomboidal and shifted by 90° in advance, the operation of the BLDC drive can be performed because the speed is controlled with the coupled DC drive, during the state defined by the zero vector, in this case 111, all the converter's switches are open and the current goes to zero.

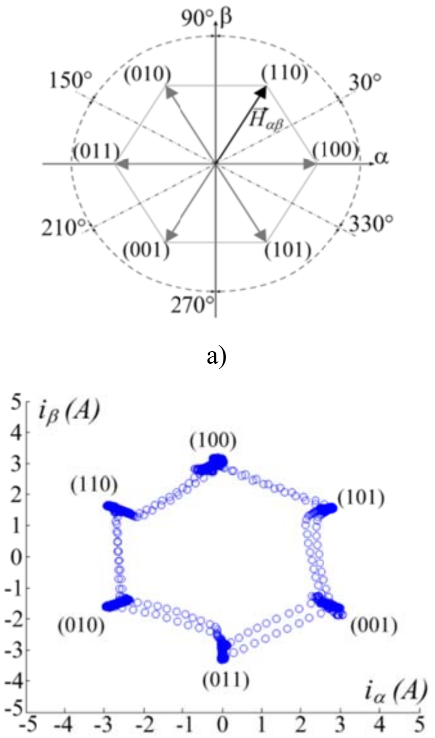

a)

b)

Figure 5.34 Quantized loci in the stationary reference frame in normal BLDC operation: a) position vector $H_{\alpha\beta}$ b) current vector $i_{\alpha\beta}$.

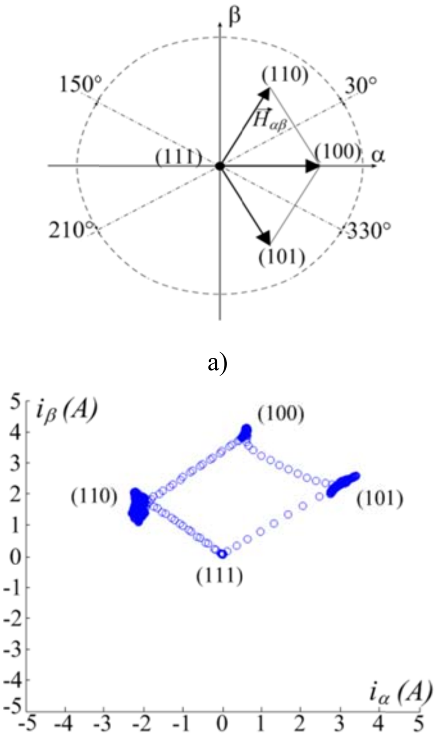

a)

b)

Figure 5.35 Quantized loci in the stationary reference frame for a $H_1 = 1$ single fault: a) position vector $H_{\alpha\beta}$ b) current vector $i_{\alpha\beta}$.

The current locus in case of double fault is shown in Figure 5.36 and Figure 5.37, in both cases only two vector states are assumed each of them for 180° electrical, hence, also in these cases the current locus is equal and 90° rotated with respect to that one of the hall position sensors. It can also be noted that in Figure 5.36 the zero vector appears while in the other does not exist.

Figure 5.38 shows the current components I_α and I_β that are reported on the $\alpha\beta$ plane which describes the locus during a fault transient. This figure has been achieved implementing the speed control on the BLDC and using the VTO, but the same results can be obtained also with the ZOA and HO. At the beginning the drive runs at a steady state and all the position sensors are healthy, the locus of the current is hexagonal as shown in Figure 5.34, when the fault is applied, in this case H_1=1 there is a transient where the locus is still hexagonal but its amplitude is increased and only when the fault is identified and compensated, the current locus during post fault operation becomes equal to that one as in normal operation.

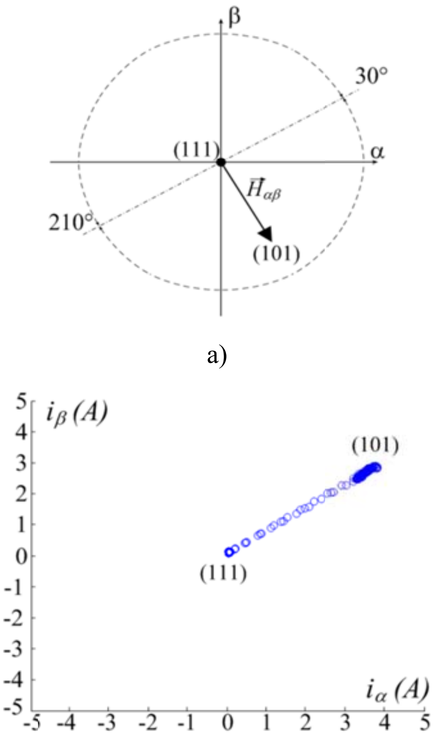

a)

b)

Figure 5.36 Quantized loci in the stationary reference frame for a H_1=1 and H_3=1 double fault: a) position vector $H_{\alpha\beta}$ b) current vector $i_{\alpha\beta}$.

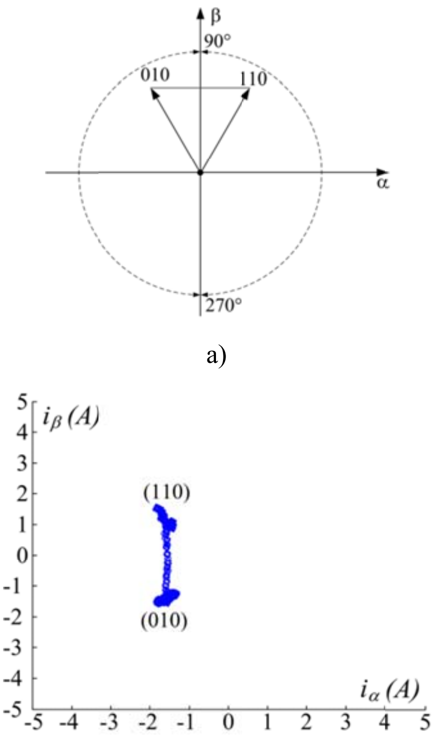

a)

b)

Figure 5.37 Quantized loci in the stationary reference frame for a H_2=1 and H_3=0double fault: a) position vector $H_{\alpha\beta}$ b) current vector $i_{\alpha\beta}$.

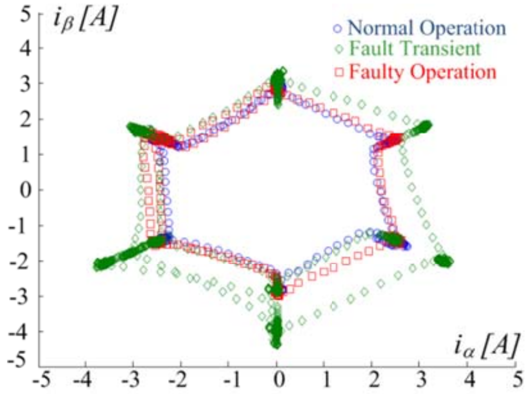

Figure 5.38 Evolution of the $i_{\alpha\beta}$ locus during a H_1=1 fault when using the fault-tolerant VTO.

5.4 Fault tolerant Multi-Drive Systems with Binary Hall-Effect Sensors

The concept of healthy drives that supports a faulty drive can be applied also in this particular case. In fact, all the approaches listed in the present chapter, can be greatly improved by considering that in case of a multi-drive application in which the mechanical variable is, in some way, correlated among the drives, the feedback signal of healthy drives participate to improve the estimation in faulty drives. Indeed, reliability and cost reduction can be greatly improved by considering that MDS with “n” drives, if they are synchronized, allow the rotor position estimation with the proposed algorithms, by using, in theory, only the hall sensors signal provided by one drive. For the considered MDS, the rotor position can be correctly estimated also in case of fault on one or two hall sensors, in fact it can be possible to use the hall sensors signal provided by another drive.

The cooperative approach that allows to create a current path, exploiting the configurations described in Chapters 2, 3 and 4, now is intended in the sense of sharing information.

5.5 Conclusions

In this chapter another aspect of the fault tolerant concept has been investigated. With respect to the previous chapters where a topology structure has been analyzed, here the fault tolerant capacity is restricted on a single drive, although the stability of a single drive is the base for the stability of a MDS. In particular, attention has been focused on BLDC drives that can be employed in commercial and low-cost applications guarantee high control performance over the entire speed region, using low cost hall effect position sensors. The possibility of one or more failures that can arise on the position sensors could lead to uncontrollability of the drive hence three standard algorithms: Vector Tracking Observer, the Zero Order Algorithm and the Hybrid Observer, have been suitably modified in order to provide the correct rotor position information in case of one or two sensor faults. With respect to other solutions no additional measures nor external hardware are necessary for post fault operations, but only a software reconfiguration is required, based on stored data on LUTs that can be easily saved on the DSP and called up when the fault is identified.

The proposed solutions have been compared by means of simulations and experimental tests.

Although in this case only three hall position sensors have been considered to define the rotor position, the fault tolerant capability as well as the stability and the disturbance rejection of the drive can be improved considering a higher number of hall effect position sensors, as in case of multi-drive systems.

5.6 References

[1] K. Iizuka, H. Uzuhashi, M. Kano, T. Endo and K. Mohri, “Microcomputer Control for Sensorless Brushless Motor”, IEEE Trans. Ind. Appl., vol. 21, no. 4, pp. 595 – 601, May/Jun. 1985.

[2] S. Ogasawara and H. Akagi, “An Approach to Position Sensorless Drive for Brushless dc Motors”, IEEE Trans. Ind. Appl., vol. 27, no. 5, pp. 928 – 933, Nov./Dec. 1991.

[3] Application Note “AN1946 SENSORLESS BLDC MOTOR CONTROL AND BEMF SAMPLING METHODS WITH ST7MC”

[4] Application note“Brushless DC Motor Control Using PIC18Fxx31 Microcontrollers”.

[5] J.X. Shen, Z.Q. Zhu, and D. Howe, “Sensorless Flux-Weakening Control of Permanent-Magnet Brushless Machines Using Third Harmonic Back EMF”, IEEE Trans. Ind. Appl., vol. 40, no. 6, pp. 1629 – 1636, Nov./Dec. 2004.

[6] J.X. Shen, Z.Q. Zhu, and D. Howe, “Practical Issues in Sensorless Control of PM Brushless Machines Using Third-Harmonic Back-EMF”, in proc. of IEEE Power Electronics and Motion Control Conference, IPEMC 2006, pp. 1-5, Jun. 2006.

[7] Shen, J. X.; and Iwasaki, S.; “Sensorless Control of Ultrahigh-Speed PM Brushless Motor Using PLL and Third Harmonic Back EMF,” IEEE Trans. Ind. Appl., vol. 53, no. 2, pp.: 421 – 428, April 2006.

[8] Gui-Jia Su; McKeever, J.W.”Low-Cost Sensorless Control of Brushless dc Motors with Improved Speed Range,”. Power Electronics, IEEE Transactions on, 2004, vol.: 19, no. 2, pp.: 296-302.

[9] T. Kim, H-W. Lee and M. Ehsani “Position sensorless brushless DC motor/generator drives: review and future trends,” Electric Power Applications, IET, 2007, vol. 1, no.: 4, pp.: 557-564.

[10] A. Consoli, G. Scarcella, and A. Testa, “Industry Application of Zero-Speed Sensorless Control Techniques for PM Synchronous Motors”, IEEE Trans. Ind. Appl., vol. 37, no. 2, pp. 513 – 521, Mar./Apr. 2001.

[11] A. Gaeta, G. Scelba, and A. Consoli, “Sensorless Vector Control of PM Synchronous Motor During Single-Phase Open-Circuit Faulted Conditions” IEEE Trans. Ind. Appl., vol. 48, no. 6, pp. 1968 – 1979, Nov./Dec. 2012.

[12] A. Griffo, et al., “The Effect of Magnetic Saturation on Sensorless Control of a Brushless Permanent Magnet Motor under AC and DC Excitation”, in proc. of IEEE Energy Conversion Congress and Exposition, ECCE 2011, pp. 1582-1589, Sep. 2011.

[13] G. Scarcella, G. Scelba, and A. Testa, “High Performace Sensorless Controls Based on HF Excitation: a Viable Solution for Future AC Motor Drives”, in proc. of IEEE Workshop on Electrical Machines Design Control and Diagnosis, WEMDCD 2015, pp 178-187, Mar. 2015.

[14] T. Tesch, “Dynamic torque estimation in a sensor limited environment,” Ph.D. preliminary examination presentation, Dept. Mech. Eng., Univ. Wisconsin, Madison, Aug. 2000.

[15] S. Morimoto, M. Sanada, and Y. Takeda, “Sinusoidal Current Drive System of Permanent Magnet Synchronous Motor with Low Resolution Position Sensors”, in proc. of IEEE IAS Annu. Meeting, IAS 1996, pp. 9-13, Oct. 1996.

[16] F. Giulii Capponi, G. De Donato, L. Del Ferraro, O. Honorati, M.C. Harke, R.D. Lorenz, “AC Brushless Drive With Low-Resolution Hall-Effect Sensors for Surface-Mounted PM Machines,” IEEE Trans. Ind. Appl, vol. 42, no. 2, pp. 526 – 535, March/April 2006.

[17] M.C. Harke, G. De Donato, F. Giulii Capponi, T.R. Tesch, and R.D. Lorenz, “Implementation Issues and Performance Evaluation of Sinusoidal, Surface-Mounted PM Machine Drives With Hall-Effect Position Sensors and a Vector-Tracking Observer”, IEEE Trans. Ind. Appl., vol. 44, no. 1, pp. 161 – 173, Jan./Feb. 2008.

[18] K.A. Corzine, and S.D. Sudhoff, “A Hybrid Observer for High Performance Brushless DC Motor Drives”, IEEE Trans. Ene. Conver., vol. 11, no. 2, pp. 318 – 323, Jun. 1996.

[19] Pillay, P.; Krishnan, R.; “Modeling, Simulation, and Analysis of Permanent-Magnet Motor Drives, Part II: The Brushless DC Motor Drive”, IEEE Trans. Ind. Appl., vol. 25, no. 2, pp. 274 – 279, March/April 1989.

[20] G. Scelba, G. De Donato, G. Scarcella, F. Giulii Capponi, and F. Bonaccorso, “Fault-Tolerant Rotor Position and Velocity Estimation Using Binary Hall-Effect Sensors for Low-Cost Vector Control Drives”, IEEE Trans. Ind. Appl., vol. 50, no. 5, pp. 1629 – 1636, Sep./Oct. 2014.

[21] Robert D. Lorenz, and Keith W. Van Patten “High-Resolution Velocity Estimation for All-Digital, ac Servo Drives”, IEEE Trans. Ind. Appl., vol. 27,no 4, pp. 701 – 705, July./August. 1991.

[22] P. L. Jansen and R. D. Lorenz, “Transducerless position and velocity estimation in induction and salient AC machines,” IEEE Trans. Ind. Appl., vol. 31, pp. 240–247, Mar./Apr. 1995.

[23] Matthew J. Corley and Robert D. Lorenz, “Rotor Position and Velocity Estimation for a Salient-Pole Permanent Magnet Synchronous Machine at Standstill and High Speeds”, IEEE Trans. Ind. Applicat., vol. 34,no 4, pp. 784 – 789, July./August. 1998.

[24] S. Zaim, J.P. Martin, B. Nahid-Mobarakeh, F. Meibody-Tabar “High Performance Low Cost Control of a Permanent Magnet Wheel Motor Using a Hall Effect Position Sensor”, Vehicle Power and Propulsion Conference (VPPC), 2011 IEEE, pp.: 1-6.

[25] Lidozzi, A.; Solero L.; Crescimbini, F.; Di Napoli, A; “SVM PMSM Drive With Low Resolution Hall-Effect Sensors”, IEEE Trans. Power Electronics, vol. 22, no. 1, Jan. 2007.

[26] Pooya Alaeinovin, Sina Chiniforoosh, and Juri Jatskevich, “Evaluating Misalignment of Hall Sensors in Brushless DC Motors”, 2008, IEEE Electrical Power & Energy Conference,pp.:1-6.

[27] Samoylenk, N.; Han, Q.; Jatskevich J.; “Dynamic Performance of Brushless DC Motors With Unbalanced Hall Sensors” IEEE Trans. Energy. Conv., vol. 23, no 3, pp. 752 – 763, Sept. 2008.

[28] S. Tsotoulidis, A. Safacas, “Side-effects of Hall Sensors Misplacement on BLDC Motor Drive Operation”, Electrical Machines (ICEM), 2014 International Conference on, 2014, pp.: 1825-1830.

[29] Sam-Young Kim, Chinchul Choi, Kyeongjin Lee, and Wootaik Lee, “An Improved Rotor Position Estimation With Vector-Tracking Observer in PMSM Drives With Low-Resolution Hall-Effect Sensors”, IEEE Trans. Ind. Elec., vol. 58, no 9, pp. 4078 – 4086, Sept. 2011.

[30] Philip B. Beccue, Steven D. Pekarek, Bradley J. Deken, and Andreas C. Koenig “Compensation for Asymmetries and Misalignment in a Hall-Effect Position Observer Used in PMSM Torque-Ripple Control” IEEE Trans. Ind. Appl., vol. 43,no 2, pp. 560 – 570, March./April 2007.

[31] P. Beccue, J. Neely, S. Pekarek, and D. Stutts, “Measurement and control of torque ripple-induced frame torsional vibration in a surface mount permanent magnet machine,” IEEE Trans. Power Electron., vol. 20, no. 1, pp. 182–191, Jan. 2005.

[32] Dalala, Z.M.; Younghoon Cho; Jih-Sheng Lai, “Enhanced Vector Tracking Observer for Rotor Position Estimation for PMSM Drives with Low Resolution Hall-Effect Position Sensors”, Electric Machines & Drives Conference (IEMDC), 2013 IEEE International, 2013, pp.: 484-491.

[33] A. Tashakori, and M. Ektesabi, “A Simple Fault Tolerant Control System for Hall Effect Sensors Failure of BLDC Motor”, in proc. of IEEE Industrial Electronics and Applications, ICIEA 2013, pp. 1011-1016, Jun. 2013.

[34] Hrishikesh Mehta, Ujjwala Thakar, Vrunda Joshi, Kirti Rathod and Pradeep Kurulkar “Hall Sensor Fault Detection and Fault Tolerant Control of PMSM Drive System” Industrial Instrumentation and Control (ICIC), 2015 International Conference on, 2015, pp.:624-629.

Chapter 6 Conclusions and recommended future work

The main line of this research activity has been focused on the study and implementation of fault-tolerant multi-drive systems; after a detailed overview of the state of art, mostly oriented to single drives, a MDS consisting of multiple three-phase drives has been investigated in Chapter 2. The presence of many electric drives allows to form a structure that, intrinsically, offers more freedom degrees of a single drive and can be used to tolerate continuous and safety operation after one or more faults. In particular, an alternative fault tolerant topology based on a cooperative approach has been presented in Chapter 2, where the healthy drives support the faulty ones during post fault operations. The evaluation of pros and cons of the proposed configuration shows that it can be easily applied without increase significantly the MDS cost, ensuring a limited performance reduction compared with other technical solutions.

In Chapter 3, the fault tolerant topology presented in Chapter 2 has been applied to a Wind Power System equipped with a PMSG and a transformer. Also in this case, a single fault on the generator side or in the primary side of the transformer, could cause serious losses of incoming and perturbation on the main grid, hence the capability of the whole system to deliver power to the grid, also after a fault on the generator or on the primary side of the transformer, is significant.

A common property that allows to faulty three phase drives to operate, is the application of two independent currents on the healthy phases, this is possible thanks to the connection of the neutral point of the stator windings of the faulty machines with that one of the healthy machines. The sharing of the current that flows from the faulty to the healthy drives, has been investigated in detail in Chapter 4, where three different current sharing methods have been presented, evaluating the additional power losses caused by the flow of the additional zero current flow.

Another key aspect of fault tolerant related to motor drives regards the capability to overcome single or multiple faults in the rotor position sensors. Chapter 5 is dedicated to this issue, and a suitable fault tolerant rotor position estimation is studied and implemented in case the rotor position is provided with low cost hall effect sensors. As well know, high performance vector control implementation requires the knowledge of the rotor position and in particular for BLDC drives, this is used to select the power converter states; when the rotor position information is wrong or not correct estimated, the power converter firing sequence is wrong too and the drive will be unstable. This issue has to be avoided especially in a MDS where healthy drives could be stressed by torque ripple caused by the faulty units. The activity reported in this chapter has been dedicated to the estimation of the correct rotor position also when one or more hall effect sensors are faulty, using a suitable compensation; three different estimation algorithms have been tested and compared.

On the base of the activity aforementioned some aspects could be further investigated in order to improve the fault tolerant capability and performance of the drive:

The transient from healthy to faulty condition in a single or more drives is crucial and the behavior between these two status, including the modification required to the PWM and the operation in flux weakening region need to be investigated with more detail.

Experimental tests with MDS consisting of multiple faulty drives have not been made. Although theoretically investigated, multiple faulty drives could require other adjustment in terms of harmonic compensation, similarly to what has been done in case of single faulty unit. This aspect should be verified from practice tests.

The cooperative approach that allows to create a current path, exploiting the configurations described in Chapters 2, 3 and 4, can be used as a way for sharing information and shared information can help faulty drives in low cost applications as in Chapter 5.

The connection among the neutral point of the stator windings of the faulty and healthy machines could be used to carry out other useful information, for instance, estimating the operative conditions of the drives and rotor position.

The DC bus utilization is reduced from healthy to faulty operative conditions, therefore could be useful to improve the DC bus utilization factor also in faulty conditions, especially when the faulty drive also works in flux-weakening region.

Application of different type of control techniques such as “model predictive control” that are recently presented and represent a new frontier in the drive control, could be applied also in the faulty drives and could be remarkable to evaluate the drive performance with these type of techniques.

Appendix

Tuning procedure of the current and speed control loops

The following general procedure can be applied both for IM and PMSM drives considering that the cross-coupling terms of the current and speed loops are perfectly decoupled.

A. Continuous time domain

In continuous time domain, this procedure can be followed:

1) The equation of the plant in Laplace domain is defined from the time domain differential equations.
2) The transfer function, fdt, of the closed loop system is calculated, including the controller.
3) Considering the denominator of the fdt, the desired poles have to be set.
4) Calculate the controller gains.

Current loop with standard PI controller

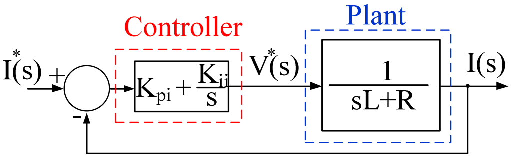

Figure A1 Closed loop system in Laplace domain in case of the current control.

Step 1)

$$V(t) = Ri(t) + L\frac{d}{dt}i(t) \rightarrow V(s) = (R+sL)I(s) \rightarrow \frac{I(s)}{V(s)} = \frac{1}{sL+R} \qquad (1)$$

V is the voltage

I is the current

L is the inductance

R is the resistence

Step 2)

$$\frac{I(s)}{I^*(s)} = \frac{K_{pi}\,s + K_{ii}}{s^2L+(K_{pi}+R)s+K_{ii}} = \frac{(1/L)(K_{pi}\,s+K_{ii})}{s^2+\frac{(K_{pi}+R)}{L}s+\frac{K_{ii}}{L}} \qquad (2)$$

Step 3)

$$s^2+\frac{(K_{pi}+R)}{L}s+\frac{K_{ii}}{L} = s^2+(P_{1i}+P_{2i})s+P_{1i}\,P_{2i} \qquad (3)$$

$s^2+(P_{1i}+P_{2i})s+P_{1i}\,P_{2i}$ is the polynomial expression containing the desired poles P_{1i} and P_{2i}.

$P_{1i} = 2\pi\, f_{1i}$; $P_{2i} = 2\pi\, f_{2i}$;

f_{1i} and f_{2i} are the poles frequency and can be set: $f_{2i} = (5\div10)f_{1i}$.

Step 4)

The controller gains are expressed with the following expressions:

$$K_{pi}=L\,(P_{1i}+P_{2i})-R$$
$$K_{ii}=L\,P_{1i}\,P_{2i} \tag{4}$$

Speed loop with standard PI controller

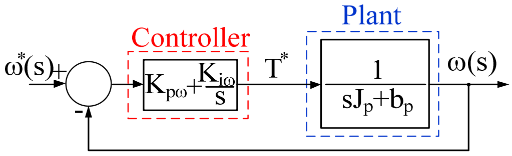

Figure A2 Closed loop system in Laplace domain in case of speed control.

Step 1)

$$T_e(t) = b_p\omega(t) + J_p\frac{d}{dt}\omega(t) \rightarrow T_e\,(s) = (b_p+s\,J_p)\omega(s) \rightarrow \frac{\omega(s)}{T_e(s)} = \frac{1}{sJ_p+b_p} \tag{5}$$

T_e is the electromagnetic torque

ω is the angular speed

J_p is the system inertia

b_p is the viscous dumping

Step 2)

$$1)\quad \frac{\omega(s)}{\omega^*(s)} = \frac{K_{p\omega}\,s+K_{i\omega}}{s^2J_p+(K_{p\omega}+b_p)s+K_{i\omega}} = \frac{(1/J_p)(K_{p\omega}\,s+K_{i\omega})}{s^2+\frac{(K_{p\omega}+b_p)}{J_p}s+\frac{K_{i\omega}}{J_p}} \tag{6}$$

Step 3)

$$s^2+\frac{(K_{p\omega}+b_p)}{J_p}s+\frac{K_{i\omega}}{J_p} = s^2+(P_{1\omega}+P_{2\omega})s+P_{1\omega}\,P_{2\omega} \tag{7}$$

$P_{1\omega} = 2\pi\, f_{1\omega}$; $P_{2\omega} = 2\pi\, f_{2\omega}$

Step 4)

The controller gains are expressed with the following expressions:

$$K_{i\omega}= J_p\,P_{1\omega}\,P_{2\omega}$$
$$K_{p\omega}= J_p\,(P_{1\omega}+P_{2\omega})-b_p \tag{8}$$

B. Discrete time domain design

The controller tuning in discrete time domain [1] can be performed following the proposed approach and assuming that the power converter acts as an amplifier with unitary gain and the manipulated inputs are keeping constant for the sample time T_S.

1) The equation of the plant in Laplace domain is defined from the time domain differential equation.
2) Apply the "Latch" interface at the manipulated input of 1).
3) Transform in Z domain 2), defining the so called "New system dynamic" NSD.
4) The transfer function, fdt, in Z domain, of the closed loop system is calculated including the controller.
5) Considering the denominator of the fdt, the desired poles can be set.
6) Controller gains determination.

The standard method of the sequential tuning is followed starting from the inner current loop and going on with the outer speed loop.

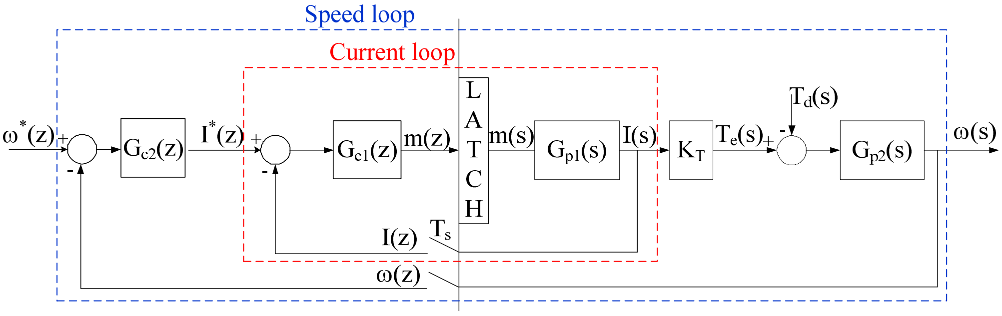

Figure A3 Closed loop system for computer control.

Current loop

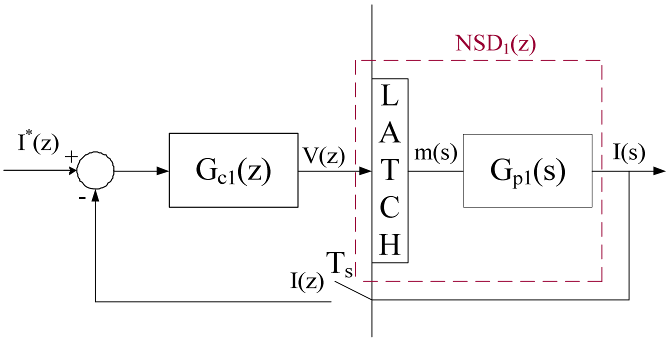

Figure A4 Current control in discrete domain.

Step 1) $G_{p1}(s)$ is the Laplace transform of the real system based on the differential equation with the initial condition sets to 0:

$$G_{p1}(s) = \frac{I(s)}{V(s)} = \frac{1}{sL+R} \quad (9)$$

Step 2) and Step 3) The New System Dynamic, indicated with $NSD_1(z)$, is obtained applying the following relation:

$$\begin{aligned} NSD_1(z) &= \frac{I(z)}{V(z)} = Z\{\text{Latch}\frac{1}{sL+R}\} = Z\{\frac{1-e^{-sT_s}}{s}\frac{1}{sL+R})\} = \\ &= \frac{z-1}{z} Z\{\frac{1}{s}\frac{1}{sL+R})\} = \frac{1}{R}\frac{z-1}{z}\frac{z(1-e^{-aT_s})}{(z-1)(z-e^{-aT_s})} = \frac{1}{R}\frac{(1-e^{-aT_s})}{(z-e^{-aT_s})} \end{aligned} \quad (10)$$

$$a = \frac{R}{L}$$

Step 4) $G_{c1}(z)$ is the state controller in discrete time domain that has for this kind of system the following expression:

$$G_{c1}(z) = K_{co} + \frac{zT_s}{z-1}K_{ico}$$

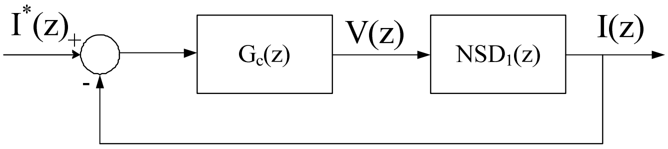

Figure A5 Compact representation of Figure A4.

The tuning process for the current loop will be performed considering the closed loop transfer function of the system as below presented.

$$(I^*(z) - I(z))\,(K_{co} + \frac{zT_s}{z-1}K_{ico})\frac{1}{R}\frac{(1-e^{-aT_s})}{(z-e^{-aT_s})} = I(z)$$

$$I(z)\,[1 + (K_{co} + \frac{zT_s}{z-1}K_{ico})\frac{1}{R}\frac{(1-e^{-aT_s})}{(z-e^{-aT_s})}] = (K_{co} + \frac{zT_s}{z-1}K_{ico})\frac{1}{R}\frac{(1-e^{-aT_s})}{(z-e^{-aT_s})}I^*(z)$$

$$[\frac{R(z-1)(z-e^{-aT_s}) + K_{co}(z-1)(1-e^{-aT_s}) + zT_sK_{ico}(1-e^{-aT_s})}{R(z-1)(z-e^{-aT_s})}]\,I(z) =$$

$$= \frac{K_{co}(z-1)(1-e^{-aT_s}) + zT_sK_{ico}(1-e^{-aT_s})}{R(z-1)(z-e^{-aT_s})}I^*(z)$$

$$\frac{I(z)}{I^{*}(z)} = \frac{\dfrac{K_{co}(z-1)(1 - e^{-aT_s}) + zT_sK_{ico}(1 - e^{-aT_s})}{R\,(z - 1)\,(z - e^{-aT_s})}}{\left[\dfrac{R\,(z - 1)\,(z - e^{-aT_s}) + K_{co}(z-1)(1 - e^{-aT_s}) + zT_sK_{ico}(1 - e^{-aT_s})}{R\,(z - 1)\,(z - e^{-aT_s})}\right]}$$

$$\frac{I(z)}{I^{*}(z)} = \frac{K_{co}(z-1)(1 - e^{-aT_s}) + zT_sK_{ico}(1 - e^{-aT_s})}{R\,(z - 1)\,(z - e^{-aT_s}) + K_{co}(z-1)(1 - e^{-aT_s}) + zT_sK_{ico}(1 - e^{-aT_s})} \tag{11}$$

Step 5) Looking at the denominator of (11), it is possible to set the poles defining the gains of the controller.

$$Rz^2 + [-R - R\,e^{-aT_s} - K_{co}\,(e^{-aT_s} - 1) - K_{ico}T_s(\,e^{-aT_s} - 1)]z + R\,e^{-aT_s} + K_{co}(\,e^{-aT_s} - 1)$$

The characteristic polynomial expression is (12):

$$(z - P_1)(z - P_2) = z^2 - (P_1 + P_2)z + P_1P_2 \tag{12}$$

It is possible to set P_1 and P_2 as the desired poles and matching the denominator with (12) and thus determine the gains controller equations.

$$\frac{[-R - R\,e^{-aT_s} - K_{co}\,(e^{-aT_s} - 1) - K_{ico}T_s(\,e^{-aT_s} - 1)]}{R} = -\,(P_1 + P_2)$$

$$\frac{Re^{-aT_s} + K_{co}(e^{-aT_s} - 1)}{R} = P_1P_2$$

Step 6) Controller gain equations:

$$K_{co} = \frac{R(P_1P_2 - e^{-aT_s})}{(e^{-aT_s} - 1)} \tag{13}$$

$$K_{ico} = \frac{R(P_1+P_2) - K_{co}(e^{-aT_s} - 1) - R - R\,e^{-aT_s}}{T_s(e^{-aT_s} - 1)} \tag{14}$$

$P_1 = e^{-2\pi f_1T_s}$; $P_2 = e^{-2\pi f_2T_s}$

f_1 and f_2 are the desired cut-off frequencies, usually $f_2 = (5\div10)\,f_1$.

Speed loop.

The following procedure for the speed loop controller tuning is simplified because it is assumed that the instantaneous velocity is known. In reality only sensor positions are used and they provide the rotor position; starting from this information the average velocity can be calculated and not the instantaneous one.

Since the dynamic of the electrical system is faster than that of the mechanical one, the speed loop tuning can be made, considering the current loop as an amplifier with unitary gain.

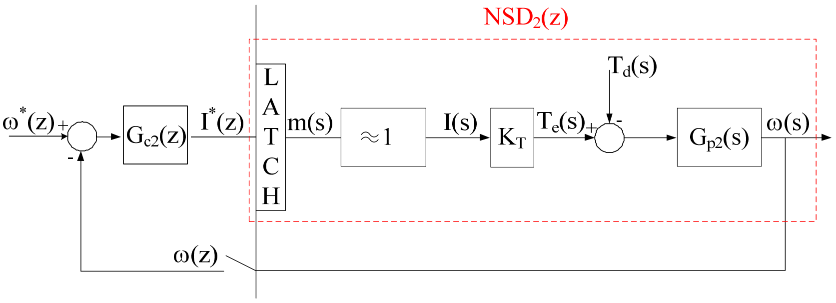

Figure A6 Speed closed loop for computer control.

Applying the previous procedure we get:

Step 1) The Laplace transform of the differential equation, considering the initial condition 0:

$$G_{p2}(s) = \frac{\omega(s)}{T_e(s)} = \frac{1}{sJ_p + b_p} \tag{15}$$

Equation (15) links the speed and the torque; this last relationship can be expressed as $T_e = K_T I$, where K_T is the torque constant.

Step 2) and Step 3) The $NSD_2(z)$ is defined in equation (16):

$$\begin{aligned} NSD_2(z) &= \frac{\omega(z)}{T_e(z)} = Z\{\text{Latch}\,\frac{1}{sJ_p+b_p}\} = Z\{\frac{1-e^{-sT_s}}{s}\,\frac{1}{sJ_p+b_p})\} = \\ &= \frac{z-1}{z} Z\{\frac{1}{s}\,\frac{1}{sJ_p+b_p})\} = \frac{1}{b_p}\,\frac{z-1}{z}\,\frac{z(1-e^{-aT_s})}{(z-1)(z-e^{-aT_s})} = \frac{1}{b_p}\,\frac{(1-e^{-aT_s})}{(z-e^{-aT_s})} \end{aligned} \tag{16}$$

$$a = \frac{b_p}{J_p}$$

Considering the relation between torque and current:

$$NSD_2(z) = \frac{\omega(z)}{I(z)} = \frac{K_T}{b_p}\,\frac{(1-e^{-aT_s})}{(z-e^{-aT_s})} \tag{17}$$

Step 4) $G_{c2}(z)$ is the state controller in discrete time domain represented in the following expression as:

$$G_{c2}(z) = K_{p\omega} + \frac{zT_s}{z-1} K_{i\omega}$$

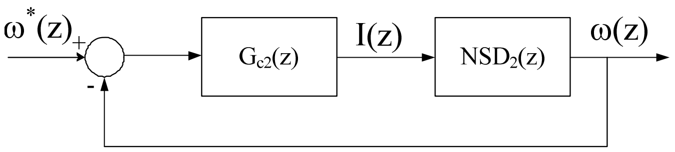

Figure A7 Equivalent representation of Figure A6.

The closed loop transfer function is:

$$\frac{\omega(z)}{\omega^*(z)} = \frac{K_T K_{p\omega}(z-1)(1 - e^{-aT_s}) + zT_s K_T K_{i\omega}(1 - e^{-aT_s})}{b_p\,(z - 1)\,(z - e^{-aT_s}) + K_T K_{p\omega}(z-1)(1 - e^{-aT_s}) + zT_s K_{i\omega}\,K_T\,(1 - e^{-aT_s})} \qquad (18)$$

Step 5) Considering the denominator of (17)

$$b_p z^2 + [-b_p - b_p\,e^{-aT_s} - K_T K_{p\omega}\,(e^{-aT_s} - 1) - K_T K_{i\omega} T_s(\,e^{-aT_s} - 1)]z + b_p\,e^{-aT_s} + K_T K_{p\omega}(\,e^{-aT_s} - 1)$$

and defining a characteristic polynomial expression as (19):

$$(z - P_{1\omega})(z - P_{2\omega}) = z^2 - (P_{1\omega} + P_{2\omega})z + P_{1\omega}P_{2\omega} \qquad (19)$$

The results shown in Step 6) will be obtained comparing the two previous equations:

Step 6)

$$K_{p\omega} = \frac{b_p\,(P_{1\omega}P_{2\omega} - e^{-aT_s})}{K_T\,(e^{-aT_s} - 1)} \qquad (20)$$

$$K_{iw} = \frac{b_p\,(P_{1w}+P_{2w}) - K_T K_{pw}(e^{-aT_s} - 1) - b_p - b_p\,e^{-aT_s}}{K_T T_s(e^{-aT_s} - 1)} \qquad (21)$$

$P_{1\omega} = e^{-2\pi f_{1\omega} T_s}$; $P_{2\omega} = e^{-2\pi f_{2\omega} T_s}$

$f_{1\omega}$ and $f_{2\omega}$ are the desired cut-off frequencies, usually $f_{2\omega} = (5 \div 10)\, f_{1\omega}$.

References

[1] R.D. Lorenz, lecture notes from the course ME 601/547 “Physics Based Modeling for computer control”, University of Wisconsin, Madison, 2014.

[2] G. Scarcella, lecture notes from the course of “Electric Drives”, University of Catania, Catania, 2014.

[3] G. Nunnari, lecture notes from the course of “Automatic control systems”, University of Catania, Catania, 2008.

[4] P. Bolzern, R. Scattolini, N. Schiavoni, “Fondamenti di controlli automatici”, McGraw-Hill.